Spin and energy transport in boundary-driven low-dimensional open quantum systems

Juan José Mendoza Arenas

Jesus College, Oxford

A thesis submitted to the Mathematical and Physical Sciences Division

for the degree of Doctor of Philosophy in the University of Oxford

Trinity Term, 2014

Atomic and Laser Physics,

University of Oxford

Spin and energy transport in boundary-driven low-dimensional open quantum systems

Juan José Mendoza Arenas, Jesus College, Oxford

Submitted for the degree of Doctor of Philosophy

Trinity Term 2014

Abstract

In spite of being the subject of intense research, several key but complex questions on the nonequilibrium physics of correlated quantum systems remain controversial. For example, the nature of particle and energy transport in different interacting regimes, the relevance of integrability and the impact of environmental coupling are still under active debate. These problems can now be approached numerically, due to the development of powerful algorithms which allow the efficient simulation of the dynamics of correlated systems.

In the present thesis we study numerically and analytically the transport properties of low-dimensional quantum systems. In particular, we consider the steady-state spin and energy conduction through XXZ boundary-driven spin-1/2 chains. In the first part, we analyse the transport through chains with only coherent processes in the bulk. For spin transport induced by a magnetisation imbalance between the boundaries, previously identified ballistic, diffusive and negative differential conductivity regimes are reproduced. We provide a comprehensive explanation of the latter. The energy conduction induced by this driving scheme features the same properties as spin transport. For thermally-driven chains, we discuss the nature of energy transport and the emergence of local thermal states when the integrability of the Hamiltonian is broken.

In the second part of the thesis we analyse the effect of bulk incoherent effects on the transport properties previously discussed. First we find that for weak particle-particle interactions, pure dephasing degrades spin and energy conduction. In contrast, for strong interactions dephasing induces a significant transport enhancement. We identify the underlying mechanism and discuss its generality. Finally, motivated by the lattice structure of several organic conductors, we study the interplay between coherent and incoherent processes in systems of weakly-coupled chains. We find an enhancement effect due to incoherent interchain hopping, stronger than that by dephasing, which increases with the chain length and relates to superdiffusive transport.

Acknowledgements

Throughout the four years I spent in Oxford, several people have provided me their support, for which I am very grateful. First of all, I would like to thank my supervisor, Prof. Dieter Jaksch, for giving me the opportunity to work under his direction. His deep insight into physics has provided a fundamental guidance for the work developed in the present thesis, and his high expectations have been both strongly challenging and motivating.
Second, I would like to specially acknowledge the large input of Dr. Stephen Clark into the research discussed in my thesis. I have learnt a lot from my work with him, from physics to what being a researcher means. I am very thankful I could closely work with him for various years.
I am also very grateful to the several colleagues who I had the pleasure to work with. Firstly I wish to thank Thomas Grujic, who guided me during my first year in Oxford. Similarly I want to thank Mark Mitchison, with whom I performed a fruitful and enjoyable research in the second half of my DPhil. I also thank Sarah Al-Assam, Pierre-Louis Giscard, Javier Prior and Martin Plenio for their valuable collaboration in the different projects in which I was involved during my time in Oxford, and Giovanni Cotungo, Santiago Caballero and Christian Schilling for the friendly conversations in which a few times we were involved.
I am also indebted with many people outside the office. I wish to thank my two-year flatmate and friend Jaqueline, with whom I enjoyed several-hour conversations of any topic we could encounter. I also largely appreciate the friendship of Jed, Tom, and several of the Colombians I met during the last year. I extend my thanks to Felix, with whom I shared many great times. I also thank a lot Esteban, Sergio, Kristell, Diego and Jorge for their friendship through the distance.
Finally, I want to express how much I owe to my family, specially to my parents Juan José and Amparo, and my sister Sandra. During these four years, their constant support and advise have been the most valuable gift I have received. The realisation of this work would have not been possible without them. It is they to whom this thesis is dedicated.

Juan José Mendoza Arenas, Oxford, 2014

Contents

List of Figures

Chapter 1

Introduction

1.1 Transport properties of one-dimensional quantum spin lattices

For several years, a massive amount of attention has been directed towards the physics of correlated quantum systems. The strong correlations emerging from interactions between particles lead to several fascinating many-body quantum effects such as high-temperature superconductivity [1], topological insulating states [2] and magnetic ordering [3, 4]. In particular, one-dimensional spin chains constitute some of the most extensively studied systems in condensed matter, being well known even from the early days of quantum mechanics. However, in spite of being often described by simple Hamiltonians, spin systems contain intricate physics whose unravelling can be quite involved. Additionally, their number of degrees of freedom grows exponentially with their size. Several of their properties thus remain controversial, and more efforts are required to clarify them. The aim of the present work is to help elucidate some of these properties, in particular those of magnetisation and energy transport under different conditions.

One of the best known spin models, which describes very well several mag-

netic materials, is given by the one-dimensional spin-1/2 XXZ Hamiltonian. This model features the simplest competition between excitation hopping and interaction processes, and thus stands as a testbed to illustrate general physical properties of low-dimensional quantum systems. Even though the model is exactly solvable by means of the Bethe ansatz technique [5, 6], and its ground state phase diagram is very well known [7], a widely-accepted picture regarding some of its transport properties has just recently emerged. Specifically, several studies have evidenced that the spin transport is ballistic in the weakly interacting regime and diffusive for strong interactions [8–13], while the energy transport is ballistic for any interaction regime [8, 13–19].

Interestingly, very recent research has shown that this is not the end of the story. Using a non-equilibrium driving mechanism of unequal boundary reservoirs, several new transport properties have been identified in the XXZ model, including negative differential conductivity [20, 21], superdiffusion [12, 22], and different anomalies [23–25] and current scaling forms [25] induced by particular boundary driving schemes. The first part of the present thesis is precisely devoted to explore, under similar driving conditions, novel features of non-equilibrium steady states of spin-1/2 XXZ chains supporting magnetisation and energy transport.

Over the years, several methods have been developed to overcome the challenges of studying correlated one-dimensional quantum systems. Some of the most significant advances in this regard have been achieved during the last decade, including powerful tensor network algorithms. These methods constitute the most successful numerical approaches to efficiently calculate properties of large systems such as ground states and low-lying excitations (see [26–29] for extensive reviews). Time evolution under unitary and dissipative dynamics can also be efficiently simulated by one of the most renowned tensor network algorithms, the Time Evolving Block Decimation (TEBD) [30–32]. This method has been extensively used to anal-

yse transport properties of several correlated systems, including those of the XXZ model previously mentioned [9–13, 20–22]. Given its success in performing efficient simulations of the time evolution of these systems, TEBD constitutes the main calculation tool of our research.

In parallel to the development of tensor network algorithms, seminal advances have been made on the implementation of quantum simulators [33], and particularly on cold atomic gases in optical lattices [34]. These configurations were conceived, among others, as a means to reproduce the properties of models describing complex condensed matter systems, thus helping researchers understand the physics of such systems. Some examples of their success, in relation to our research, correspond to the recent simulation of antiferromagnetic ordering [35] and transport of magnetic excitations [36]. Additionally, setups of out-of-equilibrium cold gases induced by thermal or particle boundary driving have been recently implemented [37–39]. Thus these systems represent an ideal setting to observe experimentally several predictions regarding the behaviour of low-dimensional correlated systems, including the transport properties discussed in the present work.

1.2 Conduction enhancement by environmental coupling

The unavoidable coupling of a quantum system to environmental degrees of freedom has usually been considered to be a negative feature. Intuitively, it is expected that minimising the impact of this coupling improves the performance of the system to realise tasks governed by quantum dynamics. In fact, the large timescale of environmental couplings of cold atomic gases in optical lattices (compared to the timescale of physical processes of interest) makes them very appealing realisa-

tions of this desired behaviour. Nevertheless, recent experimental and theoretical research has shown that under some circumstances, the coupling of the system to the environment is actually beneficial.

Most of this unexpected insight has come from the physics of biological systems, and in particular from natural light-harvesting complexes. These systems, existing in plants and several other living organisms, collect energy from sunlight, and efficiently transfer it in the form of excitons towards reaction centers. Once there, chemical processes leading to photosynthesis are triggered. Since light-harvesting complexes exist at conditions of ambient temperature and humidity, it would be natural to assume that the exciton transfer process is completely governed by classical hopping between the constituting sites. But surprisingly, recent spectroscopic experiments showed that quantum coherences between sites could be sustained even at ambient temperature, on the timescale of the exciton transfer process [40, 41]. Expecting that nature would have evolved to optimise biological processes, it was argued that the most efficient transfer could be achieved by a proper balance between coherent exciton transfer and decoherence effects due to the coupling to the environment. Theoretical studies on toy models for light-harvesting complexes showed that this is in fact the case [42, 43].

A beneficial role of environmental coupling of quantum systems has been identified in various scenarios, including transfer processes in different types of configurations [44], and other biological processes [45], which correspond to single-particle phenomena. Less known are schemes where many-body physics can receive a positive impact from the environment. Some examples correspond to the dissipative engineering of correlated many-body states [46, 47], and the emergence of power-law time-decaying correlations in systems which, in the absence of environmental coupling, would feature an exponential decay [48]. However, no many-body environment-assisted transport schemes had been found. The second part of the

present thesis is focused on identifying true many-body magnetisation and energy transport enhancement effects in XXZ spin chains due to environmental coupling, and to unravel the physical processes underlying them.

1.3 Thesis overview

In the present thesis we explore the non-equilibrium steady state transport properties of spin-1/2 chains described by the one-dimensional XXZ model, driven by unequal reservoirs at the boundaries. We start by revisiting previously-observed effects of spin transport, mostly focusing on the origin of negative differential conductivity and ferromagnetic domains at maximal driving. We then explore the energy transport properties induced by different types of driving. When the transport is induced by a temperature imbalance, the notion of local thermalisation arises for systems in the non-integrable regime. Subsequently we study the effect of environmental coupling on transport properties previously described, and show the existence of a conduction-enhancement effect due to local dephasing processes in the strongly interacting regime of the Hamiltonian. An even stronger enhancement effect is then seen to arise by environment-mediated spin hopping between neighbouring spin chains. Since the XXZ Hamiltonian corresponds to a generic model containing the most basic competition between hopping and interaction processes, we expect that the effects uncovered by our work have a more general application. The thesis is structured as follows.

- In Chapter 2 we describe the main features of the one-dimensional spin-1/2 XXZ model, which is the main object of study of the thesis. We first explain its equivalence to a model of spinless fermions, which illustrates the generality of the physics it contains. We then describe the ground state phase diagram of the model and its limit of a small number of excitations. We pay special atten-

tion to the concept of magnon bound states, which is to play a very important role in the physics described in subsequent chapters. Next we provide a brief description of the basic features of the entire eigenstructure of the model. Afterwards we consider the integrability breaking of the Hamiltonian, which is very important for the discussion of Chapter 6. We conclude by discussing experimental realisations of spin models, in magnetic systems and quantum simulators.

- In Chapter 3 we present an introduction to the spin and energy transport properties of the XXZ model. We first describe the spin and energy currents to be studied throughout the thesis, and the types of transport characterising different parameters of the model, namely ballistic and diffusive. Then we discuss the relation between the integrability of the XXZ model and its transport properties. Afterwards we describe various experimental and theoretical methods used in previous research to study the type of transport of the model, and the results obtained. This discussion includes the non-equilibrium scheme that will be used in subsequent chapters to study the conduction of magnetisation and energy through XXZ spin chains.

- In Chapter 4 we give a detailed description of the main method used in our research, the Time Evolving Block Decimation (TEBD). After establishing the types of systems to which the formalism can be applied, we explain the matrix product structure that can be associated to their states. We emphasise the existence of weak correlations in the systems of interest of the present work, which allow the efficient representation of their states by a matrix product structure. We then show how several operations can be performed within this type of description, with the aid of a simple graphical representation. Subsequently we describe the TEBD method, and give some details of its

implementation to calculate non-equilibrium steady states.

- In Chapter 5 we present our results regarding the spin and energy transport properties of systems driven out of equilibrium by a magnetisation imbalance. After describing the driving scheme, we explain the different spin transport regimes known to exist from previous studies [11, 21], namely ballistic transport for weak interactions, diffusive transport for strong interactions and weak driving, negative differential conductivity for intermediate driving, and an insulating state for maximal driving. We perform an analysis on the origin of the latter configuration, and show it to be a genuine many-body effect. We then observe the emergence of energy transport in the same configuration when a homogeneous magnetic field is included. Due to the symmetries of the driving scheme, the features of the energy current are found to be exactly the same as those of the spin current. The emergence of diffusive transport when breaking the integrability of the system is also discussed.

- In Chapter 6 we consider the energy transport induced in the system by a thermal gradient. We find that in the strongly nonintegrable regime, where the energy transport is diffusive, the reduced density operators of neighbouring sites are well approximated by local thermal states, plus corrections to account for the energy current. As the Hamiltonian approaches the integrable regime, this behaviour is lost, and the identification of local temperatures is no longer clear. The emergence of magnetothermal effects is also described.

- From Chapter 7 onwards we consider the transport properties of systems coupled to environmental degrees of freedom in the bulk. First we describe the motivation to consider such a situation, corresponding to the experimental observations of long-lived quantum coherences in light-harvesting complexes. We discuss previous theoretical findings evidencing environment-assisted trans-

port, and mention several other scenarios in which the coupling of a system to its environment results in positive consequences. We also present the model of environmental coupling to be considered in the subsequent two Chapters.

- In Chapter 8 we describe the mechanism of dephasing-assisted spin and energy transport in strongly interacting systems. We consider the configuration of Chapter 5 and include dephasing processes resulting from coupling to local vibrational reservoirs. In the regime of weak interactions, dephasing monotonically degrades transport. On the other hand, for strong interactions, dephasing significantly enhances the conduction through the system. While the effect is stronger at maximal driving, its existence at weak driving is quite surprising. We unravel the mechanism responsible of this enhancing effect, which corresponds to transitions from bound to scattering states induced by energy dissipation. We conclude by discussing the generality of this phenomenon.

- In Chapter 9 we study an even stronger effect of environment-assisted transport. In this case we consider a system composed of one-dimensional spin chains, coupled with each other by means of an environment-mediated incoherent hopping. After discussing the motivation to consider such a configuration, provided by several condensed matter systems, we describe the model to be studied in detail, including a mean-field approximation which makes the numerical simulation of the system feasible. The interchain incoherent coupling is seen to enhance the spin transport even more than dephasing, due to a larger energy dissipation rate. Additionally, the enhancement gets larger with the size of the system, which is related to superdiffusive spin transport.

- We conclude the main body of the thesis in Chapter 10, where the main results are summarised. Possible directions of future research are also discussed.

Chapter 2

Model for interacting spin chains: the XXZ Hamiltonian

For several decades, models of interacting spins have attracted a lot of attention due to their fascinating physical properties. The most prominent example is undoubtedly the spin-1/2 Heisenberg model, which was recognised from the early days of quantum mechanics as a key element to understand the origin of the ferromagnetic behaviour of several systems. This model corresponds to an effective Hamiltonian for a lattice of interacting electrons with overlapping wave functions, and arises from the Pauli exclusion principle and the Coulomb repulsion [3, 4]. The effective spin coupling resulting from the combination of these two effects, known as the exchange interaction, features a very simple form. Nevertheless, extracting information from it has proven to be a quite challenging task, and several analytical and numerical methods have been developed over the years for that purpose. Even now, open questions exist regarding its physical properties, and a lot of effort is still performed to find an answer to them.

Several variations of the Heisenberg model have also proven to be fundamental to describe the physics of several systems. One of the most important is the one-dimensional spin-1/2 XXZ model, which is the simplest spin Hamiltonian describing

the competition between hopping and interactions of excitations. Because of this, it has become one of the most studied models in condensed matter physics, and is usually considered as a testbed to identify general many-body phenomena applicable beyond magnetic systems. This is precisely the case of the research discussed in the present thesis, where studying the physics of the XXZ model has allowed us to identify several novel effects regarding the conduction of excitations and energy, which are expected to be present in a variety of other systems.

Given that our research is mainly focused on the one-dimensional spin-1/2 XXZ model, we start by describing some of its basic properties in the present Chapter. First we explain the form and symmetries of the model, and the meaning of each one of its components. Then we describe some of its eigenstates, including its ground state. We pay significant attention to the concept of bound states of excitations, which is to play a very important role in the research presented in subsequent chapters. We then describe additional terms that break the integrability of the model. Finally we discuss its experimental realisation in different types of systems.

2.1 The XXZ model

Our object of study is the one-dimensional spin-1/2 XXZ model with open boundary conditions and site-dependent magnetic field. For a chain of N sites, the Hamiltonian is[1]

$$H = \sum_{j=1}^{N-1} \tau(\sigma_j^x \sigma_{j+1}^x + \sigma_j^y \sigma_{j+1}^y + \Delta \sigma_j^z \sigma_{j+1}^z) + \sum_{j=1}^{N} B_j \sigma_j^z. \tag{2.1}$$

Here σ_j^α, with $\alpha = x, y, z$, are the Pauli matrices of site j, which satisfy

$$[\sigma_j^\alpha, \sigma_k^\beta] = 2i\epsilon_{\alpha\beta\gamma}\sigma_j^\gamma \delta_{jk}, \quad \text{with } \epsilon_{\alpha\beta\gamma} \text{ the Levi-Civita tensor.} \tag{2.2}$$

[1]Throughout the entire thesis, we set the Planck constant $\hbar$, Boltzmann constant k_B and Bohr magneton μ_B to one.

The coupling $\tau > 0$ represents the exchange interaction between nearest neighbours, Δ is the anisotropy along the z direction (the quantisation axis) and B_j is the magnetic field at site j. The Heisenberg model corresponds to the particular case $\Delta = 1$. Other well-known limits are the XY Hamiltonian, for which $\Delta = 0$, and the Ising model, which corresponds to $\Delta/\tau \to \infty$. An even more general model, the XYZ Hamiltonian, includes a different exchange coupling along x and y directions. These related spin models have also been significantly studied over the years; see for example [4, 7] for discussions regarding several of their properties.

Note that the total magnetisation operator $S^z = \frac{1}{2}\sum_{j=1}^{N} \sigma_j^z$ commutes with the Hamiltonian. This means that the model features rotational symmetry about the z axis, which is known as $U(1)$ symmetry. In addition, when $B_j = 0$ and $\Delta = \pm 1$ the Hamiltonian commutes with the total spin operator along x and y directions $S^{x,y} = \frac{1}{2}\sum_{j=1}^{N} \sigma_j^{x,y}$. Since at those points the Hamiltonian commutes with the total spin operator $\vec{S} = (S^x, S^y, S^z)$, it possesses $SU(2)$ symmetry there. For any anisotropy Δ, the Hamiltonian is also invariant under transformations of the form $\sigma_j^x \to -\sigma_j^x$, $\sigma_j^y \to -\sigma_j^y$, $\sigma_j^z \to \sigma_j^z$ at every site of the chain (flipping along two directions maintains the commutation relations between Pauli matrices). So the Hamiltonian also has $\mathbb{Z}_2$ symmetry. Due to the open boundary conditions, the model is not translationally invariant.

2.2 Equivalence to spinless fermion model

To better understand the role of each term in the Hamiltonian (2.1), we start by transforming it to an equivalent Hamiltonian of spinless fermions. Initially, one would be tempted to associate the ladder operators σ_j^+ and σ_j^-, given by

$$\sigma_j^+ = \frac{1}{2}\left(\sigma_j^x + i\sigma_j^y\right), \quad \sigma_j^- = \frac{1}{2}\left(\sigma_j^x - i\sigma_j^y\right), \tag{2.3}$$

with the creation and annihilation operators of a fermionic excitation, respectively, given that they anti-commute on the same site, i.e. $\{\sigma_j^+, \sigma_j^-\} = 1$. Nevertheless, the ladder operators commute at different sites, so such a simple association does not give the appropriate statistics[2]. To establish a complete equivalence between spin and fermionic operators, the correct commutation relations must be fulfilled everywhere. This is achieved by means of the Jordan-Wigner transformation [49,50]

$$b_j = e^{i\phi_j}\sigma_j^-, \quad b_j^\dagger = e^{i\phi_j}\sigma_j^+, \quad n_j \equiv b_j^\dagger b_j = \sigma_j^+\sigma_j^- = \frac{1}{2}\left(1+\sigma_j^z\right). \tag{2.4}$$

The phase factor ϕ_j at site j is π times an operator that counts the number of spin up operators to the left of j, i.e.

$$\phi_j = \pi \sum_{k=1}^{j-1} b_k^\dagger b_k = \pi \sum_{k=1}^{j-1} \frac{1}{2}\left(1+\sigma_k^z\right). \tag{2.5}$$

With this choice of the phase factor, $b_j^\dagger$ and b_j satisfy fermionic anti-commutation relations, $\{b_j^\dagger, b_k\} = \delta_{j,k}$. Since these operators do not include actual spin degrees of freedom, they are referred to as spinless fermion operators. Thus we have that $b_j^\dagger$ and b_j create and annihilate a spinless fermion at site j respectively, and n_j is the corresponding number operator. Performing the Jordan-Wigner transformation to the Hamiltonian (2.1) without magnetic fields, we get

$$H = 4\tau \sum_{j=1}^{N-1} \left[\frac{1}{2}\left(b_i^\dagger b_{i+1} + b_i b_{i+1}^\dagger\right) + \Delta\left(n_j - \frac{1}{2}\right)\left(n_{j+1} - \frac{1}{2}\right)\right]. \tag{2.6}$$

The first term, corresponding to the $\sigma_j^x\sigma_{j+1}^x + \sigma_j^y\sigma_{j+1}^y$ term of Hamiltonian (2.1), represents the nearest-neighbour hopping of spinless fermions. The second term, which corresponds to $\sigma_j^z\sigma_{j+1}^z$, refers to a nearest-neighbour density-density interac-

[2]This actually corresponds to a map to hard-core bosons, described in Appendix A.

tion with strength Δ. In terms of the spin model, this interaction represents an energy penalty when two neighbouring spins are both aligned in the same direction, i.e. when both are up or down.

Due to the correspondence between Hamiltonians (2.1) and (2.4), in the present thesis we refer to the cases $0 < |\Delta| < 1$ and $|\Delta| > 1$ as weakly- and strongly-interacting regimes, respectively. The case $\Delta = 0$ corresponds to the non-interacting limit, in which the spin excitations (or spinless fermions, in Hamiltonian (2.4)) hop freely between neighbouring lattice sites.

Finally, it is important to make a few remarks. First, the Jordan-Wigner transformation is only valid in 1D. Generalisations to arbitrary spatial dimensions have also been proposed [51]. Second, note that the equivalence between Hamiltonians (2.1) and (2.4) indicates that the physics contained in the XXZ model is not exclusive of magnetic systems, but can also be observed in fermionic systems where both hopping and interactions are present. This motivates using the XXZ model as a testbed for studying general phenomena of correlated one-dimensional quantum systems.

2.3 Ground state phase diagram

Now we discuss some important features of the eigenstructure of the XXZ model. We start by describing its ground state phase diagram, shown in figure 2.1, which in the thermodynamic limit can be exactly obtained from Bethe ansatz calculations [6, 7, 52]. We first consider the case without magnetic field, $B = 0$. For $\Delta < -1$, the ground state is ferromagnetic. It consists of a fully polarised configuration along the z direction, being of the form $|\uparrow\uparrow\cdots\uparrow\rangle$ or $|\downarrow\downarrow\cdots\downarrow\rangle$. Since there is no preference along any z direction, both states are degenerate. For $\Delta > 1$, the ground state is antiferromagnetic. It is tempting to associate the ground state to configurations of

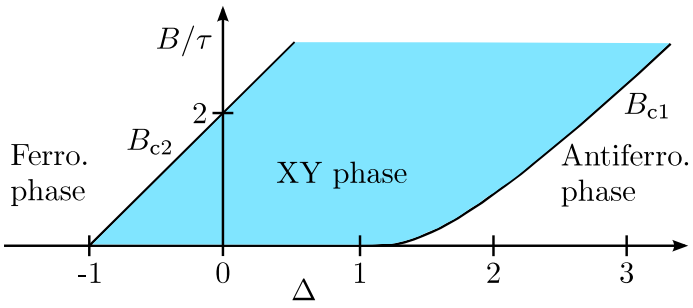

Figure 2.1. Ground state phase diagram of the XXZ model with a homogeneous magnetic field.

the form $|\uparrow\downarrow\uparrow\downarrow\cdots\uparrow\downarrow\rangle$ or $|\downarrow\uparrow\downarrow\uparrow\cdots\downarrow\uparrow\rangle$, corresponding to two interpenetrating sublattices of opposite polarisation. Nevertheless, it is verified by inspection that neither them, nor their symmetric or antisymmetric superpositions are eigenstates of the Hamiltonian for cases different to the Ising limit $\Delta \to \infty$. The actual ground state can be calculated exactly from the Bethe ansatz [6, 7]. In the intermediate regime $-1 < \Delta < 1$ no magnetic order exists. This case is known as XY or paramagnetic state, and by means of bosonisation calculations, it can be shown to correspond to a Luttinger liquid in the continuum limit [53]. Since a finite amount of energy is required to create an excitation over both the ferromagnetic and antiferromagnetic states, they are said to be gapped (or massive). On the other hand, excitations can be created with vanishing energy in the XY phase, so it is gapless (or massless).

When a finite and homogeneous magnetic field is turned on, the phase diagram is significantly altered [6,7]. Since the spins are forced to point along the direction of the field, the ferromagnetic state with polarisation parallel to the field is favoured. The critical magnetic fields B_c separating the magnetically-ordered and disordered phases monotonically increase with Δ. In particular, the critical field B_{c2} separating the ferromagnetic and XY phases is simply $B_{c2} = 2\tau(1 + \Delta)$. The expression for the critical field B_{c1} separating the paramagnetic from the antiferromagnetic phase is more complicated; see [7] for details.

2.4 Dilute limit and magnon bound states

In the present Section we discuss the dilute limit of the XXZ model, in which only a few excitations exist. For simplicity, we consider periodic boundary conditions (so sites 1 and N are also coupled by an exchange interaction), and no magnetic field. Note that for $\Delta < -1$ the following description corresponds to the states of lowest energy, while for $\Delta > 1$ it refers to the highest part of the spectrum. This distinction is important for the physical processes described in subsequent Chapters, where $\Delta \geq 0$ is considered.

2.4.1 Zero excitations

We will take as the state of zero excitations the ferromagnetic configuration in which all spins are pointing down, i.e. $|F\rangle = |\downarrow\downarrow\cdots\downarrow\rangle$[3], whose energy is $E_0 = \tau\Delta N$. Recall that for $\Delta > 1$, this is the most energetic state.

2.4.2 One excitation

With a single excitation in the system (over the state $|F\rangle$), the interaction strength Δ plays no role besides causing an energy shift[4]. Thus the state is that of a free particle in a lattice with periodic boundary conditions, which corresponds to a plane wave. If we denote by $|n\rangle$ the state in which the excitation is located at site n, so $|n\rangle = \sigma_n^+|F\rangle$, and take the lattice spacing equal to 1, the eigenstates of this case are

$$|\psi(k)\rangle = \frac{1}{\sqrt{N}}\sum_{n=1}^{N} e^{ikn}|n\rangle, \quad k = \frac{2\pi m}{N}, \quad \text{with} \quad m = 0, 1, \ldots, N-1. \tag{2.7}$$

[3]The discussion can be equally done considering excitations over the state with all spins pointing up, due to the symmetry of the model.

[4]Note that if the system has open boundary conditions, Δ does play a role, since it provides an on-site potential that is different at the boundaries; see Appendix A.

The corresponding energy is simply given by

$$E(k) = E_0 - 4\tau(\Delta - \cos k) \equiv E_0 + \omega(k), \tag{2.8}$$

with $\omega(k)$ the dispersion relation. These magnetic excitations of bosonic nature are known as magnons, and correspond to spin waves of wavelength $\lambda = 2\pi/k$.

2.4.3 Two excitations

Now we see the case of two excitations, in which the important effect of Δ is first observed. This is done by means of the celebrated Bethe ansatz [5], which can be used to solve the problem for any number of excitations [6,7,52]. To understand the idea behind the ansatz, consider a case in which the two excitations are far from each other, so they propagate as free particles. The first excitation has wave number k_1, and the second k_2. The total energy and momentum are given by $E = E(k_1)+E(k_2)$ and $P = k_1 + k_2$, both being conserved quantities. Now assume that the two excitations get close to each other and scatter, getting new wave numbers k_1' and k_2'. Due to the conservation of energy and momentum, only two outcomes are possible: (1) $k_1' = k_1$ and $k_2' = k_2$, which corresponds to the excitations passing through one another. (2). $k_1' = k_2$ and $k_2' = k_1$, so the momenta are exchanged. The outgoing wave function thus has the form

$$|\psi\rangle = \sum_{1 \le n_1 < n_2 \le N} a(n_1, n_2)|n_1, n_2\rangle, \tag{2.9}$$

where $|n_1, n_2\rangle = \sigma_{n_1}^+ \sigma_{n_2}^+ |F\rangle$ indicates the state where the spins at sites n_1 and n_2 have been flipped, and

$$a(n_1, n_2) = Ae^{i(k_1 n_1 + k_2 n_2)} + A'e^{i(k_1 n_2 + k_2 n_1)}. \tag{2.10}$$

The first term of equation (2.10) corresponds to case (1), and the second to case (2). Also, the relation between both amplitudes is just a phase shift, $A/A' \equiv e^{i\theta}$. Inserting this ansatz into the Schrödinger equation $H|\psi\rangle = E|\psi\rangle$, it is obtained that

$$\frac{A}{A'} = e^{i\theta(k_1,k_2)} = \frac{2\Delta e^{ik_1} - 1 - e^{ik_1+ik_2}}{2\Delta e^{ik_2} - 1 - e^{ik_1+ik_2}}, \tag{2.11}$$

with the energy given by $E = E_0 + \omega(k_1) + \omega(k_2)$, and the dispersion relations being those of equation (2.8) (see details in [6, 52]). If translation invariance is required, by the condition $a(n_1, n_2) = a(n_2, n_1 + N)$, the *fundamental equations* for k_1 and k_2 are obtained,

$$Nk_1 = 2\pi m_1 + \theta, \quad Nk_2 = 2\pi m_2 - \theta, \tag{2.12}$$

where $m_i = 0, 1, \ldots N-1$ are the Bethe quantum numbers. Expressions (2.11) and (2.12) are the Bethe ansatz equations, are their solutions for different types of wave numbers k_1 and k_2 represent states with very different properties. Details of the procedure to obtain analytically and numerically the possible solutions can be found in [6, 52]. Here we describe the main qualitative results. The first case corresponds to k_1 and k_2 being real, which represents two-magnon scattering states. These are superpositions of nearly-free one-magnon states. The second case corresponds to states with complex wave numbers, which satisfy $k_1 = k_2^*$. If we define the relative and center-of-mass coordinates

$$X = n_1 + n_2, \quad K = k_1 + k_2, \quad r = n_2 - n_1 > 0, \quad k = k_1 - k_2, \tag{2.13}$$

so the wave numbers can be written as

$$k_1 = \frac{K}{2} + i\frac{\kappa}{2}, \quad k_2 = \frac{K}{2} - i\frac{\kappa}{2}, \quad \kappa = ik > 0, \tag{2.14}$$

it is easily shown that the amplitude of state $|n_1, n_2\rangle$ is given by

$$a(n_1, n_2) = e^{iKX/2} e^{-i\theta/2} \left(e^{\kappa r/2} e^{i\theta} + e^{-\kappa r/2} \right). \tag{2.15}$$

For the amplitude to be normalised in the limit $N \to \infty$, the phase $e^{i\theta}$ must vanish. From equation (2.11), it is found that for $|\Delta| \geq 1$ this is possible for any total wave number K. On the other hand, in the gapless regime $-1 < \Delta \equiv \cos(\nu) < 1$, this can only be satisfied for total wave numbers above a certain threshold, so these states only exist if $|K| > 2\nu \bmod 2\pi$. Thus for any value of Δ and a certain regime of wave numbers K, the normalised amplitude $a(n_1, n_2)$ decays exponentially with the relative separation between the two magnon excitations r. This corresponds to a configuration where the magnons are very close to each other, having a large interaction energy. In other words, it corresponds to a *bound state* of magnetic excitations. The energy of the state is found to be

$$E = E_0 - 4\tau\Delta + \frac{2\tau}{\Delta}[1 + \cos(K)]. \tag{2.16}$$

The final case corresponds to $k_1 = k_2$, which separates scattering and bound states.

2.4.4 Spinons

We have emphasised that the dilute limit discussed above corresponds to the low-energy zone of the eigenspectrum of the $\Delta < -1$ regime, whose ground state is ferromagnetic, while it describes the highest-energy states for $\Delta > 1$. Notably, the lowest-lying excitations over an antiferromagnetic state are not magnons. Here, for completeness, we give a brief description of the nature of these excitations in the Ising limit $\Delta \to \infty$. The corresponding zero-magnetisation ground state is $|\cdots \downarrow\uparrow\downarrow\uparrow\downarrow\uparrow\downarrow \cdots\rangle$. Now imagine that the central spin is flipped, so the new state

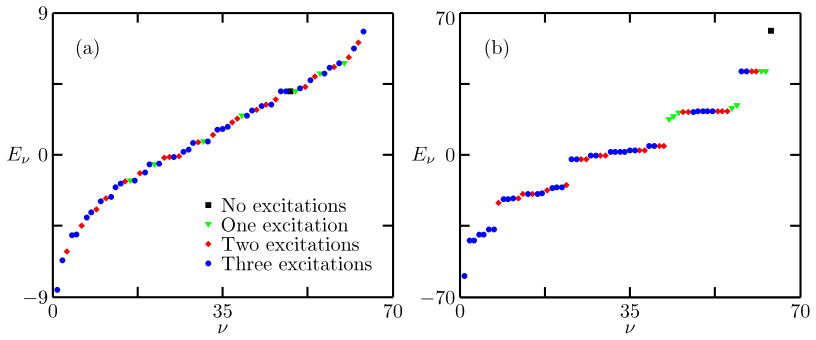

Figure 2.2. Eigenspectrum of the XXZ Hamiltonian for (a) weak interaction $\Delta = 0.5$, (b) strong interaction $\Delta = 10$, which allows the easy identification of the different bands. Here ν denotes the eigenvalue index. The results correspond to $N = 7$ and the sectors $n = 0, 1, 2, 3$. The sectors $n = 7, 6, 5, 4$ give the same bands, due to spin up-spin down symmetry (or particle-hole symmetry, in spinless-fermion language).

has magnetisation $\langle S^z \rangle = -1$. This state has the form $|\cdots\downarrow\uparrow\downarrow\downarrow\downarrow\uparrow\downarrow\cdots\rangle$, where the blue arrow indicates the flipped spin. Since the alignment of the three central spins is energetically expensive, the neighbours of the central spin also flip. The system keeps reducing its energy by spreading out the excitation, in the form $|\cdots\downarrow\uparrow\uparrow\downarrow\uparrow\uparrow\downarrow\cdots\rangle \rightarrow |\cdots\downarrow\downarrow\uparrow\downarrow\uparrow\downarrow\downarrow\cdots\rangle \rightarrow \cdots$. Thus the excitation can be seen as two propagating domain walls, each of spin-1/2, separating blocks of opposite antiferromagnetic ordering. These fermionic excitations are known as spinons. From the Bethe ansatz, the existence of bound spinon states is also predicted [54]. It will become clear from the discussion of Chapters 5 and 8 that even for a regime with antiferromagnetic ground state, it is the magnon bound states who play a pivotal role in several non-equilibrium effects of the XXZ model.

2.5 Eigenspectrum

The complete set of eigenvalues and eigenstates of the XXZ model, for any number of excitations, can in principle be obtained from Bethe ansatz calculations, which

generalise equations (2.9) and (2.10) to consider all possible two-body scattering processes and their corresponding phase shifts. The solutions of the resulting Bethe equations become more intricate as the number of excitations and size of the system increase, but they still predict the existence of bound states of more than two magnons, favoured mostly in the strongly interacting regime $|\Delta| > 1$. Instead of describing these analytic results, we discuss the properties of the eigenstructure of the XXZ model obtained from exact numerical diagonalisation of small systems. Technical details of this implementation, using the magnetisation-conservation symmetry, are given in Appendix B.

To perform the discussion, we go back to the case of open boundary conditions of equation (2.1), which is the model we actually study in our research[5]. In figure 2.2 we show the eigenstructure of a system of 7 sites, in both the weakly- and strongly-interacting regimes, with zero magnetic field. Different colors and symbols correspond to different number of excitations n, defined by

$$n = \frac{1}{2}\left(N + \sum_{j=1}^{N} \langle \sigma_j^z \rangle\right). \tag{2.17}$$

Different types of energy bands are seen depending on the interaction strength. In the case of weak interactions, a single wide band is observed, indicating high mobility[6]. For strong interactions $\Delta > 1$, several bands emerge, which can be well obtained from perturbation theory in the limit $\Delta \gg 1$, as described in Appendix A. The state of highest energy corresponds to zero excitations, i.e. the ferromagnetic state $|F\rangle = |\downarrow\downarrow \cdots \downarrow\rangle$, which is highly unfavored due to the antiferromagnetic nature of the coupling. The following bands, separated between them by gaps of $O(\Delta)$, mix states of different number of excitations. As explained in Appendix A, the

[5] In the strongly-interacting regime, these boundary conditions lead to more bands than those existing with translation invariance, which can be understood from the discussion in Appendix A.4.

[6] Analogous to single-particle bands in a crystal, where curvature relates to an effective mass of the excitation, flattened energy bands imply low mobility.

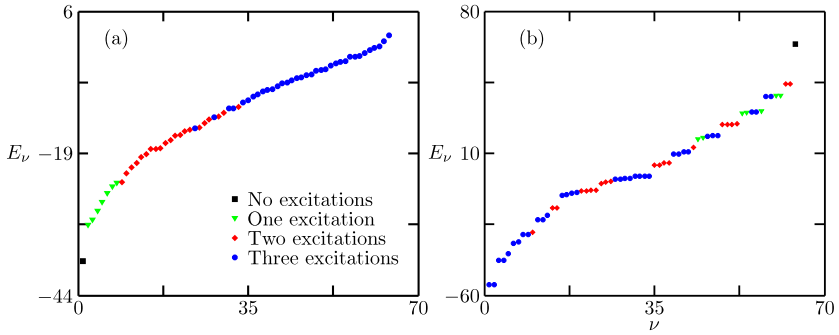

Figure 2.3. Examples of the eigenspectrum of the XXZ Hamiltonian with finite magnetic field. (a) Energies for homogeneous field $B = 3$ and $\Delta = 0.5$. (b) Energies for staggered field $B = 3$ with $\Delta = 10$. Here ν denotes the eigenvalue index. The results correspond to $N = 7$ and the sectors of $n = 0, 1, 2$ and 3 excitations.

highest (and flattened) bands correspond to magnon bound states, with their large energy arising from the strong interaction between the components of the effective bound excitation. The lower and wider bands correspond to scattering states, so their interaction energy is much lower and have more mobility. Note that if Δ takes negative values, the eigenspectra shown in figure 2.2 are inverted. In particular, for $\Delta < -1$, the ground state becomes the zero-excitation (ferromagnetic) state, and the antiferromagnetic configuration becomes the state of highest energy.

If a finite and homogeneous magnetic field B is included in the system, the eigenspectrum is significantly modified. This is illustrated in figure 2.3(a) for the weakly interacting regime, where a large field has been used to emphasise its effects. To understand the result, consider a spin sector of n excitations. Since the spins up are aligned with the field while the spins down point in the opposite direction, all the states of the spin sector are shifted in energy by an amount $B(2n - N)$. As a consequence, the sectors with a larger imbalance between spins up and down have the larger energy shift. It is important to emphasise that the bands of different spin sectors are shifted with respect to each other by the magnetic field, but the internal structure of each spin sector remains unaffected.

2.6 Non-integrable XXZ models

Consider the following variation of the XXZ model,

$$H = \sum_{j=1}^{N-1} \tau_j (\sigma_j^x \sigma_{j+1}^x + \sigma_j^y \sigma_{j+1}^y + \Delta \sigma_j^z \sigma_{j+1}^z) + B \sum_{j=1}^{N} (-1)^j \sigma_j^z, \tag{2.18}$$

with local couplings $\tau_j = (1 + (-1)^j \delta)$. Two new elements have been included, namely a staggered magnetic field of amplitude B, and dimerisation characterised by the parameter δ. As described in Chapters 5 and 6, these terms severely affect the physics resulting from the original XXZ Hamiltonian (2.1). Here we describe the particular effect of the staggered magnetic field on the model.

First we observe how the eigenspectrum of the XXZ model is affected by a finite staggered magnetic field. This is shown in figure 2.3(b), for the strongly-interacting regime. In general, a staggered field splits the energy bands existing in the case $B = 0$, depending on the spatial distribution of the spin excitations. The simplest case to illustrate this point is that of one excitation in an even chain with $\Delta \to \infty$. If $B = 0$, the states $|\uparrow\downarrow\downarrow \cdots \downarrow\rangle$ and $|\downarrow \cdots \downarrow\downarrow\uparrow\rangle$ are degenerate, while if $B > 0$ they experience negative and positive energy shifts, respectively. Nevertheless, highly energetic bound states and more conducting states of lower energy are also present.

A more important consequence of the terms included in Hamiltonian (2.18) is that both break the integrability of the model[7]. In the literature, quantum systems are usually said to be integrable if an infinite number of different local conserved quantities exist, i.e. if an infinite number of operators of the form $Q_n = \sum_j q_{n,j}$ that commute with the Hamiltonian can be built, with $q_{n,j}$ an operator acting on n consecutive sites [57,58][8]. This definition includes all the systems that can be solved by the Bethe ansatz or other analytic techniques, such as the one-dimensional spin-

[7]Except for the noninteracting case $\Delta = 0$, which remains integrable with dimerisation [8, 56].
[8]There is still debate about the best definition of quantum integrability; see for example [59].

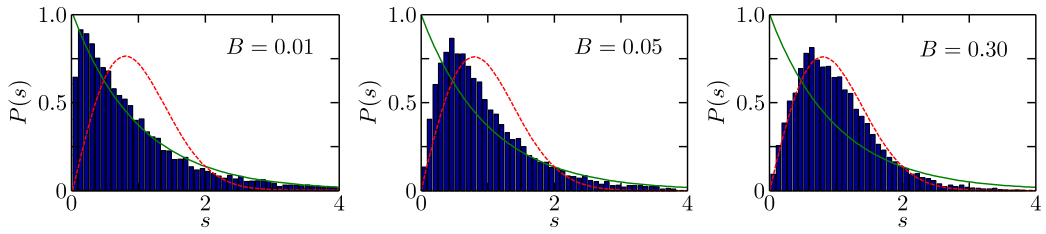

Figure 2.4. Level spacing distribution $P(s)$ for the XXZ Hamiltonian with staggered magnetic field. The solid green line corresponds to the exponential distribution, while the dashed red line indicates the Wigner-Dyson distribution. The results are for $N = 16$, $\Delta = 0.5$, magnetisation sector $\langle S^z \rangle = 0$ and energies $-8 \leq E_\nu \leq 8$. We note that the description by exponential or Wigner-Dyson distributions is only correctly obtained when we restrict to a symmetry sector of the model [55]. In addition, the application of the random matrix theory requires breaking spatial reflection symmetry. For this, the staggered field is not applied to the first site of the chain [21].

1/2 XXZ model (2.1). Determining whether a model is integrable, however, is far from being a simple task, and no systematic method for doing so exists [60].

On the bright side, it has become widely accepted (although not formally demonstrated) that a good indicator of the integrability of a quantum system is given by its Level Spacing Statistics (LSS) [21, 55, 60–64]. For integrable systems, it is expected that neighbouring energy levels correspond to different sets of all the possible conserved quantities, being completely independent from each other. The energy levels thus constitute a Poisson process (i.e. a sequence of randomly-occurring events), and their differences $s_n = E_{n+1} - E_n$ (normalised to the average level spacing) follow an exponential distribution $P_{\mathrm{P}}(s) = e^{-s}$ [65]. On the other hand, chaotic behaviour is expected for strongly non-integrable systems, so the LSS follows a Wigner-Dyson distribution, as obtained from random matrix theory [66]. For systems with time-reversal invariance, and within sectors defined by the other existing symmetries, this is given by[9]

$$P_{\mathrm{WD}}(s) = \frac{\pi s}{2} e^{-\frac{\pi s^2}{4}}. \tag{2.19}$$

[9]Different Wigner-Dyson distributions are obtained with other symmetries; see [60, 66].

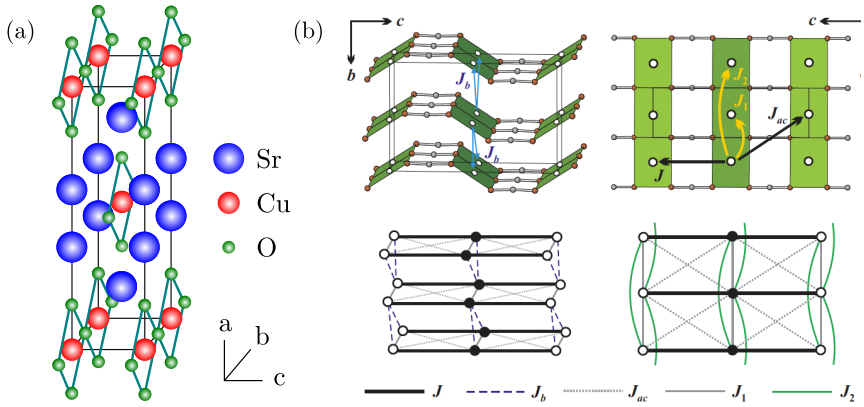

Figure 2.5. Examples of magnetic materials described by one-dimensional spin-1/2 models, (a) antiferromagnetic Sr_2CuO_3 system, and (b) antiferromagnetic CuNCN, seen in different planes. The open circles represent Cu atoms in the center of CuN_4 plaquettes (shadded). The dominant intrachain exchange coupling is $J \sim 2500$ K; the interchain (ferromagnetic) coupling is $J_1 \sim -500$ K; other couplings < 100 K induce small frustration effects. The system can thus be described as consisting of independent spin chains along the c direction. Reproduced from [67] with permission of the authors. Copyright (2014) by the American Physical Society.

In figure 2.4 we show the distribution of the level spacing for the case of a staggered magnetic field; details of the diagonalisation procedure are given in Appendix B. When B is very small, the integrability is weakly broken, so the distribution follows the exponential form. As B increases, the distribution smoothly shifts from the exponential to the Wigner-Dyson tendency, until reaching the latter for large fields.

2.7 Experimental realisation of spin models

2.7.1 Magnetic materials

We finish the present Chapter by briefly discussing some systems that are known to correspond to one-dimensional spin-1/2 models. Firstly, several magnetic systems have been observed to be well described by the XXZ model. The best known realisation of the antiferromagnetic one-dimensional spin-1/2 Heisenberg model ($\Delta = 1$) is the Sr_2CuO_3 spin chain [68–71], whose crystalline structure is shown in figure 2.5.

Neighbouring Cu^{2+} ions located along the b axis interact with each other by an exchange interaction mediated by the intermediate oxygen atoms (a phenomenon known as superexchange [4]). This effective interaction is very large, $\tau \sim 1300-2200$ K. On the other hand, the interaction τ' between Cu^{2+} ions along other directions is very small, $\tau' \sim 0.02 - 0.04$ K [68, 72]. Thus the interchain interactions can be neglected, and the system can be regarded as being composed of independent, one-dimensional spin-1/2 chains.

Several other materials are well described by the one-dimensional Heisenberg model, such as CuNCN [67,73] (whose structure and possible exchange interactions are shown in figure 2.5(b)), $BaCu_2Si_2O_7$ [74], $A_2CuP_2O_7$ (A =Na, Li) [75] and CuPzN [76–78]. Various examples are also known for quasi-one dimensional spin chains in the Ising limit, such as $CoCl_2{\cdot}2H_2O$ [79], $BaCo_2V_2O_8$ [80] and $CoNb_2O_6$ [81]. Less common systems are those featuring $|\Delta| > 1$ but away from the Ising limit. This type of strong anisotropy has been proposed for magnetic materials such as $(NO)Cu(NO_3)_3$ [82], $LiCuVO_4$ [83], TiOCl [84] and $CuGeO_3$ [85], which are usually described by more complicated Hamiltonians than the XXZ chain.

Another important group of materials corresponds to the so-called spin ladders, such as $SrCuO_2$ [71], $(C_7H_10N)_2CuBr_4$ [86], $BiCu_2PO_6$ [87], $CaCu_2O_3$ [88], $Sr_{14-x}Ca_xCu_{24}O_{41}$ [89,90] and some organic radicals [91]. These systems can be described by one-dimensional spin chains coupled with each other by weak exchange interactions. Although we do not analyse their physics in the present thesis, we do propose them as an interesting area of future research, as explained in Section 10.2.

We note that several experiments on magnetic systems verifying the existence of magnon bound states have been performed for almost five decades. This has been achieved by comparing theoretical results including bound-states effects with the results of various types of experiments. Some examples include spectroscopic [92] and magnetic susceptibility measurements [93].

2.7.2 Ultracold atomic systems

Importantly, spin Hamiltonians can also be realised in other types of systems. Schemes to implement these Hamiltonians in several quantum simulators such as optical cavities, trapped ions and superconducting circuits have been extensively discussed; see [33] for a recent review. In particular, ultracold atoms in optical lattices have proven to constitute an ideal setting for such an implementation, due to their high degree of controllability, isolation from the environment [34], and the existence of schemes for single-atom resolution [94, 95]. The simulation of spin models is possible given that for very strong interactions, the Bose-Hubbard model (which describes the physics of ultracold bosons in optical lattices) can be mapped to the spin-1/2 XXZ Hamiltonian [96]. An alternative method corresponds to mapping motional degrees of freedom of each atom to spins. This approach was recently used to simulate one-dimensional antiferromagnetism from a Mott insulating state [35].

A significant advantage of using quantum simulators is their capacity to allow the direct observation of the time evolution of particular states of interest, hard to realise in real materials. A remarkable example is the recent experimental study of the dynamics of magnon bound states [36], which constitutes the first realisation of a quantum walk of interacting excitations in a magnetic system. Using an ultracold bosonic gas in an optical lattice, a one-dimensional isotropic Heisenberg ferromagnet was initially prepared. Then, two neigbouring spins were flipped, resulting in the state $|\cdots\downarrow\downarrow\downarrow\uparrow\uparrow\downarrow\downarrow\downarrow\cdots\rangle$. The evolution of this state, being a superposition of bound and scattering states, was then followed. It was possible to distinguish the dynamics resulting from the scattering and bound-state components, the latter being much slower due to its larger effective mass. This experiment represents a very important step for the future observation of more complex magnetic phenomena in quantum simulators, including the non-equilibrium effects studied in the present thesis.

Chapter 3

Transport properties of the one-dimensional XXZ model

Energy and spin transport properties of one-dimensional spin-chain systems have recently attracted a lot of attention. This is not only caused by the fascinating properties they feature. It is also largely due to the development of quantum simulators with the capability of reproducing physical effects predicted by analytical or numerical analysis [33,34], including transport phenomena. In parallel, the development of powerful numerical techniques based on tensor network structures has also motivated an intense study of the transport properties of low-dimensional systems, including the spin-1/2 XXZ model [9–13, 19, 21, 97–99].

In spite of this massive interest, several controversial questions on transport phenomena remain open, even for the testbed one-dimensional spin-1/2 XXZ Hamiltonian. Since the present thesis is focused on the transport properties of this particular model, an overview of the most important related results obtained from previous research is required. This discussion constitutes the purpose of the present Chapter. We start by introducing the concepts of f and thermal conductivities and Drude weights, basic in the theory of linear response. Then we provide the expressions for spin and energy currents of the XXZ model, which will be considered exten-

sively along the thesis. Subsequently we discuss the implications of integrability on transport properties. Afterwards we describe different nonequilibrium schemes used to study the spin and energy transport of several low-dimensional quantum systems, and discuss the conclusions obtained to date for the XXZ model. These correspond to quantum quenches and boundary driving. Since the latter constitutes the nonequilibrium configuration we use throughout the entire thesis, we establish the particular driving setup to be considered, and the main features of the equation of motion to be simulated. We conclude this Chapter by describing the most important experimental results regarding magnetisation and energy conduction in systems well described by an XXZ Hamiltonian.

3.1 Introduction to linear response theory

We start by briefly reviewing the properties of spin and energy transport within linear response [50, 100, 101]. This regime is characterised by transport processes of the system proportional to external perturbations. If such perturbations are given by gradients of temperature (∇T) and chemical potential ($\nabla \mu$), the induced spin ($\langle \mathcal{J}_1 \rangle$) and thermal ($\langle \mathcal{J}_2 \rangle$) currents are given by

$$\begin{pmatrix} \langle \mathcal{J}_1 \rangle \\ \langle \mathcal{J}_2 \rangle \end{pmatrix} = - \begin{pmatrix} L_{11} & L_{12} \\ L_{21} & L_{22} \end{pmatrix} \begin{pmatrix} \nabla \mu \\ \nabla T \end{pmatrix}, \tag{3.1}$$

where L_{ij} $(i, j = 1, 2)$ are the transport coefficients, and $\mathcal{J}_1$ and $\mathcal{J}_2$ are the total spin and thermal current operators, respectively. The diagonal coefficients represent direct transport. Namely, L_{11} is the spin conductivity in the absence of thermal gradient, and L_{22} the thermal conductivity in the absence of chemical potential gradient[1]. The off-diagonal coefficients correspond to magnetothermal effects. Namely,

[1]The spin conductivity is defined with the condition $\nabla T = 0$. On the other hand, the total thermal conductivity is usually defined under the condition $\langle \mathcal{J}_1 \rangle = 0$, allowing for a finite $\nabla \mu$.

a finite value of L_{12} indicates that a contribution to the spin current is induced by a thermal gradient, a phenomenon known as Seebeck effect. Similarly, a finite L_{21} corresponds to a contribution to the thermal current by means of a gradient of chemical potential, which is known as Peltier effect. Both magnetothermal coefficients are connected by the Onsager relation $L_{21} = TL_{12}$.

The transport coefficients L_{ij} can be directly calculated from the time integrals (in t and t') of current-current correlation functions of the form $\langle \mathcal{J}_i \mathcal{J}_j(t + it') \rangle$, as determined by Kubo formulas (see details, for example, in [50, 101]). From this it can be shown that the real part of each frequency-dependent coefficient L_{ij} is

$$\mathrm{Re}L_{ij}(\omega) = 2\pi D_{ij}\delta(\omega) + L_{ij}^{\mathrm{reg}}(\omega). \tag{3.2}$$

The factor D_{ij}, which multiplies a zero-frequency delta function, is known as the Drude weight; the second term is known as the regular part. A massive amount of research has been devoted to calculate these quantities for the XXZ (see Section 3.3.1) and other models, since they determine the nature of the conduction through the system. Namely, if $D_{ij} > 0$ the corresponding transport coefficient L_{ij} is infinite. This behaviour is referred to as *ballistic transport*. On the other hand, if $D_{ij} = 0$ the transport coefficient is given by the regular part, whose low-frequency limit indicates the type of conduction that the system supports. Specifically, this analysis allows to identify the existence of *diffusive transport* [57,58,99,103–106]. For spin dynamics, in particular, the idea of diffusion was introduced by phenomenological theories of inelastic magnetic scattering [107–109], where the magnetisation of the system satisfies a diffusion equation locally and thus has a finite dc conductivity $L_{11}^{\mathrm{reg}}(\omega \to 0)$ [58][2].

So in general the thermal conductivity is $L_{22} - L_{21}^2/TL_{11}$, reducing to L_{22} in the absence of magnetothermal effects [50, 101, 102].

[2] In 1D spin diffusion can also be identified by a time dependence of spin autocorrelation functions $\langle \sigma_i^z(t)\sigma_i^z(0) \rangle \propto t^{-1/2}$, obtained from the phenomenological approaches [57, 58, 109, 110].

Note that in real systems, measurements of transport coefficients do not give an infinite value. Even if a ballistic response is expected, processes such as scattering with impurities and dissipation broaden the delta function multiplying the Drude weight. Nevertheless, very large conductivities and mean-free paths are usually assumed to indicate ballistic transport of the underlying model, as discussed in Section 3.6 for the XXZ Hamiltonian.

3.2 Spin and energy currents

In this Section we give explicit expressions for the spin and energy current operators of the one-dimensional spin-1/2 XXZ model (2.1), obtained from the corresponding continuity equations [14]. For the case of spin transport, we have

$$\frac{d\sigma_i^z}{dt} = i[H, \sigma_i^z] = J_{i-1} - J_i, \tag{3.3}$$

with $[.,.]$ the commutator between two operators, H the XXZ Hamiltonian (2.1), J_i the spin current operator at site i, and $J_i - J_{i-1}$ the discrete version of the divergence of the spin current. This leads to the definition

$$J_i = 2\tau(\sigma_i^x\sigma_{i+1}^y - \sigma_i^y\sigma_{i+1}^x), \qquad i = 1, \ldots, N-1, \tag{3.4}$$

where the current $\mathcal{J}_1$ introduced in Section 3.1 is $\mathcal{J}_1 = \sum_j J_j$. Note that $\mathcal{J}_1$ is a conserved quantity, i.e. it commutes with the Hamiltonian, only when $\Delta = 0$.

For the thermal current, we consider first the case with zero magnetic field, and define the local Hamiltonian

$$h_{i,i+1} = \tau(\sigma_i^x\sigma_{i+1}^x + \sigma_i^y\sigma_{i+1}^y + \Delta\sigma_i^z\sigma_{i+1}^z), \quad \text{so} \quad H = \sum_{i=1}^{N-1} h_{i,i+1}. \tag{3.5}$$

The energy current operator J_i^{XXZ} follows from the continuity equation

$$\frac{dh_{i,i+1}}{dt} = i[H, h_{i,i+1}] = J_i^{\mathrm{XXZ}} - J_{i+1}^{\mathrm{XXZ}}. \tag{3.6}$$

This leads to the definition

$$\begin{aligned} J_i^{\mathrm{XXZ}} = i[h_{i-1,i}, h_{i,i+1}] &= 2\tau^2(\sigma_{i-1}^y\sigma_i^z\sigma_{i+1}^x - \sigma_{i-1}^x\sigma_i^z\sigma_{i+1}^y) \\ &+ \Delta\tau^2(\sigma_{i-1}^z\sigma_i^x\sigma_{i+1}^y - \sigma_{i-1}^y\sigma_i^x\sigma_{i+1}^z) + \Delta\tau^2(\sigma_{i-1}^x\sigma_i^y\sigma_{i+1}^z - \sigma_{i-1}^z\sigma_i^y\sigma_{i+1}^x), \end{aligned} \tag{3.7}$$

where the current $\mathcal{J}_2$ of Section 3.1 is $\mathcal{J}_2 = \sum_j J_j^{\mathrm{XXZ}}$. In contrast to the total spin current, the total thermal current operator $\mathcal{J}_2$ is conserved for all values of Δ. This important feature determines the nature of energy conduction through the XXZ model, as discussed in Section 3.3.

Finally we note that in the presence of a homogeneous magnetic field B, the thermal current operator becomes

$$\mathcal{J}_2 = \sum_j \left(J_j^{\mathrm{XXZ}} + BJ_j\right); \tag{3.8}$$

details are discussed in Section 5.6. We note that in the literature, $\mathcal{J}_2$ is also referred to as the heat current, and J_i^{XXZ} is the local energy current [50, 101, 102, 111]. When $B = 0$, both names (heat and energy current) are used without distinction.

3.3 Integrability and transport

A very important insight can be obtained about the transport properties of a quantum system from the integrability properties of its underlying Hamiltonian. To illustrate this, imagine that we are interested in the transport characterised by the total current operator $\mathcal{J}$ (such as $\mathcal{J}_1$ or $\mathcal{J}_2$ of Section 3.1, being a spatial sum of local

currents). Then its corresponding Drude weight, denoted by D, satisfies [14, 58]

$$D = \frac{1}{2NT} \lim_{t\to\infty} \langle \mathcal{J}(t)\mathcal{J}(0)\rangle \geq \frac{1}{2NT} \sum_k \frac{\langle \mathcal{J}Q_k\rangle^2}{\langle Q_k^2\rangle}. \tag{3.9}$$

Here N is the size of the system, T is the temperature, and Q_k are commuting local conserved quantities satisfying $\langle Q_k Q_l\rangle = \langle Q_k^2\rangle \delta_{kl}$. These operators are given by $Q_k = \sum_{j=1}^{N} q_j^k$, where q_j^k are density operators of k consecutive sites around site j (and thus are *local* [14, 58]). The first relation indicates that ballistic transport is manifested in non-decaying current autocorrelation functions even in the long-time limit. The second relation[3] is known as Mazur inequality [113], and provides a lower bound for the Drude weight D. If the current of interest $\mathcal{J}$ has a finite overlap with at least one conserved local quantity, equation (3.9) immediately implies that $D > 0$, and the corresponding transport process is ballistic. This is precisely the case for the energy current operator J^{XXZ}, which is itself a conserved quantity since it commutes with the integrable XXZ Hamiltonian for any interaction strength Δ.

This behavior differs from that of the spin transport of the integrable XXZ model. Away from zero magnetisation (half-filled limit, in terms of the equivalent spinless-fermion picture) a finite lower bound is found for the spin Drude weight, indicating ballistic transport [14]. On the other hand, at zero magnetisation there is no overlap between the spin current operator and known local conserved quantities. Recent studies, however, have demonstrated the existence of quasilocal conservation laws[4] with finite overlap with the spin current operator in the weakly-interacting regime $|\Delta| < 1$, leading to a finite spin Drude weight in the thermodynamic limit [114, 115]. For the case $|\Delta| \geq 1$ no lower bound for the Drude weight is known at zero magnetisation, so different approaches are required to identify the

[3] The relation becomes an equality if all local and nonlocal conservation laws are considered [112].

[4] These correspond to finite-norm rapidly-converging series of local operators, whose commutator with the Hamiltonian is given by boundary operators and thus becomes irrelevant in the thermodynamic limit [114].

nature of the corresponding spin transport. Some of these approaches are discussed in the present Chapter.

The previous discussion indicates that the integrability of a model can help demonstrate that its conduction is ballistic, although does not necessarily imply it. For nonintegrable models, in which nontrivial local conservation laws are absent, it is usually expected (although not formally proven) that the corresponding Drude weights vanish, possibly leading to diffusive transport. Even though this is in fact the case for several models, others seem to indicate otherwise. Throughout the rest of the Chapter we provide examples reported so far supporting each conclusion.

3.3.1 Calculation of Drude weights

An intense effort has been performed during several years to calculate Drude weights or current autocorrelation functions of the XXZ model, so the nature of spin and energy transport can be elucidated. Here we summarise the most important results.

Regarding spin transport, most studies have obtained ballistic conduction in the weakly-interacting regime $|\Delta| < 1$, and a zero Drude weight for strong interactions $|\Delta| > 1$, at zero [116, 117], finite [8, 98, 99, 117–119] and infinite temperatures [106, 120][5]. Some of the methods used include the Bethe ansatz [118], exact diagonalisation [8], finite-temperature density matrix renormalisation group (DMRG) [98, 99], and calculations using the concept of quantum typicality [120]. Note that alternative results have also been proposed. In particular, early Monte Carlo calculations suggested finite Drude weights independent of integrability at very low temperatures [121].

Interestingly, the isotropic point $\Delta = 1$ has been a source of unresolved controversy. For example, independent Bethe ansatz calculations give opposing re-

[5] Actually, the regimes very close to $\Delta = 1$ are hard do identify unambiguously. For example, reference [8] obtains that due to the small size of the systems considered, the transport in the region $1 < \Delta < 1.5$ cannot be determined.

sults about the spin Drude weight in this limit, indicating a vanishing [118] or a finite value [117] at any temperature. Exact diagonalisation [8] and DMRG calculations [98, 99] cannot rule out a finite Drude weight at finite temperatures. Using quantum typicality, a very small Drude weight (consistent with a vanishing value in the thermodynamic limit) was found at infinite temperature, while at finite temperatures a finite weight was obtained [120]. For nonintegrable cases, an unified picture has not emerged yet. In some gapped systems, including chains with dimerisation, frustration and a ladder structure, the spin Drude weight was found to vanish at large N [8]. In addition, recent studies with time-dependent DMRG have indicated finite conductivities in systems with weak staggered magnetic fields [55]. On the other hand, a finite weight could not be ruled out in the gapless frustrated system [8, 18].

Studies of the regular part of the spin conductivity $L_{11}^{\mathrm{reg}}(\omega)$ have also shed light into the spin transport properties of the system. Importantly, even if a finite Drude weight exists, the system can still support a diffusive channel, as indicated by the low-frequency behaviour of $L_{11}^{\mathrm{reg}}(\omega)$ [57, 58]. Observations of diffusive spin transport from this type of analysis have been made in the different interaction regimes of the XXZ model, namely for $\Delta < 1$ [57, 58], $\Delta = 1$ [104] and $\Delta > 1$ [103] (where the latter found anomalous pseudo-gaps in the low-frequency regime, which disappear when a size scaling analysis is performed).

For energy transport, finite-temperature calculations of thermal Drude weights and autocorrelation functions indicate ballistic conduction for all anisotropies Δ [8, 15, 18, 56, 122], as expected from the Mazur inequality (3.9). Ballistic magnetothermal transport has also been observed in this form [17, 111, 123]. As in the case of spin transport, a unified result for nonintegrable systems has not been found. Exact diagonalisation studies show a vanishing Drude weight in the thermodynamic limit for ladders, dimerised and frustrated systems [8, 18]. The same conclusion has been obtained for systems with weak staggered magnetic fields [55]. However, recent

time-dependent DMRG calculations indicate ballistic energy transport in dimerised systems [122].

In conclusion, the large amount or research performed on Drude weights and current autocorrelations has suggested the following widely-accepted picture. For integrable systems, spin transport is ballistic for weak interactions and diffusive for strong interactions, while the energy transport is always ballistic. For most integrability-breaking mechanisms, the transport becomes diffusive. However, a definitive result for some particular regimes, including the isotropic limit and some nonintegrable cases, has not been found yet.

3.4 Transport analysis by quantum quenches

The transport properties of several quantum systems have been extensively studied by methods different to the direct calculation of Drude weights and current autocorrelation functions. In particular, a great amount of effort has focused on studying particle and energy transport of low-dimensional systems by directly simulating their real-time evolution. In this section we describe some of the prominent configurations in which this type of analysis has been performed, and discuss the most important conclusions obtained so far for the spin-1/2 one-dimensional XXZ model.

Nonequilibrium configurations of a quantum system can be induced by means of the rapid variation of one or more parameters of its underlying Hamiltonian. If such configurations enforce the flow of particles, energy or magnetisation through the system, they can be used to study its transport properties. This method is known as *quantum quench*, and has been extensively used to analyse the dynamical properties of systems such as cold atoms in optical lattices [124–126] and spin chains [9, 10, 13, 19, 97]. It has also been widely applied to approach related problems such as thermalisation [127, 128] and disorder-induced localisation [64].

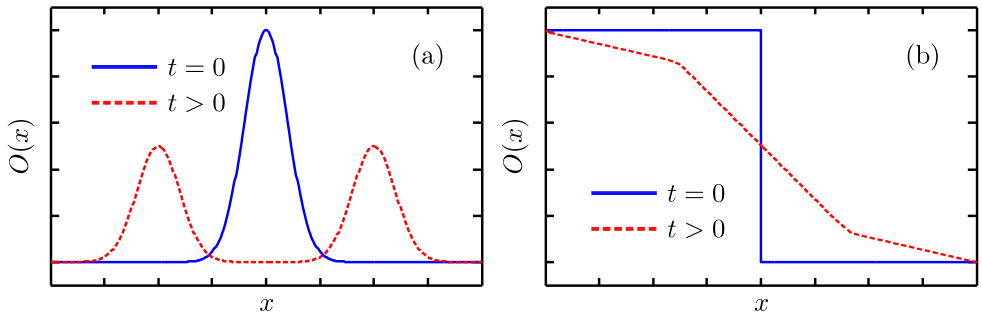

Figure 3.1. Common configurations to study numerically spin and (or) energy transport, corresponding to (a) expansion of a wave packet, (b) dynamics of domain walls. Here we denote by x the spatial coordinate. $O(x)$ refers to the initial magnetisation of energy profile of the system.

For the XXZ model, two types of quantum quenches are commonly used, studied by time-evolving tensor network algorithms for systems much larger than those reached by exact diagonalisation. The first one, depicted in figure 3.1(a), consists of preparing a confined wave packet at time $t = 0$, with a Gaussian or other inhomogeneous state, which evolves for $t > 0$. The features of the long-time expansion allow to identify the nature of the induced transport. This is done, for example, by means of the variance $\sigma^2(t)$, which characterises how fast the initial wave packet expands. For zero background spin and energy densities, it is defined as [13]

$$\sigma_\nu^2(t) = \frac{1}{\mathcal{N}_\nu} \sum_i \rho_i^\nu(t)\,(i - i_0^\nu) \tag{3.10}$$

with $\nu = s, e$ for spin and energy respectively, i_0^ν the center of the initial distribution, $\rho_i^s = \langle \sigma_i^z \rangle$ the magnetisation at site i, $\rho_i^e = \langle h_{i,i+1} \rangle$ the local energy density for sites $i, i+1$, $\mathcal{N}_s = \sum_i \rho_i^s$ the total magnetisation, and $\mathcal{N}_e = \sum_i \rho_i^e$ the total energy density. Ballistic dynamics is identified if $\sigma_\nu^2(t) \propto t^2$, while diffusive transport corresponds to $\sigma_\nu^2(t) \propto t$, as obtained from the solution of the diffusion equation. Research following this scheme has identified, for the integrable XXZ model, ballistic spin transport in the regime $|\Delta| < 1$ and diffusive dynamics for $|\Delta| > 1$, at zero [10] and

high temperatures [13, 97]. Energy dynamics, on the other hand, was found to be ballistic for all interactions Δ, at zero [19] and finite temperatures [13].

The second type of quantum quench, used to study spin transport, corresponds to the time evolution of an initial state of domains of opposite polarisation, as sketched in figure 3.1(b). By analysing the integrated flow of magnetisation through the center of the chain as a function of time [9], and the dynamics of the domain wall [97], ballistic transport was observed in the regime $|\Delta| < 1$, while localisation of the domain wall due to self-trapping was found for strong interactions.

The analysis of transport properties by quantum quenches has thus provided strong evidence for the commonly-accepted picture of magnetisation and energy conduction of the integrable XXZ model with $\Delta \neq 1$. Unfortunately, this is still not quite the case for the isotropic model and nonintegrable systems. For the integrable $\Delta = 1$ case, diffusive or superdiffusive spin conduction regimes were initially suggested at zero temperature [9]. More recently, transport close to ballistic has been proposed at low temperature, and a superdiffusive regime at infinite temperature [13]. In nonintegrable ladders and massive frustrated systems, transport was found to be diffusive [10, 13]. On the other hand, it was found to be ballistic in dimerised [9] and gapless frustrated systems [10], a puzzling result given their lack of integrability. More research, with larger systems and evolution times, is required to understand the transport properties of these particular regimes.

3.5 Boundary-driven systems

A different form to induce a nonequilibrium state on a quantum spin chain corresponds to connecting its boundaries to reservoirs with different temperatures or chemical potentials, as depicted in figure 3.2. In this form, magnetisation and (or) energy imbalances are imposed across the chain. In the long-time limit, the system

reaches a nonequilibrium steady state (NESS), which supports an homogeneous spin or energy current from one boundary to the other. The analysis of the NESS currents, magnetisation and energy profiles reveals the nature of the transport through the system. In particular, if the conduction is diffusive, the system satisfies locally the diffusion equation. For spin transport, this reads[6]

$$J^{\mathrm{S}} \equiv \langle J_i \rangle = \kappa_{\mathrm{S}} \nabla \sigma_i^z \sim \kappa_{\mathrm{S}} \frac{\Delta \sigma^z}{N}, \tag{3.11}$$

where J^{S} is the homogeneous NESS local spin current, $\nabla \sigma_i^z = \langle \sigma_{i+1}^z \rangle - \langle \sigma_i^z \rangle$ is the local magnetisation gradient, $\Delta \sigma^z$ is the magnetisation difference between the boundaries, and κ_{S} is the spin conductivity. So for a fixed $\Delta \sigma^z$, diffusive spin transport is reflected by a spin current which scales with the system size as $J^{\mathrm{S}} \propto N^{-1}$, and by a linear magnetisation profile $\langle \sigma_i^z \rangle$ (i.e. with homogeneous gradient). A similar diffusion equation holds for the energy transport,

$$J^{\mathrm{XXZ}} \equiv \langle J_i^{\mathrm{XXZ}} \rangle = \kappa_{\mathrm{XXZ}} \nabla E_i^{\mathrm{XXZ}} \sim \kappa_{\mathrm{XXZ}} \frac{\Delta E}{N}, \tag{3.12}$$

where J^{XXZ} is the homogeneous NESS local energy current, $\nabla E_i^{\mathrm{XXZ}} = \langle h_{i,i+1} \rangle - \langle h_{i-1,i} \rangle$ is the local energy density gradient, ΔE is the energy density difference between the boundaries, and κ_{XXZ} is the energy conductivity. Diffusive energy transport is thus manifested by features similar to those of diffusive spin transport. Note that we do not describe the diffusion equation in terms of local temperatures, whose definition in nonequilibrium configurations is not trivial [11]. This problem is one of the major points we address in Chapter 6.

The system possesses very different features if the transport is ballistic. Even though the conductivities are infinite, the resistance due to the contact with bound-

[6] By $\sim$ we mean that the actual equation is slightly different due to boundary effects. In the following Chapters, the correct diffusion equation is specified for each calculation performed.

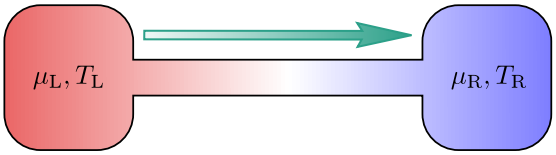

Figure 3.2. Scheme of a system connecting two unequal reservoirs, with temperatures $T_L \neq T_T$ and (or) chemical potentials $\mu_L \neq \mu_R$. This drives the system to a nonequilibrium configuration, supporting energy and (or) excitation transport.

ary reservoirs leads to finite values of the currents (see, for example, discussions in reference [129]). These currents are independent of the size of the system, and are proportional to the driving established by the reservoirs. In addition, the corresponding spin or energy profiles are completely flat in the bulk.

A common procedure to study the transport properties of boundary-driven systems consists of tracing out the degrees of freedom of the reservoirs under certain approximations. This leads to a master equation for the reduced density operator of the system, which governs its dynamics. Some master equations obtained in this way can be extremely hard to solve, due to a very intricate mathematical structure [130]. Nevertheless, a particular type of equation possesses a very convenient mathematical form which allows a solution to be obtained with well-known techniques, including efficient real-time simulations by means of tensor-network algorithms [31,32]. This is known as Lindblad master equation, and corresponds to the most general trace-preserving and completely-positive map[7] describing non-unitary evolution of the reduced density operator of the system [130]. We now indicate the most important features of this type of equation, and then discuss the insight it has provided regarding the transport properties of the XXZ model.

[7]This map is defined from the space of reduced density operators into itself.

3.5.1 Lindblad master equation approach

Let ρ denote the density operator of the spin chain, coupled to environmental degrees of freedom. The Lindblad master equation that governs the dynamics of ρ is

$$\frac{d\rho}{dt} \equiv \mathcal{L}(\rho) = -i[H, \rho] + \sum_k \mathcal{L}_k(\rho). \tag{3.13}$$

The first term, containing the commutator, represents the coherent dynamics of the system. The second term corresponds to the environmental effect, where each dissipator $\mathcal{L}_k(\rho)$ is given by

$$\mathcal{L}_k(\rho) = L_k \rho L_k^\dagger - \frac{1}{2}\{L_k^\dagger L_k, \rho\}, \tag{3.14}$$

with L_k the jump operators representing the coupling of the system to the environment, and $\{.,.\}$ the anti-commutator. This type of equation is obtained from tracing out the environmental degrees of freedom of the motion equation of the total universe (system and environment), after some considerations. These include the Born approximation, consisting of a weak system-environment coupling, and the Markov approximation, which assumes that the environment has very short memory effects. To obtain a Lindblad form, we also consider the wide-band limit, in which the bandwidths of the reservoir are assumed to be much larger than that of the system. Details of the derivation of the Lindblad master equations used throughout the present thesis are given in Appendix C.

The solution of the master equation (3.13) can be expressed in the form

$$\rho(t) = \exp(\mathcal{L}t)\rho(0). \tag{3.15}$$

For one-dimensional spin-1/2 chains of up to $N = 8$ sites, equation (3.15) can

be calculated exactly for any time t from the matrix exponential, using a modern desktop computer. In addition, the NESS can be obtained as the zero-eigenvalue eigenstate of the matrix representation of the Lindblad superoperator $\mathcal{L}$; see details in Appendix B. For large systems this is no longer possible, since the size of the operator space grows as 4^N. Fortunately, tensor-network algorithms, and in particular the Time Evolving Block Decimation [31, 32], are capable of efficiently simulating the evolution described by equation (3.15) for interacting one-dimensional systems. Since this method constitutes the most important calculation tool of our research, we describe it in detail in Chapter 4.

3.5.2 Transport in systems driven by Lindblad reservoirs

Now we discuss how to approach the problem of transport phenomena in driven spin chains by means of Lindblad master equations. The jump operators L_k of equation (3.14) represent the injection and ejection of spin excitations from the reservoirs to the boundary sites. In general they have the form[8]

$$L^{+}_{\mathrm{L,R}} = \sqrt{\gamma^{+}_{\mathrm{L,R}}}\sigma^{+}_{1,N}, \quad L^{-}_{\mathrm{L,R}} = \sqrt{\gamma^{-}_{\mathrm{L,R}}}\sigma^{-}_{1,N}, \tag{3.16}$$

with σ^{+}_{i} and σ^{-}_{i} the ladder operators of site i defined in equation (2.3), and $\gamma^{+,-}_{\mathrm{L,R}}$ the rates of the injection (+) and ejection (−) processes at the left (L) and right (R) boundaries. These rates depend on details of the reservoirs, and thus manifest the imbalances that induce spin or energy currents through the system. If all the rates are equal, spin excitations are injected to and ejected from the system at the same rate, so in the corresponding steady state no currents exist. The opposite limit corresponds to maximal driving, where $\gamma^{+}_{\mathrm{L}} = \gamma^{-}_{\mathrm{R}} \neq 0$, and $\gamma^{-}_{\mathrm{L}} = \gamma^{+}_{\mathrm{R}} = 0$ (or

[8] A more precise form of the jump operators used to study spin transport in the present work is given in Chapter 5 and Appendix C.2. For energy transport, discussed in Chapter 6, we use a different driving scheme, as detailed in Appendix C.4.

viceversa); here spin excitations are only injected at the left boundary of the chain, and at the same rate they are ejected at the right boundary, establishing a left-to-right spin current. If the imbalance between injection and ejection processes at each boundary is weak, the transport can approximately be described in linear response, as discussed in Chapter 5.

This type of boundary driving has been used to analyse the transport properties of several low-dimensional systems, including those described by Hubbard [131,132], Bose-Hubbard [133] and spin ladder models [134,135]. For the XXZ model, research based on the same nonequilibrium scheme has provided further evidence of ballistic spin transport in the weakly-interacting regime, and of diffusive transport for strong interactions in the linear response regime, mostly at high temperatures [11, 12, 21, 97, 114]; see Chapter 5 for details. In the isotropic case $\Delta = 1$, superdiffusive spin transport has been found at high temperatures [12, 22], as manifested by a scaling of the spin current of the form

$$J^{\mathrm{S}} \sim \kappa_{\mathrm{S}} \frac{\Delta\sigma^z}{N^\alpha}, \tag{3.17}$$

with $0 < \alpha < 1$ indicating a conduction regime intermediate between ballistic ($\alpha = 0$) and diffusive ($\alpha = 1$) responses. Regarding the effect of integrability breaking, induced by a staggered magnetic field, it was found to lead to diffusive spin transport for both weak and strong interactions [21].

A few studies have used a similar driving scheme to study energy transport, finding ballistic conduction for $\Delta = 0$ [136] and $\Delta = 1$ [137] in small systems. However, different work has found a contrasting behaviour. Using a Redfield equation (a more complicated master equation than that in Lindblad form), it was found that both the spin and energy transport are ballistic in the noninteracting regime only [138]. In addition, by means of a different Lindblad equation [139], ballistic and diffusive

transport regimes were seen to be separated by an interaction strength $\Delta = 1.6$ [140]. As discussed in Section 5.6, we attribute these results to the small systems considered (up to $N = 12$ in most calculations), and due to the study of an energy current different to J^{XXZ} in reference [140], namely of BJ^{S} with B the homogeneous magnetic field. Due to the lack of more convincing results in thermally-driven systems, part of our research was motivated to provide evidence of high-temperature ballistic energy transport for other interaction strengths and much larger spin chains, as described in Chapter 6.

3.5.3 Alternative driving schemes

Other driving schemes have also been used to analyse the transport properties of the XXZ model. One example corresponds to a system composed of two semi-infinite leads, modeled by Heisenberg spin chains with $\Delta = 1$ and at different temperatures, which are connected by a lattice of several sites [141]. Another proposed model consists of a noninteracting lattice coupled to mesoreservoirs at its boundaries, which in turn are thermalised by Lindblad reservoirs of different temperature [142]. These studies found direct energy transport and magnetothermal response of ballistic nature. We provide more evidence for these results with our analysis of thermally-driven systems of Chapter 6, using different interaction strengths and large systems.

3.6 Transport experiments on spin-chain systems

3.6.1 Magnetic materials

Several experiments have been performed to date to understand the energy transport properties of spin chain materials. Usual techniques of energy conductivity measurements correspond to *steady-state methods*, widely used from low to room

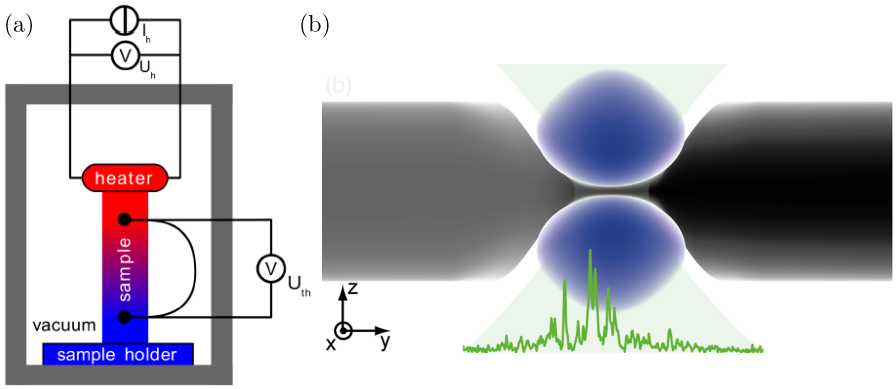

Figure 3.3. Schemes of experimental setups to study transport properties. (a) Steady state method for measurement of thermal conductivity of magnetic materials. The device is operated by means of the electrical current I_h, which along with the voltage drop U_h determines the energy current. The temperature gradient can be obtained from measurements of the thermal voltage U_{th}. See details in reference [72], from which the figure is taken. (b) An inhomogeneous ultracold fermionic gas is transformed into a system of two terminals connected by a two-dimensional channel, due to the splitting effect of a laser beam (blue). The green pattern projected onto the channel indicates a disordered configuration. Figure taken from [143] with permission of the authors. Copyright (2014) by the American Physical Society.

temperatures. Details of a specific implementation, depicted in figure 3.3(a), can be found in reference [72]. The temperature difference between the boundaries of the sample induces an energy current from the hot to the cold reservoir. The measurements of this current and of temperature gradients are performed in the steady state, which gives the name to the method.

Note that the energy current flowing parallel to the spin chains of the sample does not only contain a contribution from magnetic excitations (magnons [144, 145] or spinons [69, 74, 88, 146–148], depending on the material). It also contains a phononic contribution due to the vibration of the underlying lattice structure[9]. This can be identified in highly-pure materials by measuring the thermal conductivity in directions perpendicular to the spin chains, which do not contain magnetic contributions.

[9]We refer to electrically insulating materials, so electronic contributions are negligible [71, 146].

The difference between the total energy conductivity and the phononic component (approximately the same along the different axis) thus gives the magnetic contribution to the conductivity, which is the quantity of interest [71, 146].

Several experimental studies on one-dimensional spin chain materials have obtained very large thermal conductivities and mean-free paths of magnetic excitations, including Sr_2CuO_3 [69, 71] and $BaCu_2Si_2O_7$ [74]. These results thus support the picture of ballistic energy transport emerging due to the integrability of the underlying spin model, where scattering with phonons and defects leads to a finite value of the conductivity. They also agree with theoretical studies of the energy transport of spin chains weakly coupled to phonons, which found very large conductivity [70,149,150]. Interestingly, similar results have been obtained for the spin ladders $SrCuO_2$ [69,71,146,151], $Sr_{14}Cu_{24}O_{41}$, $Ca_9La_5Cu_{24}O_{41}$ [144] and $CaCu_2O_3$ [88], in which the energy conductivity parallel to the spin chains also has a large contribution from magnetic excitations.

It has also been observed that bond disorder induced by substituting Sr with Ca in Sr_2CuO_3 [148] strongly suppresses the magnetic contribution to the energy conductivity, by increasing the scattering of spinons. Thus even tiny amounts of disorder break the ballistic nature of the energy transport. This was argued to evidence the importance of integrability of the spin-1/2 Heisenberg chain, since the effect was not observed in nonintegrable spin chains where the energy transport was diffusive before adding disorder (such as square spin lattices [152]).

Regarding the experimental study of spin transport in magnetic materials, much less can be said. To date, direct measurements of spin currents or conductivities have note been performed in these systems. The experimental evidence of different spin transport regimes comes from other types of measurements. Using nuclear magnetic resonance, results of the low-frequency dynamic spin susceptibility of Sr_2CuO_3 are found to be consistent with ballistic spin transport at $T = 0$, while diffusive

transport emerges at finite temperature [153]. Muon spin relaxation experiments on the spin-1/2 one-dimensional antiferromagnet DEOCC-TCNQF$_4$, well described by the isotropic Heisenberg model, are consistent with diffusive spin transport [154]. On the other hand, results of muon spin relaxation in $SrCuO_2$ are consistent with ballistic spin transport [155]. Many more experiments in magnetic systems are thus needed to establish a complete picture of their spin transport properties.

3.6.2 Ultracold atomic systems

We described in Section 2.7.2 how systems of ultracold atoms in optical lattices can be used to simulate spin models [35, 96], and that the dynamics of a magnon bound state has already been analysed experimentally thanks to this capability [36]. Thus we expect that in the near future, the dynamics of many-body spin systems can be studied by means of these quantum simulators.

First experiments in this direction considered the expansion of an initially-confined cloud. This type of nonequilibrium scheme, discussed in Section 3.4 for spin systems, has been considered experimentally several times. Some of these studies are particularly relevant for the transport properties described in the present thesis. For example, reference [156] shows that in the absence of interactions, a fermionic gas expands ballistically along the containing homogeneous optical lattice, while weak interactions strongly suppress the dynamics; strong interactions lead to an almost-localised state. A more recent experiment on the expansion of ultracold bosons in one- and two-dimensional optical lattices shows that the transport is ballistic in the integrable limits of the underlying lattice models, while indications of diffusive transport are found away from these regimes [125]. A third important example is discussed in reference [157], where the expansion of a bosonic cloud in the presence of particle-particle interactions, disorder and noise is studied both experi-

mentally and numerically. This allows to identify regimes of many-body localisation, different types of diffusion and self-trapping. Some results of this study are closely connected to part of our research presented in Chapter 8.

An alternative and recently-developed nonequilibrium scheme [37, 38], sketched in figure 3.3(b), constitutes a very promising tool for the simulation of transport phenomena. It consists of two unequal reservoirs connected by a two-dimensional channel, where the latter is created by the action of a laser beam on an inhomogeneous ultracold gas. If a population imbalance between the two reservoirs exists, a particle current is established. This experimental setup has allowed the observation of ballistic and diffusive transport in ordered and disordered systems respectively [37], superfluid transport of strongly-correlated fermions [38], the transition from superfluid to poorly-conducting state as a function of disorder [143], and quantised conductance of neutral matter [158]. By including a temperature imbalance between the reservoirs [159], thermoelectric effects have also been recently observed in the noninteracting regime [39]. There, ballistic and diffusive thermoelectric responses were found for ordered and disordered systems respectively.

Since our research focuses on boundary-driven systems, the latter transport scheme emerges as an ideal candidate to observe some of the results discussed in the present thesis. A combination of this driving setup with the capability of optical lattices to implement XXZ spin chains could allow the observation of ballistic and diffusive transport regimes. In addition, exploiting techniques to induce noise [157] could lead to observe the transport enhancement mechanism of Chapters 8 and 9.

Chapter 4

Numerical simulation of time evolution of one-dimensional quantum systems

In the present thesis we study the transport properties of nonequilibrium low-dimensional spin chains under different conditions. Our analysis is mostly based on simulations of the dynamics of systems much larger than those accessible by exact numerical diagonalisation. To perform these simulations, we extensively use the Time Evolving Block Decimation (TEBD) [30, 31, 160, 161]. This method is one of the best known Tensor Network algorithms [26–28], and has emerged as one of the most powerful numerical tools developed so far to study the dynamical properties of one-dimensional correlated quantum lattices.

First we describe some general features of the systems we are interested in studying. Then we introduce the concept of Matrix Product States, which provides a compact and efficient representation of the systems of interest due to their weakly-correlated nature. Afterwards we present a graphical representation of matrix product structures, which clearly illustrates how different manipulations of the states can be performed. Finally we describe the most important features of the TEBD method, and the software we used to perform our simulations.

4.1 General description of systems of interest

We start by establishing some properties of the systems to be considered in the present thesis. Although we restrict to the XXZ model, we perform the discussion in a general notation, so it is clear to which system the formalism applies. First we note that the Hamiltonians of interest truly correspond to one dimensional systems with short-ranged interactions, and in general have the form

$$H = \sum_{n=1}^{N} \sum_{\nu=1}^{K_1} h_n^\nu + \sum_{n=1}^{N-1} \sum_{\nu=1}^{K_2} h_{n,n+1}^\nu, \tag{4.1}$$

which consists on K_1 types of one-site terms and K_2 types of nearest-neighbour couplings, acting across the entire system. This Hamiltonian can be conveniently rewritten as a sum of two-site terms only,

$$H = \sum_{n=1}^{N-1} H_{n,n+1}, \tag{4.2}$$

with the two-site terms given by

$$H_{n,n+1} = \frac{1}{2}(1+\delta_{n,1}) \sum_{\nu=1}^{K_1} h_n^\nu + \sum_{\nu=1}^{K_2} h_{n,n+1}^\nu + \frac{1}{2}(1+\delta_{n,N-1}) \sum_{\nu=1}^{K_1} h_{n+1}^\nu \tag{4.3}$$

To analyse non-equilibrium phenomena, we are particularly interested in solving Lindblad master equations of the form (3.13). Since we only consider Hamiltonians of the form (4.1), and dissipative processes that act on at most two sites (see Appendix C), the corresponding Liouville superoperator can be written as a sum of two-site terms,

$$\mathcal{L} = \sum_{n=1}^{N-1} \mathcal{L}_{n,n+1}. \tag{4.4}$$

This structure will be seen to be fundamental for the particular numerical method used in the present thesis. To explicitly build the two-site terms, as described in

Appendix B, a particular local basis $\{\sigma_j^{n_j}\}$ of the operator space for each site j must be defined. In our particular case the natural choice is the Pauli basis

$$\sigma_j^1 = \frac{1}{2}I, \quad \sigma_j^2 = \frac{1}{2}\sigma^z, \quad \sigma_j^3 = \frac{1}{2}\sigma^x, \quad \sigma_j^4 = \frac{1}{2}\sigma^y, \tag{4.5}$$

where without loss of generality the first element is taken to be proportional to the local identity operator I. Given the inner product operation $P(O_\beta, O_\gamma) = \mathrm{Tr}(O_\beta^\dagger O_\gamma)$, this set of matrices is readily verified to constitute an orthonormal basis.

Our aim is to solve the equation $\mathcal{L}(\rho) = 0$, so the non-equilibrium steady state (NESS) ρ is obtained. A natural first attempt to do so corresponds to an exact numerical calculation, in which the zero-eigenvalue eigenstate of the superoperator $\mathcal{L}$ is obtained by standard exact diagonalisation routines. Since the size of the operator space of the system grows exponentially with its size as d^N, with d the dimension of the local operator space ($d = 4$ in our case), it is not possible to consider large systems with this method[1]. Nowadays, thanks to the development of efficient tensor network algorithms, it is possible to solve the problem in a different way for large systems, namely by directly simulating equation (3.15) in the long time limit $t \to \infty$ using the TEBD method to evolve in time a Matrix Product structure. The condition that a system must fulfill so this method can be applied efficiently is that it features *weak classical and quantum correlations*. In the following sections we explain the meaning of this requirement.

4.2 Matrix product states and operators

We start by explaining how physical states can be efficiently described by a compact tensor network, the so-called *Matrix Product State* structure. This formulation was

[1]Modern desk computers can handle systems of up to $N = 7$ for a complete diagonalisation of the Liouvillian.

originally introduced for pure states [26,30,161,162]. Nevertheless, it can be directly extended to mixed states [11, 31], where the tensor network receives the name of *Matrix Product Operator*. Since we are interested in the properties of mixed states, we describe the formulation for the second case, and mention the equivalent concepts in the case of pure states. To do so, we initially introduce some important concepts that are necessary for the development of the formalism.

4.2.1 Singular value decomposition, Schmidt decomposition and entropy

A basic mathematical tool used repeatedly in the formalism to be explained is the Singular Value Decomposition (SVD) [163]. For an arbitrary rectangular matrix C of dimension $m \times n$, with $p = \min(m, n)$, the SVD reads

$$C = USV^{\dagger}, \tag{4.6}$$

where the matrices U, S and V satisfy the following properties:

1. U has dimension $m \times p$, and $U^{\dagger}U = I$, with I the identity matrix.

2. S is a diagonal matrix of dimension $p \times p$, whose elements $s_{\alpha} \equiv S_{\alpha,\alpha}$, known as Schmidt coefficients, are non-negative. The number r of non-zero coefficients is known as the Schmidt rank. From now on, we assume $s_1 \geq s_2 \geq \cdots \geq s_r > 0$.

3. $V^{\dagger}$ has dimension $p \times n$, and satisfies $V^{\dagger}V = I$.

This concept leads to a very important decomposition of the (pure or mixed) state of the system. We exemplify this for a mixed state. To do so, consider a bipartition of the system where the left part (A) has l sites and an orthonormal basis $\{\sigma^i_{\mathrm{A}}\}$, and the right part ($B$) has $N-l$ sites and an orthonormal basis $\{\sigma^i_{\mathrm{B}}\}$. An arbitrary

mixed state of this bipartition is written as

$$\rho = \sum_{i=1}^{d^l} \sum_{j=1}^{d^{N-l}} \rho_{ij} (\sigma_{\mathrm{A}}^i \otimes \sigma_{\mathrm{B}}^j), \tag{4.7}$$

with d the dimension of the local orthonormal basis. Performing a SVD on the matrix of coefficients ρ_{ij}, namely

$$\rho_{ij} = \sum_{\alpha=1}^{\chi} U_{i\alpha} S_{\alpha\alpha} V_{j\alpha}^*, \tag{4.8}$$

with $\chi = \min(d^l, d^{N-l})$, the state can be written in the form

$$\rho = \sum_{\alpha=1}^{\chi} s_\alpha (O_\alpha^{\mathrm{A}} \otimes O_\alpha^{\mathrm{B}}), \quad \text{where} \quad O_\alpha^{\mathrm{A}} = \sum_{i=1}^{d^l} U_{i\alpha} \sigma_{\mathrm{A}}^i, \quad O_\alpha^{\mathrm{B}} = \sum_{j=1}^{d^{N-l}} V_{j\alpha}^* \sigma_{\mathrm{B}}^j. \tag{4.9}$$

The sets of operators $\{O_\alpha^{\mathrm{A}}\}$ and $\{O_\alpha^{\mathrm{B}}\}$ are orthonormal, i.e. they satisfy

$$P\left(O_\alpha^{\mathrm{A}}, O_{\alpha'}^{\mathrm{A}}\right) = \delta_{\alpha,\alpha'} \quad \text{and} \quad P\left(O_\alpha^{\mathrm{B}}, O_{\alpha'}^{\mathrm{B}}\right) = \delta_{\alpha,\alpha'}, \tag{4.10}$$

as obtained directly from the normalisation properties of U and V. The factorisation given in equation (4.9) is known as the Schmidt Decomposition [163] of the state ρ.

Some remarks are necessary at this point. First, the values of the Schmidt coefficients s_α determine the amount of correlations between the two parts of the system. For example, if only $s_1 > 0$, the state of the system is just a product of states from A and B, and no correlations exist between the two parts. In the opposite limit of a (maximally correlated) random state, the Schmidt coefficients are almost equal. On the other hand, if the Schmidt coefficients s_α decay rapidly with α, a good approximation $\tilde{\rho}$ to the state of the system can be obtained by truncating

the Schmidt decomposition (4.9) up to a small number of terms $\tilde{\chi} < \chi$, so

$$\tilde{\rho} = \sum_{\alpha=1}^{\tilde{\chi}} s_\alpha (O_\alpha^{\mathrm{A}} \otimes O_\alpha^{\mathrm{B}}), \quad \text{with error} \quad \epsilon \equiv ||\rho - \tilde{\rho}||_{\mathrm{F}} = \left(\sum_{\alpha=\tilde{\chi}+1}^{\chi} s_\alpha^2 \right)^{1/2}. \tag{4.11}$$

The error of the truncation, calculated by means of the Frobenius norm[2] $||O||_{\mathrm{F}} = \sqrt{\mathrm{Tr}(O^\dagger O)}$, is given by the sum of the square of the discarded Schmidt coefficients.

The amount of correlations can be measured by the following entropy definition [164][3], obtained from the Schmidt coefficients (normalised so $s_1 = 1$ [11]) as

$$S_{\mathrm{O}} = -\sum_{\alpha=1}^{\chi} s_\alpha^2 \log_2 s_\alpha^2. \tag{4.12}$$

This quantity is nothing more than the extension to the operator space of the more familiar von Neumann entanglement entropy, which naturally emerges when the previous discussion is performed for pure states [29]. Nevertheless, in contrast to the latter, the entropy of equation (4.12) does not quantify the amount of entanglement only. It also measures the amount of classical correlations, as well as of discord[4]. In other words, the entropy (4.12) quantifies the amount of both classical and quantum correlations. Note that this quantity has been considered theoretically very few times, and its properties are not understood as well as those of the von Neumann entanglement entropy. Nevertheless, it captures the decay of the Schmidt coefficients [11], which we describe in Section 4.2.3.

[2]Other forms to quantify the distance between ρ and $\tilde{\rho}$ could be used, such as the trace distance, discussed in Chapter 6. The Frobenius norm, however, gives a simpler form of the difference between the two states. To our knowledge, no definitive error for the truncation in mixed states has been established. We note that the error in equation (4.11) has been proposed before [11].

[3]This quantity has been named Operator Space Entanglement Entropy [11, 164]. Nevertheless we feel that this name is misleading since it not only determines the existence of entanglement, as described in the main text.

[4]In brief, discord corresponds to the quantum correlations not accounted by entanglement. Some mixed states, for example, can possess non-classical correlations even if they are separable; these correlations are known as discord. See a recent detailed review in reference [165].

4.2.2 Matrix product structure of a mixed state

Now we explain how the concepts introduced in Section 4.2.1 lead to a compact and efficient parametrisation of the state of the system. We follow the notation of reference [29], where the description was performed for pure states. First consider the most general form in which a mixed state of the system can be written, namely

$$\rho = \sum_{n_1,n_2,\ldots,n_N}^{d} c_{n_1,n_2,\ldots,n_N} \left(\sigma_1^{n_1} \otimes \sigma_2^{n_2} \otimes \cdots \otimes \sigma_N^{n_N}\right), \tag{4.13}$$

where $\sigma_i^{n_i}$ is the n_ith element of the local basis of site i. This state contains d^N coefficients $c_{n_1,n_2,\ldots,n_N}$, which makes its numerical manipulation only possible for a few sites. To transform it into a more efficient representation, we first reshape the c vector as a $d \times d^{N-1}$ matrix Ψ, with entries

$$\Psi_{n_1,(n_2,\ldots,n_N)} \equiv c_{n_1,n_2,\ldots,n_N}. \tag{4.14}$$

Now, performing a SVD on the matrix Ψ we obtain

$$\Psi_{n_1,(n_2,\ldots,n_N)} = \sum_{\alpha_1=1}^{r_1} U_{n_1,\alpha_1} S_{\alpha_1,\alpha_1} (V^\dagger)_{\alpha_1,(n_2,\ldots,n_N)} \equiv \sum_{\alpha_1=1}^{r_1} U_{n_1,\alpha_1} c_{\alpha_1,n_2,\ldots,n_N}, \tag{4.15}$$

where the elements of S and $V^\dagger$ have been multiplied to give a vector $c_{\alpha_1,n_2,\ldots,n_N}$. The Schmidt rank is $r_1 \leq d$, since at most d Schmidt coefficients are finite. Now the matrix U is reshaped as a collection of d row vectors, with entries $A_{\alpha_1}^{n_1} = U_{n_1,\alpha_1}$. In addition, similarly to equation (4.14), the vector $c_{\alpha_1,n_2,\ldots,n_N}$ is reshaped into a new matrix Ψ of dimensions $r_1 d \times d^{N-2}$, with entries

$$\Psi_{(\alpha_1,n_2),(n_3,\ldots,n_N)} \equiv c_{\alpha_1,n_2,\ldots,n_N}. \tag{4.16}$$

As in equation (4.15), a SVD is performed on the new matrix Ψ, which leads to

$$\begin{aligned} c_{n_1,n_2,\ldots,n_N} &= \sum_{\alpha_1=1}^{r_1} A^{n_1}_{\alpha_1} \sum_{\alpha_2=1}^{r_2} U_{(\alpha_1 n_2),\alpha_2} S_{\alpha_2,\alpha_2} (V^\dagger)_{\alpha_2,(n_3,\ldots,n_N)} \\ &= \sum_{\alpha_1=1}^{r_1} \sum_{\alpha_2=1}^{r_2} A^{n_1}_{\alpha_1} A^{n_2}_{\alpha_1,\alpha_2} c_{\alpha_2,n_3,\ldots,n_N}. \end{aligned} \tag{4.17}$$

Here the new matrix U has been reshaped as a collection of d matrices of dimension $r_1 \times r_2$ ($r_2 \leq d^2$), so $A^{n_2}_{\alpha_1,\alpha_2} = U_{(\alpha_1 n_2),\alpha_2}$, and the vector $c_{\alpha_2,n_3,\ldots,n_N}$ results from the product of S and $V^\dagger$. Repeating the process until the final site of the lattice, it is obtained that

$$c_{n_1,n_2,\ldots,n_N} = \sum_{\alpha_1,\ldots,\alpha_N} A^{n_1}_{\alpha_1} A^{n_2}_{\alpha_1,\alpha_2} A^{n_3}_{\alpha_2,\alpha_3} \cdots A^{n_{N-1}}_{\alpha_{N-2,N-1}} A^{n_N}_{\alpha_{N-1}}, \tag{4.18}$$

with $A^{n_N}_{\alpha_{N-1}} = c_{\alpha_{N-1},n_N}$ a collection of d column vectors. This results in a compact *Matrix Product Operator* (MPO) representation of the mixed state[5]

$$\rho = \sum_{n_1,n_2,\ldots,n_N=1}^{d} A^{n_1}_{[1]} A^{n_2}_{[2]} \cdots A^{n_N}_{[N]} \left(\sigma_1^{n_1} \otimes \sigma_2^{n_2} \otimes \cdots \otimes \sigma_N^{n_N}\right). \tag{4.19}$$

From the normalisation of the U matrices, namely $U^\dagger U = I$, it follows that

$$\sum_{n_i} \left(A^{n_i}_{[i]}\right)^\dagger A^{n_i}_{[i]} = I. \tag{4.20}$$

The matrices that satisfy this condition are called left normalised, and the MPO whose matrices are left-normalised is called *left-canonical*.

Note that the MPO representation of a mixed state is not unique. For example,

[5]For sub- and super-indices of the A tensors, we follow the notation that numbers inside [.] denote the site to which they belong, and coefficients outside [.] refer to the indices of the tensor. For example, $A_{[i]}$ is the tensor at site i, and $A^{n_i}_{[i]}$ is the n_ith matrix of site i. We do not include [.] if it is not needed and would complicate the notation, as in the equations previous to (4.19).

we can start the process described above from the right boundary, and obtain the representation

$$\rho = \sum_{n_1,n_2,\ldots,n_N=1}^{d} B_{[1]}^{n_1} B_{[2]}^{n_2} \cdots B_{[N]}^{n_N} \left(\sigma_1^{n_1} \otimes \sigma_2^{n_2} \otimes \cdots \otimes \sigma_N^{n_N}\right), \tag{4.21}$$

where the $B_{[i]}^{n_i}$ come from the $V^\dagger$ matrices of the SVD processes, and thus satisfy the normalisation condition

$$\sum_{n_i} B_{[i]}^{n_i} \left(B_{[i]}^{n_i}\right)^\dagger = I. \tag{4.22}$$

These matrices are called right-normalised, and the state of equation (4.21) is referred to as *right-canonical*.

Similarly, combining the processes of left and right normalisation so they meet at site l leads to the MPO representation [29]

$$\rho = \sum_{n_1,\ldots,n_N=1}^{d} A_{[1]}^{n_1} \cdots A_{[l]}^{n_l} S_{[l]} B_{[l+1]}^{n_{l+1}} \cdots B_{[N]}^{n_N} \left(\sigma_1^{n_1} \otimes \cdots \otimes \sigma_N^{n_N}\right), \tag{4.23}$$

where the singular values of the SVD at site l appear explicitly. This representation, known as *mixed-canonical*, is nothing more than the Schmidt decomposition (4.9) of the state at site l, with Schmidt coefficients $s_{[l]\alpha} = (S_{[l]})_{\alpha,\alpha}$ and

$$\begin{aligned} O_\alpha^A &= \sum_{n_1,\ldots,n_l=1}^{d} \left(A_{[1]}^{n_1} \cdots A_{[l]}^{n_l}\right)_{1,\alpha} \left(\sigma_1^{n_1} \otimes \cdots \otimes \sigma_l^{n_l}\right), \\ O_\alpha^B &= \sum_{n_{l+1},\ldots,n_N=1}^{d} \left(B_{[l+1]}^{n_{l+1}} \cdots B_{[N]}^{n_N}\right)_{\alpha,1} \left(\sigma_{l+1}^{n_{l+1}} \otimes \cdots \otimes \sigma_N^{n_N}\right). \end{aligned} \tag{4.24}$$

The sets of operators $\{O_\alpha^{\mathrm{A}}\}$ and $\{O_\alpha^{\mathrm{B}}\}$ are orthonormal by construction.

As a very simple example of a MPO, consider a lattice with magnetisation $\langle \sigma_i^z \rangle =$

μ_i at site i. When the local basis of the operator space of each site is given by the Pauli basis of equation (4.5), a product state satisfying the magnetisation condition is obtained when the matrices $A^{n_i}_{[i]}$ of each site i are scalars given by

$$\begin{aligned} &A^1_{[i]} = 1 \quad \text{so} \quad \mathrm{Tr}(\rho) = 1, \\ &A^2_{[i]} = \mu_i, \quad A^3_{[i]} = A^4_{[i]} = 0. \end{aligned} \tag{4.25}$$

A ferromagnetic state is obtained when $A^2_{[i]} = 1$ for all i, and antiferromagnetic state corresponds to $A^2_{[i]} = (-1)^i$. The maximally mixed (infinite temperature) state, i.e. the identity operator, results when $A^2_{[i]} = 0$. Examples of MPO representations of more complicated states are shown in Appendix D.

4.2.3 Why using a MPO representation?

So far, we have only written the state (4.13) in a different form, which is equally intractable numerically given that as we go deeper into the lattice, the dimensions of the matrices A and B grow exponentially. So at first sight, it appears that we have obtained no benefits regarding the tractability of the state by reformulating it as a MPO. Nevertheless, the advantages of this formulation become clear when considering that the systems of interest are weakly-correlated. This is evidenced from the fast decay of the Schmidt coefficients s_α, observed in non-equilibrium states supporting spin or energy transport [11], thermal states [31,164] or states of systems subject to dephasing [31]. The corresponding Schmidt coefficients can decay as a power law or even exponentially, as shown in figure 4.1. Due to this behaviour, each possible Schmidt decomposition (4.9) of the state can be well approximated by a truncation of the form (4.11), keeping the error small. If we apply this truncation for every SVD performed when building the MPO structure of equation (4.19), keeping at most $\tilde{\chi}$ Schmidt coefficients on each case, we can approximate the state of the

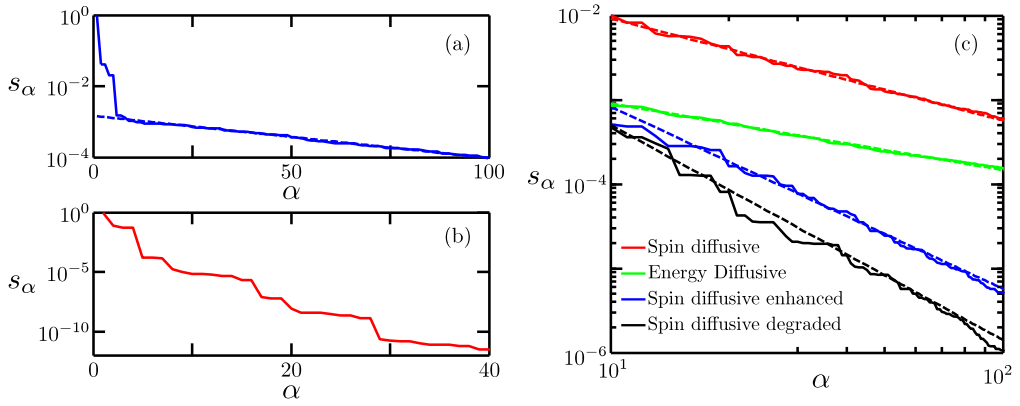

Figure 4.1. Decay of Schmidt coefficients s_α for several NESSs of chains of size $N = 40$. The solid lines are guides to the eye, and the dashed lines are fits to simple functions proposed in reference [11]. (a) Schmidt coefficients of a NESS displaying ballistic spin transport, with $\Delta = 1.5$ and $f = 0.1$ (f is the driving strength, see Chapter 5 for notation). The decay follows the exponential function $s_\alpha \propto \exp(-\alpha/36.5(6))$. (b) Coefficients of a thermal state with $\Delta = 1.5$ and $T = 20$. (c) Coefficients for several cases in which the decay follows a power law $s_\alpha \propto \alpha^{-p}$. The top data corresponds to a NESS showing spin diffusion, with $\Delta = 1.5$, $f = 0.1$ and $p = 1.21(2)$. The second corresponds to energy diffusion, with $\Delta = 1.5$, $T^{\mathrm{L}}_{\mathrm{targ}} = \infty$, $T^{\mathrm{R}}_{\mathrm{targ}} = 20$, staggered magnetic field $B = 0.4$ and $p = 0.79(1)$ (see Chapter 6 for notation). The third corresponds to a NESS with dephasing-assisted spin transport, with $\Delta = 1.5$, $f = 0.1$, dephasing rate $\gamma = 0.5$ and $p = 2.16(6)$. The bottom data corresponds to a NESS showing dephasing-degraded spin transport, with $\Delta = 0.5$, $f = 0.1$, $\gamma = 0.5$ and $p = 2.5(2)$.

system with high accuracy by N matrices A of dimension $\tilde{\chi} \times \tilde{\chi}$ or less[6]. The faster the coefficients decay, the lower $\tilde{\chi}$ is required, making the numerical manipulation easier. So instead of requiring an exponential number of coefficients to describe the state of the system, we can do it efficiently with $O(Nd\tilde{\chi}^2)$ coefficients, embedded in a matrix product structure.

At this point it is important to briefly discuss some points of the corresponding matrix product formalism for pure states. There a matrix product representation is also efficient if the corresponding Schmidt coefficients decay fast, as manifested

[6]More precisely, the matrices of site 1 (N) are of dimension $1 \times d$ ($d \times 1$), those of site 2 ($N-1$) are of $d \times d^2$ ($d^2 \times d$), and so on up to some site k (l) where $d^k (d^{N-l}) > \tilde{\chi}$. From that site the truncation actually takes place, the matrices $A^{n_i}_{[i]}$ being of dimension $\tilde{\chi} \times \tilde{\chi}$ ($k < i < l$).

by weak entanglement. Specifically, it was discovered a decade ago that the ground state von Neumann entanglement entropy of one-dimensional nearest-neighbour spin Hamiltonians saturates with the size of the system away from criticality, while it diverges very slowly (as a logarithmic function) at criticality [166]. Since then, similar conclusions have been reported for several one-dimensional locally-interacting systems (see [167] for a review). This feature has been explained by the existence of the so-called Area Laws [168, 169], which state that the entanglement entropy between two regions of a system depends only on their boundary, which for one-dimensional systems is constant for any size. The area law is slightly violated at criticality, but even there the entanglement is exponentially lower than that of a random state [27].

The case of mixed states has been much less studied. Similar relations between correlations, area laws and nonequilibrium criticality are yet to be established, although studies in this direction have been performed [164]. Additionally, in contrast to the case of pure states, the existence of weak entanglement does not guarantee an efficient MPO representation of a mixed state. If its classical correlations are strong, arising for example from decoherence processes, then its MPO representation can be highly inefficient; an example is discussed in reference [170]. Since for the systems studied in the present thesis this is not the case, as shown in figure 4.1, MPO representations of the corresponding mixed states are highly convenient.

In summary, due to the weakly-correlated nature of the systems analysed in the present thesis, we can parametrise them with a number of elements that scales linearly with N, instead of exponentially. Furthermore, such a parametrisation can be arranged compactly in a matrix product structure. As discussed in the following Sections, this tensor network representation offers several other advantages, like the efficient calculation of reduced density operators, expectation values and time evolution. It also has a nice graphical representation that makes the implementation of such operations very neat and clear.

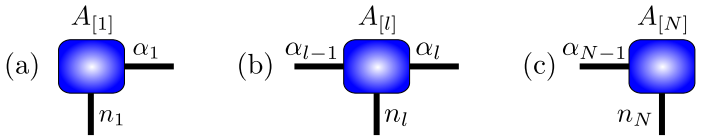

Figure 4.2. Graphical representation of single-site tensors, (a) at the left boundary, (b) in the bulk, and (c) at the right boundary. The vertical lines correspond to the physical indices. The horizontal lines represent the rows and columns of each tensor.

4.3 Manipulation of matrix product structures

4.3.1 Graphical representation

To simplify the manipulation of MPOs, a very simple but convenient graphical representation is conventionally used [27, 29]. The basic building blocks of this representation are shown in figure 4.2. The idea consists of representing the tensor $A_{[l]}$ of each site l of the structure (4.19) (i.e. the d set of matrices $\{A^{n_l}_{[l]}\}$) as a block with several legs. The vertical leg corresponds to the physical index of the tensor, n_l. The horizontal legs run over the rows (leg to the left of the block) and columns (leg to the right of the block) of each matrix. With this convention, figure 4.2(a) represents the tensor of site 1, where the index α_1 runs over the columns of each one of the d row vectors $A^{n_1}_{[1]}$. Figure 4.2(b) represents the bulk tensors, where α_{l-1} runs over the rows of each one of the d matrices $A^{n_l}_{[l]}$, and α_l sweeps over the columns $(1 < l < N)$. Finally, figure 4.2(c) corresponds to the tensor of site N, where α_{N-1} runs over the rows of each one of the d column vectors $A^{n_N}_{[N]}$.

To represent graphically the entire MPO structure, a simple rule is followed: a contraction between tensors is performed when they are connected by a common leg. This shared leg corresponds to the index over which the contraction is done. Thus the operation specified in equation (4.18) is represented by figure 4.3, where the tensor of site l is contracted to those of sites $l-1$ and $l+1$.

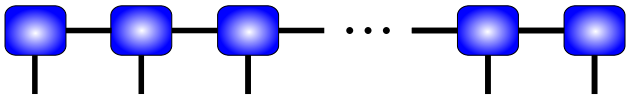

Figure 4.3. Graphical representation of the matrix product operator structure of a mixed state.

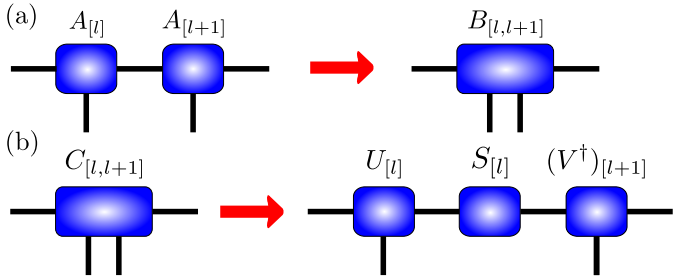

Figure 4.4. Graphical representation of basic tensor operations, corresponding to (a) contraction of tensors of neighbouring sites, and (b) singular value decomposition.

4.3.2 Basic operations within a MPO structure

Using the graphical representation introduced in Section 4.3.1, the manipulation of the MPO to perform different calculations becomes easy to visualise. A first example to look at is the actual contraction between two neighbouring three-leg tensors $A_{[l]}$ and $A_{[l+1]}$. As shown in figure 4.4(a), this corresponds to the emergence of a single tensor $B_{[l,l+1]}$, where the common leg has disappeared since the contraction was carried out though it. The resulting tensor now has four legs: two physical legs, one row and one column leg. Thus figure 4.4(a) represents an operation of the form

$$\sum_{\alpha_l} A^{n_l}_{\alpha_{l-1},\alpha_l} A^{n_{l+1}}_{\alpha_l,\alpha_{l+1}} = B^{n_l,n_{l+1}}_{\alpha_{l-1},\alpha_{l+1}}. \tag{4.26}$$

A second simple example is the representation of a SVD. The particular calculation depicted in figure 4.4(b) corresponds to the operation

$$C^{n_l,n_{l+1}}_{\alpha_{l-1},\alpha_{l+1}} = \sum_{\alpha_l} U^{n_l}_{\alpha_{l-1},\alpha_l} S_{\alpha_l,\alpha_l} (V^\dagger)^{n_{l+1}}_{\alpha_l,\alpha_{l+1}}, \tag{4.27}$$

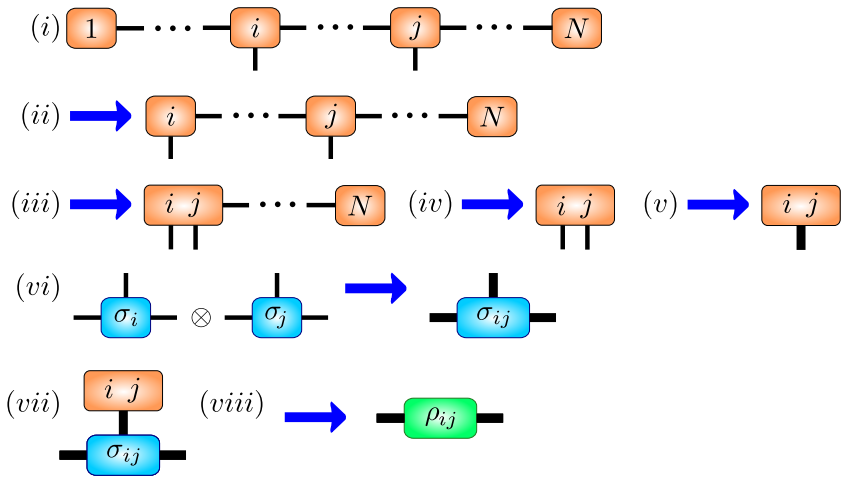

Figure 4.5. Calculation of a two-site reduced density operator. (i) Prepare MPO. (ii) Contract tensors from left to right until reaching site i. (iii) Continue left-to-right contraction until reaching site j. From the last contraction, a three-leg tensor with two physical legs appears. (iv) Continue left-to-right contraction until site N is reached. (v) Reshape the result into a single-leg tensor. Since the single leg represents an index running over the physical indices of both sites i and j, it is said to be "fat". (vi) Define the elements of the total basis of sites i and j. (vii) Contract these elements with the single-leg tensor. (viii) The reduced density operator of sites i and j is finally obtained, corresponding to a two-leg tensor with fat legs.

which is used repeatedly during the TEBD process, as explained in Section 4.4.

More complicated operations that can be visualised easily within the MPO structure are, for example, the calculation of reduced density matrices and expectation values. To illustrate the first, we consider the calculation of the two-site reduced density matrix ρ_{ij} of two sites i and j which are not necessarily nearest neighbours. Recalling that the first element of the local basis is proportional to the identity operator, and the only basis element with finite trace, ρ_{ij} is given by

$$\rho_{ij} = \mathrm{Tr}(\rho)_{(i,j)'} = \sum_{n_i,n_j=1}^{d} A^1_{[1]} A^1_{[2]} \cdots A^{n_i}_{[i]} \cdots A^{n_j}_{[j]} \cdots A^1_{[N]} (\sigma_i^{n_i} \otimes \sigma_j^{n_j}), \tag{4.28}$$

where $\mathrm{Tr}(\rho)_{(i,j)'}$ indicates that the partial trace over all sites except i and j is taken on ρ. The calculation is schematised in figure 4.5. First the MPO is prepared by

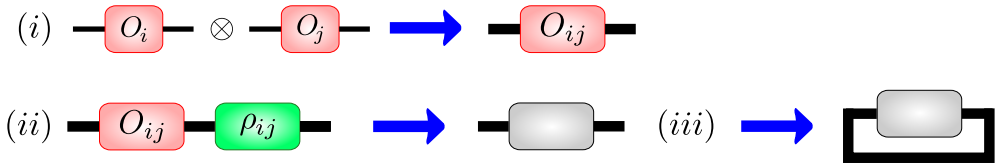

Figure 4.6. Calculation of a two-site expectation value. (i) Define the two-site operator of interest from the single-site operators O_i and O_j. This results in a two-leg tensor O_{ij} with fat legs. (ii) Contract O_{ij} with the operator ρ_{ij} obtained from the process shown in figure 4.5. (iii) Take the trace of the resulting object, to finally obtain the expectation value.

only retaining the first matrix $A^1_{[k]}$ of all sites $k \neq i, j$; this is represented by the elimination of the physical index on these sites, as depicted on step (i) of figure 4.5. Then the contraction of the network is performed from left to right, to calculate the element $A^1_{[1]}A^1_{[2]} \cdots A^{n_i}_{[i]} \cdots A^{n_j}_{[j]} \cdots A^1_{[N]}$, as shown in steps (ii-iv). The resulting two-leg tensor is reorganised into a one-leg tensor by defining a "fat" leg, as shown in step (v). We represent the local bases of sites i and j by three-leg tensors σ_i and σ_j (with elements $\{\sigma_i^{n_i}\}$ and $\{\sigma_j^{n_j}\}$ respectively), as indicated in step (vi). The total basis of the two sites is thus represented by a tensor σ_{ij} with three fat legs. The vertical leg runs over all combinations of indices n_i and n_j, and the horizontal legs correspond to the rows (left) and columns (right) of the basis elements $\{\sigma_i^{n_i} \otimes \sigma_j^{n_j}\}$. After defining the tensor σ_{ij}, it is contracted with the previously-obtained one-leg tensor, thus performing the sum over n_i and n_j indicated in equation (4.28). This results in the reduced density operator ρ_{ij}, as indicated in step (viii).

After getting the reduced density operator, expectation values are easily obtained. For example, to calculate $\langle O_{ij} \rangle = \mathrm{Tr}(\rho_{ij} O_{ij})$, with $O_{ij} = O_i \otimes O_j$ and O_i an observable of site i, we only need to follow the process sketched in figure 4.6. After defining O_{ij} as indicated in step (i), we contract it with ρ_{ij}, as shown in step (ii). The resulting object is a two-leg tensor, i.e. a matrix. Finally we take its trace, which as shown in step (iii) is just the contraction of its rows with the columns.

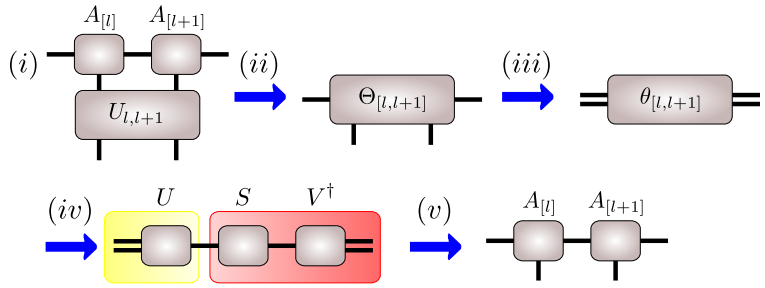

Figure 4.7. Application of a two-site gate to a MPO structure. (i) The tensors of the two sites are contracted with the gate. (ii) The MPO structure is lost when the contraction is performed. (iii) Reshape the resulting object into a matrix. (iv) Perform a SVD. (v) Recover the MPO structure by reshaping the matrices resulting from the SVD.

4.3.3 Application of a two-site gate to a MPO

One of the most important operations to be performed with a matrix product structure is the application of a local two-site gate. As discussed in Section 4.4, this operation is used extensively during the time evolution algorithm. Its graphical representation is shown in figure 4.7. Imagine that a gate $U_{l,l+1}$ is applied to the adjacent sites l and $l+1$. Such a gate has the general form

$$U_{l,l+1} = \sum_{\substack{p_l,p_{l+1}=1 \\ q_l,q_{l+1}=1}}^{d} U_{q_l,q_{l+1}}^{p_l,p_{l+1}} (\sigma_l^{p_l} \otimes \sigma_{l+1}^{p_{l+1}})(\sigma_l^{q_l} \otimes \sigma_{l+1}^{q_{l+1}})^\dagger, \tag{4.29}$$

where $\{\sigma_l^{p_l} \otimes \sigma_{l+1}^{p_{l+1}}\}$ are the basis elements of the two-site operator space. Also assume that matrices $A_{[l]}^{n_l}$ of the MPO are of dimension $\chi_{l-1} \times \chi_l$. When applying the gate to the MPO we get

$$\sum_{\substack{n_1,\ldots,n_{l-1},p_l, \\ p_{l+1},n_{l+2},\ldots,n_N=1}}^{d} A_{[1]}^{n_1} \cdots A_{[l-1]}^{n_{l-1}} \Theta_{[l,l+1]}^{p_l,p_{l+1}} A_{[l+2]}^{n_{l+2}} \cdots A_{[N]}^{n_N} (\sigma_1^{n_1} \otimes \cdots \otimes \sigma_l^{p_l} \otimes \sigma_{l+1}^{p_{l+1}} \otimes \cdots \otimes \sigma_N^{n_N}),$$

with $\Theta_{[l,l+1]}^{p_l,p_{l+1}} = \sum_{q_l,q_{l+1}=1}^{d} U_{q_l,q_{l+1}}^{p_l,p_{l+1}} A_{[l]}^{q_l} A_{[l+1]}^{q_{l+1}}$. This contraction is shown in steps (i-ii) of figure 4.7. Observe that when the gate is applied, the MPO structure is altered

at sites l and $l+1$. To bring the matrix product structure back, the steps (iii-v) are followed. Namely, the tensor $\Theta_{[l,l+1]}$, of dimension $d \times d \times \chi_{l-1} \times \chi_{l+1}$, is first reshaped into a matrix $\theta_{[l,l+1]}$ of dimension $(d\chi_{l-1}) \times (d\chi_{l+1})$, by combining horizontal and vertical legs into "fat legs". Its elements are defined by $\theta_{(\alpha_{l-1},p_l),(\alpha_{l+1},p_{l+1})} = \Theta^{p_l,p_{l+1}}_{\alpha_{l-1},\alpha_{l+1}}$. Then, $\theta_{[l,l+1]}$ is decomposed by means of a SVD, as

$$\theta_{(\alpha_{l-1},p_l),(\alpha_{l+1},p_{l+1})} = \sum_{\alpha_l=1}^{\tilde{\chi}_l} U_{(\alpha_{l-1},p_l),\alpha_l} S_{\alpha_l,\alpha_l} (V^\dagger)_{\alpha_l,(\alpha_{l+1},p_{l+1})}, \tag{4.30}$$

with $\tilde{\chi}_l \leq \min(d\chi_{l-1}, d\chi_{l+1})$. The resulting matrix U is reshaped into a new three-leg tensor $A_{[l]}$ of left-normalised matrices $A^{n_l}_{[l]}$, and the product $SV^\dagger$ into a new three-leg tensor $A_{[l+1]}$ of matrices $A^{n_{l+1}}_{[l+1]}$. In this form, the MPO structure of the state is recovered[7].

Observe that due to the SVD performed to bring the state back to a MPO structure, the Schmidt coefficients at site l are directly obtained. In addition, the Schmidt rank at site l might have changed, and typically $\tilde{\chi}_l > \chi_l$. If various gates are applied to each pair of sites of the entire system, the Schmidt rank of each site will increase, and eventually the numerical manipulation of the total MPO will be no longer possible. To prevent this problem from occuring, we truncate the number of Schmidt coefficients retained at each site, as discussed in Section 4.2.1. If we choose a maximum site-independent Schmidt rank χ, we will deal with a MPO of $O(Nd\chi^2)$ coefficients during its entire manipulation. The error of each truncation is given by the sum of all the discarded Schmidt coefficients across the system, as expressed in equation (4.11).

[7]The S matrix can multiply U instead of $V^\dagger$ to obtain a different MPO, with the resulting $A^{n_{l+1}}_{[l+1]}$ matrices being right-normalised. The choice depends on the particular context in which the gate is applied. This will be seen clearly in Section 4.4.1, where the TEBD algorithm is explained.

4.4 Time evolving block decimation method

After introducing the matrix product description of a quantum state, we can examine how to simulate its time evolution efficiently. The method used in the research discussed in the present thesis, the Time Evolving Block Decimation (TEBD), constitutes the most powerful numerical algorithm to date to calculate such an evolution for one-dimensional many-body systems. This method was originally introduced by Vidal to obtain the time evolution of pure states [30]. Shortly afterwards it was translated by two independent works [160, 161] into the language of the celebrated Density Matrix Renormalisation Group (DMRG) [171,172][8], thus receiving the name of time-dependent DMRG (which is mathematically equivalent to TEBD [29]). Subsequently the method was extended to calculate the evolution of mixed states [31,32], which is the case of interest of the present thesis. In this Section we describe the basics of TEBD, focused on its application to Lindblad master equations [11, 31].

4.4.1 Trotter expansion

We are interested in obtaining the time evolution of an initial state $\rho(t = 0) = \rho(0)$ due to the Lindblad master equation (3.13) with time-independent Hamiltonian and environmental couplings. This problem is solved by calculating

$$\rho(t) = \exp(\mathcal{L}t)\rho(0) \tag{4.31}$$

for the desired evolution time t, with $\mathcal{L}$ the matrix form of the Liouville superoperator (see Appendix B), which can be written as a sum of two-site terms as specified

[8]The DMRG method, developed by White more than 20 years ago [171,172], became a milestone for the numerical analysis of ground and low-lying states of many-body one-dimensional systems (see comprehensive reviews in [26, 29]). The idea of translating TEBD to the DMRG notation was thus to allow several researchers familiar with DMRG to perform simple modifications to their codes to implement a time evolution algorithm [160].

in equation (4.4). To simulate equation (4.31), we start by discretising the total evolution time t into M small intervals of extent δt, so $t = M\delta t$. By choosing δt smaller than the characteristic timescale set by the Liouville superoperator[9], we can break the total operation into M steps, evolving the state $\rho(t_m)$ into $\rho(t_{m+1})$ for $m = 0, 1, 2, \ldots, M - \delta t$, with $t_{m+1} - t_m = \delta t$. So the evolution superoperator can be expressed as

$$\exp(\mathcal{L}t) = \prod_{m=1}^{M} \exp(\mathcal{L}\delta t) = [\exp(\mathcal{L}\delta t)]^{t/\delta t}. \tag{4.32}$$

After this time discretisation, we still need to deal with applying the evolution operator of each time interval to the entire system, which gets exponentially hard as N increases. To get across this complication, we decompose the evolution operator at each time interval by means of a second-order Suzuki-Trotter expansion [173]

$$\begin{aligned}
\exp(\mathcal{L}\delta t) &= \left(\prod_{n=1}^{N-1} \exp(\mathcal{L}_{n,n+1}\delta t/2)\right) \times \left(\prod_{n=N-1}^{1} \exp(\mathcal{L}_{n,n+1}\delta t/2)\right) + O(\delta t^3) \\
&= \big(\exp(\mathcal{L}_{1,2}\delta t/2) \cdots \exp(\mathcal{L}_{N-1,N}\delta t/2)\big) \\
&\times \big(\exp(\mathcal{L}_{N-1,N}\delta t/2) \cdots \exp(\mathcal{L}_{1,2}\delta t/2)\big) + O(\delta t^3).
\end{aligned} \tag{4.33}$$

In this form, the evolution operator of the entire system at each time step is approximated by two sweeps, one from left to right and other from right to left. In each sweep, two-site gates $U_{n,n+1} = \exp(\mathcal{L}_{n,n+1}\delta t/2)$ are applied in an ordered sequence, as illustrated in figure 4.8. Using a MPO structure to describe the state, this process is performed efficiently as explained in Section 4.3.3, until reaching the desired final time t. Note that in the left-to-right sweep, the S matrix defined at each SVD multiples the corresponding $V^\dagger$ matrix, so at the end of the sweep the

[9]For time-dependent Liouville superoperators $\mathcal{L}(t)$, δt should be smaller than the timescale of the fastest varying Hamiltonian coupling or incoherent rate, so at each step t_m of the simulation, $\mathcal{L}(t_m)$ is well approximated by being constant in time.

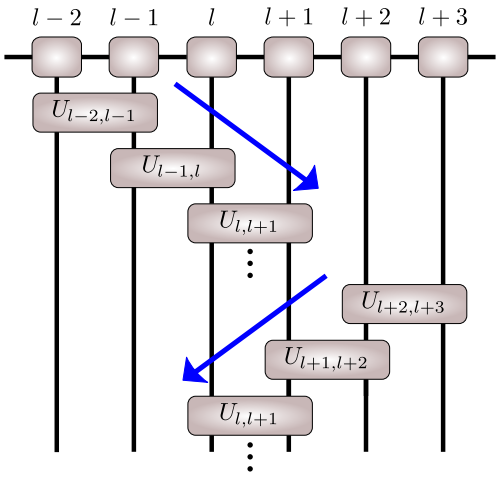

Figure 4.8. TEBD sweep process. At each time step, the evolution operator of the entire system is approximated by a left-to-right sweep of ordered contractions of the MPO with local two-site gates $U_{l,l+1}$, followed by a right-to-left sweep.

state if left-canonical. On the other hand, in the right-to-left sweep, S multiples the corresponding U matrix, so at the end of the time step the state is right-canonical.

During the simulation of transient dynamics, the correlations across the system usually grow with time, as manifested by the increase of the dimensions of the matrices within the MPO. Thus an approximation is eventually required to make the evolution numerically tractable. This is achieved by using a maximum Schmidt rank χ, which leads to a total truncation error given by the sum of the truncation errors of each SVD performed (equation (4.11)). The larger the value of χ is, the lower the error induced since fewer Schmidt coefficients are discarded at each SVD. This of course makes the TEBD simulation harder; fortunately not very large values of χ are needed to obtain accurate results.

4.4.2 Obtaining the NESS

In the present thesis we are only interested in performing TEBD simulations in the long-time limit, so the NESS is obtained. Thus an important point to discuss is

whether the NESS of the driven systems we consider is actually unique. To our knowledge, no rigorous proof of this result exists. Nevertheless, arguments suggesting that this is the case do exist. For example, from our discussion in Chapter 5 on the interplay between magnetic driving and the eigenstructure of the XXZ model, it follows that no states of the configuration space are dynamically isolated from others, i.e. it is in principle possible to reach any configuration of the spin lattice from any other, by hopping processes or driving by the boundary reservoirs. Additionally, we have tested numerically that different initial states lead to the same NESS (see also reference [11]).

To obtain the NESS in our TEBD simulations, we perform the evolution of the system up to a time t long enough so that the properties of interest (currents, magnetisation and energy profiles, and correlation functions) do not change appreciably any more. Even though our tests indicate that the NESS is independent of the initial state, it is important to select the latter so the time of calculation is not very long. For example, for the study of spin transport with magnetic driving at the boundaries (see Chapters 5, 8 and 9), we choose as initial state a product whose magnetisation is a spin ramp, going linearly from $\langle\sigma_1^z\rangle = f$ to $\langle\sigma_N^z\rangle = -f$ (f being the driving strength). This corresponds to the MPO of equation (4.25), with

$$\mu_i = \frac{-2f}{N-1}(i-1) + f. \tag{4.34}$$

This state, in spite of not having any current, has a magnetisation close to that obtained for driving f when the transport is diffusive (see Section 5.2). Because of this, the NESS is obtained much faster with this initial state than with several other possible choices, such as a product state with homogeneous magnetisation.

In addition, a good strategy to perform the time evolution consists of evolving the state for different periods of time with increasing values of χ. During the first

period we evolve the initial state using a small value of χ, which takes the system somewhat close to the NESS. The outcome is then renormalised (so its trace is 1) and used as the initial state of a new simulation with larger χ, which improves the quality of the results. The same process is repeated until the NESS is obtained, which is recognised when the increase of χ and a longer time evolution do not affect the expectation values of the state. The NESS is also identified when the (spin and/or energy) currents through the system become homogeneous; in practice we identify it when the standard deviation of the currents across the system is very small, $\lesssim 0.5\%$.

As an example, consider the case of spin transport in the linear-response regime, described in Chapter 5. In the strongly-interacting limit with $\Delta = 2$ and $N = 40$, the sequence of Schmidt ranks $\chi = 30, 60, 120, 200$ with corresponding number of time steps $M = 4, 3, 2, 1 \times 10^3$ and time step $\delta t = 0.05$ is enough to take the system to the corresponding NESS, selecting the initial state determined by equation (4.34). In the weakly-interacting regime, just using $\chi = 30, 60$ with half of the time is enough to get the NESS, given the lower amount of correlations than in the case of strong interactions.

4.4.3 Errors in the TEBD method

Different sources of error emerge when performing a TEBD simulation. The first corresponds to the truncation error that results by fixing the maximal Schmidt rank to a value χ, which accumulates in time due to the sequential use of SVDs in the process. For simulations of transient dynamics, at some point (known as the runaway time [9]) the total truncation error becomes so large that the results are no longer reliable. This time increases with the value of χ.

A second source of error comes from the expansion (4.33), which at each time step

is of $O(\delta t^3)$. This Trotter error can be reduced by using higher-order expansions, which involve more complicated gate sequences [173]. For nth-order, the error is of $O(\delta t^{n+1})$ at each time step. Since $M = t/\delta t$ steps are performed, the total Trotter error is of $O((\delta t)^n t)$. This error is also known to be proportional to N [9].

We emphasise that since we are only interested in the NESS of the system and not in transient dynamics, we do not need to worry about the accumulation of the truncation or Trotter errors in time. Since the NESS of a set of system parameters is unique [11], we can imagine as initial state the outcome of a previous simulation with a smaller value of χ, disregarding the transient states that took place before. The values of χ and δt are chosen so that the simulations give the correct NESS (χ being large enough to account for the weak correlations, δt being short enough so the fastest processes taking place in the system are not missed) while requiring the shortest calculation time.

4.4.4 Calculation of thermal states

The TEBD method can also be used to obtain thermal states

$$\rho_\beta = \frac{e^{-\beta H}}{Z(\beta)}, \qquad Z(\beta) = \mathrm{Tr}(e^{-\beta H}), \tag{4.35}$$

with H the Hamiltonian of the system, $\beta = 1/k_\mathrm{B}T$ the inverse temperature ($k_\mathrm{B} = 1$) and $Z(\beta)$ the partition function. To obtain this state, we perform an evolution for an imaginary time $\beta/2$ of the identity operator I of the entire system [31, 32], since

$$\rho_\beta \propto e^{-\beta H} = e^{-(\beta/2)H} I e^{-(\beta/2)H}. \tag{4.36}$$

The thermal state is thus obtained by simulating

$$\rho_\beta = e^{-\beta\tilde{T}} I, \quad T[A] = \frac{1}{2}(HA + AH), \tag{4.37}$$

where $\tilde{T}$ is the matrix representation of the superoperator T, defined by its action on an operator A as specified in equation (4.37). Note that the division of the exponential of time β into two exponentials of time $\beta/2$ leads to a reduction of the simulation time by one half. The result is finally normalised by the partition function to ensure that $\mathrm{Tr}(\rho_\beta) = 1$.

Similarly to an evolution governed by a Lindblad master equation, $e^{-\beta\tilde{T}}$ is approximated by a Suzuki-Trotter expansion, where two-site gates are applied across the system. The local gate applied to sites l and $l+1$ is

$$U_{l,l+1}(\beta) = e^{-\beta\tilde{T}_{l,l+1}}, \quad T_{l,l+1}[A] = \frac{1}{2}\big(H_{l,l+1}A + AH_{l,l+1}\big), \tag{4.38}$$

where $\tilde{T}_{[l,l+1]}$ is the matrix representation of the superoperator $T_{l,l+1}$. This matrix representation is obtained in the same form as that of the Liouvillian superoperator (see Appendix B). That is, we calculate $T_{l,l+1}\left[\sigma^\gamma_{l,l+1}\right]$ for all basis elements of the operator space of two sites $\sigma^\gamma_{l,l+1}$, $\gamma = 1, \ldots, d^2$. The projection of $T_{l,l+1}\left[\sigma^\gamma_{l,l+1}\right]$ onto basis element α, i.e. onto $\sigma^\alpha_{l,l+1}$, is the component (α, γ) of $\tilde{T}_{l,l+1}$.

4.5 Software: Open-source TNT Library

Finally, we note that most of the TEBD calculations in the present thesis were performed using the Tensor Network Theory (TNT) open-source library [174], developed within our research group. This library contains highly optimised routines for several algorithms based on a tensor network structure, including all the calculations described in the present Chapter. Notably, it provides a performance

enhancement of up to 30 times compared to previously existing codes in our group, making it possible to solve hard-to-simulate problems with accessible computational resources. The simulations of Chapter 5 represent the first extensive use of this library.

Chapter 5

Spin and heat transport in the magnetically-driven XXZ model

In the present Chapter we discuss the spin and heat transport through a one-dimensional chain characterised by the XXZ model, when it is driven to a nonequilibrium configuration by magnetic reservoirs at its boundaries. We solve the Lindblad master equation that governs the dynamics of the system and obtain its steady state using the Time Evolving Block Decimation. First we focus on spin transport, and reproduce results reported in previous research on the same configuration [11, 20, 21]. At weak driving, these correspond to the existence of ballistic, superdiffusive and diffusive transport in the weakly ($\Delta < 1$), intermediate ($\Delta = 1$) and strongly ($\Delta > 1$) interacting regimes, respectively. The effect of breaking the integrability of the Hamiltonian, namely to induce diffusive transport even for weak interactions, is also observed. For strong driving, we reproduce the observation of ballistic transport for $\Delta < 1$, and of negative differential conductivity for $\Delta > 1$, which leads to an insulating state at maximal driving.

The unexpected existence of negative differential conductivity in the XXZ chain was found a few years ago [20, 21]. Nevertheless, the qualitative justification of its emergence was not clear, and relied on single-particle physics. Here we give a com-

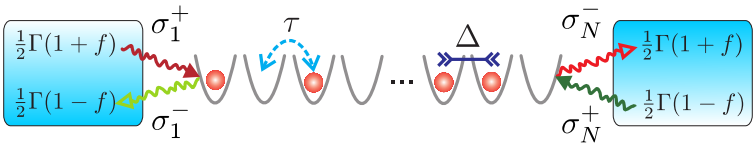

Figure 5.1. Scheme of a system driven out of equilibrium due to magnetic reservoirs. Spin excitations hop with amplitude $\tau_j = \tau$ across a chain, subject to a nearest-neighbour interaction of strength Δ and boundary driving that injects/ejects excitations at a rate $\propto \Gamma$ and driving bias f. The driving process induces a forward (upper arrows) and a backward (lower arrows) flow of particles, and the bias f determines the imbalance between both.

prehensive explanation for the origin of this effect, proving that it is a genuine many-body phenomenon. We show how at maximal driving, the interplay between the eigenspectrum of the Hamiltonian and the driving scheme preferentially populates a state of ferromagnetic domains, which prevents the transport of excitations and causes an insulating state. We then describe the effects of diminishing the driving. These results have been published in reference [175].

Subsequently we study the heat transport induced by the same driving scheme, which thus constitutes a magnetothermal (Peltier) response. We find that in the presence of a homogeneous magnetic field, the induced heat current has the same properties of the spin current. These results have been published in reference [176].

5.1 Model for spin transport

We start by describing the configuration used to study the properties of spin conduction, which will also be considered in most of the work in subsequent Chapters. This consists of a one-dimensional interacting spin-$\frac{1}{2}$ XXZ chain, with Hamiltonian

$$H = \sum_{j=1}^{N-1} \tau_j (\sigma_j^x \sigma_{j+1}^x + \sigma_j^y \sigma_{j+1}^y + \Delta \sigma_j^z \sigma_{j+1}^z) + \sum_{j=1}^{N} B_j \sigma_j^z \tag{5.1}$$

and hopping $\tau_j = \tau(1+\delta_j)$, connecting two reservoirs of unequal magnetisation, as depicted in figure 5.1. The energy scale is set by taking the hopping rate $\tau = 1$. The degrees of freedom of the reservoirs are discarded from the total equation of motion using standard techniques of the theory of open quantum systems [130,177], including the assumptions of weak system-reservoir coupling (Born approximation) and of fast time decay of reservoir correlation functions (Markov approximation); see Appendix C for details. The resulting equation of motion for the state of the spin chain ρ is given by the following Lindblad master equation

$$\frac{d\rho}{dt} = \mathcal{L}(\rho) = -i[H,\rho] + \sum_k \mathcal{L}_k(\rho) = -i[H,\rho] + \mathcal{L}^{\mathrm{L}}_{\mathrm{driv}}(\rho) + \mathcal{L}^{\mathrm{R}}_{\mathrm{driv}}(\rho), \tag{5.2}$$

where each dissipative superoperator $\mathcal{L}_k(\rho)$ is given by

$$\mathcal{L}_k(\rho) = L_k \rho L_k^\dagger - \frac{1}{2}\{L_k^\dagger L_k, \rho\}, \tag{5.3}$$

and L_k are jump operators representing the coupling of the chain to the reservoirs. The dissipators $\mathcal{L}^{\mathrm{L}}_{\mathrm{driv}}(\rho)$ and $\mathcal{L}^{\mathrm{R}}_{\mathrm{driv}}(\rho)$ represent the boundary driving of the chain to a nonequilibrium configuration, and correspond to the jump operators [21]

$$L^+_{\mathrm{L,R}} = \sqrt{\Gamma(1 \pm f)/2}\,\sigma^+_{1,N} \quad L^-_{\mathrm{L,R}} = \sqrt{\Gamma(1 \mp f)/2}\,\sigma^-_{1,N}. \tag{5.4}$$

These operators create and annihilate spin excitations at the boundary sites of the system, with f the driving strength that establishes the imbalance between both processes ($0 \leq f \leq 1$) and Γ the coupling strength to the spin reservoirs (we take $\Gamma = 1$ for the numerical calculations). The driving strength f controls the nonequilibrium forcing, and in isolation it would impose unequal average spin polarisations in the boundaries, $\langle \sigma^z_1 \rangle = f$ and $\langle \sigma^z_N \rangle = -f$ [178]. A zero bias $f = 0$ leads to a steady state $\rho = \mathbb{1}/2^N$ [179], indicating that the system is formally at

infinite temperature; no spin current exists in this case since spin-flip excitations are created and annihilated at the same rate on both boundaries. At finite driving f, spin excitations are effectively injected to the chain at the left boundary, and are ejected with the same rate at the right boundary. So a net spin current flow is established due to the asymmetry between the two edges. At maximum bias $f = 1$ the boundary jump operators reduce to σ_1^+ and σ_N^-.

By directly simulating equation (5.2) and taking the long-time limit, the state $\rho(t)$ converges to the time-independent nonequilibrium steady state (NESS) of the system. We perform this calculation efficiently by applying the Time Evolving Block Decimation (TEBD) algorithm, described in Chapter 4. This method allows us to consider a large parameter range, including the regime beyond linear response $f \ll 1$. Once the NESS is obtained, we calculate the properties relevant for the analysis of transport response, namely the magnetisation $\langle \sigma_i^z \rangle$ and the local spin current $\langle J_i \rangle$. To obtain the latter, note that directly from the master equation (5.2) we have

$$\left\langle \frac{d\sigma_i^z}{dt} \right\rangle = \mathrm{Tr}\left(\sigma_i^z \frac{d\rho}{dt} \right) = \langle J_{i-1} \rangle - \langle J_i \rangle + \mathrm{Tr}(\sigma_1^z \mathcal{L}_{\mathrm{driv}}^{\mathrm{L}}(\rho))\delta_{i,1} + \mathrm{Tr}(\sigma_N^z \mathcal{L}_{\mathrm{driv}}^{\mathrm{R}}(\rho))\delta_{i,N} = 0, \tag{5.5}$$

where J_i is the spin current operator shown in Section 3.2,

$$J_i = 2(1+\delta_j)(\sigma_i^x \sigma_{i+1}^y - \sigma_i^y \sigma_{i+1}^x), \quad i = 1, \ldots, N-1. \tag{5.6}$$

Now consider the cases $i = 1, N$. Since equation (5.6) does not apply for $i = 0, N$, we can define from (5.5) the boundary currents [176, 180]

$$\begin{aligned} \langle J_0 \rangle &= \mathrm{Tr}(\sigma_1^z \mathcal{L}_{\mathrm{driv}}^{\mathrm{L}}(\rho)) = \Gamma(f - \langle \sigma_1^z \rangle), \\ \langle J_N \rangle &= \mathrm{Tr}(\sigma_N^z \mathcal{L}_{\mathrm{driv}}^{\mathrm{R}}(\rho)) = \Gamma(f + \langle \sigma_N^z \rangle). \end{aligned} \tag{5.7}$$

Thus across the entire chain we have that in the NESS, $\langle J_i \rangle - \langle J_{i+1} \rangle = 0$, so the

spin current is homogeneous, $J^{\mathrm{S}} \equiv \langle J_i \rangle$. Equation (5.7) also indicates that the spin current is directly given by the deviation of the magnetisation of the boundary spins from the one that would be imposed by the reservoirs to isolated spins ($\pm f$). This was previously found for the case $\Delta = 0$ (see Ref. [181] and Appendix D). Equation (5.7) shows that the same applies for all interaction strengths Δ.

Finally, note that at small driving f the states induced in the system just slightly deviate from the infinite temperature state $\rho = \mathbb{1}/2^N$ (as shown in Appendix D for $\Delta = 0$), with an energy density close to zero [12]. So the states induced by the driving scheme of equation (5.4) are known in the literature as NESSs at infinite temperature [12, 131, 135, 182]. In Chapter 6 we will discuss a different driving scheme that induces states at finite temperature; see also Appendix C.4.

Now we proceed to describe the different spin transport regimes already seen in previous research of this driven system, for weak and strong interactions, and for weak and strong driving [11, 20, 21].

5.2 Spin transport in linear response

We start by considering the system without magnetic fields ($B_j = 0$) or dimerisation ($\delta_j = 0$), in the regime of weak driving $f \ll 1$. Depending on the value of the interaction strength Δ, the system shows a distinctive type of spin transport. For weak interactions $\Delta < 1$, the magnetisation profile is flat in the bulk and the spin current is independent of the size of the system N, as shown in figure 5.2. This indicates that the spin transport is ballistic, i.e. the system behaves as an ideal magnetic conductor. This conclusion is consistent with most studies on the spin transport through an XXZ one-dimensional spin chain, as indicated in Chapter 3.

For the non-interacting case, the exact spin current and magnetisation can actually be calculated analytically, as shown in references [178, 181] (see also Ap-

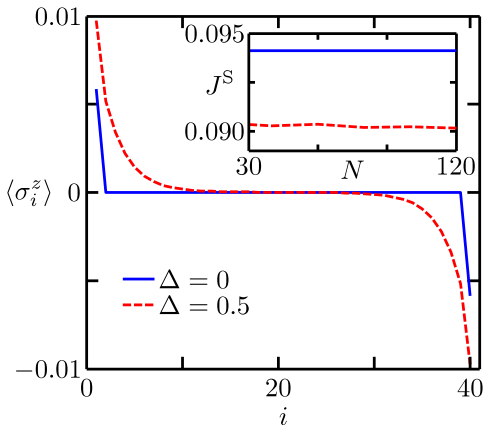

Figure 5.2. Spin transport properties of the weakly-interacting regime of the XXZ model. Main panel: Magnetisation profiles for $N = 40$. Inset: Spin current as a function of the size of the system N. The calculations are for $f = 0.1$ and $\Gamma = 1$. The results for $\Delta = 0$ correspond to the analytical expressions of equations (5.8) and (5.9). The results for $\Delta = 0.5$ were obtained with the TEBD method.

pendix D). In this case the current is given by

$$J^{\mathrm{S}} = \frac{4f}{(\Gamma/4) + (4/\Gamma)}, \tag{5.8}$$

which is size-independent and grows linearly with the driving. The magnetisation is

$$\langle\sigma_1^z\rangle = f - \frac{J^{\mathrm{S}}}{\Gamma}, \quad \langle\sigma_i^z\rangle = 0 \text{ for } i = 2, \ldots, N-1, \quad \langle\sigma_N^z\rangle = -f + \frac{J^{\mathrm{S}}}{\Gamma}. \tag{5.9}$$

Note that the finite value of the current arises due to the resistance caused by the contact of the system with the reservoirs. Also, the current acquires its optimal value for the coupling $\Gamma_{\mathrm{opt}} = 4$.

In the strongly-interacting regime $\Delta > 1$, studied by means of TEBD simulations, the results indicate diffusive transport in the NESS [11,21]. As shown in figure 5.3(a), the magnetisation profile has the form of a ramp, going smoothly from $\langle\sigma_1^z\rangle \approx f$ to $\langle\sigma_N^z\rangle \approx -f$. In addition, as indicated in figure 5.3(b), the spin current scales with

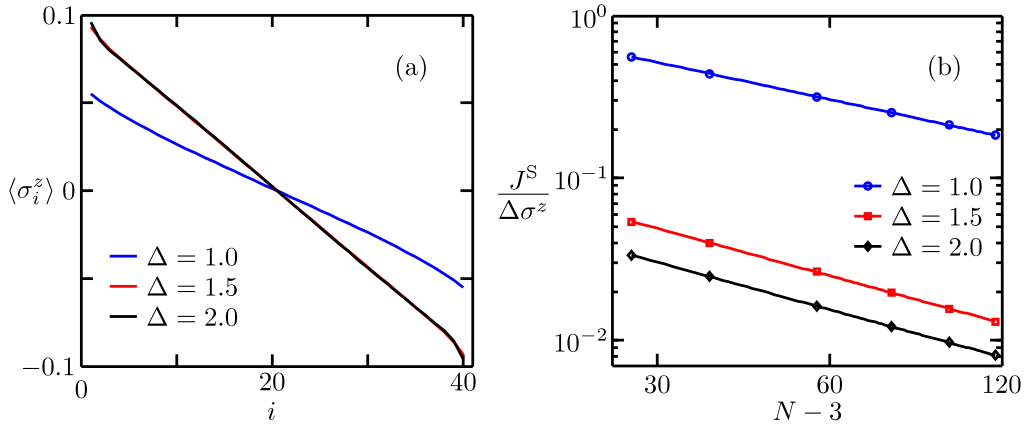

Figure 5.3. Spin transport properties of the strongly-interacting regime of the XXZ model. (a) Magnetisation profiles for $N = 40$. The profiles for $\Delta = 1.5$ and $\Delta = 2.0$ are almost indistinguishable. (b) Scaling of $J^S/\Delta\sigma^z$ with the system size. The symbols correspond to the numerical simulations, and the solid lines to the fits to equation (5.10). The calculations are for $f = 0.1$ and $\Gamma = 1$. The results of the fit are $\kappa_S = 6.85(2)$ and $\alpha = 0.760(2)$ for $\Delta = 1$, $\kappa_S = 1.3(1)$ and $\alpha = 0.97(2)$ for $\Delta = 1.5$, and $\kappa_S = 0.83(2)$ and $\alpha = 0.971(7)$ for $\Delta = 2$ (for $\Delta > 1$, similar to results of [11, 13, 106]).

the size of the system in the form specified by the diffusion equation (3.11), namely

$$\frac{J^S}{\Delta\sigma^z} = -\frac{\kappa_S}{(N-3)^\alpha} \qquad \Delta\sigma^z = \langle\sigma_{N-1}^z\rangle - \langle\sigma_2^z\rangle, \tag{5.10}$$

where $\Delta\sigma^z$ is the magnetisation difference between the boundaries (we have discarded sites 1 and N to avoid the resistance from the contact to the reservoirs), κ_S is the spin conductivity and $\alpha \approx 1$. The existence of diffusive transport in linear response of the strongly-interacting regime $\Delta > 1$ observed in the boundary-driven configuration is consistent with the conclusions obtained from different techniques, as discussed in Chapter 3.

Finally, as indicated in figure 5.3, the system shows a different type of spin transport in the isotropic point. Here the spin current decays with the size of the system according to equation (5.10), but with $0 < \alpha < 1$. The spin transport is in an intermediate regime between normal diffusion ($\alpha = 1$) and ballistic behaviour

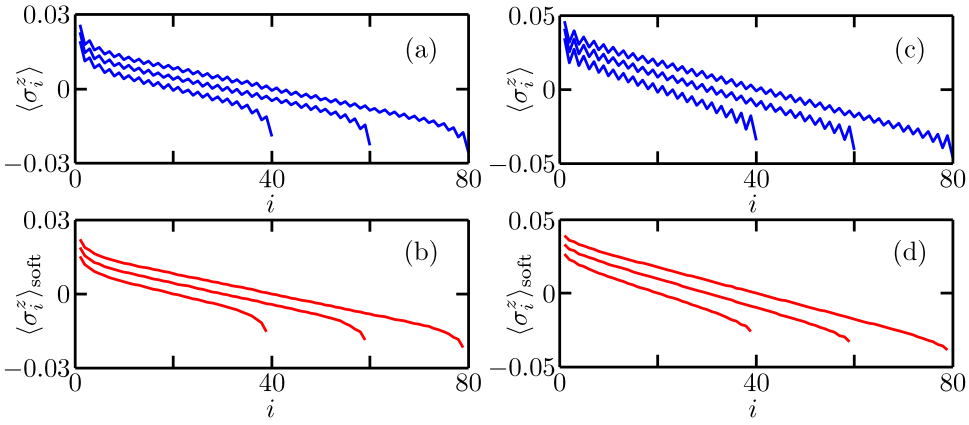

Figure 5.4. Magnetisation of the NESS for several non-integrable weakly-interacting Hamiltonians. Left panels. For staggered magnetic field $B = 0.1$. (a) Magnetisation profile. (b) Softened magnetisation. Right panels. For dimerisation $\delta = 0.1$. (c) Magnetisation profile. (d) Softened magnetisation. The results are for $f = 0.1$, $\Gamma = 1$, $\Delta = 0.5$ and $N = 40, 60, 80$.

($\alpha = 0$), and thus has been recently identified as superdiffusive [12]. This behaviour has also been suggested by studies based on quantum quenches [13], where a temperature-dependent wave-packet expansion intermediate between ballistic and diffusive responses was found. Nevertheless, as described in Chapter 3, the spin transport in the isotropic point has been the object of a lot of controversy, so more effort is required to completely clarify its true nature.

5.2.1 Non-integrable models

Now we consider the effects of the transport properties of integrability breaking terms, in particular of staggered magnetic field $B_j = (-1)^j B$ and dimerisation $\delta_j = (-1)^j \delta$[1], focusing on the weakly-interacting regime. We consider the specific forms given in equation (2.18). As shown in figures 5.4(a) and (c) for staggered field and dimerisation respectively, the magnetisation profiles are no longer flat in the bulk, but have the form of a ramp with local oscillations. To have a quantitative

[1]Recall that the noninteracting case $\Delta = 0$ remains integrable with dimerisation [8, 56].

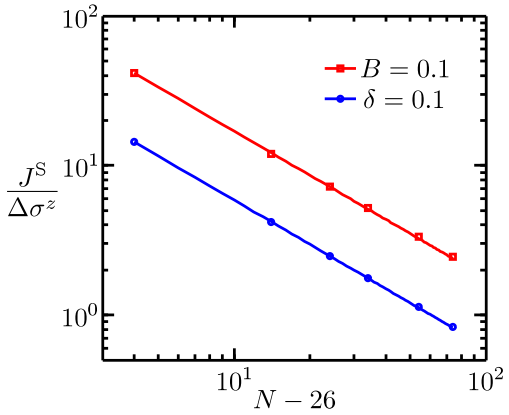

Figure 5.5. Scaling of $J^S/\Delta\sigma^z$ with the system size, for non-integrable Hamiltonians. The results correspond to $f = 0.1$, $\Gamma = 1$ and $\Delta = 0.5$. For $B = 0.1$, $\kappa_S = 161(4)$, $\alpha = 0.98(1)$. For $\delta = 0.1$, $\kappa_S = 56.2(5)$, $\alpha = 0.982(5)$. To reduce boundary effects, 12 sites at each edge were discarded for the calculation of the scaling, as indicated in equation (5.12).

idea of the nature of the transport, we define a softened magnetisation, given by

$$\langle\sigma_i^z\rangle_{\text{soft}} = \frac{1}{2}\left(\langle\sigma_i^z\rangle + \langle\sigma_{i+1}^z\rangle\right). \tag{5.11}$$

This softened magnetisation is shown in figures 5.4(b) and (d), and shows better the ramp behaviour. We observe in figure 5.5 that the spin current scales with the size of the system N in the form

$$\frac{J^S}{\Delta\sigma^z_{\text{soft}}} = -\frac{\kappa_S}{(N-26)^\alpha} \qquad \Delta\sigma^z_{\text{soft}} = \langle\sigma^z_{N-13}\rangle_{\text{soft}} - \langle\sigma^z_{13}\rangle_{\text{soft}}, \tag{5.12}$$

where 12 sites have beed discarded at each edge of the chain to avoid the strong effect of the reservoirs seen in figures 5.4(b) and (d). For both cases, $\alpha \approx 1$. This indicates that even for the weak integrability-breaking parameters considered here, the spin transport becomes diffusive in the weakly interacting regime [11]. The existence of diffusive transport in the driven strongly interacting case with staggered field has also been reported previously [21]. Thus in general, it is concluded that

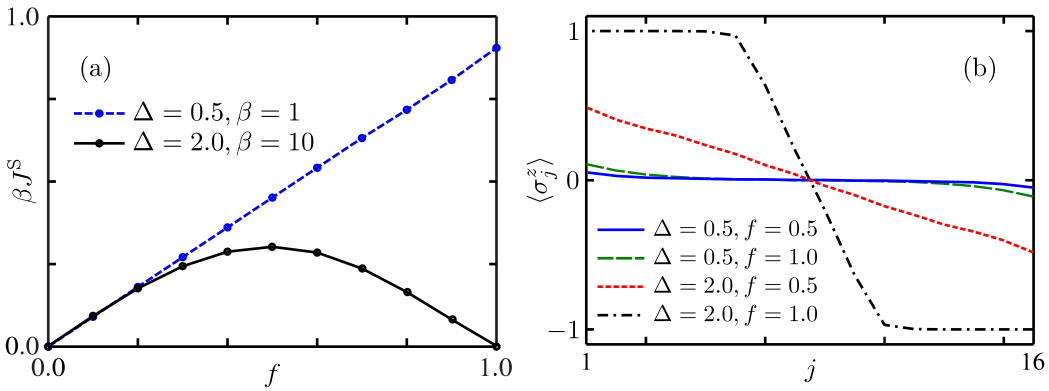

Figure 5.6. (a) Spin current as a function of the driving strength f, for weak and strong interactions. The current for $\Delta = 2.0$ has been scaled for the sake of clarity in the figure, with β determining the scaling factor. (b) Magnetisation profiles beyond linear response. The results correspond to $N = 16$ and $\Gamma = 1$.

when the integrability of the Hamiltonian of the lattice is broken, its spin transport becomes diffusive. This is consistent with the general picture of spin diffusion in non-integrable high-temperature systems that has emerged from research based on different methods, namely on the explicit calculation of Drude weights at high temperature [8, 18], on the expansion of an initially-prepared wave packet [10], and on arguments based on the disappearance of nontrivial conservation laws [14].

5.3 Negative differential conductivity

We now consider the system strongly driven out of equilibirum (large f). In the weakly-interacting case, no new physics emerges. The size-independent spin current increases linearly with f, and the magnetisation profile remains flat in the bulk, as shown in figures 5.6(a) and (b). The spin transport is then ballistic for any driving. The situation, however, is entirely different in the strongly-interacting regime. As seen in figure 5.6(a), for $f \gtrsim 0.2$ the spin current no longer increases linearly with f. At $f \approx 0.5$ it becomes maximal. For larger driving the current decreases with f,

until becoming negligibly small (in the figure, of $O(10^{-8})$) at the maximal driving $f = 1.0$; in this limit, the spin current was actually shown to decay exponentially with the size of the system [182]. This non-monotonic tendency of the current with the driving is called negative differential conductivity (NDC) [20, 21].

The general form of the magnetisation profile of the chain is also significantly affected by the driving. For intermediate values of f, it still has the form of a spin ramp, going from $\langle\sigma_1^z\rangle \approx f$ to $\langle\sigma_N^z\rangle \approx -f$. Nevertheless, at $f = 1$, the magnetisation profile is completely different. As seen in figure 5.6(b), it corresponds to two ferromagnetic domains (of almost completely aligned spins) of opposite polarisation, each pinned to one of the boundaries of the chain. The domain pinned to the right boundary, where spin excitations are only ejected (this is, where only σ_N^- acts), has negative polarisation, while that pinned to the right boundary, where spin excitations are only injected (this is, where only σ_1^+ acts), has positive polarisation. Both ferromagnetic domains have the same extension, of almost half of the chain, and are separated by a region of intermediate magnetisation. Importantly, the existence of NDC and ferromagnetic domains was found to be stable against asymmetric driving and integrability breaking [21].

It is intuitive to see why a NESS of opposite ferromagnetic domains corresponds to an insulating state at $f = 1$. Since the spins near the boundaries are almost completely polarised, spin flips by the reservoirs are strongly inhibited. It takes an exponentially long time for a spin excitation to travel across the chain, and for the ferromagnetic domains to grow [21][2]. A more interesting question is why this NESS of ferromagnetic domains arises on the first place.

A qualitative description of the emergence of the NDC was given in reference [21]. There it was shown that the single-excitation Hamiltonian, i.e. the effective Hamil-

[2]It is because of this exponentially long time of convergence to the NESS that only the dynamics of small systems such as those considered in figure 5.6 can be calculated numerically.

tonian for a single spin up hopping in a lattice of spins down, has two exponentially localised eigenstates, each around one boundary, if $\Delta > 1$. These states, of the form

$$|\psi_L\rangle \propto \sum_{m=1}^{N} e^{-(m-1)\chi}|m\rangle, \qquad |\psi_R\rangle \propto \sum_{m=1}^{N} e^{-(N-m)\chi}|m\rangle \tag{5.13}$$

for the left and right boundary respectively, have a localisation length $l \approx 1/\chi = 1/\ln(\Delta)$. It was argued that at maximal driving $f = 1$, these localised states are populated, so the excitations injected at one edge of the chain take an exponentially large time to reach the other edge, the system thus behaving as an insulator.

In this picture, however, it is not clear why the driving preferentially populates these states, or how the ferromagnetic domains arise. More important, this qualitative explanation is based on a single-particle effective Hamiltonian. The role of the interaction strength is thus limited to providing an on-site energy which is homogeneous everywhere except at the boundaries of the chain (see equations (20) and (D1) of reference [21], and Appendix A.1). The exponential localisation of the excitation results from this inhomogeneity of the effective on-site potential, and thus is not a many-body effect.

In the following Section we provide a comprehensive explanation of the origin of the ferromagnetic domains and of NDC, which are proven to be true many-body phenomena. Our approach not only clarifies how the driving populates the energy levels of the system, but also provides a good quantitative description of the NESS of the chain at maximal driving.

5.4 Emergence of ferromagnetic domains and NDC

We now discuss the physical mechanism underlying NDC. Specifically, we show that these effects arise due to an interplay between the eigenstructure of the strongly-

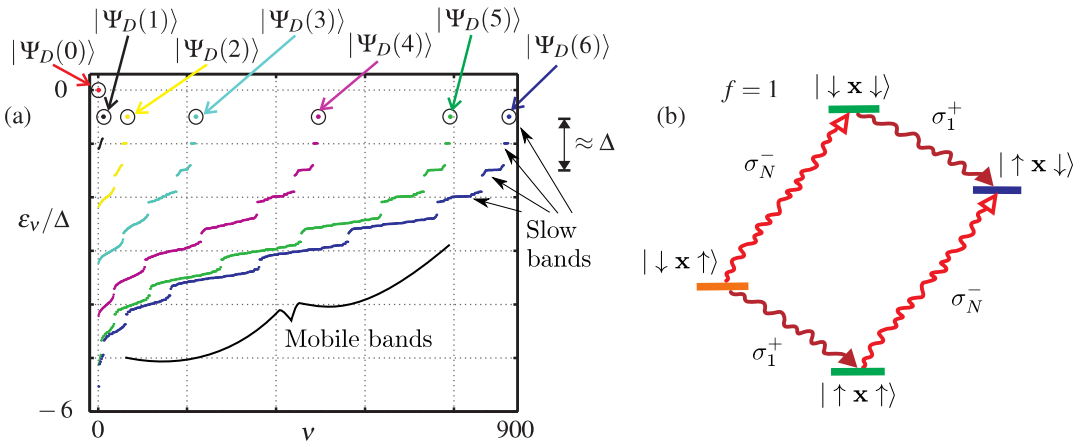

Figure 5.7. (a) The energy eigenspectrum of the XXZ Hamiltonian for $N = 12$ and $\Delta = 10$. Energies ϵ_ν have been shifted by $\Delta(N-1)$ so the state $|\Psi_D(0)\rangle = |\downarrow\downarrow \ldots \downarrow\downarrow\rangle$ has zero energy. Since the spectra arising from the excitation number sectors $n = 0, \cdots, 5$ are identical to those of $n = 7, \ldots, 12$, only the former are shown, in addition to $n = 6$. The highest lying eigenstate for each sector $|\Psi_D(n)\rangle$ is highlighted and seen to be isolated by a gap of $O(\Delta)$ from eigenstates composed of break-away configurations. The brace indicates the location of mobile bands for $n = 6$. (b) For any f, the driving alone incoherently connects a quadruplet of configurations $|\downarrow \mathbf{x} \downarrow\rangle, |\downarrow \mathbf{x} \uparrow\rangle, |\uparrow \mathbf{x} \downarrow\rangle, |\uparrow \mathbf{x} \uparrow\rangle$. The case of $f = 1$ is shown, where the driving only pumps into the dark configuration $|\uparrow \mathbf{x} \downarrow\rangle$.

interacting chain Hamiltonian and the boundary driving. In the present Section we discuss the ideas behind the explanation of NDC, and in Section 5.5 we present the supporting technical details.

As already described in Section 2.5, and as illustrated in figure 5.7(a) for a small but representative system size with very strong interactions $\Delta \gg 1$, the eigenspectrum consists of nearly flat high-energy bands of bound states of low conductivity, separated by gaps of order Δ from more mobile bands of states with lower energy. As we shall now show, strong boundary driving preferentially populates only the most energetic bound states, resulting in an insulating NESS.

To see this is more detail, it is instructive to first consider maximally biased driving $f = 1$ in the extreme $\Delta \to \infty$ limit. In this case configuration states such as $|\uparrow\downarrow\uparrow\uparrow\downarrow \cdots \downarrow\uparrow\uparrow\rangle$, where the excitation occupancy on each site of the chain is explicitly

specified, are exact eigenstates of the Hamiltonian. A key property of the boundary driving is that it only incoherently connects configurations within a quadruplet of states $|\downarrow \mathbf{x} \downarrow\rangle, |\downarrow \mathbf{x} \uparrow\rangle, |\uparrow \mathbf{x} \downarrow\rangle, |\uparrow \mathbf{x} \uparrow\rangle$ for any value of f, where $\mathbf{x}$ is any length $N-2$ occupancy bit string and thus defines each quadruplet. This is illustrated in figure 5.7(b). Consequently, if $\mathbf{x}$ has $(n-1)$ spins up, the driving couples states within the total particle number sectors $n-1, n$, and $n+1$. This structure constrains the evolution caused by the driving processes to shuffling population between states in these isolated quadruplets. At $f = 1$ there is one configuration $|\uparrow \mathbf{x} \downarrow\rangle$ within each quadruplet which, owing to it having a spin up on the leftmost site and a spin down on the rightmost site, is entirely decoupled from the driving (i.e. there is no action of the driving on such a configuration), while also being the sink for all driving transitions; see figure 5.7(b). The effect of this incoherent evolution alone is thus to eventually drive all the population among the quadruplet of states into this *dark-configuration*. Of particular relevance are the dark configurations

$$|\, B_n\rangle = |\, \overbrace{\uparrow\uparrow\uparrow \cdots \uparrow\uparrow\uparrow}^{n} \underbrace{\downarrow\downarrow\downarrow \cdots \downarrow\downarrow\downarrow}_{N-n}\rangle, \tag{5.14}$$

which possess a ferromagnetic domain of n spins up pinned to the left boundary, and another domain of $N-n$ spins down pinned to the right boundary. For each excitation number sector n the state $|\, B_n\rangle$ is separated from other configurations by an energy gap $O(\Delta)$, akin to a domain binding energy (see examples in Appendix A).

As we move to the limit of finite, but strong interactions $\Delta \gg 1$, hopping between configuration states results in each configuration $|\, B_n\rangle$ giving rise to an eigenstate $|\, \Psi_D(n)\rangle$ of bound excitations. For each excitation number n, $|\, \Psi_D(n)\rangle$ is the highest state in the eigenspectrum, as indicated in figure 5.7(a). Its properties are readily determined by treating hopping as a perturbation. Specifically, to lowest-order in $(2\Delta)^{-1}$, hopping hybridises, across an energy gap of Δ, the state $|\, B_n\rangle$ with the

break-away configuration

$$|\overbrace{\uparrow\uparrow\uparrow\cdots\uparrow\uparrow}^{n-1}\downarrow\uparrow\underbrace{\downarrow\downarrow\cdots\downarrow\downarrow\downarrow}_{N-n-1}\rangle, \tag{5.15}$$

where the outermost spin up of the domain has broken away. As discussed in Section 5.5, the hybridisation of $|\,B_n\rangle$ with more distant break-away configurations decays exponentially with the distance from the domain wall with a length scale $\xi \sim 1/\ln(2\Delta)$. Crucially almost all of these break-away configurations are dark to the driving like $|\,B_n\rangle$. Only the configurations where either a spin down or spin up has reached the boundary couple to the driving, and their amplitude is exponentially suppressed by this localisation.

The emergence of an insulating NESS in the strongly-interacting regime at $f = 1$, having ferromagnetic domains of opposite polarisation of size $N/2$, and thus the domain wall farthest from the boundaries, follows from the combination of two results in the perturbative approach:

i As $n \to N/2$, $|\,\Psi_D(n)\rangle$ becomes an exponentially close approximation to a dark state of $f = 1$ driving, with increasing N.

ii The boundary driving at $f = 1$ preferentially populates $|\,\Psi_D(n)\rangle$ leaving a NESS that is well approximated by a statistical mixture

$$\rho = \sum_{n=0}^{N} p_n\,|\,\Psi_D(n)\rangle\,\langle\Psi_D(n)\,|\,, \tag{5.16}$$

with the probability p_n exponentially peaked at $n = N/2$.

The technical details of the proof of points (i) and (ii) are presented in Section 5.5. It is then seen that they arise for sizes $N \geq 4$.

Finally, we describe what happens if we move away from the maximal driving

regime. When reducing f slightly from the $f = 1$ limit, a small backward pumping process appears in addition to the dominant forward pumping of spin excitations. Since excitations are then injected and ejected by the driving at both boundaries, all the states of every quadruplet become populated and there are no longer dark configurations decoupled from the driving. A finite current is therefore established in the NESS as the population in the approximate dark states $|\,\Psi_D(n)\rangle$ diminishes. This tendency, combined with the increase of the current with f at the linear response regime, leads to the emergence of NDC at intermediate driving.

5.5 Existence of an insulating state at maximal driving in the strongly-interacting regime

We now demonstrate that at maximal driving and very strong interactions, the system becomes an insulator. This configuration is sketched in figure 5.8(a).

Formally, a dark state $|\,\psi\rangle$ of an open quantum system is a pure state which is simultaneously an eigenstate of the Hamiltonian $H\,|\,\psi\rangle = E\,|\,\psi\rangle$ and a zero-eigenvalue eigenstate of all the jump operators comprising the dissipator $\mathcal{L}$ that describes the noise acting on the system (this is, $\mathcal{L}(|\,\psi\rangle\,\langle\psi\,|) = 0$). In this Section, we show that deep in the strongly-interacting limit $\Delta \gg 1$, with maximal $f = 1$, there exists a state $|\,\Psi_D\rangle$ which, as the system size N grows, becomes exponentially close to satisfying these requirements and is thus an approximate dark state. As mentioned in Section 5.4, the demonstration consists of two parts.

5.5.1 Existence of a dark state for maximal driving $f = 1$

As shown in figure 5.7(b), the driving scheme of the strongly-interacting limit $\Delta \to \infty$ couples the four eigenstates $|\downarrow \mathbf{x} \downarrow\rangle, |\downarrow \mathbf{x} \uparrow\rangle, |\uparrow \mathbf{x} \downarrow\rangle, |\uparrow \mathbf{x} \uparrow\rangle$, establish-

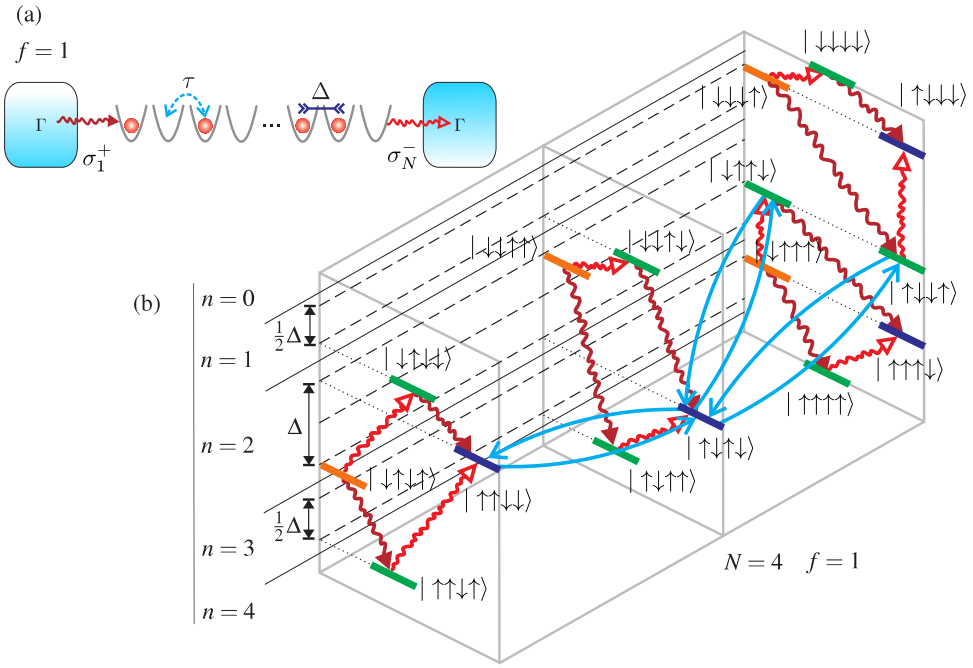

Figure 5.8. (a) A schematic of the system in the limit of maximal driving $f = 1$. In this case the driving incoherently pumps particles into the system at site 1 and ejects them at site N, both at a rate Γ. (b) For $N = 4$ sites and $f = 1$ the complete set of driving quadruplets and the transitions induced by coherent hopping between them from the half-filled domain state $|\uparrow\uparrow\downarrow\downarrow\rangle$ is shown. The vertical axis displays the particle number sectors and energy gaps between configurations. We observe that for $N = 4$ one hop connects $|\uparrow\uparrow\downarrow\downarrow\rangle$ to $|\uparrow\downarrow\uparrow\downarrow\rangle$, which is a dark configuration of its quadruplet, and a further hop is needed before it is coherently connected to a configuration that is not dark to the $f = 1$ driving. This disconnection between the half-filled domain configuration and the driving only occurs for $N \geq 4$, and so this is the smallest size which displays NDC.

ing a quadruplet defined by the string $\mathbf{x}$. At $f = 1$ the states $|\uparrow \mathbf{x} \downarrow\rangle$ become dark, of which the domain configurations $|B_n\rangle$ play a prominent role. Namely, for finite but large interaction Δ, they weakly hybridise with break-away configurations, resulting in the high-energy bound eigenstates $|\Psi_D(n)\rangle$. In figure 5.8(b) the pattern of incoherent driving transitions and coherent hopping for $N = 4$ is illustrated. Note that in this case $|B_2\rangle = |\uparrow\uparrow\downarrow\downarrow\rangle$ has no direct coherent transition to any configurations which couples to the $f = 1$ driving. It only couples to the state $|\uparrow\downarrow\uparrow\downarrow\rangle$, which is also a dark configuration. More generally, so long as $N \geq 4$ and $n \geq 2$, the

break-away configuration for any domain state $|\,B_n\rangle$ is also a dark configuration of its own quadruplet.

We now compute the high-order corrections to the states $|\,B_n\rangle$ due to hopping, to build a perturbative picture of the bound eigenstates $|\,\Psi_D(n)\rangle$. Since $\Delta \gg 1$ it is instructive to do this approximately by focusing on states describing a single break-away spin up or spin down propagating away from the domain wall at site n. These have the form

$$|\psi_k\rangle_{\rm u} = \sigma^+_{n+k}\sigma^-_n|B_n\rangle, \qquad |\psi_k\rangle_{\rm d} = \sigma^-_{n-k+1}\sigma^+_{n+1}|B_n\rangle, \tag{5.17}$$

denoting a spin up and a spin down that have hopped k sites from the domain wall to the right and left direction, respectively. As discussed in Appendix A.3, the amplitude of each one of these processes scales as $O((2\Delta)^{-k})$, leading to a state[3]

$$|\Psi_D(n)\rangle \sim |B_n\rangle + \sum_{j=1}^{n-1}\left(\frac{1}{2\Delta}\right)^{n-j+1}(1+\delta_{j,1})|\psi_{n-j+1}\rangle_{\rm d} + \sum_{j=n+1}^{N}\left(\frac{1}{2\Delta}\right)^{j-n}(1+\delta_{j,N})|\psi_{j-n}\rangle_{\rm u}. \tag{5.18}$$

This indicates that the spin up/spin down propagation through the regions of negative/positive polarisation is suppressed with its distance from the domain wall. For each n, the eigenstate $|\,\Psi_D(n)\rangle$ is therefore predicted by this spin up/spin down (ud) picture to have a domain wall that remains exponentially localised at site n, within a length scale $\sim 1/\ln(2\Delta)$ [21]. Specifically, in this spin up/spin down picture, the deviation

$$\delta_n(j) = |\langle\Psi_D(n)|n_j|\Psi_D(n)\rangle - \langle B_n|n_j|B_n\rangle| \tag{5.19}$$

of the excitation population $n_j = (1/2)(1+\sigma^z_j)$ at site j of state $|\Psi_D(n)\rangle$ from that

[3]Note that in Appendix A.3 we describe the problem in the equivalent picture of hard-core bosons, thus referring to particles (p) and holes (h). Here these correspond to spins up (u) and spins down (d).

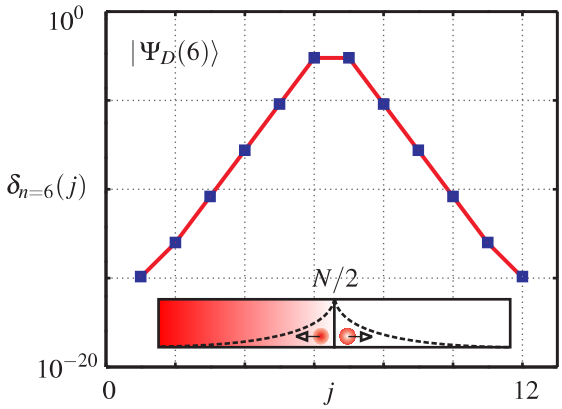

Figure 5.9. Exact density deviation $\delta_{n=6}(j)$ of the eigenstate $|\,\Psi_D(6)\rangle$ from the boundary domain configuration $|\,B_6\rangle$ (■), for $N = 12$ and $\Delta = 10$. The deviation $\delta_n^{\mathrm{ud}}(j)$ predicted by considering a single spin up/down propagation (solid line) is also shown. The inset shows a schematic of the expected exponential localisation of the domain wall.

of the perfect domain configuration $|\,B_n\rangle$ is given by

$$\delta_n^{\mathrm{ud}}(j) = \begin{cases} \frac{4}{(2\Delta)^{2n}}, & j = 1 \\ \left(\frac{1}{2\Delta}\right)^{2(n-j+1)}, & 1 < j \leq n \\ \left(\frac{1}{2\Delta}\right)^{2(j-n)}, & n < j < N \\ \frac{4}{(2\Delta)^{2(N-n)}}, & j = N \end{cases}, \tag{5.20}$$

as discussed in Appendix A.3. The validity of this perturbative picture is established by comparing the previous result to the actual density deviation $\delta_n(j)$ of the eigenstate $|\,\Psi_D(n)\rangle$ obtained from exact diagonalisation. In Fig. 5.9 this is done for $|\,\Psi_D(N/2)\rangle$ with $N = 12$ and $\Delta = 10$; the agreement between $\delta_n(j)$ and $\delta_n^{\mathrm{ud}}(j)$ is seen to be excellent.

Since hopping predominately connects $|\,B_n\rangle$ with dark-configurations of the form $|\uparrow \mathbf{x} \downarrow\rangle$, the leading order contribution to the amplitude in $|\,\Psi_D(n)\rangle$ for a configuration which is not dark is $O(\Delta^{-\min(n,|n-N/2|)})$. This corresponds to whether the spin down or the spin up has the shortest path to the left or right boundary, respectively. In the $\Delta \gg 1$ limit we therefore conclude that the eigenstates $|\,\Psi_D(n)\rangle$,

with $0 \leq n \leq N/2$, form a hierarchy of states with n, characterised by a decreasing amplitude for any configuration to be coupled to the $f = 1$ boundary driving. Eigenstates $|\,\Psi_D(n)\rangle$ with a domain size n scaling with N thus become exponentially close to being zero eigenstates of the $f = 1$ driving with increasing system size. Of these states the one with $n = N/2$, where the domain spans exactly half the chain, has the most suppressed coupling $O(\Delta^{-N/2})$ to the driving and is thus the closest approximation of all of them to an exact dark state. Now we show that this is precisely the state preferentially populated by the driving process.

5.5.2 Structure of the NESS in the $|\Delta| \gg 1$ limit

The open dynamics of excitation number conserving systems like that considered here have been studied extensively [21,179] with regard to their ergodic and mixing properties, and it has been established that a unique NESS exists for any f. The key property ensuring this is that for a finite hopping amplitude every configuration within each excitation number sector can be reached from any other, while the incoherent ejection/injection of excitations by the driving connects neighbouring sectors. As a result, the complete state space of the system can be accessed. Furthermore, the NESS for this open system will be block diagonal in the excitation number sectors. At $f = 1$, the approximate dark states $|\,\Psi_D(n)\rangle$ for each sector n, given in equation (5.18), are expected to play a prominent role due to their ability to trap population. This can be better understood by approximating the NESS as a statistical mixture, with probabilities p_n, of these eigenstates in each sector as

$$\rho = \sum_{n=0}^{N} p_n \,|\,\Psi_D(n)\rangle\,\langle\Psi_D(n)\,|\,. \tag{5.21}$$

The probabilities p_n are determined by demanding that at stationarity there is a detailed balance condition between the incoherent transition rates connecting

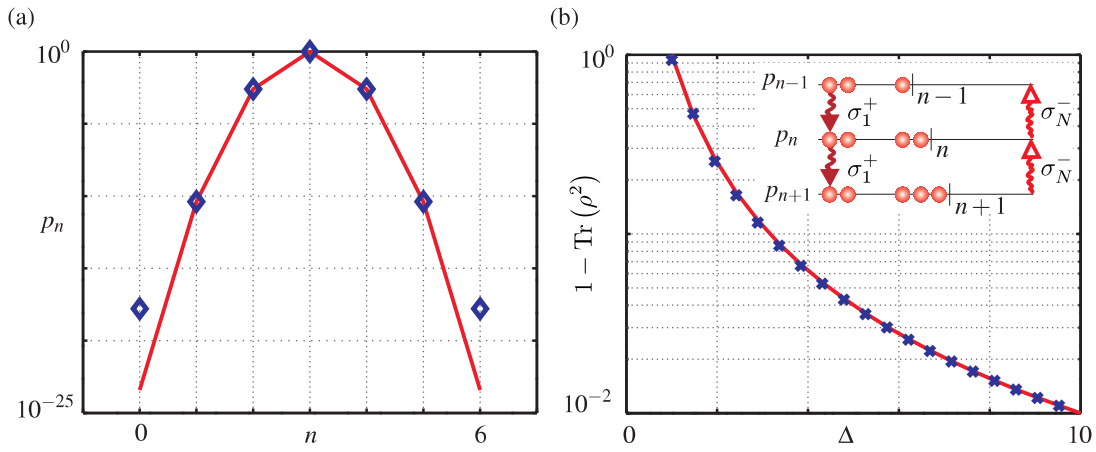

Figure 5.10. Perturbative properties of the strongly-interacting NESS at maximal driving. (a) Probability p_n, on a logarithmic scale, of the NESS ρ occupying the n spin excitation sector, for an exact calculation ($\diamond$) for $N = 6$ and $\Delta = 10$, and the predicted form (solid line) given in Eq. (5.26). (b) Purity $1 - \mathrm{Tr}(\rho^2)$ against Δ of the NESS ρ on a logarithmic scale for an exact calculation ($\times$) for $N = 6$ and the predicted form (solid line) given in Eq. (5.27). The inset shows a schematic of the detailed balance approximation applied to compute these predictions, where each sphere represents a spin up.

neighbouring number sectors (see inset of figure 5.10(b)). For sector n, assumed to be frozen in the state $|\,\Psi_D(n)\rangle$, the transition probability to sector $n+1$ is given by

$$P_{n\to n+1} = p_n \Gamma \langle \Psi_D(n)|\sigma_1^-\sigma_1^+|\Psi_D(n)\rangle = 4\Gamma p_n \left(\frac{1}{2\Delta}\right)^{2n}, \tag{5.22}$$

where $\langle \Psi_D(n)|\sigma_1^-\sigma_1^+|\Psi_D(n)\rangle$ is the probability of creating a spin up at site 1. Similarly, the transition probability to sector $n-1$ is

$$P_{n\to n-1} = p_n \Gamma \langle \Psi_D(n)|\sigma_N^+\sigma_N^-|\Psi_D(n)\rangle = 4\Gamma p_n \left(\frac{1}{2\Delta}\right)^{2(N-n)}, \tag{5.23}$$

where $\langle \Psi_D(n)|\sigma_N^+\sigma_N^-|\Psi_D(n)\rangle$ is the probability of creating a spin down at site N. Similarly, the transition probabilities towards sector n from the neighbouring sectors

$n-1$ and $n+1$ are

$$P_{n-1\to n} = 4\Gamma p_{n-1}\left(\frac{1}{2\Delta}\right)^{2(n-1)} \qquad P_{n+1\to n} = 4\Gamma p_{n+1}\left(\frac{1}{2\Delta}\right)^{2(N-n-1)}. \tag{5.24}$$

Thus, the following detailed balance condition for the transition probabilities involving sector n must be fulfilled in the NESS:

$$P_{n\to n+1} + P_{n\to n-1} = P_{n-1\to n} + P_{n+1\to n}. \tag{5.25}$$

These equations are solved inwards from the extremal $n = 0$ and $n = N$ sectors, where $|\Psi_D(0)\rangle = |\downarrow\downarrow\ldots\downarrow\downarrow\rangle$ and $|\Psi_D(N)\rangle = |\uparrow\uparrow\ldots\uparrow\uparrow\rangle$. The result is

$$p_n = p\left(\frac{1}{|2\Delta|}\right)^{2|n-N/2|^2}, \tag{5.26}$$

for $n = 0, 1, \ldots, N$ and where $p = p_{N/2}$ is fixed by the normalisation condition $\sum_{n=0}^{N} p_n = 1$. In figure 5.10(a) these predicted probabilities of occupation for each sector n are plotted against the exact values for the NESS with $N = 6$ and $\Delta = 10$, and found to yield excellent agreement aside from the extremal sectors. Owing to the hierarchy of approximate dark states, this indicates that the NESS will be predominately a mixture of $|\Psi_D(n)\rangle$ peaked around the "best" dark state with $n = N/2$, this is, the state with ferromagnetic domains of equal extension and opposite polarisation.

This result is reinforced by looking at the purity of the NESS, $\mathrm{Tr}(\rho^2) = \sum_{n=0}^{N} p_n^2$. The previous approach predicts that to lowest order in Δ^{-1}, the purity of ρ is

$$\mathrm{Tr}(\rho^2) \approx p_{N/2}^2 \approx 1 - \frac{1}{\Delta^2} + \ldots, \tag{5.27}$$

which is independent of the size of the system. So the NESS of the system at maximal

driving is better described by the single dark state $|\Psi_D(N/2)\rangle$ as the interaction strength between spin excitations increases. In Fig. 5.10(b) this prediction is plotted against the exact value of $1-\mathrm{Tr}(\rho^2)$ of the NESS for $N=6$ as a function of Δ, again showing excellent agreement even as $\Delta \to 1$. The purity of the NESS is reduced only through mixing between sectors, which occurs when we move away from the maximal driving configuration.

5.6 Heat transport in the magnetically-driven spin chain

After observing the spin conduction properties of the NESS of the driven system depicted in figure 5.1, we draw our attention to the heat transport of the same driving configuration. We consider the integrable Hamiltonian (5.1) with a homogeneous magnetic field $B_j = B$, which as explained below, is required for the heat current to exist. First we define the heat currents, and then we calculate their expectation values and the energy profiles.

5.6.1 Definition of heat current

We denote by J_i^{H} the heat current operator at site i. To obtain its expectation value, we first write the Hamiltonian in the form

$$H = \sum_{i=1}^{N-1} \varepsilon_{i,i+1} = \sum_{i=1}^{N-1} (h_{i,i+1} + b_{i,i+1}), \tag{5.28}$$

where $h_{i,i+1}$ and $b_{i,i+1}$ correspond to the XXZ coupling and magnetic field terms, respectively, and are given by

$$h_{i,i+1} = \sigma_i^x\sigma_{i+1}^x + \sigma_i^y\sigma_{i+1}^y + \Delta\sigma_i^z\sigma_{i+1}^z, \quad b_{i,i+1} = \frac{B}{2}[\sigma_i^z(1+\delta_{i,1}) + \sigma_{i+1}^z(1+\delta_{i+1,N})], \tag{5.29}$$

where δ denotes the Kronecker delta. Then we calculate the rate of change of the local energy density $\varepsilon_{i,i+1}$. From master equation (5.2), we have that in the NESS

$$\frac{d\langle\varepsilon_{i,i+1}\rangle}{dt} = i\langle[H,\varepsilon_{i,i+1}]\rangle + \mathrm{Tr}(\varepsilon_{1,2}\mathcal{L}^{\mathrm{L}}_{\mathrm{driv}}(\rho))\delta_{i,1} + \mathrm{Tr}(\varepsilon_{N-1,N}\mathcal{L}^{\mathrm{R}}_{\mathrm{driv}}(\rho))\delta_{i+1,N} = 0, \quad (5.30)$$

where $i = 1,\ldots,N-1$. Next we consider the continuity equation at each pair of neighbouring sites in the steady state

$$\frac{d\langle\varepsilon_{i,i+1}\rangle}{dt} = -\nabla\langle J^{\mathrm{H}}_i\rangle + \left.\frac{d\langle\varepsilon_{i,i+1}\rangle}{dt}\right|_{\mathrm{Env}} = 0, \quad (5.31)$$

where $\nabla\langle J^{\mathrm{H}}_i\rangle = \langle J^{\mathrm{H}}_{i+1}\rangle - \langle J^{\mathrm{H}}_i\rangle$ is the heat current gradient, and $(d\langle\varepsilon_{i,i+1}\rangle/dt)|_{\mathrm{Env}}$ is the rate of change of the local energy density due to the coupling of the system with the environment. By comparing equations (5.30) and (5.31), we identify

$$i\langle[H,\varepsilon_{i,i+1}]\rangle = -\nabla\langle J^{\mathrm{H}}_i\rangle = \langle J^{\mathrm{H}}_i\rangle - \langle J^{\mathrm{H}}_{i+1}\rangle \quad \rightarrow \quad \langle J^{\mathrm{H}}_i\rangle = i\langle[\varepsilon_{i-1,i},\varepsilon_{i,i+1}]\rangle, \quad 2 \leq i \leq N-1. \quad (5.32)$$

If we define the boundary currents

$$\langle J^{\mathrm{H}}_1\rangle = \mathrm{Tr}(\varepsilon_{1,2}\mathcal{L}^{\mathrm{L}}_{\mathrm{driv}}(\rho)) \qquad -\langle J^{\mathrm{H}}_N\rangle = \mathrm{Tr}(\varepsilon_{N-1,N}\mathcal{L}^{\mathrm{R}}_{\mathrm{driv}}(\rho)), \quad (5.33)$$

then we have a consistent definition of the heat current over the entire system, since the continuity equation for any pair of nearest neighbours gives

$$\langle J^{\mathrm{H}}_{i+1}\rangle - \langle J^{\mathrm{H}}_i\rangle = 0. \quad (5.34)$$

This is, in the NESS the heat current is homogeneous throughout the system. In order to understand the features of the heat transport, we separate the heat current in equation (5.32) into two contributions: that arising from XXZ interactions only,

given at site i $(2 \leq i \leq N-1)$ by

$$\begin{aligned}\langle J_i^{\mathrm{XXZ}}\rangle = i\langle[h_{i-1,i}, h_{i,i+1}]\rangle = 2\langle(\sigma_{i-1}^y\sigma_i^z\sigma_{i+1}^x - \sigma_{i-1}^x\sigma_i^z\sigma_{i+1}^y) \\ + \Delta(\sigma_{i-1}^z\sigma_i^x\sigma_{i+1}^y - \sigma_{i-1}^y\sigma_i^x\sigma_{i+1}^z) + \Delta(\sigma_{i-1}^x\sigma_i^y\sigma_{i+1}^z - \sigma_{i-1}^z\sigma_i^y\sigma_{i+1}^x)\rangle,\end{aligned} \tag{5.35}$$

and the current carried by the net flow of spin excitations, corresponding to

$$\langle J_i^{\mathrm{B}}\rangle = i\langle[\varepsilon_{i-1,i}, \varepsilon_{i,i+1}]\rangle - i\langle[h_{i-1,i}, h_{i,i+1}]\rangle = \frac{B}{2}\langle(J_{i-1}^{\mathrm{S}} + J_i^{\mathrm{S}})\rangle \tag{5.36}$$

We define similar contributions at the boundaries. For site $i = 1$,

$$\begin{aligned}\langle J_1^{\mathrm{XXZ}}\rangle &\equiv \mathrm{Tr}(h_{1,2}\mathcal{L}_{\mathrm{driv}}^{\mathrm{L}}(\rho)) = -\Gamma(\langle h_{1,2}\rangle + \Delta\langle\sigma_1^z\sigma_2^z\rangle)/2 + \Gamma f\Delta\langle\sigma_2^z\rangle, \\ \langle J_1^{\mathrm{B}}\rangle &\equiv \mathrm{Tr}(b_{1,2}\mathcal{L}_{\mathrm{driv}}^{\mathrm{L}}(\rho)) = \Gamma B(f - \langle\sigma_1^z\rangle).\end{aligned} \tag{5.37}$$

The corresponding definitions for site N are

$$\langle J_N^{\mathrm{XXZ}}\rangle = \Gamma(\langle h_{N-1,N}\rangle + \Delta\langle\sigma_{N-1}^z\sigma_N^z\rangle)/2 + \Gamma f\Delta\langle\sigma_{N-1}^z\rangle, \qquad \langle J_N^{\mathrm{B}}\rangle = \Gamma B(f + \langle\sigma_N^z\rangle). \tag{5.38}$$

The total heat current operator at site i is then $J_i^{\mathrm{H}} = J_i^{\mathrm{XXZ}} + J_i^{\mathrm{B}}$.

Since the spin current of the steady state of the system is homogeneous, so is J_i^{B}. We thus define $J^{\mathrm{B}} = \langle J_i^{\mathrm{B}}\rangle = BJ^{\mathrm{S}}$ (observe from equation (5.7) that $\langle J_1^{\mathrm{B}}\rangle = B\langle J_0\rangle$ and $\langle J_N^{\mathrm{B}}\rangle = B\langle J_N\rangle$).

5.6.2 Features of the heat transport

After defining the currents through the system, we discuss the heat transport in different parameter regimes. We start by noting that if the magnetic field is absent $(B = 0)$, there is no net energy flow through the chain, in spite of the existence

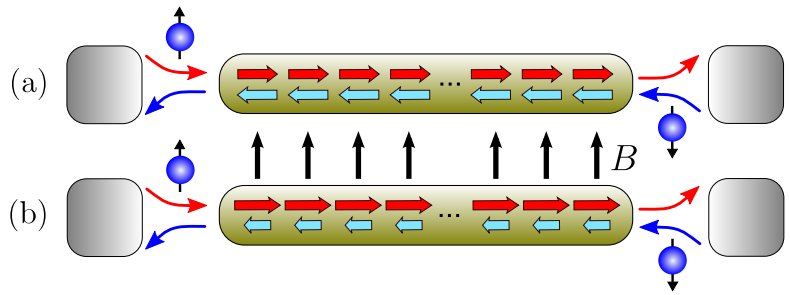

Figure 5.11. Schematic representation of heat transport. (a) If $B = 0$, the heat current of spins up injected at site 1 (dark arrows) cancels with that of spins down injected at site N (light arrows), and the net current is zero. (b) If $B > 0$, the first current becomes larger than the second, and a net current emerges.

of a finite spin current. This can be understood qualitatively by considering the strongly-driven case $f = 1$, in which only spins up are injected at site 1 and only spins down are injected at site N (the argument is easily extended to $f < 1$). At each site of the chain, the total heat current is the superposition of two contributions: one current flowing from right to left, carrying energy associated with the spins down injected at site N, and other flowing from left to right, carrying energy associated with the spins up injected at site 1. Without any energetic asymmetry in the system, the contributions cancel with each other since there is no preference for any z direction, as illustrated in figure 5.11(a). If a homogenous magnetic field is turned on, an asymmetry is established, and a total heat current emerges. If $B > 0$ (as in our work), the left-to-right flow carries energy of spins aligned with the field, so it becomes larger than the right-to-left flow. The net heat current is thus positive, as schematised in figure 5.11(b).

The vanishing of the heat current at $B = 0$ can be formally demonstrated by considering the symmetries of the Lindblad master equation (5.2) with XXZ Hamiltonian and the boundary driving of equation (5.4), as discussed in [183]. In this case, the NESS of the system is invariant under the transformation $U = \Omega^{\alpha} R$,

where $\Omega^\alpha = \sigma_1^\alpha \otimes \sigma_2^\alpha \otimes \cdots \otimes \sigma_N^\alpha$, $\alpha = x, y$, and R is a reflection operator, so $R(A_1 \otimes B_2 \otimes \cdots \otimes C_N) = (C_1 \otimes \cdots \otimes B_{N-1} \otimes A_N)R$ [183]. This means that

$$\rho = U\rho U^\dagger = \Omega^\alpha R\rho R\Omega^\alpha. \tag{5.39}$$

Since J_i^{XXZ} changes sign when transformed by U ($U^\dagger J_i^{\mathrm{XXZ}} U = -J_i^{\mathrm{XXZ}}$), the symmetry of equation (5.39) leads to the following property [183]

$$\begin{aligned} \langle J_i^{\mathrm{XXZ}} \rangle &= \mathrm{Tr}(J_i^{\mathrm{XXZ}}\rho) = \mathrm{Tr}(J_i^{\mathrm{XXZ}} U\rho U^\dagger) = \mathrm{Tr}(U^\dagger J_i^{\mathrm{XXZ}} U\rho) \\ &= -\mathrm{Tr}(J_i^{\mathrm{XXZ}}\rho) = -\langle J_i^{\mathrm{XXZ}} \rangle \quad \rightarrow \quad \langle J_i^{\mathrm{XXZ}} \rangle = 0. \end{aligned} \tag{5.40}$$

So if $B = 0$, both J^{B} and $\langle J_i^{\mathrm{XXZ}} \rangle$ vanish, and $\langle J_i^{\mathrm{H}} \rangle = 0$ for all i.

We now discuss the properties of the heat transport for $B > 0$. The first important observation is that in the NESS, the spin current remains unmodified if a homogeneous magnetic field is present in the system. This occurs because the effect of the magnetic field is to vary the relative energies of the sectors of fixed spin quantum number in the spectrum of the model, while leaving the internal structure of each sector unchanged, as seen in Section 2.5. This does not affect the spin transport through the chain, which is governed by processes that conserve the number of spin excitations. The independence of the NESS on B was demonstrated analytically in the non-interacting limit $\Delta = 0$ [178]. We have seen in our numerical simulations that this actually holds for any interaction Δ. The second important point is that similarly to the spin current, $\langle J_i^{\mathrm{XXZ}} \rangle$ is independent of the magnetic field in the NESS. This can be seen by rewriting equation (5.35) in terms of σ^+ and σ^-. For example, the first term is

$$\sigma_{i-1}^y \sigma_i^z \sigma_{i+1}^x - \sigma_{i-1}^x \sigma_i^z \sigma_{i+1}^y = 2i(\sigma_{i-1}^- \sigma_i^z \sigma_{i+1}^+ - \sigma_{i-1}^+ \sigma_i^z \sigma_{i+1}^-). \tag{5.41}$$

The resulting terms are spin-conserving, so they only involve processes within each spin sector separately. The same applies to the other terms of equation (5.35). So a magnetic field does not affect the expectation values of J_i^{XXZ} in the NESS, and for any homogeneous magnetic field $\langle J_i^{\mathrm{XXZ}} \rangle = 0$. This is reflected in the absence of spatial imbalance of the energy density inducing J_i^{XXZ}, i.e., $\langle h_{i,i+1} \rangle$ is homogeneous through the system. These results mean that $\langle J_i^{\mathrm{H}} \rangle \equiv J^{\mathrm{H}} = J^{\mathrm{B}} = BJ^{\mathrm{S}}$, so the heat current possesses all the features of the spin current. In particular, at weak interactions the heat transport is ballistic, and at strong interactions it satisfies

$$J^{\mathrm{H}} = \kappa_{\mathrm{H}} \nabla E \qquad \text{with} \qquad \nabla E = \langle \varepsilon_{i,i+1} \rangle - \langle \varepsilon_{i-1,i} \rangle = \langle b_{i,i+1} \rangle - \langle b_{i-1,i} \rangle. \tag{5.42}$$

This is the discrete version of Fourier's law, with κ_{H} the energy conductivity, and ∇E the constant energy gradient in the bulk. In addition, we observe that

$$J^{\mathrm{H}} = BJ^{\mathrm{S}} = \kappa_{\mathrm{H}}(\langle b_{i,i+1} \rangle - \langle b_{i-1,i} \rangle) = \frac{B}{2} \kappa_{\mathrm{H}}(\langle \sigma_{i+1}^z \rangle - \langle \sigma_{i-1}^z \rangle) = B \kappa_{\mathrm{H}} \nabla S. \tag{5.43}$$

This means that the energy and spin conductivities are equal, i.e. $\kappa_{\mathrm{H}} = \kappa_{\mathrm{S}}$.

We emphasise that the symmetry (5.39) specifically applies to the Lindblad driving scheme of equation (5.4). Different simple driving configurations might lead to similar symmetries, resulting in vanishing particle or heat currents [183]. Nevertheless, for other types of driving, these symmetries do not apply, leading to contributions of both J^{B} and $\langle J_i^{\mathrm{XXZ}} \rangle$ to the total current, and thus to different transport regimes than those observed here. This is considered in Chapter 6.

5.6.3 Discussion and relation to results of previous research

A first important point to emphasise about the results of Section 5.6.2 is that the heat transport studied is not induced by a temperature gradient, but by a mag-

netisation imbalance between the boundaries. This is, the conduction of energy in the setting considered corresponds to a magnetothermal (Peltier) effect. Transport induced by a thermal bias will be considered in Chapter 6.

The results of Section 5.6.2 indicate that the critical point separating ballistic and diffusive heat transport regimes is $\Delta = 1$. This occurs because the heat current of the present configuration is entirely given by the magnetic field and the spin current. This result contrasts with previous analysis of heat transport through chains driven by external reservoirs, which indicate ballistic transport for the non-interacting case only [138] and for interactions $\Delta < 1.6$ [140]. It also differs from the commonly-accepted result of finite thermal Drude weight and ballistic energy transport for all interactions strengths Δ [14, 17, 19, 123], supported by integrability arguments. Nevertheless, it is important to emphasise the differences of each one of these studies. The research performed in reference [138] mostly considered systems of up to 10 sites driven by thermal reservoirs, whose dynamics was governed by a master equation more complicated to simulate than a Lindblad equation. It was also strongly based on determining the type of transport from the temperature profiles. These points question the validity of these results for large spin chains. The work in reference [140] considers the same type of current that we do here, i.e. $J^{\mathrm{H}} = BJ^{\mathrm{S}}$, so a critical point $\Delta = 1$ separating ballistic and diffusive heat transport would have been expected. Nevertheless, it is possible that they obtained the critical point $\Delta < 1.6$ due to the small systems considered (of up to 16 sites) to perform extrapolations to the thermodynamic limit. Other studies have focused on settings and transport schemes where J^{XXZ}, absent in our setting, contributes to the heat transport in direct [14, 19] or magnetothermal response [17, 123], so the same type of energy conduction than the one described here should not be expected.

It is also important to note that the type of ground state phase diagram of the system does not determine the nature of the (spin or energy) transport response

seen here, since the equilibrium quantum critical points of the XXZ model strongly depend on the magnetic field (see reference [7] and Section 2.3). The interaction strength Δ separating the different transport regimes, on the other hand, is field-independent ($\Delta = 1$). Thus, the NESS transport properties of the chain are determined by the structure of its complete eigenspectrum, which qualitatively changes from being continuous for $\Delta < 1$ to consisting of separated bands for $\Delta > 1$ (see, for example, reference [6] and Section 2.5).

5.7 Summary

In this Chapter we have used the Time Evolving Block Decimation method to study the spin and heat transport properties of a magnetically-driven spin-1/2 XXZ system. To do so, we first analysed the current and magnetisation profiles of the NESS of the chain driven out of equilibrium at its boundaries by Markovian reservoirs. Initially we have reproduced results reported in previous research, regarding transport properties at different parameter regimes of the model. This corresponds to the existence of ballistic spin transport in the weakly-interacting regime for any driving, of diffusive transport in the linear response regime for strong interactions [11, 12, 21, 181], and of superdiffusive transport in the isotropic case $\Delta = 1$ [12, 22]. The effects on the transport properties of two different integrability-breaking terms, namely a staggered magnetic field and dimerisation, were discussed. These were seen to induce diffusive spin transport in the weakly-interacting regime. We then described the existence of negative differential conductivity (NDC), which corresponds to a decrease of the spin current as the driving strength f increases. In the limit of maximal driving, the system becomes an insulator [21, 114].

After showing these results, we analysed the mechanism underlying the emergence of NDC and of the insulating state at maximal driving. These phenomena

result from the combination of the particular features of the eigenstructure of the XXZ model and of the form in which the driving is performed. First, considering the case $f = 1$ for infinite interaction strength, we identified the existence of dark configurations of the driving. We then considered finite but strong interactions, and showed that the perturbative correction to one of these dark states, namely to that with a ferromagnetic domain of positive (negative) polarisation of $N/2$ sites pinned to the left (right) boundary, becomes exponentially closed to be the dark state of the driving. Finally we showed that this dark state is preferentially populated by the reservoirs, The combination of these results lead to the emergence of the insulating NESS at $f = 1$. The NDC effect results when going smoothly and continuously from the linear response regime at weak driving to the insulating case at strong driving.

We have also studied the heat transport properties of the same driven system that emerge when a homogeneous magnetic field is present. The resulting heat current is just the product of the magnetic field by the spin current. Thus all the features described for the spin transport (ballistic transport for weak interactions, diffusive transport for strong interactions and weak driving, and NDC at strong driving) also apply to heat transport. This result seems to contrast with the usual picture of ballistic energy transport in the XXZ model for all interaction strengths Δ. Nevertheless, we emphasise that the heat current we obtained here does not result from a thermal imbalance but from a magnetisation imbalance, thus corresponding to a magnetothermal (Peltier) response. Also, due to the particular symmetries of the driving scheme considered, the current to which ballistic transport is usually associated (J^{XXZ}) is zero. In the following Chapter we will observe that a different induction of the magnetothermal response leads to a ballistic nature, as commonly expected.

Chapter 6

Energy transport and local thermal states in the driven XXZ model

The present Chapter is devoted to study the physical properties of one-dimensional spin-1/2 XXZ chains thermally-driven at the boundaries, in the high-temperature regime. Using the Time Evolving Block Decimation to obtain the steady state of the system, we discuss two main phenomena: energy transport and local thermalisation.

The first has been previously studied by several methods. Most of them obtain that in the integrable regime of the Hamiltonian the transport is ballistic, while it becomes diffusive when the integrability is broken (see Chapter 3 for a review). However, not much strong evidence of these conclusions has been provided from the analysis of currents and energy profiles induced by thermal boundary driving. Previous research based on this type of configuration has been restricted to small systems [136, 138–140], or has focused on a single interaction strength Δ, namely $\Delta = 0$ [137,142] or $\Delta = 1$ [136,141]. In addition, one of these recent studies proposes an alternative picture of energy transport, in which only regimes that can be mapped to a model of noninteracting fermions are ballistic [138]. Given this scenario, the first part of the present Chapter is focused on providing stronger evidence to support the picture of energy transport initially described. For this we consider larger sizes than

in previous studies with boundary-driven spin chains [136,138–140], and values of Δ in the different interacting regimes. To break the integrability of the Hamiltonian, staggered magnetic fields are considered.

The second problem to be described corresponds to the thermalisation properties of thermally-driven systems. For this study we combine two different ideas from the theory of thermalisation of quantum states. The first is that of the existence of local temperatures in a global thermal state. This problem has been considered several times in previous research [184–186], and arguments for the existence of local thermal states have been provided. In particular, for the Ising model it has been found that at high temperatures, and away from critical points, such a local description by thermal states is possible, with coinciding global and local temperatures. For low temperatures this type of description holds, but for a different effective local temperature [186]. The second idea corresponds to the link between thermalisation and integrability. It was found a few years ago that closed quantum systems taken to a nonequilibrium configuration do not relax to a thermal state if the Hamiltonian is integrable [187], but tend towards a generalised Gibbs state [188]. On the other hand, nonintegrable systems were found to relax to a Gibbs state, by means of a mechanism known as eigenstate thermalisation [127, 189] (although alternative mechanisms have been proposed [190]). The thermalisation properties of open driven systems are much less well known, although a similar relation between integrability and the relaxation towards a bulk thermal state has been found [63].

The main objective of the second part of the Chapter is to apply the idea of local thermalisation to nonequilibrium thermally-driven spin chains, and to see whether a relation to the integrability of the Hamiltonian exists. First we revisit the regime with no temperature imbalance, establish our procedure of analysis and present an improvement on the form in which local thermalisation is identified [63]. Then we consider the case with temperature imbalance, and find that local thermal states can

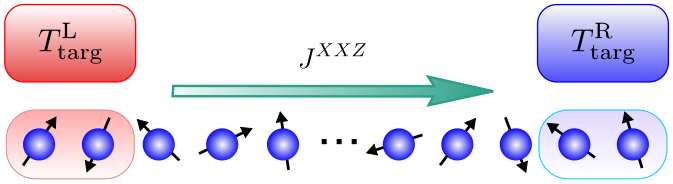

Figure 6.1. Scheme of a system thermally driven out of equilibrium. At the boundaries of the chain, thermal reservoirs of temperatures $T^{\mathrm{L}}_{\mathrm{targ}} > T^{\mathrm{R}}_{\mathrm{targ}}$ induce local thermal states on two neighbouring spins. This imbalance induces a positive energy current J^{XXZ} through the chain.

also be well defined if the Hamiltonian of the system is nonintegrable. We also see that this local description becomes better when the integrability-breaking parameter and the size of the system increase. An article containing the results described in this Chapter will be submitted for publication soon.

6.1 Driving scheme

First we describe the driving scheme to be considered in the present Chapter, sketched in figure 6.1. Recall that in the case of magnetic driving of Chapter 5, the Lindblad boundary superoperators were such that when acting on an isolated spin, they induced a state with magnetisation $\langle\sigma^z\rangle = \pm f$. This idea is extended by defining Lindblad jump operators that induce a thermal state at temperature T

$$\rho_2(T) = Z^{-1}\exp(-\varepsilon_{1,2}/T), \quad Z = \mathrm{Tr}(\exp(-\varepsilon_{1,2}/T)) \tag{6.1}$$

when acting on $N = 2$ spins coupled by an XXZ Hamiltonian $\varepsilon_{1,2}$, given by

$$\varepsilon_{j,j+1} = \tau(\sigma^x_j\sigma^x_{j+1}+\sigma^y_j\sigma^y_{j+1}+\Delta\sigma^z_j\sigma^z_{j+1})+\frac{(-1)^j B}{2}[(1+\delta_{j,1})\sigma^z_j-\sigma^z_{j+1}(1+\delta_{j+1,N})]. \tag{6.2}$$

Here we follow the notation introduced in equation (5.28), with B the amplitude of a staggered magnetic field. In addition, all the calculations are performed with $\tau = 1$, which sets the energy scale.

Note that we consider this type of driving, introduced in reference [11], given that in the integrable case $B = 0$, at least two sites are required to induce a finite-temperature thermal state defined by the Hamiltonian couplings of interest (i.e. XXZ interactions). Details of its implementation are given in Appendix C.4. Driving schemes of more sites would involve more complicated MPO operations than those described in Chapter 4, and thus are not considered.

Now imagine a chain of several sites, in which operators of this form are applied to the two leftmost and rightmost spins, with respective *target*[1] temperatures $T^{\mathrm{L}}_{\mathrm{targ}}$ and $T^{\mathrm{R}}_{\mathrm{targ}}$. This corresponds to a system whose boundary sites are coupled to thermal reservoirs, as indicated in figure 6.1. If $T^{\mathrm{L}}_{\mathrm{targ}} = T^{\mathrm{R}}_{\mathrm{targ}}$, the steady state of the system does not show any energy transport. On the other hand, if the temperatures are different, a nonequilibrium state is induced, in which an energy current flows from the hot to the cold reservoir. To our knowledge, this two-site driving has only been used in a nonequilibrium setup to show energy diffusion in the nonintegrable Ising model [11]. When applied to the XXZ model, due to the absence of a net spin current, the current $\langle J^{\mathrm{B}} \rangle$ defined in Section 5.6.1 vanishes. In addition, the symmetry described in Section 5.6.2 no longer holds. As a result, the total energy current operator at site j is given by J^{XXZ}_j, defined in equation (3.7). In the nonequilibrium steady state, this current is homogeneous throughout the chain, and denoted by $J^{\mathrm{XXZ}} = \langle J^{\mathrm{XXZ}}_j \rangle$.

Observe that the driving scheme can be easily extended and used for different

[1] By *target* we mean that the reservoirs are trying to impose these values on the corresponding two boundary spins. As described in Section 6.4, the target temperatures are usually half of the real temperatures induced, due to strong boundary effects [22].

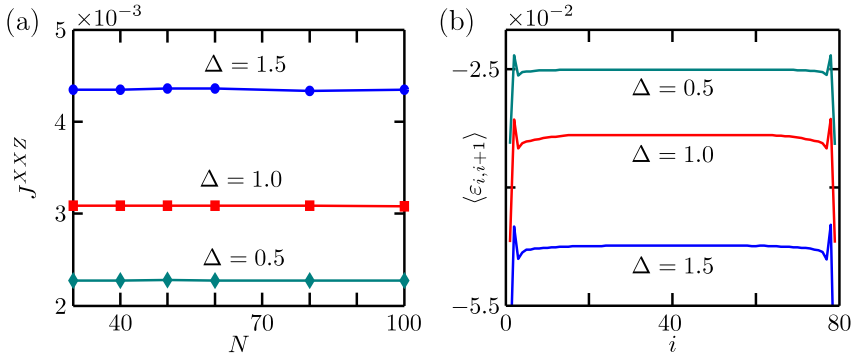

Figure 6.2. Energy transport properties of integrable XXZ spin chains. The results correspond to $T^{\mathrm{L}}_{\mathrm{targ}} = \infty$, $T^{\mathrm{R}}_{\mathrm{targ}} = 20$ and different interactions Δ. (a) Energy current as a function of N. (b) Energy profiles for $N = 80$.

purposes. If the state to be imposed at the boundary sites is grand-canonical,

$$\rho_2(T, \mu) = Z^{-1} \exp(-\varepsilon_{1,2}/T + \mu M), \quad Z = \mathrm{Tr}(\exp(-\varepsilon_{1,2}/T + \mu M)), \tag{6.3}$$

with μ a chemical potential and M the magnetisation operator of the boundary sites, we can induce several types of nonequilibrium states. For example, if the *target* chemical potentials of the left and right reservoirs are $\mu^{\mathrm{L}}_{\mathrm{targ}} = -\mu^{\mathrm{R}}_{\mathrm{targ}}$, but $T^{\mathrm{L}}_{\mathrm{targ}} = T^{\mathrm{R}}_{\mathrm{targ}}$, spin transport at finite temperature can be simulated [22]. In addition, if we have thermal or magnetisation gradients, and $\mu^{\mathrm{L}}_{\mathrm{targ}} \neq -\mu^{\mathrm{R}}_{\mathrm{targ}}$ so a finite magnetisation is imposed to the system, magnetothermal effects arise. We discuss this behaviour in more detail in Section 6.3.

6.2 Direct energy transport

We start our investigation of thermally-driven systems by examining the nature of the direct energy transport through an XXZ spin chain, in which the target temperatures $T^{\mathrm{L,R}}_{\mathrm{targ}}$ that the left and right reservoirs try to impose are different. Strong boundary effects are observed in most cases, so we focus on bulk properties.

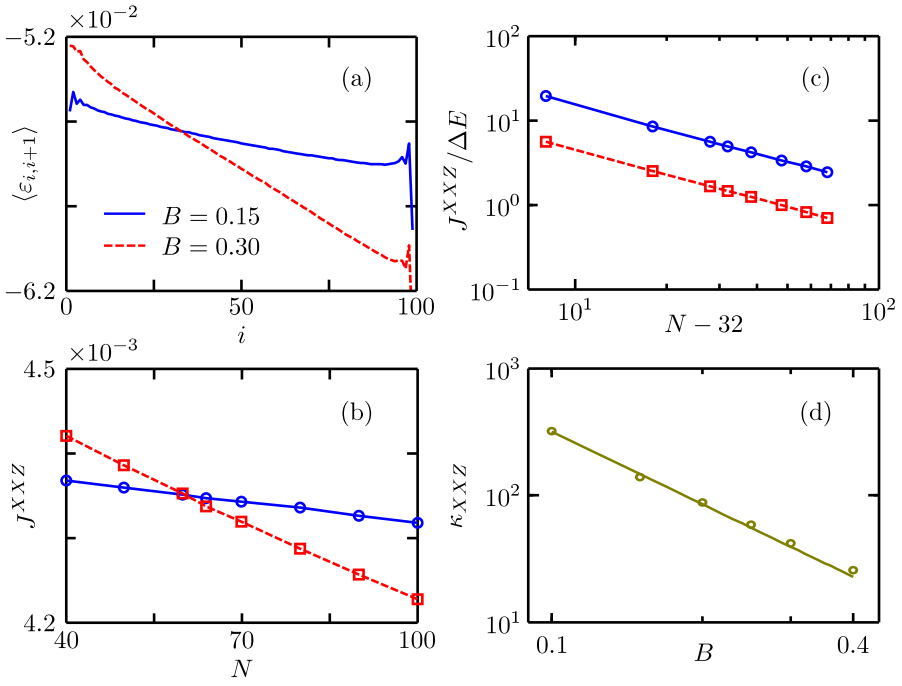

Figure 6.3. Energy transport properties of the XXZ model with staggered magnetic field. The simulations correspond to $\Delta = 1.5$, $T^{\mathrm{L}}_{\mathrm{targ}} = \infty$ and $T^{\mathrm{R}}_{\mathrm{targ}} = 20$. (a) Examples of energy profiles for two staggered magnetic fields. (b) Corresponding energy currents as a function of N. The symbols represent the TEBD results, and the lines are guides to the eye. (c) Scaling of the ratio $\langle J^{\mathrm{XXZ}} \rangle / \Delta E$ with the size of the system. The symbols are the numerical data, and the lines represent the fits to equation (6.4). For $B = 0.15$, the fit gives $\kappa_{\mathrm{XXZ}} = 145(5)$ and $\alpha = 0.98(1)$, and for $B = 0.30$ it gives $\kappa_{\mathrm{XXZ}} = 40.6(5)$ and $\alpha = 0.97(1)$. (d) Conductivity of the system as a function of B. The solid line corresponds to the fit $\kappa_{\mathrm{XXZ}} = 4.0(1.3)B^{-1.9(1)}$.

Consider first the integrable case, with magnetic field $B = 0$. In figure 6.2(a) we show for three interaction strengths Δ that the energy current through the system, J^{XXZ}, is independent of its size. In addition, we show in figure 6.2(b) that the energy profiles are flat in the bulk. This indicates that the energy transport is ballistic for the different interaction regimes of the XXZ model. Our results thus provide novel evidence to support the picture of energy transport in integrable systems proposed by different approaches [8, 13, 14, 17–19] (see Sections 3.3, 3.4 and 3.5).

Now consider the nonintegrable case with staggered magnetic field $B > 0$. As

shown in figure 6.3(a), the energy profiles are no longer flat, but acquire a ramp form that becomes more steep as B increases. Also, as shown in figure 6.3(b), the energy current is no longer independent of the size of the system, but decreases with N. The energy transport is no longer ballistic. Instead, as indicated in figure 6.3(c), it satisfies a diffusion equation in the bulk, namely

$$\frac{J^{\mathrm{XXZ}}}{\Delta E} = \frac{\kappa_{\mathrm{XXZ}}}{(N-2n-2)^{\alpha}}, \quad \Delta E = \langle \varepsilon_{N-n-1,N-n} \rangle - \langle \varepsilon_{n+1,n+2} \rangle \tag{6.4}$$

with κ_{XXZ} the energy conductivity, n the number of sites discarded at each boundary[2], ΔE the energy difference between the leftmost and rightmost pairs of sites retained, and $\alpha \approx 1$. In addition, note that as shown in figure 6.3(d), the energy conductivity diverges with the staggered magnetic field as $\kappa_{\mathrm{XXZ}} \sim B^{-2}$ when $B \to 0$, as expected from previous calculations [55, 191]. So our results indicate that when the integrability of the Hamiltonian is broken, the energy transport becomes diffusive. The same conclusion has been obtained for systems with staggered magnetic fields from calculations of current autocorrelation functions [55, 122], as well as in cases where the integrability is broken by different terms such as interchain couplings [8, 13, 191] and next-nearest neighbour coupling leading to frustration [8]. We note that for the dimerised case, where the local exchange interactions are given by $\tau_j = (1 + (-1)^j \delta)$, the nature of the energy transport is less clear, since different studies have obtained ballistic [122] and diffusive [8, 18] regimes. More research is required to solve this problem.

In conclusion, by using a transport scheme different to those considered in previous research, we have provided evidence to support the picture of energy transport through an XXZ chain. In the integrable case, the transport is ballistic. On the

[2]Discarding several sites close to the edges of the chain is necessary due to strong boundary effects [11]. This leads to the particular form of equation (6.4). We have taken $n = 15$ for all values of N considered. Larger values of n do not modify the results, since the energy gradient is homogeneous in the region of the chain retained.

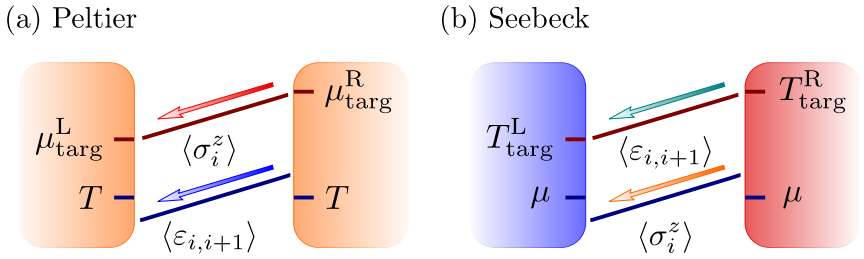

Figure 6.4. Scheme of the magnetothermal effects induced in boundary-driven systems with a finite average magnetisation. (a) Peltier effect, in which an energy current is induced by a magnetic imbalance ($T^{\mathrm{L}}_{\mathrm{targ}} = T^{\mathrm{R}}_{\mathrm{targ}} = T$). (b) Seebeck effect, in which a spin current is induced by a temperature imbalance ($\mu^{\mathrm{L}}_{\mathrm{targ}} = \mu^{\mathrm{R}}_{\mathrm{targ}} = \mu$). The arrows indicate spin and energy currents. The solid lines represent magnetisation and energy profiles.

other hand, the transport becomes diffusive when the integrability is broken, in this case by a staggered magnetic field.

6.3 Magnetothermal transport

We now briefly consider the magnetothermal effects that can be induced in the system with the two-site driving scheme, schematised in figure 6.4. We emphasise that it is not our intention to provide an extensive description of these effects. Instead we expect to show how they emerge, and that their nature may depend on the particular form in which they are induced. We thus restrict to the integrable regime of the Hamiltonian.

Recall that in Section 5.6 we considered the heat conduction produced by a magnetisation imbalance (Peltier effect) in the presence of a homogeneous magnetic field. Due to the symmetry of the driving [183], $J^{\mathrm{XXZ}} = 0$ so the total heat current was just the product of the magnetic field and the spin current J^{S}. Thus the transport was ballistic for weak interactions and diffusive in the strongly-interacting regime. Here the situation is completely different. We do not have magnetic fields, and the driving does not feature the symmetry described in Section 5.6.2. So the

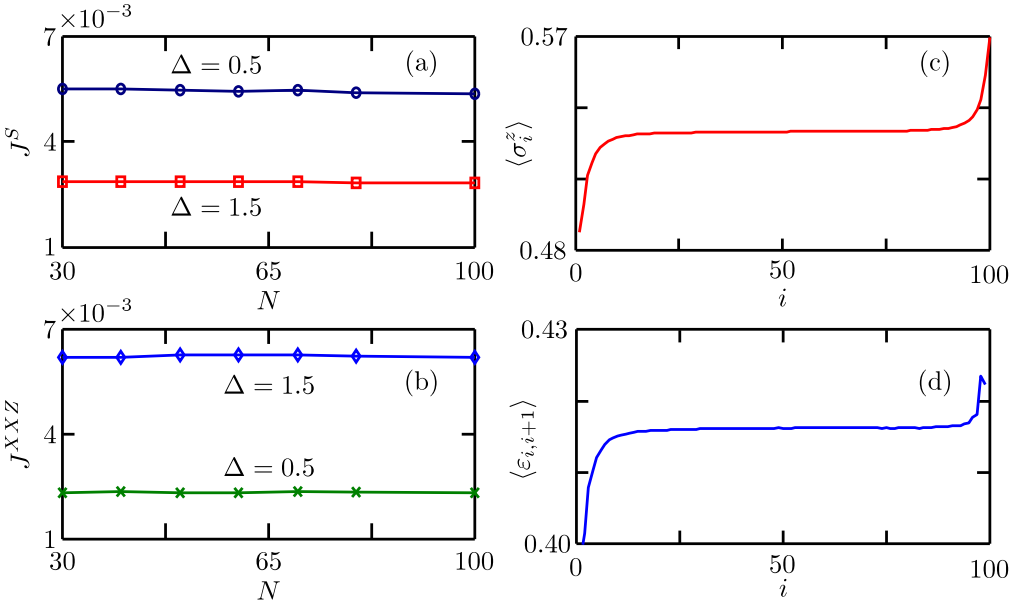

Figure 6.5. Transport properties induced by a magnetisation imbalance across an XXZ chain, with finite magnetisation. The results correspond to $\mu^{\mathrm{L}}_{\mathrm{targ}} = 0.5$, $\mu^{\mathrm{R}}_{\mathrm{targ}} = 0.7$ and $T^{L,R}_{\mathrm{targ}} = 100$. (a) Spin current as a function of N. (b) Energy current as a function of N. (c) Magnetisation profile for $\Delta = 1.5$ and $N = 100$. (d) Energy profile for $\Delta = 1.5$ and $N = 100$.

heat current is entirely given by J^{XXZ}. This will lead to a different nature of the magnetothermal response of the system.

We start by discussing how an energy current can be induced through the system in the absence of a temperature imbalance, i.e. when $T^{\mathrm{L}}_{\mathrm{targ}} = T^{\mathrm{R}}_{\mathrm{targ}}$. Similarly to Section 5.6.2, this is achieved by breaking the symmetry between up and down spins. Now we do not use a magnetic field, but instead impose a finite magnetisation through the system by means of the driving. For example, if the chemical potentials of the two boundary reservoirs are $\mu^{\mathrm{L,R}}_{\mathrm{targ}} > 0$, a finite and homogeneous magnetisation is induced in the bulk of the chain, favouring the energy current carried by spins up. A net flow of energy results, in addition to the spin current directly induced by the magnetisation gradient. As shown in figures 6.5(a) and (b), the energy and spin currents are independent of the size of the system, in both the weakly- and the

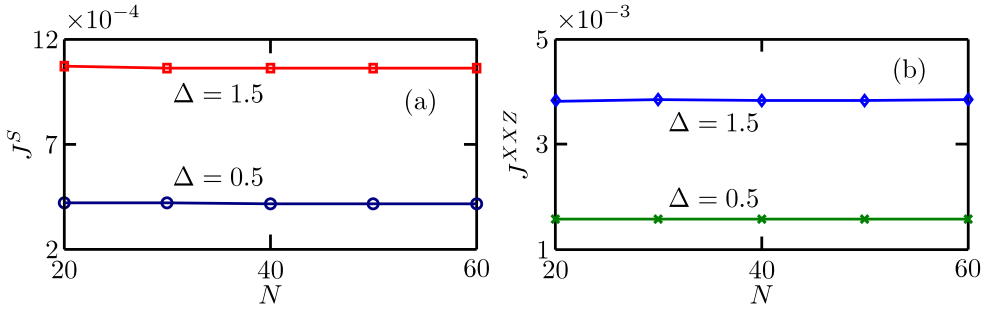

Figure 6.6. Transport properties induced by a temperature imbalance across an XXZ chain, with finite magnetisation. The calculations correspond to $\mu^{\mathrm{L,R}}_{\mathrm{targ}} = 0.7$, $T^{R}_{\mathrm{targ}} = 20$ and $T^{L}_{\mathrm{targ}} \to \infty$. (a) Spin current as a function of N. (b) Energy current as a function of N.

strongly-interacting regimes. Additionally, the magnetisation and energy profiles are flat in the bulk, as shown in figures 6.5(c) and (d) respectively. The spin and energy transport induced by this driving scheme is thus ballistic. Similar results have been obtained in previous research performed with different methods. For instance, ballistic energy transport induced by an alternative magnetisation driving has been reported in an integrable noninteracting system [142]. Ballistic magnetothermal conduction has also been obtained from analysis in the linear response regime, exact diagonalisation and Monte Carlo calculations [17]. In addition, from the conservation of the energy current operator, ballistic spin transport for any interaction strength was concluded to emerge away from half filling, i.e. when the magnetisation of the system is finite [14].

With the two-site driving scheme, it is also possible to induce a spin current by means of a temperature imbalance, a phenomenon known as Seebeck effect. Following the rationale of the Peltier effect, the Seebeck effect also emerges when a finite magnetisation is imposed on the system. Specifically, if in the steady state the magnetisation of the system is zero, energy-carrying up and down spins are on average injected into the chain at the same rate by the hot reservoir, and are ejected

towards the cold reservoir also at the same rate. Thus a finite energy current is established, with no spin current. A finite magnetisation is imposed in the system if, for example, more spins up are injected into the chain than spins down. This also leads to a net spin current through the chain. In figure 6.6 we show the spin and energy currents induced by this driving scheme for weak and strong interactions Δ, as a function of N. In both cases the currents are independent of the size of the system, which corresponds to ballistic transport.

In conclusion, using the two-site driving scheme to analyse magnetisation and energy profiles and current scaling, we have shown new evidence supporting the existence of ballistic magnetothermal responses in the integrable XXZ, for both weakly- and strongly-interacting regimes.

6.4 Local thermalisation for symmetric driving

After studying the transport properties of the thermally-driven XXZ model, where our results provide new evidence in support of the commonly-accepted picture for both magnetothermal and energy conduction, we turn our attention to a fundamental related problem. This corresponds to whether the steady state of the driven system can be described in terms of local thermal equilibrium, and under which conditions [192, 193]. To analyse this question, we start by describing the case in which a spin chain is driven by boundary reservoirs of the same target temperature, i.e. when $T^{\mathrm{L}}_{\mathrm{targ}} = T^{\mathrm{R}}_{\mathrm{targ}} = T_{\mathrm{targ}}$. This configuration has already been studied a few years ago for the Ising and XXZ models [63]. In this Section we revisit the latter, in the high-temperature regime, using a different approach. This will allow us to discuss the concept of local thermalisation [186] and the role that integrability plays for it [63]. The configuration with $T^{\mathrm{L}}_{\mathrm{targ}} \neq T^{\mathrm{R}}_{\mathrm{targ}}$ will be discussed in Section 6.5.

Let us first establish the main conclusions. In the steady state, the system

does not thermalise if its Hamiltonian is (or is close to being) integrable. On the other hand, the system thermalises if its Hamiltonian is strongly nonintegrable [63], similarly to closed quantum systems [127,128,187,189]. For high temperatures, this thermalisation of nonintegrable driven chains not only occurs globally (in the bulk of the chain, away from the boundaries) but also locally, with the temperatures of the global and local thermal states being the same [186]. Although we do not consider low temperatures in the present work, we note that for such a case, effective local temperatures can be well defined away from quantum critical points, but being significantly different from global temperatures [186][3].

To perform this study, we carry out TEBD simulations to obtain the NESS of a thermally-driven system in which the same target temperature $T_{\text{targ}} = 100$ is used for both left and right boundaries. In addition, we break the integrability of the Hamiltonian by applying a staggered magnetic field of amplitude B (see equation (6.2)). To determine if the spin chain thermalises, we proceed as follows. First we calculate the reduced density operators of all pairs of neighbouring sites in the bulk of the driven system, which we denote as $\tilde{\rho}_2$[4]. Then we sweep over a range of *trial* temperatures T_{trial} and calculate their corresponding two-site thermal state (6.1), with Hamiltonian (6.2). Then for each pair of neighbouring sites with reduced density operator $\tilde{\rho}_2$, we identify the closest two-site thermal state $\rho_2(T_{\text{trial}})$ by determining the trial temperature T_{trial} that minimises the trace distance [163]

$$D(\rho_2(T_{\text{trial}}), \tilde{\rho}_2) = \frac{1}{2}\text{Tr}\left[\sqrt{(\rho_2(T_{\text{trial}}) - \tilde{\rho}_2)^2}\right]. \tag{6.5}$$

Finally, we compare expectation values of each $\tilde{\rho}_2$ with those of the closest thermal

[3]This low-temperature study was only performed for the Ising model. Using the TEBD method to calculate thermal states, as described in Section 4.4.4, it could be extended to other models, to check the generality of this conclusion.

[4]Reduced density operators are denoted by $\tilde{\rho}_n$, identified by $\sim$. Thermal states are simply denoted as ρ_n. In both cases, the sub-index n refers to the number of sites of the density operators.

state. If their difference is much smaller than the actual values of the expectation values, $\tilde{\rho}_2$ corresponds to a local thermal state.

A few points must be discussed before presenting our results. First, note that this procedure represents a significant improvement over previous work of reference [63], which relied on comparing a few expectation values to determine thermalisation. To better understand why, consider two states ρ and σ, and an observable G with spectral decomposition $G = \sum_j g_j |j\rangle\langle j|$. If $p_j = \mathrm{Tr}(\rho|j\rangle\langle j|)$ and $q_j = \mathrm{Tr}(\sigma|j\rangle\langle j|)$ denote the probabilities of obtaining outcome j in a measurement of G, the corresponding expectation values are

$$\langle G\rangle_\rho = \mathrm{Tr}(\rho G) = \sum_j g_j p_j, \qquad \langle G\rangle_\sigma = \mathrm{Tr}(\sigma G) = \sum_j g_j q_j. \tag{6.6}$$

Their difference is

$$|\langle G\rangle_\rho - \langle G\rangle_\sigma| = \left|\sum_j g_j (p_j - q_j)\right| \leq |g^*| \sum_j |p_j - q_j| \equiv 2|g^*| D(p_j, q_j) \leq 2|g^*| D(\rho, \sigma), \tag{6.7}$$

where g^* is the eigenvalue of G of maximal amplitude, $D(p_j, q_j)$ is the L_1 distance between the probability distributions $\{p_j\}$ and $\{q_j\}$, and where we have used that the trace distance $D(\rho, \sigma)$ upper-bounds $D(p_j, q_j)$ [163]. Thus the trace distance of two states upper-bounds the difference between the corresponding expectation values of *any* observable (with finite eigenvalues). The calculation of trace distances then constitutes a much better form to determine the closest thermal state $\rho_2(T_{\mathrm{trial}})$ to each $\tilde{\rho}_2$ than a comparison of a few expectation values [63].

Second, it is important to discuss the use of Hamiltonian (6.2) to calculate local thermal states. It is not in principle clear that when thermalisation occurs, the two-site reduced density operators should be described by a local Hamiltonian which does not consider the interaction to nearest neighbours, even under some approximation.

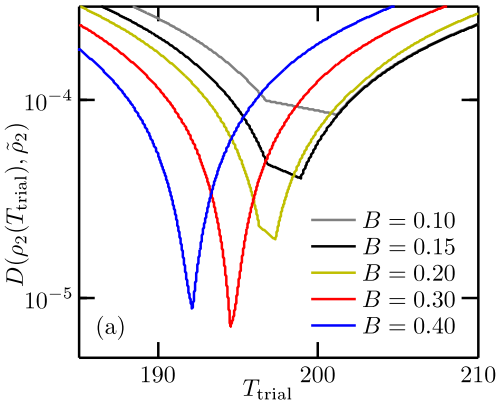

Figure 6.7. Trace distance between two-site reduced density operators $\tilde{\rho}_2$ in the center of the driven system and two-site thermal states $\rho_2(T_{\rm trial})$, as a function of the trial temperature $T_{\rm trial}$, for different staggered magnetic fields B. For a better visibility the case $B = 0$ has not been included; it corresponds to $T_{\rm trial} \approx 235 - 239$ and a minimal trace distance of $D \approx 3 \times 10^{-4}$. The results are for $N = 60$, $\Delta = 1.5$, $T_{\rm targ} = 100$, and values of $T_{\rm trial}$ separated by steps of $\delta T_{\rm trial} = 5 \times 10^{-3}$. Note that for $B < 0.3$, a sharp change of D as a function of $T_{\rm trial}$ occurs before the minimum. This feature is observed in all the subsequent figures of D. So far we have not determined its origin.

An intuitive argument to justify using the local Hamiltonian (6.2) is that in the high-temperature regime, where the total density operator of the system is

$$\rho_N = Z^{-1} \exp(-H/T) \approx \frac{1}{2^N} \left[I_N - \frac{1}{T} H + O\left(\frac{1}{T}\right)^2 \right], \tag{6.8}$$

the reduced density operator of sites j and $j+1$ is very well approximated by

$$\tilde{\rho}_2 = \mathrm{Tr}(\rho_N)_{(j,j+1)'} \approx \frac{1}{4} \left[I_2 - \frac{1}{T} \varepsilon_{j,j+1} + O\left(\frac{1}{T}\right)^2 \right] = Z^{-1} \exp(-\varepsilon_{j,j+1}/T), \tag{6.9}$$

where I_m is the identity operator of m sites, and where we have considered that all the local operators in the Hamiltonian are traceless. Hamiltonian (6.2) thus leads to the correct reduced density operator of the state[5].

[5]The use of a Hamiltonian of the form (6.2) to check thermalisation works in the low-temperature regime too, although the effective local temperatures differ from the global ones [186].

6.4.1 Local thermalisation and integrability

Now we proceed to discuss our results. In figure 6.7 we show, for a particular set of parameters, that the minimal trace distance between $\tilde{\rho}_2$ and the closest $\rho_2(T_{\text{trial}})$ diminishes with B. Specifically, the trace distance decreases by an order of magnitude when going from $B = 0.1$ (close to integrability) to $B = 0.4$ (strongly nonintegrable). The form of the curves of trace distance as a function of T_{trial} also becomes sharper with B. These results indicate that the reduced density operators of the system become better described by local thermal states as the integrability-breaking parameter B gets larger[6].

To support the relation between local thermalisation and lack of integrability, we compare the $\langle \sigma_i^\alpha \sigma_{i+1}^\alpha \rangle$ correlations ($\alpha = x, z$) directly obtained from the reduced density operators of the driven system with those of the corresponding closest thermal state, as shown in figure 6.8. From equation (6.7) we already know that the difference between the two expectation values is bounded by the trace distance between the two states, since the eigenvalues of the $\sigma_i^\alpha \sigma_{i+1}^\alpha$ operators are bounded. Nevertheless we need to compare such a difference with the actual value of the correlations, to establish how significant it is. We observe that while for $B = 0.4$ the bulk expectation values of the two types of states coincide very well, for $B = 0.1$ they do not. The largest difference occurs for $B = 0$ (not shown), where the $\langle \sigma_i^z \sigma_{i+1}^z \rangle$ correlations of the two-site reduced density operators $\tilde{\rho}_2$ and their closest thermal state ρ_2 differ by $\approx 9\%$. These results lead to the conclusion that if the Hamiltonian of the system is integrable, or weakly nonintegrable, it does not locally thermalise with the driving scheme imposed. On the other hand, if the Hamiltonian is deeply situated in the nonintegrable regime, local thermalisation is achieved. The transi-

[6] Also note that the values of the local temperatures, which decrease with B, are approximately two times the target temperature of the driving. This large deviation between target and actual temperatures has been noted before, being attributed to strong boundary effects [22, 63].

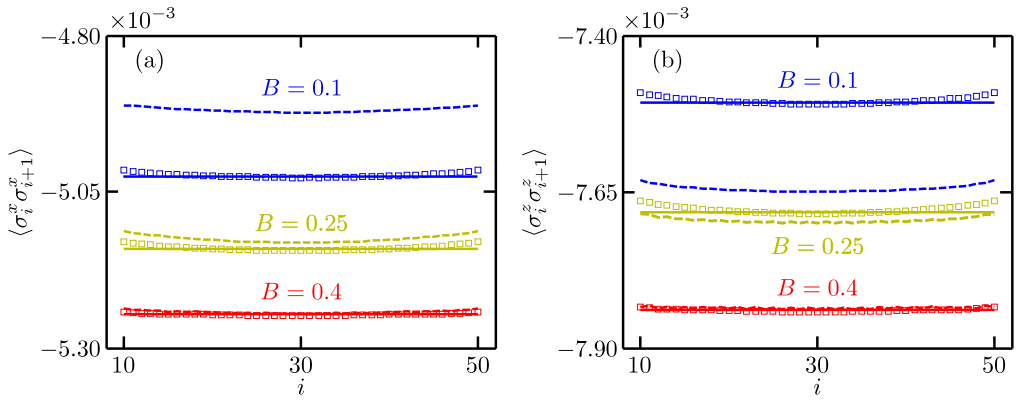

Figure 6.8. Expectation values of $\langle \sigma_i^\alpha \sigma_{i+1}^\alpha \rangle$ correlations across the system, calculated directly from the state of the driven system (dashed lines), from the closest two-site thermal states ρ_2 (□), and from global thermal states ρ_N of the same temperature (solid lines), (a) for $\alpha = x$, (b) for $\alpha = z$. The results are for $N = 60$, $\Delta = 1.5$ and $T_{\text{targ}} = 100$. The 10 sites closest to both boundaries were discarded, due to strong boundary effects.

tion from absence to existence of thermalisation is not sharp but smooth, similarly to the crossover found for closed quantum systems [128].

The following point to discuss is whether global thermalisation also exists, and for which value of temperature. The connection between local and global thermalisation was extensively discussed in reference [186] for the Ising model. There it was concluded that for high temperatures, global and local temperatures coincide[7]. We now find the same for the XXZ model, as expected from the simple expansion of equation (6.9). Here the global thermal states were built by performing imaginary-time evolution with the TEBD method as explained in Section 4.4.4. We see that regardless of the integrability of the Hamiltonian, the two-site reduced density operators of high-temperature global thermal states are very well described by local thermal states of almost the same temperature. For example, for the parameters of figure 6.8, $B = 0.4$ and a global temperature $T_{\text{global}} = 192.10$, the minimal trace

[7]Specifically, if a system of N sites is described by a global thermal state $\rho_N(T)$ at high-temperature T, its two-site reduced density operators correspond to thermal states $\rho_2(T)$ at the same temperature.

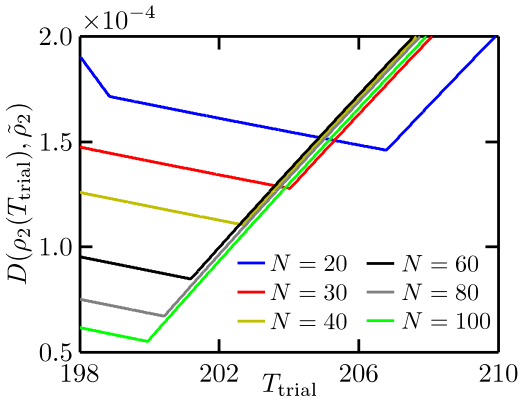

Figure 6.9. Trace distance between central two-site reduced density operators of the driven system ($\tilde{\rho}_2$) and two-site thermal states ($\rho_2(T_{\text{trial}})$) as a function of the trial temperature T_{trial}, for different sizes N. The results correspond to $B = 0.1$, $\Delta = 1.5$, $T_{\text{targ}} = 100$ and steps of $\delta T_{\text{trial}} = 5 \times 10^{-3}$.

distance between the two states is $D = 8.3 \times 10^{-6}$ for $T_{\text{trial}} = 192.13$. For $B = 0.1$ and $T_{\text{global}} = 200.53$, $D = 1.9 \times 10^{-6}$ for $T_{\text{trial}} = 200.57$. In consequence, the expectation values of local and global thermal states coincide in the bulk, as illustrated in figure 6.8. In conclusion, for the set of parameters we considered, it is found that away from integrability, the driven system globally and locally thermalises in the bulk, with coinciding global and local temperatures. On the other hand, if the system is integrable or the integrability-breaking term is weak, thermalisation does not occur.

Note that the size of the system has a significant impact on its thermalisation properties. In figure 6.9 we show the trace distance between $\tilde{\rho}_2$ and $\rho_2(T_{\text{trial}})$ for the central sites, as a function of the trial temperature, for the nonintegrable Hamiltonian with the weakest staggered field considered ($B = 0.1$) and several values of N. We see that the minimal trace distance, identifying the closest $\rho_2(T_{\text{trial}})$ to $\tilde{\rho}_2$, decreases monotonously with the system size. As a consequence, the expectation values of the driven system become better reproduced by local thermal states as N increases. For example, for $N = 20$, the differences between $\langle \sigma_i^z \sigma_{i+1}^z \rangle$ correla-

tions across the driven chain and those from the closest thermal states are $\sim 4\%$, while for $N = 100$ the differences are $\gtrsim 1\%$[8]. The latter case is thus much closer to thermalisation. Unfortunately, the range of parameters we have considered is not sufficiently large to provide enough information to solve a fundamental open problem. This corresponds to whether for very large systems, thermalisation can be achieved even when being arbitrarily close to integrability, or if there is a finite and sharp critical point separating thermalised and non-thermalised regimes [128]. Much larger systems with weaker integrability-breaking parameters, whose dynamics is very hard to simulate with the two-site driving scheme used in our work, need to be considered to give an answer to this problem. Very recent developments of finite-temperature time-dependent tensor network algorithms could provide the means to perform such calculations more efficiently [98, 122, 194–196].

6.5 Thermalisation with temperature imbalance

So far we have discussed the nature of energy transport in XXZ spin chains driven to a NESS by a temperature imbalance between the boundaries, and the thermalisation properties of driven systems with no imbalance. Now we merge both problems, and discuss the extension of the concept of local thermalisation to the out-of-equilibrium scenario with $T^{\mathrm{L}}_{\mathrm{targ}} \neq T^{\mathrm{R}}_{\mathrm{targ}}$. Note that previous studies have defined local temperatures in NESSs by matching values of local energy density $\langle \varepsilon_{i,i+1} \rangle$ across the lattice to those of two-site thermal states [62,138]. In this line of thoughts and for the high-temperature regime, local temperatures would correspond to $T_i \sim -1/\langle \varepsilon_{i,i+1} \rangle$ [62]. In this Section we discuss whether the definition of local temperatures is actually plausible in nonequilibrium driven configurations. Similarly to the case with sym-

[8] At first sight these difference seem too large for the $O(10^{-5} - 10^{-4})$ values of the trace distance. Nevertheless, it only bounds the difference of expectation values (which we have verified in our results) but does not indicate how small it is. For example, for the case of $N = 20$, the difference of $\langle \sigma^z_i \sigma^z_{i+1} \rangle$ values is $\approx 3 \times 10^{-4}$, while the actual values of these correlations are $\approx 8 \times 10^{-3}$.

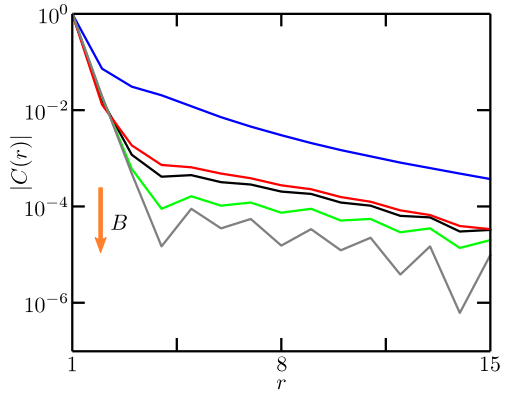

Figure 6.10. Spin-spin correlations of the XXZ model with staggered magnetic field, for $\Delta = 1.5$, $N = 100$, $T^{\mathrm{L}}_{\mathrm{targ}} = \infty$ and $T^{\mathrm{R}}_{\mathrm{targ}} = 20$. From top to bottom, the lines correspond to $B = 0, 0.15, 0.20, 0.30, 0.35$. The field amplitude B thus increases as indicated by the arrow.

metric thermal driving, we find that such a definition is feasible in the nonintegrable regime of the Hamiltonian. This constitutes the main result of the present Chapter.

A first point to evaluate regarding the possible existence of local thermal states in the NESS of the system is whether long-range correlations emerge. In reference [192] (see also [193]) it was shown that for boundary driving inducing spin transport, at finite and infinite temperature, a nonequilibrium quantum phase transition characterised by the spontaneous emergence of long-range correlations occurs at a finite interaction strength Δ (see an example of these type of correlations in figure 8.9(a)). Thus it was proposed that these results could demonstrate the total absence of well-defined local temperatures in nonequilibrium one-dimensional many-body systems. But interestingly, this turns out not to be the case in nonintegrable systems driven out of equilibrium by a thermal imbalance, as shown in figure 6.10. There we plot the bulk-averaged correlation functions $C(r) = \langle C(j,r)\rangle_j$, with

$$C(j,r) = \langle \sigma^z_j \sigma^z_{j+r}\rangle - \langle \sigma^z_j\rangle\langle \sigma^z_{j+r}\rangle, \tag{6.10}$$

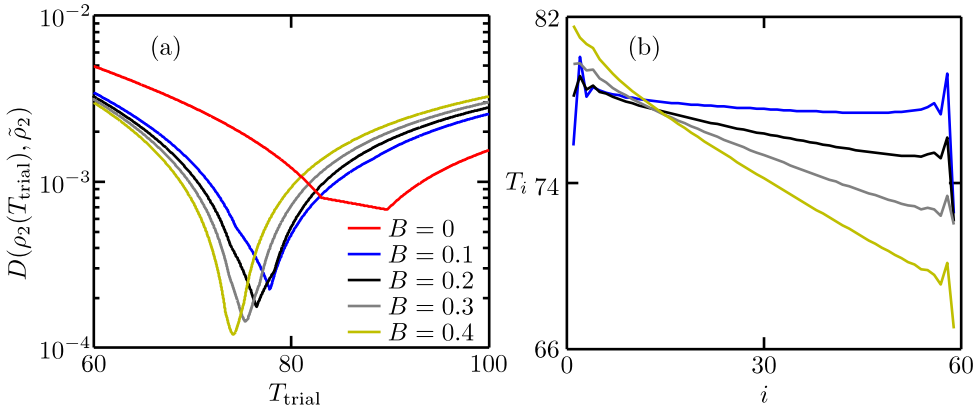

Figure 6.11. Analysis of local thermalisation in driven spin chains with temperature imbalance. (a) Trace distance between the reduced density operator of the two central sites $\tilde{\rho}_2$ and two-site thermal states with temperature $T_{\rm trial}$, for different staggered magnetic fields B. (b) Corresponding temperature profiles across the system. The lines of the same color in both panels correspond to the same value of B. The (flat) profile of $B = 0$ is not shown in panel (b) since it corresponds to temperatures ≈ 92. The calculations were performed for $N = 60$, $T^{\rm L}_{\rm targ} \to \infty$, $T^{\rm R}_{\rm targ} = 20$, $\Delta = 1.5$ and $\delta T_{\rm trial} = 5 \times 10^{-3}$.

as a function of the separation r between spins[9]. Apart from oscillations due to the staggered field, the correlations tend to decay fast with the spin separation. Importantly, the correlations also decrease with B. This suggests that as the integrability-breaking parameter gets larger, a description of the system by means of local properties becomes more feasible.

Motivated by this observation, we now consider whether in nonequilibrium states, the two-site reduced density operators of the thermally-driven system can be well approximated by two-site thermal states. For this, we apply the same procedure followed in Section 6.4. First we use the trace distance to identify the local thermal state ρ_2 closest to each two-site reduced density operator $\tilde{\rho}_2$ of the nonequilibrium chain. This is illustrated in figure 6.11(a) for the two central sites and various staggered magnetic fields B. We see that similarly to the case where $T^{\rm L}_{\rm targ} = T^{\rm R}_{\rm targ}$,

[9]The notation $\langle . \rangle_j$ indicates that the correlations $C(j, r)$ with fixed r are averaged over the spin chain, excluding sites near the boundaries.

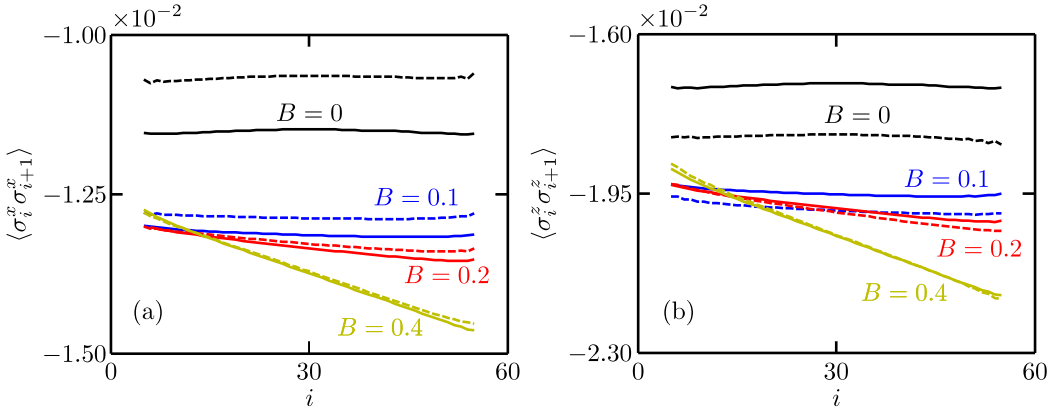

Figure 6.12. Comparison between expectation values $\langle \sigma_i^\alpha \sigma_{i+1}^\alpha \rangle$ directly obtained from the numerical simulations of driven systems with temperature imbalance (dashed lines), and those of the chosen two-site thermal states (solid lines), (a) for $\alpha = x$, (b) for $\alpha = z$. The calculations correspond to $N = 60$, $T^{\mathrm{L}}_{\mathrm{targ}} \to \infty$, $T^{\mathrm{R}}_{\mathrm{targ}} = 20$ and $\Delta = 1.5$.

the trace distance between the two types of states decreases as the staggered field B increases. The resulting temperature profiles for each value of B are shown in figure 6.11(b), which for $B > 0.2$ show a homogeneous gradient away from the boundaries and thus are consistent with diffusive energy transport. Then we compare the corresponding $\langle \sigma_j^\alpha \sigma_{j+1}^\alpha \rangle$ expectation values of the two types of states, for $\alpha = x$ and $\alpha = z$, as detailed in figures 6.12(a) and (b) respectively. For $B = 0$, the maximum difference of expectation values is $\approx 8\%$. It significantly diminishes for $B = 0.1$ ($\approx 2.3\%$), and becomes very small for $B = 0.4$ (0.7%)[10]. These results show that the closest local thermal state to each two-site reduced density operator reproduces very well the expectation values deep in the nonintegrable regime. On the other hand, close to the integrable limit, the two states have significantly different expectation values. Thus we conclude that away from the integrable limit of the Hamiltonian, the NESS of the thermally-driven system is locally well described

[10]Similarly to the case with $T^{\mathrm{L}}_{\mathrm{targ}} = T^{\mathrm{R}}_{\mathrm{targ}}$, we have verified that the trace distance bounds the difference between expectation values. The differences we show here are quite large because they are relative to the actual values of the correlations.

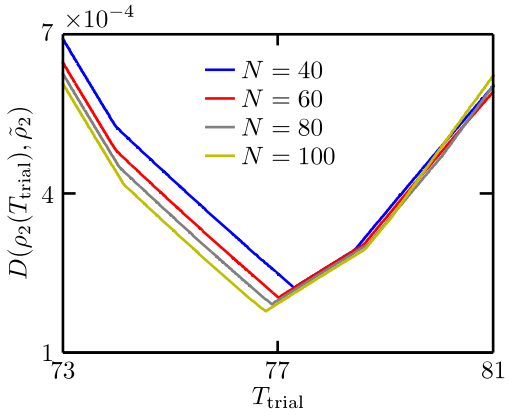

Figure 6.13. Trace distance between the reduced density operator $\tilde{\rho}_2$ of the central two sites of the system and trial two-site thermal states $\rho_2(T_{\text{trial}})$, for various sizes N, as a function of the trial temperature T_{trial}. The results are for $B = 0.15$, $\Delta = 1.5$, $T^{\text{L}}_{\text{targ}} \to \infty$, $T^{\text{R}}_{\text{targ}} = 20$ and steps of $\delta T_{\text{trial}} = 5 \times 10^{-3}$.

by thermal states. At integrability, this local description does not hold.

Notably, just as in the case with symmetric thermal driving, the local description by thermal states in the NESS is improved when the size of the system increases. This is shown in figure 6.13 for the field $B = 0.15$, close to the integrability limit. Note, however, that the dependence of the minimal trace distance with N is significantly weaker than that seen in figure 6.9 for the symmetric driving. We expect that for lower values of B, much larger systems will be required to determine whether a finite critical point separating thermalised and non-thermalised regimes exist, or whether in the thermodynamic limit the only case that does not show thermalisation corresponds to the integrable Hamiltonian.

We finalise this Section by commenting on a connection between our results and a recent numerical study of energy transport in the XXZ model [122]. There, two semi-infinite spin chains, initially in thermal states of different temperatures T^{L} and T^{R}, are coupled through a single site. As the system evolves in time, the energy current at the interface between both chains saturates rapidly in the integrable limit, while it does not (in the accessible timescales) when the Hamiltonian

contains staggered magnetic fields. This led to conjecture that the relaxation of the energy current to a steady-state value would only occur for nonzero Drude weights. Additionally, even if the current at the interface reaches a steady-state value, the energy profile does not, the latter being expected since the system is closed. Thus in the ballistic regime the current "is not determined by local temperature gradients", but has the form $f(T^{\mathrm{L}}) - f(T^{\mathrm{R}})$ for some function f. Our research is consistent with this observation, by indicating that in the ballistic regime it is not actually possible to provide a sensible definition of local temperatures, in contrast to the strongly nonintegrable regime. It would be interesting to study local thermalisation properties in the nonequilibrium setup of reference [122], or other driving schemes, to check the generality of the qualitative results we have found.

6.6 Outlook: Description for several sites

An interesting problem for future research would be to analyse the description of the reduced density operators of thermally-driven systems for several contiguous sites. In the case of a high-temperature global thermal state, sub-blocks of any size N_{s} of the system are well described by thermal states with the same global temperature. For low temperatures, the effective temperature of the sub-block becomes closer to the global one as N_{s} increases [186]. We expect similar conclusions for nonintegrable open systems with symmetric driving. Nevertheless, the description of sub-blocks of several sites in nonequilibrium systems with temperature imbalance is much more involved. Consider, for example, the case $N_{\mathrm{s}} = 3$, and a simple ansatz of the form

$$\tilde{\rho}_3 \propto \exp\left[-\left(\frac{\varepsilon_{1,2}}{T_1} + \frac{\varepsilon_{2,3}}{T_2}\right) + \left(\frac{1}{T_1} - \frac{1}{T_2}\right) \sum_{\alpha\neq\beta\neq\gamma} c_{\alpha\beta\gamma} \sigma_1^{\alpha} \sigma_2^{\beta} \sigma_3^{\gamma}\right]. \tag{6.11}$$

The first part corresponds to the local Hamiltonians of the two pairs of sites. The second part contains the terms of the energy current operator ($\alpha, \beta, \gamma = x, y, z$). This ansatz is thus built to reproduce the expectation values of Hamiltonian operators and the energy current (with appropriate coefficients $c_{\alpha\beta\gamma}$) in the presence of a temperature imbalance. This is clearly seen by expanding $\tilde{\rho}_3$ up to $O(1/T)$ in the high-temperature regime. Preliminary numerical calculations have shown that these are in fact the dominant terms of three-site reduced density operators. Nevertheless, equation (6.11) does not properly account for smaller terms, so it should be corrected. We believe it would be interesting to determine whether a simple, improved version of state (6.11) can be established to describe local states of thermally-driven nonequilibrium systems.

6.7 Summary

In the present Chapter we have discussed the high-temperature physics of the thermally-driven one-dimensional spin-1/2 XXZ model, focusing our attention on two main problems. First we have studied the energy transport supported by the system when different temperatures are imposed at its boundaries by means of a two-site driving. The results indicate that the integrable XXZ model shows ballistic energy transport. On the other hand, when the integrability of the Hamiltonian is broken by means of a staggered magnetic field, the energy transport becomes diffusive. Magnetothermal effects can also be induced by imposing a finite magnetisation in the system. In the integrable regime, these effects are ballistic. Our results thus provide new evidence to support the picture of energy transport proposed by methods different to the one we use.

The second problem we analyse corresponds to local thermalisation. First we discussed whether a system driven at its boundaries by thermal reservoirs of the

same temperature can be locally and globally described by thermal states, a question already considered in the literature [63]. Our method is nonetheless different. It is based on comparing all the two-site reduced density operators of the bulk of the system with two-site thermal states with the same type of Hamiltonian, by means of their trace distance. This quantity is an appropriate comparison tool, given that it bounds the difference of the expectation values of the two states for any observable with bound eigenvalues. We observed that in the integrable limit of the Hamiltonian, the system is not well described by local thermal states. As the integrability-breaking parameter increases, this local description becomes better. Deep in the nonintegrable regime, the system can be regarded as being locally and globally thermalised, with the same local and global temperatures.

Interestingly, similar results are found in the nonequilibrium configuration where the temperatures imposed at the boundaries are different. As the integrability-breaking parameter increases, the two-site reduced density operators across the system become closer to two-site thermal states. This is evidenced from the decrease of the trace distance between the two types of states, and thus from the agreement of the corresponding expectation values. As the size of the system increases, the local description by thermal states is also improved. However, whether very large systems locally thermalise arbitrarily close to the integrable limit of the Hamiltonian remains an open question.

Chapter 7

Environmental coupling in interacting quantum systems

When initially studying the physics of a quantum system, it is usually assumed that it is closed and isolated, so no interactions with environmental degrees of freedom occur. In real systems, such interactions are unavoidable, and are generally expected to degrade or obscure the quantum phenomena of interest. Nevertheless, an entirely different picture of the role of environmental coupling has emerged in recent years, largely due to insights obtained from the physics of biological complexes.

In these systems, naturally existing at room temperature and in contact with all sorts of disrupting elements, the interaction with the environment cannot be disregarded. Due to "warm and wet" conditions [197], quantum effects would be expected to be completely washed out from these systems. However, seminal experimental [40, 41, 198] and theoretical [199] research on photosynthetic complexes, as well as in other examples of the emerging field known as Quantum Biology [45], indicates that quantum effects might be sustained even under these adverse conditions[1]. Furthermore, several studies have concluded that a proper balance between coherent

[1] In photosynthetic complexes, long-lived coherences surviving up to hundreds of fs [40, 200] to 1ps [41] have been found experimentally. This timescale is similar to that in which excitation transport processes occur in these systems [200].

processes and the decoherence induced by environmental coupling is necessary to allow these systems to perform excitation transport optimally [42–44, 201, 202]. In other words, the study of quantum effects in biological systems has provided strong support for the idea that under some circumstances, the efficiency of quantum transport processes can be improved by an adequate coupling to the environment.

Most of the research performed so far on the interplay between coherent transport mechanisms and incoherent effects due to environmental coupling has restricted to single-particle physics. The focus on this regime has been motivated by natural sunlight conditions and the existence of photoprotective mechanisms, which prevent photosynthetic complexes to contain more than a single excitation at a time [203]. Nevertheless, interparticle interactions are of vital importance in many other types of systems, where environmental effects are also expected to have a significant impact. These include spin chains, systems of ultracold atoms in optical lattices [204], arrays of optical cavities [205], arrays of quantum dot spin qubits [48] and organic conductors [206], among others. And yet, the physics resulting from the simultaneous presence of interparticle interactions and bulk decoherence remains largely unexplored. The goal of the research described in Chapters 8 and 9 is to show that interesting, truly many-body effects emerge from the competition between both. In particular, new mechanisms of environment-assisted transport that only occur for strongly-interacting regimes are discussed. The aim of the present Chapter is to introduce the particular models that we will consider to analyse these effects.

We start by noting that our studies are performed on spin-1/2 XXZ chains. By analysing the impact of environmental coupling on the transport properties discussed in Chapter 5, we are able to identify general features of the interplay between particle-particle interactions and incoherent effects. First we describe the model to be studied in Chapters 8, consisting of a spin chain subject to bulk dephasing. We illustrate some important effects of dephasing, namely the degradation of co-

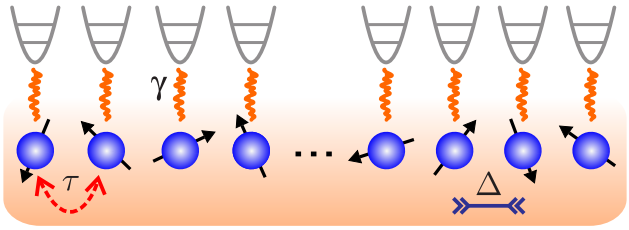

Figure 7.1. XXZ spin chain coupled to local vibrational reservoirs. The hopping parameter between neighbouring sites is τ, and the interaction strength between spin excitations is Δ. Dephasing processes take place at every site of the system, at a rate γ.

herences and the Zeno effect, by the examination of simple limits of the system. Then we discuss the motivation for the model considered in Chapter 9, consisting of incoherently-coupled spin chains. Finally we mention several interesting phenomena resulting from the coherence-decoherence interplay, including various environment-assisted effects.

7.1 Model of environmental coupling in interacting one-dimensional spin chains

In this Section we describe the first model we consider to analyse the impact of environmental effects on the transport properties of many-body systems. It corresponds to a one-dimensional spin-1/2 XXZ chain subject to bulk pure dephasing, which is studied in Chapter 8. The dephasing processes arise from coupling each site of the chain to a different vibrational reservoir, as depicted in figure 7.1. The Hamiltonian H_{T} of the total system is

$$H_{\mathrm{T}} = H_{\mathrm{S}} + H_{\mathrm{B}} + H_{\mathrm{I}}. \tag{7.1}$$

Here H_{S} denotes the Hamiltonian of the spin chain, corresponding to the XXZ model (equation (2.1)). The Hamiltonian H_{B} of the total environment, i.e. of all

the local vibrational reservoirs, is

$$H_{\mathrm{B}} = \sum_{j=1}^{N} \sum_{k} \omega_k b_{j,k}^{\dagger} b_{j,k}, \tag{7.2}$$

where the operators $b_{j,k}^{\dagger}$ and $b_{j,k}$ create and annihilate bosons (of wavelength much smaller than the distance between sites) at vibrational mode k of the reservoir coupled to site j of the chain, with site-independent frequency ω_k. The coupling between the spin chain and the environment is given by

$$H_{\mathrm{I}} = \sum_{j=1}^{N} \sum_{k} g_k \sigma_j^z \left(b_{j,k}^{\dagger} + b_{j,k} \right), \tag{7.3}$$

where g_k is the site-independent coupling strength to mode k. For a single site with a finite magnetic field, this corresponds to the well-known spin-boson model [207]. Following the procedure outlined in Appendix C, with the weak-coupling, Markov and wide-band approximations, a Lindblad master equation for the density operator of the spin chain is obtained, with a jump operator at site j given by

$$L_j^{\mathrm{d}} = \sqrt{\gamma} \sigma_j^z, \tag{7.4}$$

where the rate $\gamma \propto |g_k|^2$ of a particular bosonic mode k, and to its population on a thermal state (the state chosen for the reservoirs). Now we consider two simple examples to illustrate the dephasing effect described by equation (7.4).

7.1.1 Dynamics of a single spin

First consider the case of a single spin, with on-site energy $B = \omega/2$. If its state ρ_{S} is given by

$$\rho_{\mathrm{S}}(t) = \begin{pmatrix} \rho_{11}(t) & \rho_{10}(t) \\ \rho_{01}(t) & \rho_{00}(t) \end{pmatrix}, \tag{7.5}$$

with $\rho_{11}(t)$ and $\rho_{00}(t)$ the populations of the up and down states respectively, and ρ_{01} and ρ_{10} the corresponding coherences, it immediately follows from the Lindblad master equation (3.13) that

$$\begin{gathered}\frac{d}{dt}\rho_{01}(t) = (-i\omega - 2\gamma)\rho_{01}(t), \quad \frac{d}{dt}\rho_{10}(t) = (i\omega - 2\gamma)\rho_{10}(t), \\ \frac{d}{dt}\rho_{00}(t) = 0, \quad \frac{d}{dt}\rho_{11}(t) = 0.\end{gathered} \tag{7.6}$$

These equations indicate that the populations of the states are unaffected, while the coherences oscillate in time with frequency ω, and decay exponentially at at rate γ due to dephasing. For example, if the initial state corresponds to

$$\rho_{\mathrm{S}}(t=0) = \frac{1}{2}\begin{pmatrix} 1 & 1 \\ 1 & 1 \end{pmatrix}, \tag{7.7}$$

the state at a time t is given by

$$\rho_{\mathrm{S}}(t) = \frac{1}{2}\begin{pmatrix} 1 & e^{-i\omega t}e^{-2\gamma t} \\ e^{-i\omega t}e^{-2\gamma t} & 1 \end{pmatrix}, \tag{7.8}$$

with the coherences vanishing in the long-time limit.

7.1.2 Dynamics of two spins in single-particle subspace

A second example corresponds to two coupled spins, with $B = 0$. We restrict to the single-particle subspace, whose effective Hamiltonian is (see equation (B.5))

$$\tilde{H}_{\mathrm{S}} = \tau\begin{pmatrix} -\Delta & 2 \\ 2 & -\Delta \end{pmatrix}. \tag{7.9}$$

If the state is given by

$$\rho_{\mathrm{S}}(t) = \begin{pmatrix} \rho_{11}(t) & \rho_{12}(t) \\ \rho_{21}(t) & \rho_{22}(t) \end{pmatrix}, \tag{7.10}$$

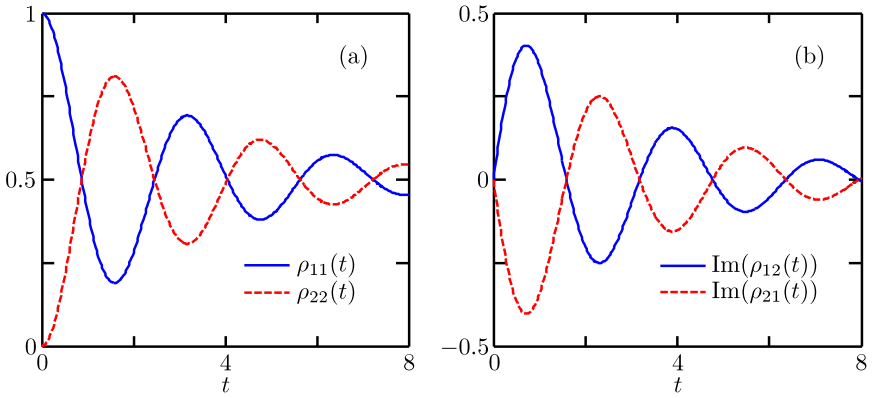

Figure 7.2. Underdamped evolution of populations (a) and coherences (b) in a two-site system subject to weak dephasing. The initial state corresponds to an excitation localised at site 1. The parameters of the calculations are $\tau = 0.5$ and $\gamma = 0.15$.

where $\rho_{11}(t)$ and $\rho_{22}(t)$ correspond to the populations of sites 1 and 2 respectively and $\rho_{12}(t)$ and $\rho_{21}(t)$ are the coherences, then the Lindblad master equation (3.13) directly leads to the set of coupled differential equations

$$\begin{aligned} \frac{d}{dt}\rho_{11} &= -i2\tau(\rho_{21} - \rho_{12}), \quad \frac{d}{dt}\rho_{22} = -i2\tau(\rho_{12} - \rho_{21}), \\ \frac{d}{dt}\rho_{21} &= -i2\tau(\rho_{11} - \rho_{22}) - 4\gamma\rho_{21}, \quad \frac{d}{dt}\rho_{12} = -i2\tau(\rho_{22} - \rho_{11}) - 4\gamma\rho_{12}. \end{aligned} \tag{7.11}$$

Note that Δ does not affect the dynamics, as expected from a single-particle regime. We assume that at time $t = 0$ the initial state corresponds to the spin excitation at site 1, i.e. that spin 1 is up and spin 2 is down. Thus there is no initial coherence between the sites. The solution of this system of equations is

$$\begin{aligned} \rho_{11}(t) &= \frac{1}{2}\left[1 + e^{-2\gamma t}\left(\cos(2\Omega t) + \frac{\gamma}{\Omega}\sin(2\Omega t)\right)\right], \\ \rho_{21}(t) &= -\frac{i\tau}{\Omega}e^{-2\gamma t}\sin(2\Omega t), \quad \rho_{22}(t) = 1 - \rho_{11}(t), \quad \rho_{12}(t) = -\rho_{21}(t), \end{aligned} \tag{7.12}$$

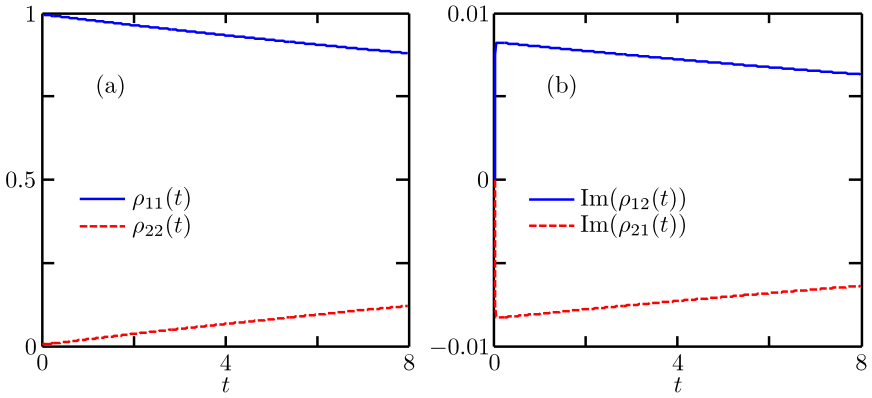

Figure 7.3. Zeno effect, manifested in the overdamped evolution of populations (a) and coherences (b) in a two-site system with strong dephasing. Initially an excitation is located at site 1. The results correspond to the parameters $\tau = 0.5$ and $\gamma = 40$.

with the frequency $\Omega = \sqrt{4\tau^2 - \gamma^2}$. These results are shown in figure 7.2 for parameters in the weak dephasing (underdamped) regime $\gamma < 2\tau$. If $\gamma = 0$, the excitation goes back and forth, with the populations and coherences oscillating at frequency 4τ. In the presence of weak dephasing, the dynamics is very different. The populations and coherences still oscillate in time, but with a frequency 2Ω. In addition, they decay exponentially with a rate determined by the dephasing. In the long-time limit, $\rho_{11}, \rho_{22} \to \frac{1}{2}$, while the coherences vanish, $\rho_{12}, \rho_{21} \to 0$. So the effect of dephasing is to lead the system to the maximally mixed state, i.e. the identity operator, in which the excitation is equally distributed between the two sites, and the phase information gained due to the coherent hopping is completely lost.

Now consider the opposite case of very strong dephasing rate $\gamma \gg 2\tau$, deep in the overdamped regime. The evolution of these populations and coherences is shown in figure 7.3. Due to the strong environmental coupling, the oscillating behaviour is entirely lost. But more importantly, the dynamics of the excitation becomes very slow, taking a long time to delocalise along both sites. In fact, for very large γ/τ and a fixed time t, $\rho_{11} \to 1$ and $\rho_{22}, \rho_{12}, \rho_{21} \to 0$. This means that if the interaction with

the environment is very strong, i.e. if the system is perturbed by the environment very frequently, it is prevented to evolve coherently, and tends to remain in its initial state. This phenomenon is known as the quantum Zeno effect, in analogy to Zeno's paradox [130]. On a broader context this effect has profound consequences, since it states that a quantum system is inhibited to evolve if a continuous measurement is perform onto it.

With the previous two simple examples, we have illustrated some basic consequences of pure dephasing in single-particle systems, namely the decay of coherences in time and the Zeno effect. In many-body systems, more complex types of phenomena can emerge from the interplay between coherent and incoherent processes; some of these are referenced in Section 7.3. For the particular case of a nonequilibrium XXZ spin chain, we provide in Chapter 8 a detailed analysis of a novel dephasing-enhanced transport scheme, which is found to be a true many-body effect.

7.2 Interplay between coherence and decoherence in systems of coupled chains

In addition to individual spin chains, we study in the present thesis the competition between coherent transport and incoherent processes in a different type of structure. This consists of a group of one-dimensional lattices, each supporting coherent intrachain particle transport, incoherently coupled to neighbouring chains due to the mediation of the environment. Several systems are known to possess this type of configuration; here we briefly discuss the most important examples.

The first corresponds to a particular conjugated polymeric system, namely poly[2-methoxy,5-(2'-ethyl-hexoxy)-1,4-phenylene-vinylene] (MEH-PPV). This organic conductor is one of the most prominent examples of artificial light-harvesting complexes,

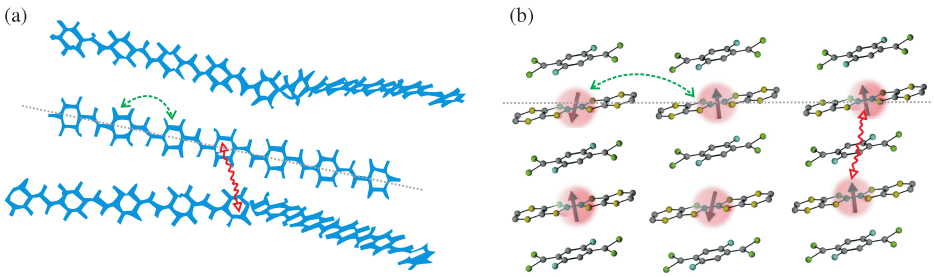

Figure 7.4. Illustration of systems of incoherently coupled chains. The red solid and green dashed lines represent interchain and intrachain hopping, respectively. (a) Excitation transport in a conjugated polymer system. Interchain hopping of excitons, observed to be incoherent [198], occurs where polymeric chains are close to each other. (b) Excitation hopping in organic salts. Coherent hopping occurs along one direction of the system, while incoherent hopping takes place along another direction, mediated by a scaffolding of different molecules.

and has attracted a lot of attention during several years due to its potential to constitute efficient organic solar cells [208]. In this system, the transport of energy absorbed from sunlight is performed by means of excitons (bound states of electrons and holes); this process is known to be very efficient for ordered samples [209]. As schematised in figure 7.4(a), MEH-PPV consists of several polymeric chains weakly coupled with each other. This allows two types of exciton transfer: an intrachain transport along the backbone of each polymeric chain (green arrow), and an interchain transport of excitons, which hop from one chain to the other at points of closeness (red arrow). Experimental studies of these systems have indicated that the intrachain exciton transport is coherent even at room temperature (lasting up to 250 fs), while the interchain transport is incoherent [198][2].

Other examples of systems constituted by incoherently-coupled lattices include

[2]The experiments allowed to separate the types of exciton transport by placing the polymer on different types of solvents. When a good solvent was used, the polymeric chain was extended, and the transport mechanism was governed by intrachain motion. On the other hand, when using a bad solvent, the polymer is strongly folded on itself, so no-connected chromophores would be very close to each other and interchain transport would be favored.

cuprates [210–212] and several organic conductors such as layered organic metals [213], and Bechgaard and Fabre salts[3] [206, 214–216]. As illustrated in figure 9.1(b), these systems share a common feature, which is a highly anisotropic structure consisting of lattice sites strongly coupled in one or two directions and weakly coupled in other directions. At not-too-low temperatures, particle transport along the strongly coupled directions is predominantly coherent, while the transport along directions with weak coupling occurs via incoherent hopping processes [206].

A complete description of these systems is extremely involved, given that in addition to the interplay between coherent intrachain and incoherent interchain hopping, many other competing effects may contribute to the transport behaviour, depending on the material in question. These include static disorder, particle interactions, excitation dissipation and recombination, and spatially correlated environments. It is thus expected that a rich variety of phenomena emerges from the interplay between these different processes. In order to disentangle the contributions from these effects, a natural strategy is to analyse the competition between just a few of them first, which can be nontrivial. Our research discussed in Chapter 9 corresponds to one step in this direction. There we focus exclusively on the physics resulting from the combination of coherent interactions and incoherent interchain processes, neglecting disorder and other complications. Thus our results set the stage for a more complete future analysis. In particular, we study a configuration in which several spin chains are coupled to their neighbours by jump operators of the form

$$L_i^{(\lambda,\mu)} = \sqrt{\gamma}\sigma_i^{+(\mu)}\sigma_i^{-(\lambda)}\delta_{\lambda,\mu\pm1}, \tag{7.13}$$

representing the incoherent hop of an excitation at site i of chain λ to site i of chain μ, at a rate γ. In Section 9.1 we discuss when this process is expected to occur.

[3]These correspond to quasi-one dimensional conductors whose building blocks are molecules known as TMTXF, X corresponding to sulphur in Bechgaard salts, and to Selenium in Fabre salts.

7.3 Beneficial effects of environmental coupling

As previously mentioned, a picture in which the coupling of a system to its environment can have positive consequences has emerged in recent years. This was largely triggered by the discovery of dephasing-assisted transport in toy models of photosynthetic complexes [42, 43]. For completeness, here we briefly mention some of the research areas in which beneficial effects from environmental coupling have also been observed and exploited.

- Single-particle transfer schemes: Transfer mechanisms of single excitations which benefit from environmental coupling, different to that of photosynthetic complexes, have been recently found. These include decoherence-assisted quantum walks [217], heat transport [218], and bulk (not edge-to-edge) transport in linear ordered chains [44].

- Generation of entanglement: Several years ago the generation of entanglement by means of white noise had already been discussed [219]. More recent schemes of entanglement generation by dissipative processes have also been proposed [220].

- Engineering many-body quantum states: Several schemes to prepare desired many-body quantum states by dissipative processes have been recently proposed, including ground states of Hamiltonians without frustration [46] and long-range-order states of non-interacting bosons [47].

- Quantum biology: The most prominent example of this emerging area is that of exciton transport in light-harvesting complexes. Nevertheless, other important biological scenarios in which quantum effects are believed to be important have been discussed, namely the olfaction mechanism and the magneto-reception in birds [45].

7.3.1 Reported effects from the interplay between particle interactions and environmental coupling

We end the present Chapter by mentioning some interesting effects that have been found as a result of the interplay between particle-particle interactions and environmental coupling. A first example corresponds to the study of long-time limit correlations $\langle \sigma_i^+ \sigma_{i+1}^- \rangle$, evolving from an antiferromagnetic initial state under different Hamiltonians [48]. In a closed XXZ system, these correlations decay exponentially in time, while in the presence of dephasing of the form (7.4), they decay as a power law. In the case of an Ising model, it was observed that for some parameters (specially at large Δ), interactions help impede the decay of coherences due to dephasing.

A similar effect of interaction-impeded decoherence has been found in systems of cold atoms in optical lattices, where the environmental coupling results from heating processes [204]. Importantly, the Lindblad jump operator of such processes is entirely equivalent to that of equation (7.4), being proportional to the local number operator. This establishes cold-atom systems as appropriate scenarios for the experimental verification of the results we describe in Chapter 8, in addition to the recent implementation of boundary driving schemes similar to those we use [37–39, 143].

Finally, in a recent numerical study of the expansion dynamics of a bosonic cloud in a disordered potential, a result intimately related to that discussed in Chapter 8 has been found. Namely, in the strongly-interacting regime, where the cloud would remain localised due to self-trapping, noise processes can significantly enhance its expansion [157]. Although we consider a different type of transport setup and a different Hamiltonian, and although we neglect disorder, we believe that the mechanism described in Chapter 8 provides enough insight to account for this effect to a large extent.

Chapter 8

Dephasing-assisted transport in strongly correlated quantum systems

A key insight from recent studies is that noise, such as dephasing, can improve the efficiency of quantum transport by suppressing coherent single-particle interference effects. However, it is not yet clear whether dephasing can enhance transport in an interacting many-body system. In the present Chapter we address this question by analysing the spin and heat transport properties of a boundary driven XXZ chain with nearest-neighbour interactions subject to bulk dephasing. In the weakly-interacting regime, we observe that dephasing induces diffusive spin and heat transport, degrading the conductivity of the system. On the other hand, we find environment enhanced spin and heat transport in the strongly interacting regime, where due to energy dissipation, dephasing is shown to induce incoherent transitions bridging the gap between flattened bands of bound states and bands of mobile eigenstates. Surprisingly the effect is significant even in the linear response regime of the system. The emergence of enhanced spin transport compared to that of the dephasing-free system is suggested to exist for any large and finite chain. The energy conduction, in contrast, is increased compared to the dephasing-free case for small systems only, due to the bulk energy dissipation. However, it still can be increased

for large systems at intermediate dephasing rates.

The response of the system to dephasing also establishes a signature of an underlying non-equilibrium phase transition between regimes of transport degradation and enhancement. The existence of this transition is shown not to depend on the integrability of the model considered. As a result dephasing enhanced transport is expected to persist in more realistic non-equilibrium strongly-correlated systems. The results of this Chapter have been published in references [175, 176].

8.1 Description of the system

The goal of this Chapter is to observe how the transport properties of the boundary-driven XXZ chain, discussed in Chapters 5 and 6, are affected by bulk dephasing processes arising from the interaction with the environment (see Section 7.1). So we consider the same transport scheme here, depicted in figure 8.1. Namely, we take a one-dimensional spin-1/2 chain with Hamiltonian

$$H = \sum_{j=1}^{N-1} \varepsilon_{j,j+1} = \tau \sum_{j=1}^{N-1} (\sigma_j^x \sigma_{j+1}^x + \sigma_j^y \sigma_{j+1}^y + \Delta \sigma_j^z \sigma_{j+1}^z) + \sum_{j=1}^{N} B_j \sigma_j^z, \tag{8.1}$$

and drive it to a NESS by coupling it to unequal Markovian reservoirs at the boundaries. This time, however, we include dephasing processes at each site of the chain. The dynamics of this system is thus governed by the Lindblad master equation

$$\frac{d\rho}{dt} = -i[H, \rho] + \mathcal{L}_{\text{driv}}^{\text{L}}(\rho) + \mathcal{L}_{\text{driv}}^{\text{R}}(\rho) + \mathcal{L}_{\text{d}}(\rho), \tag{8.2}$$

with the driven jump operators

$$L_{\text{L,R}}^{+} = \sqrt{\Gamma(1 \pm f)/2}\, \sigma_{1,N}^{+} \quad L_{\text{L,R}}^{-} = \sqrt{\Gamma(1 \mp f)/2}\, \sigma_{1,N}^{-}. \tag{8.3}$$

Figure 8.1. Scheme of a spin chain driven to a nonequilibrium configuration by boundary Markovian reservoirs and local dephasing. This is the same system shown in figure 5.1, with local dephasing processes of rate γ.

The bulk dephasing processes are described by the dissipator $\mathcal{L}_{\mathrm{d}}(\rho) = \sum_{j=1}^{N} \mathcal{L}_{\mathrm{d}}^{(j)}(\rho)$, with a homogeneous dephasing rate γ and jump operator at site j

$$L_j^{\mathrm{d}} = \sqrt{\gamma}\sigma_j^z. \tag{8.4}$$

We start by considering the impact of dephasing on spin transport. Then we observe the effect on the heat transport induced by a magnetic imbalance and a homogeneous magnetic field. As before, we use the TEBD method to obtain the NESS of the system, and then calculate the relevant expectation values.

8.2 Dephasing-degraded spin transport

To study the spin transport properties of the system, we first focus on the magnetisation profile and the spin current, the latter being the expectation value of the operator

$$J_i = 2(\sigma_i^x\sigma_{i+1}^y - \sigma_i^y\sigma_{i+1}^x), \quad i = 1, \ldots, N-1. \tag{8.5}$$

As in Section 5, the spin current is homogeneous through the system, i.e. $\langle J_i \rangle = J^{\mathrm{S}}$.

We first consider the regime of weak interactions, $\Delta < 1$, where the spin transport is ballistic in the absence of dephasing (see Chapter 5). In previous research it has been shown that the introduction of dephasing induces diffusive spin transport, so the system satisfies the diffusion equation $J^{\mathrm{S}} = \kappa_{\mathrm{S}}\nabla S$, with κ_{S} the spin conductivity

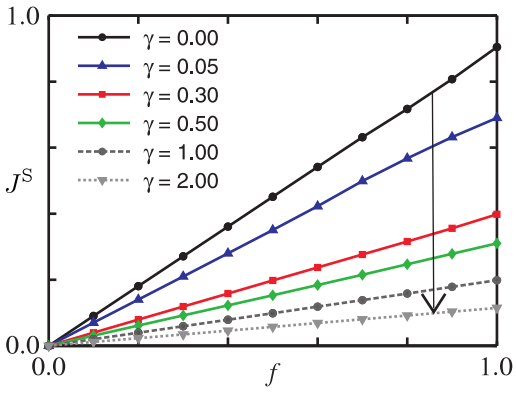

Figure 8.2. Current-driving profiles in the weakly-interacting regime $\Delta = 0.5$ for increasing (as indicated by the arrow) dephasing rates γ and $N = 16$.

and ∇S the magnetisation gradient. As a result the current scales with the size of the system as $J^S \sim f/N$, characteristic of an Ohmic conductor [181, 221]. The maximum current through the chain thus occurs at maximal bias $f = 1$, as in the dephasing-free case. In the non-interacting limit $\Delta = 0$ it has been proven rigorously that a homogeneous chain cannot exhibit any dephasing enhanced end-to-end transport [42, 44, 221]. In fact, for the driving scheme considered here, it can be shown that if $\Delta = 0$, the spin current is (see Refs. [178, 181] and Appendix D)

$$J^S(\Delta = 0) = -\frac{4f}{\frac{\Gamma}{4} + \frac{4}{\Gamma} + (N-1)\gamma}, \tag{8.6}$$

which behaves as $J^S \sim f/\gamma N$ and thus is monotonously degraded by dephasing. In addition, the magnetisation in the bulk has the form of a spin ramp, decreasing linearly with the position i in the form

$$\langle \sigma_i^z \rangle = f - J^S \left(\frac{\Gamma}{16} + \frac{1}{\Gamma} + (i-1)\frac{\gamma}{2} \right), \quad 1 < i < N. \tag{8.7}$$

This immediately leads to a spin conductivity which decays monotonously with the dephasing rate, $\kappa_S = 2/\gamma$, and which diverges when $\gamma \to 0$, as expected for a ballistic

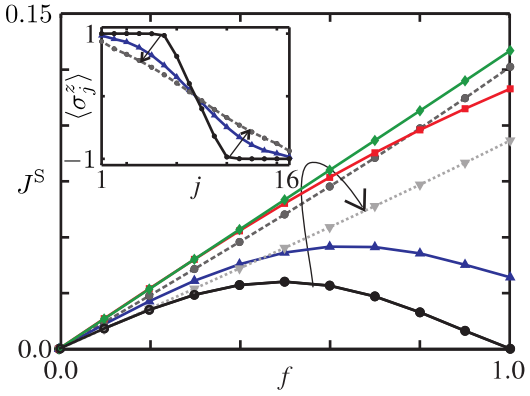

Figure 8.3. Current-driving profiles in the strongly-interacting regime $\Delta = 2.0$ for increasing (as indicated by the arrow) dephasing rates γ and $N = 16$. The rates γ are the same than those of figure 8.2. Inset. The magnetisation $\langle\sigma_j^z\rangle$ of the system when $f = 1$, corresponding to $\gamma = 0, 0.05, 1.00$.

conductor. In interacting systems with $\Delta < 1$, a similar qualitative behaviour of the spin transport has been suggested [181]. In figure 8.2 we report the current-driving profiles for $\Delta = 0.5$ showing that dephasing monotonically degrades the current for any driving, confirming that this behaviour persists even in the presence of weak interactions.

8.3 Dephasing-enhanced spin transport

The main result of the present Chapter is that for $\Delta > 1$ the presence of a small bulk dephasing can significantly enhance the spin transport. This striking behaviour is illustrated for $\Delta = 2$ in figure 8.3 where dephasing up to a moderate rate $\gamma \approx 0.5$ is seen to increase the current. This enhancement is shown to occur *for any* $f > 0$; however it is not uniform in f, resulting in the current-driving profile changing with γ. Specifically, around $\gamma \approx 0.3$ the NDC effect is lost and further increases in γ yield a linear profile with f. Near $f = 1$ dephasing therefore induces not just a quantitative increase in the current, but rather causes a major qualitative

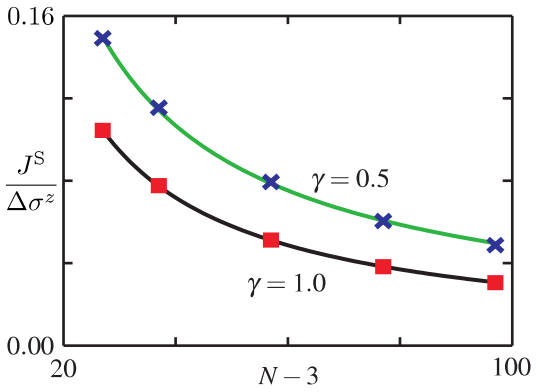

Figure 8.4. The current J^S at $f = 1$, divided by the resulting magnetisation difference $\Delta\sigma^z$ between the ends of the system (excluding the boundary), is plotted against the system size $N - 3$ up to $N = 100$ sites. The data is for dephasing rates $\gamma = 0.5$ ($\times$) and $\gamma = 1.0$ ($\blacksquare$). The solid lines show the fitting to $J^S/\Delta\sigma_z = \kappa(N-3)^{-\alpha}$ for each γ. These yield $\kappa = 1.288$ and $\alpha = 0.863$ for $\gamma = 0.5$, and $\kappa = 1.228$ and $\alpha = 0.958$ for $\gamma = 1.0$.

change in the behaviour of the system from being insulating at $\gamma = 0$ to yielding the maximal current once $\gamma > 0.3$. In the inset of figure 8.3 this change at $f = 1$ is shown to be coincident with the breakdown of the ferromagnetic domains into a nearly linear magnetisation profile, due to the increase of the dephasing rate. The transport at large driving and dephasing rates therefore resembles that of a diffusive conductor. This result is confirmed by the scaling of the current with the size of the system, shown in figure 8.4 for $\Delta = 2$ and dephasing rates $\gamma = 0.5$ and $\gamma = 1.0$. The power-law fits for each γ, which are seen to accurately model the data, indicate superdiffusive transport for $\gamma = 0.5$, where the current decays slower than $1/(N-3)$, but has approached a diffusive behaviour once $\gamma = 1.0$.

For a given driving f there is an optimal dephasing rate γ_{opt} that maximises the current (J^S_{opt}), as shown in figure 8.5. For the parameters of this figure, the enhancement at weak driving and the optimal dephasing rate is significant, e.g. $\approx 37\%$ at $f = 0.1$. As the driving increases so does the optimal dephasing rate γ_{opt}, as well as the enhancement of the current, the latter being of several orders of magnitude

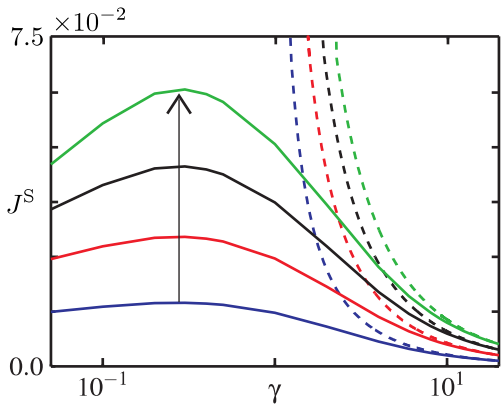

Figure 8.5. The current as a function of γ for driving biases $f = 0.1, 0.2, 0.3$ and 0.4 (from bottom to top curve) with $\Delta = 2$, and $N = 40$. The dashed lines correspond to $J^{\mathrm{S}}(\Delta = 0)$, the non-interacting analytic result (8.6).

for $f \to 1$. For $\gamma > \gamma_{\mathrm{opt}}$ the current is reduced because the $\mathcal{L}_{\mathrm{d}}$ contribution to equation (5.2) dominates over the coherent hopping terms and progressively freezes out the dynamics due to the Zeno effect [130]. In fact, for increasingly large γ the NESS current converges to the exact $\Delta = 0$ solution with dephasing given by equation (8.6). This convergence, shown in figure 8.5, thus indicates that the interaction strength Δ becomes irrelevant for very large dephasing rates.

To show that the transport enhancement is not restricted to small chains, we analyse the scaling of the optimal dephasing rate γ_{opt} with N for weak driving $f = 0.1$. The results are presented in figure 8.6(a). Although γ_{opt} decreases as N increases, extrapolations with simple trial functions (of which an exponential decay, shown in figure 8.6(a), gives the best description) indicate that even when $N \to \infty$, γ_{opt} remains finite. However, since the magnetisation imbalance between the boundaries of the chain $\Delta\sigma^z$ is bounded, $J^{\mathrm{S}} \to 0$ in the thermodynamic limit; see also the inset of figure 8.6(b), which shows that the optimal current $J^{\mathrm{S}}_{\mathrm{opt}} \to 0$ as $N \to \infty$. Nevertheless, the existence of a finite γ_{opt} in the thermodynamic limit indicates that even in the linear response regime, the transport can be enhanced by environmental coupling in systems of *any* finite size. To give more support to

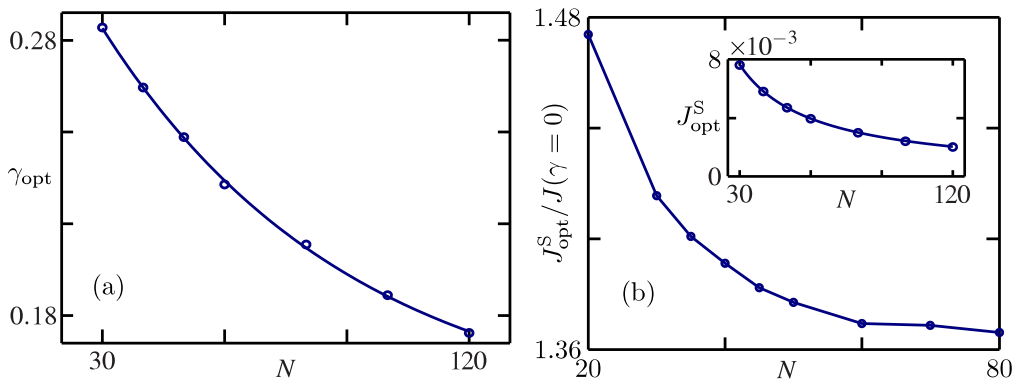

Figure 8.6. Scaling of the optimal transport properties with the system size. (a) Optimal dephasing $\gamma_{\rm opt}$ for different sizes of the system, at $f = 0.1$, $\Delta = 2$ and $\Gamma = 1$ (circles). The solid line corresponds to the exponential decay $\gamma_{\rm opt} = \gamma^{\rm TL}_{\rm opt} + a\exp(-N/b)$, with $a = 0.252$, $b = 85.9$ and $\gamma^{\rm TL}_{\rm opt} = 0.109$. (b) Spin current enhancement factor $J^{\rm S}_{\rm opt}/J(\gamma=0)$ as a function of N. The solid line is a guide to the eye. Inset: Optimal current $J^{\rm S}_{\rm opt}$ as a function of N. The solid line corresponds to the power law decay $J^{\rm S}_{\rm opt} = aN^{-b}$, with $a = 0.0948$ and $b = 0.94$; as $N \to \infty$, $J^{\rm S}_{\rm opt} \to 0$.

this claim, we show in figure 8.6(b) the corresponding current enhancement factor $J^{\rm S}_{\rm opt}/J(\gamma=0)$, which decreases for small systems but saturates as N increases. For stronger driving both the current enhancement and $\gamma_{\rm opt}$ become larger, as shown in figure 8.5, and the range of beneficial dephasing rates broadens. So the dephasing-enhanced transport should emerge in mesoscopic systems even for weak driving.

8.4 Enhancement mechanism

Now we describe the mechanism that leads to dephasing enhanced spin transport in the strongly interacting regime. For this, consider first the maximal driving configuration $f = 1$, where dephasing has the strongest impact. As discussed in Section 5.4, in the absence of dephasing the driving preferentially populates the dark state $|\Psi_D(N/2)\rangle$ of equation (5.18), whose leading component is the state $|B_{N/2}\rangle$ of ferromagnetic domains. Since local dephasing on each site, given in equation (8.4),

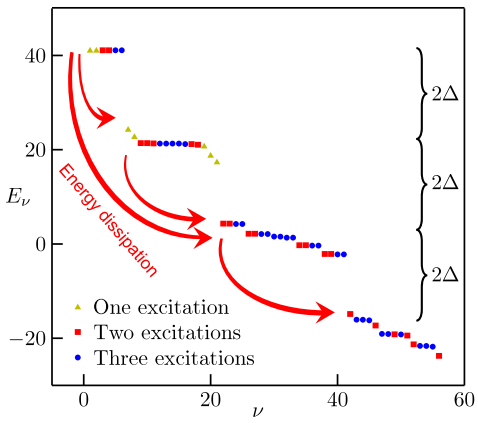

Figure 8.7. Cartoon of the eigenspectrum of the XXZ Hamiltonian in the strongly interacting regime, to illustrate the transport enhancement mechanism. ν represents the eigenvalue index. The highest bands consist of bound states with low conductivity, while lower bands contain more mobile states. The red arrows indicate possible transitions induced by energy dissipation, between states of the same spin sectors. The energy values were obtained from a chain of $N = 7$ and $\Delta = 10$.

does not commute with the chain Hamiltonian H[1], this noise process induces incoherent transitions between many-body energy eigenstates of the system. This is characterised by an energy dissipation rate

$$\frac{dE_\gamma}{dt} = \mathrm{Tr}(H\mathcal{L}_\mathrm{d}(\rho)) = -4\gamma \sum_j \langle \sigma_j^x \sigma_{j+1}^x + \sigma_j^y \sigma_{j+1}^y \rangle, \tag{8.8}$$

dependent on the kinetic energy of the state, and thus enables population to escape from the approximate dark states $|\Psi_D(n)\rangle$ to the mobile current-carrying bands of scattering states. Note that since the dephasing processes do not annihilate spin excitations in the system, the induced transitions are between states belonging to the same spin sector (see Appendix A). It is this dissipative effect, sketched in figure 8.7, which breaks the localisation in the $f = 1$ insulating NESS and significantly enhances the current, up to inducing diffusive transport as shown in figure 8.4. An optimal dephasing rate γ_opt emerges due to the competition between these dephasing induced

[1]If it did commute, $\mathrm{Tr}(H\mathcal{L}_\mathrm{d}(\rho)) = 0$, which can be readily verified.

transitions and the degradation of mobility of the scattering states by dephasing through the Zeno effect.

It could be argued that the dephasing-enhanced spin transport is not a surprising effect in the maximally-driven case $f = 1$, since a disruption is being caused to a state which is already an insulator. Nevertheless this argument is not valid for driving $f < 1$. In particular, in the linear response regime, where $f \ll 1$ and the NESS corresponds to a diffusive conductor rather than to an insulator, it is not *a priori* obvious that additional dissipation induced by dephasing will be beneficial to transport. Yet as seen in figure 8.5 and figure 8.6 a significant enhancement of the current due to dephasing for chains of any finite size is observed in the weakest driving considered, $f = 0.1$. This behaviour suggests that even in this case, where the high-energy bound states like $|\Psi_D(n)\rangle$ are only marginally populated by the driving, additional incoherent transitions bridging the numerous gaps in the spectrum to the mobile bands still enhance transport.

8.5 Signatures of nonequilibrium phase transition

The results discussed in Section 8.3 demonstrate the existence of two transport regimes in the system with different responses to moderate dephasing: degradation for weak interactions and enhancement for strong interactions. We now discuss the transition between the two regimes, characterise the critical interaction strength, analyse the correlations through the system for each regime, and show that the same regimes of response remain even when the integrability of the system is broken.

8.5.1 Transition at $\Delta = 1$

As explained in Chapters 2, 3 and 5, the interaction strength $\Delta = 1$ is of particular significance to the XXZ Hamiltonian. At zero-temperature and in the absence of

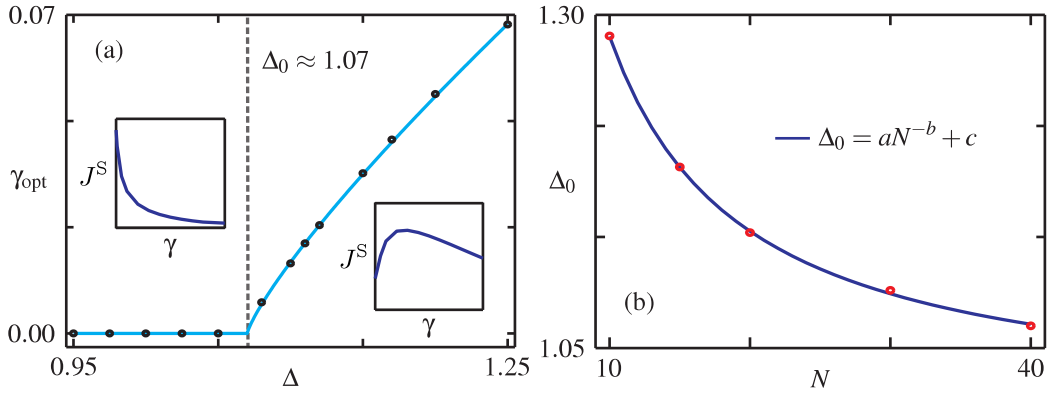

Figure 8.8. (a) The optimal dephasing rate $\gamma_{\rm opt}$ as a function of Δ, for $N = 40$, $f = 0.1$ and $\Gamma = 1$. The circles indicate TEBD results, and the solid line corresponds to the fitted function $\gamma_{\rm opt} \propto (\Delta - \Delta_0)^{\beta}$, with $\beta = 0.819$ and $\Delta_0 = 1.07$. The inset plots show the generic behaviour of $J^{\rm S}$ with γ above and below Δ_0. (b) The scaling of Δ_0 with N for $f = 0.1$ and $\Gamma = 1$, along with the fitted power-law shown, where $a = 3.906$, $b = 1.066$ and $c = 0.995$.

magnetic field, it separates the gapless and magnetically ordered (ferro- and antiferromagnetic) gapped equilibrium phases. More generally, it divides a continuous eigenspectrum for $\Delta < 1$ from one with numerous gaps for $\Delta > 1$, as illustrated in figure 2.2. In the system driven by the jump operators of equation (8.3), it was previously observed that $\Delta \approx 1$ also separates ballistic and diffusive transport regimes for weak driving. However, it is not *a priori* clear that $\Delta = 1$ necessarily separates the regimes of transport degradation and enhancement by dephasing. We now show that this is indeed the case.

In figure 8.8(a) the optimal dephasing rate $\gamma_{\rm opt}$ is shown for weak driving as a function of Δ. A threshold of $\Delta_0 \approx 1.07$ is apparent where for $\Delta < \Delta_0$, $\gamma_{\rm opt} = 0$, indicating dephasing-degraded transport, while for $\Delta > \Delta_0$, $\gamma_{\rm opt}$ is non-zero, indicating dephasing-enhanced transport, and increases monotonically with Δ. The latter behaviour is a consequence of the enhancement mechanism. As the interaction strength increases, so do the gaps between flattened and mobile bands, so a larger energy dissipation is required to populate the latter and increase the current. The

value of Δ_0 is size-dependent, and a scaling analysis shown in figure 8.8(b) demonstrates that, to good approximation, $\Delta_0 = 1$ separates the two transport regimes in the thermodynamic limit.

From the results discussed above it is tempting to associate the nature of the ground state, namely gapped or gapless, with a certain type of spin transport or response to dephasing in the NESS. This impression is misleading, as can be understood by considering a homogeneous magnetic field $B_j = B$. This field shifts the equilibrium quantum critical points [7], but leaves the spin transport of the steady state unaltered even in the presence of dephasing. As explained in Section 5.6, the latter occurs because the Hamiltonian and the current operator conserve the total magnetisation in z direction, so the various sectors of different spin number are only incoherently connected due to the driving. The internal structure of the spin sectors, unmodified by the homogeneous magnetic field as discussed in Section 2.5 (see figure 2.3), is thus what determines the steady-state transport through the chain, not the relative positions of the different sectors within the eigen-spectrum. This shows that a qualitative change of the ground state does not imply a change of non-equilibrium properties. Instead, it is the overall structure of the eigen-spectrum which leads to the NDC and dephasing-enhanced transport effects at strong interactions, as discussed in Sections 5.4 and 8.4.

8.5.2 Correlations and dephasing

Similar to equilibrium phases, the transition between the two different transport regimes, namely of current degradation and enhancement by dephasing, can be distinguished from the correlations through the system. First we consider a typical two-point correlation function

$$C_{ij} = \langle \sigma_i^z \sigma_j^z \rangle - \langle \sigma_i^z \rangle \langle \sigma_j^z \rangle, \tag{8.9}$$

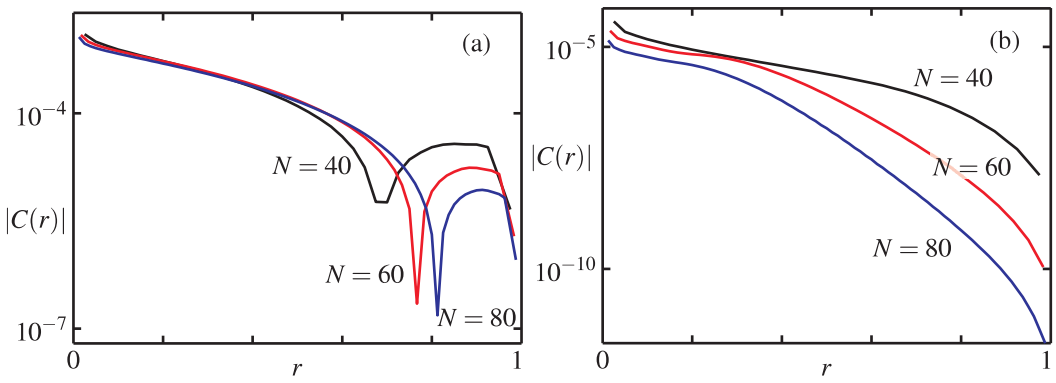

Figure 8.9. The NESS correlations $|C(r)|$ across the chain as a function of the fraction distance r about the centre for $\Delta = 2$ and $f = 0.1$. In (a) a moderate dephasing $\gamma = 0.05$ is included. The correlations are long-ranged and extend over a larger fraction when increasing N. This is evidenced by the kink, coming from $C(r)$ changing sign, moving to larger r. In (b) a strong dephasing $\gamma = 1$ is present and the correlations are short-ranged, as shown by their diminishing value and extent with increasing N.

with sites i and j symmetrically positioned around the centre of the chain. This is conveniently represented as $C(r)$ where $r = |i - j|/N$ is the fractional separation of the points for the system size N. In figure 8.9(a) $C(r)$ is plotted for different sizes N in the strongly interacting regime for a moderate dephasing rate. Finite correlations are seen to exist even for a large fractional separation r. Although these correlations decay with r, the fraction of the system they span increases with N. This property has been argued, for $\gamma = 0$ and $\Delta > 0.91$, to be evidence that the NESS possesses genuine long-range order even in the thermodynamic limit [192]. Here our results indicate that this long-range order persists even in the presence of moderate dephasing, and so correlations similar to those at $\gamma = 0$ exist in the dephasing enhanced NESS. The situation for strong dephasing, shown in figure 8.9(b), is markedly different. Now correlations are smaller and diminish faster with r than at weaker dephasing rates. In addition, the fraction of the system over which the correlations extend diminishes as N increases, a behaviour previously observed for large dephasing rates γ independently of the interaction strength Δ [181, 221]. So

like the current and magnetisation profiles, the two-point correlation functions in the strongly-interacting regime become increasingly similar to those of the weakly interacting regime for large dephasing, washing out the transition.

The signature of the non-equilibrium transition between weakly- and strongly-interacting regimes with moderate dephasing, already suggested by two-point correlation functions, can be refined by adopting a more general measure of correlations. Specifically we compute the entropy (4.12) [11, 31, 164]

$$S_{\mathrm{O}} = -\sum_{\alpha} s_{\alpha}^{2} \log_{2} s_{\alpha}^{2} \tag{8.10}$$

of the Schmidt coefficients s_α arising when the full NESS density operator ρ is factorised into two half-chains as

$$\rho = \sum_{\alpha} s_{\alpha} (O_{\alpha}^{\mathrm{A}} \otimes O_{\alpha}^{\mathrm{B}}), \tag{8.11}$$

where O_α^{A} and O_α^{B} are Hilbert-Schmidt orthogonal operators for the two halves. Both quantum and classical correlations between the two halves of the chain are quantified by S_{O} and it is readily accessible from the TEBD numerics, as described in Section 4.2.1. For zero dephasing and weak driving, figure 8.10 shows that S_{O} peaks at $\Delta \approx 1$. This indicates that a significant elevation in correlations occurs as the NESS reorganises itself across the expected non-equilibrium phase transition between ballistic and diffusive transport in this region.

In figure 8.10 we also show that for finite dephasing the entropy S_{O} monotonically decreases with γ, but interestingly the peak is maintained for moderate rates, shifting slightly to larger Δ. Therefore the abrupt on-set of dephasing enhancement shown in figure 8.8 occurs when the many-body correlations are strongest. This distinguishing feature in S_{O} is progressively washed out by increasing dephasing as the system

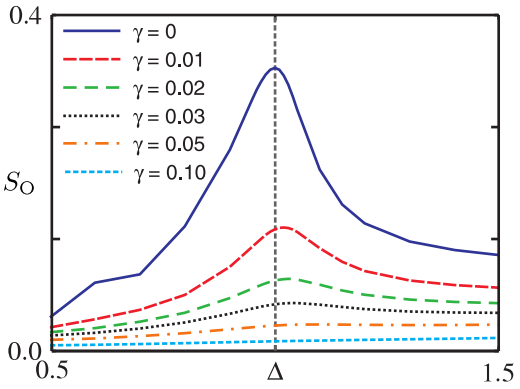

Figure 8.10. The half-chain entropy S_O as a function of Δ for different dephasing rates, $f = 0.1$ and $N = 40$. The Schmidt coefficients s_α are normalised so the largest coefficient is $s_1 = 1$.

becomes diffusive for all Δ [178, 181, 221]. Despite this, the response of the system to the dephasing processes is seen to offer an alternative and clear signature of the underlying non-equilibrium phase transition between two qualitatively different steady states.

8.5.3 Enhancement and integrability

The Hamiltonian (8.1) with $B_j = 0$ is integrable [6], so it could be considered that the dephasing enhancement observed in the present work is an artifact of this property. To show this is not the case, we obtain the NESS of the system when adding a staggered magnetic field $B_j = (-1)^j B$, which breaks the integrability. For $\gamma = 0$ this has the effect of turning the system into a diffusive conductor in the gapless regime $\Delta < 1$ for any driving, while not affecting the existence of NDC at large drivings for $\Delta > 1$ [21]. In figure 8.11(a) we see that for weak interactions, dephasing monotonically decreases the current, while for strong interactions we confirm, for a variety of field strengths B, that dephasing-enhanced transport occurs, as shown in figure 8.11(b). Thus the existence of NDC and dephasing enhancement,

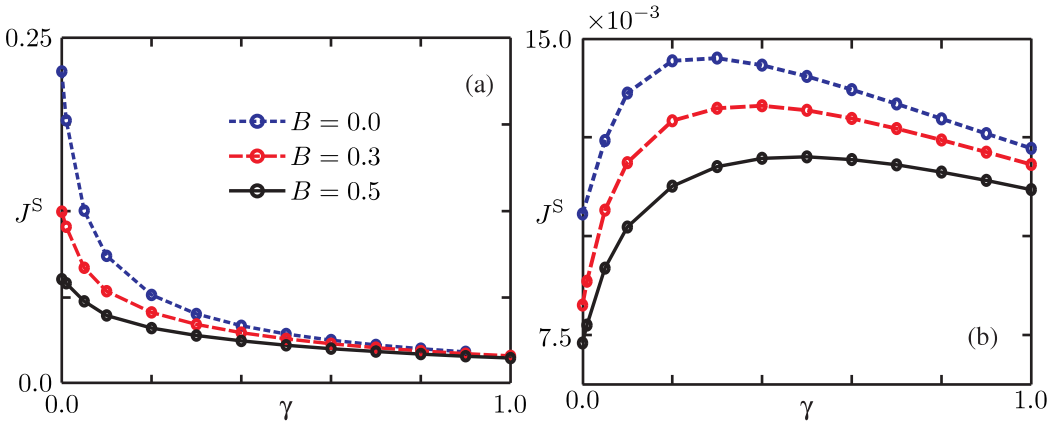

Figure 8.11. The current through the system for several staggered magnetic fields B, for $N = 40$, $f = 0.1$ and $\Gamma = 1$, with (a) $\Delta = 0.5$ and (b) $\Delta = 2.0$.

characterising the non-equilibrium phase transition between weakly- and strongly-interacting regimes, is independent of integrability. Both effects arise as long as the eigen-structure of the system possesses the features discussed in Sections 5.4 and 8.4, which for the case considered in this work is valid even if the integrability is broken, as shown in figure 2.3(b).

From the eigen-structure of the non-integrable system, the most notable features of the dephasing-enhanced transport can be understood. Namely, the increase of the optimal dephasing rate γ_{opt} with B results from the splitting of the energy bands due to the staggered potential, as shown in figure 2.3(b) (compare to figure 2.2(b)). Due to this band splitting and the emergence of new energy gaps, the states of wide bands of lowest energy become harder to populate, so a larger energy dissipation is required to induce transitions towards them, and thus to enhance the transport. In addition, note that the staggered magnetic field also flattens all the energy bands, reducing the conductivity through the chain.

8.6 Effects of dephasing on heat transport

After observing the impact of dephasing processes on the spin transport of the XXZ model, we turn our attention to heat transport. In particular, we study how the magnetothermal effect induced by the magnetic driving of equation (8.3) and a homogeneous magnetic field B, described in Section 5.6, is affected by energy dissipation processes. Thus we use here the same definitions of energy densities ($\varepsilon_{i,i+1}$, $h_{i,i+1}$, $b_{i,i+1}$) and currents (J^{H}, J^{B} and J^{XXZ}, in the bulk and the boundaries) of Section 5.6, and recall the picture of a total heat current consisting of counter-propagating flows from the boundaries.

The most important ingredient to include in this problem, compared to that of spin transport, is that the current of interest is no longer homogeneous across the system. Directly from the master equation we obtain that due to dephasing, equation (5.30) transforms into

$$\begin{aligned}\frac{d\langle\varepsilon_{i,i+1}\rangle}{dt} = i\langle[H,\varepsilon_{i,i+1}]\rangle + \mathrm{Tr}(\varepsilon_{1,2}\mathcal{L}^{\mathrm{L}}_{\mathrm{driv}}(\rho))\delta_{i,1} + \mathrm{Tr}(\varepsilon_{N-1,N}\mathcal{L}^{\mathrm{R}}_{\mathrm{driv}}(\rho))\delta_{i+1,N} \\ + \mathrm{Tr}(\varepsilon_{i,i+1}\mathcal{L}^{(i)}_{\mathrm{d}}(\rho)) + \mathrm{Tr}(\varepsilon_{i,i+1}\mathcal{L}^{(i+1)}_{\mathrm{d}}(\rho)) = 0.\end{aligned} \tag{8.12}$$

So we obtain that for any pair of neighbouring sites, the difference between their heat currents arises solely from the energy dissipation due to dephasing processes at those sites, since

$$\langle J^{\mathrm{H}}_{i+1}\rangle - \langle J^{\mathrm{H}}_{i}\rangle = \mathrm{Tr}(\varepsilon_{i,i+1}\mathcal{L}^{(i)}_{\mathrm{d}}(\rho)) + \mathrm{Tr}(\varepsilon_{i,i+1}\mathcal{L}^{(i+1)}_{\mathrm{d}}(\rho)) = -4\gamma\langle\sigma^x_i\sigma^x_{i+1} + \sigma^y_i\sigma^y_{i+1}\rangle. \tag{8.13}$$

Since the spin current J^{S} is homogeneous on the presence of dephasing, so is $\langle J^{\mathrm{B}}_i\rangle = J^{\mathrm{B}} = BJ^{\mathrm{S}}$. The spatial variation of the heat current arising from dephasing processes is then entirely contained within $\langle J^{\mathrm{XXZ}}_i\rangle$.

Now we study the heat transport in the presence of dephasing, first for weak

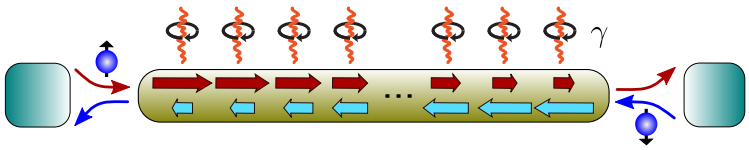

Figure 8.12. Effect of dephasing on the counter-propagating heat currents coming from each boundary. When reaching each site, the currents have been attenuated by a different amount of dephasing processes, so their local magnitudes are distinct.

interactions $\Delta < 1$, and then for strong interactions $\Delta > 1$.

8.6.1 Weakly interacting regime

Before analysing the effect of both dephasing and a homogeneous magnetic field in the heat transport properties, it is illustrative to study first the system with $B = 0$, where the local heat current is entirely given by $\langle J_i^{\mathrm{XXZ}} \rangle$ (since $J^{\mathrm{B}} = 0$). We consider the picture of two currents flowing in opposite directions, associated with spin excitations injected at each boundary, described in Section 5.6. Due to the energy dissipation, the currents do not cancel with each other. Instead, they reach each site of the system with unequal magnitudes, depending on the attenuation they have experienced due to dephasing processes along the different distances they have covered, as depicted in figure 8.12. As a result, the net current in the left half on the chain is positive, and in the right half is negative. This means that energy flows from the boundaries towards the center of the chain. In figure 8.13(a) we show the heat currents for $\Delta = 0.5$ and different dephasing rates, where the described behaviour is observed. The corresponding energy profiles are shown in the inset of figure 8.13(a), indicating that the center of the chain is the region of lowest energy. In addition, we note that the amplitude of the local currents monotonically decreases with γ, and that as γ increases, so does the amount of lost energy, as evidenced from the energy profiles.

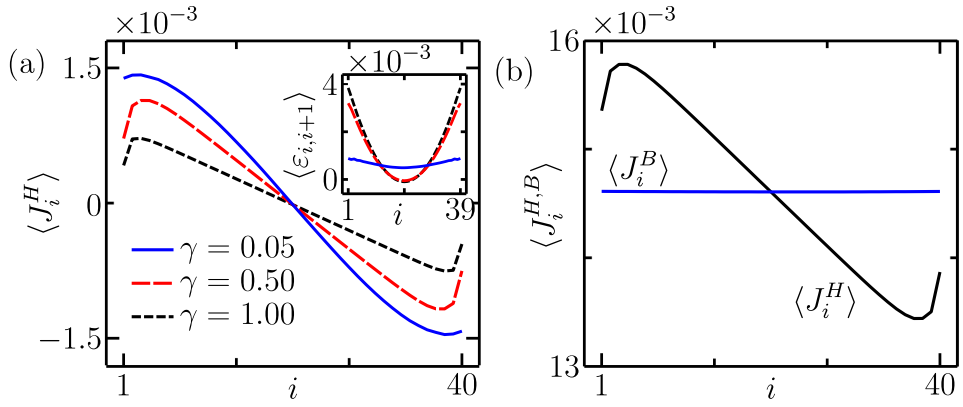

Figure 8.13. Effects of dephasing on the heat transport of the weakly-interacting regime. (a) Heat current profile for $B = 0$ and different dephasing rates. The conductivities for $\gamma = 1.00, 0.5$ and 0.05 are $\kappa_{\rm XXZ} = 1.997(12), 3.983(8)$ and $38(3)$, respectively. The uncertainties correspond to the standard deviation of the values of $\langle J_i^{\rm XXZ}\rangle/\nabla E_i^{\rm XXZ}$ obtained in the bulk of the chain. Inset: Corresponding energy profiles. (b) Heat current profile for $B = 1$ and $\gamma = 0.5$. Both panels correspond to $N = 40$, $\Delta = 0.5$, $f = 0.1$ and $\Gamma = 1$.

Importantly, the heat current of this configuration satisfies a local diffusion equation at each site i

$$\langle J_i^{\rm H}\rangle = \langle J_i^{\rm XXZ}\rangle = \kappa_{\rm XXZ}\nabla E_i^{\rm XXZ}, \quad \nabla E_i^{\rm XXZ} = \langle \varepsilon_{i,i+1}\rangle - \langle \varepsilon_{i-1,i}\rangle = \langle h_{i,i+1}\rangle - \langle h_{i-1,i}\rangle, \tag{8.14}$$

where $E_i^{\rm XXZ}$ denotes the local energy density corresponding to XXZ interactions. This is verified from our simulations, which indicate that the ratio $\langle J_i^{\rm XXZ}\rangle/\nabla E_i^{\rm XXZ}$ is indeed constant in the bulk of the system. Also the obtained conductivity is independent of the size of the chain, as expected for a diffusive conductor. For example, for the parameters of figure 8.13(a) and $\gamma = 1$, the conductivities obtained for $N = 40, 80$ and 100 are $\kappa_{\rm XXZ} = 1.997(12), 1.996(7)$ and $1.996(7)$, respectively. Therefore the net effect of dephasing is to induce diffusive heat transport from the boundaries to the center of the system.

Next we study the heat transport through the spin chain when $B > 0$ and $\gamma > 0$,

where both $\langle J_i^{\mathrm{XXZ}}\rangle$ and $\langle J_i^{\mathrm{B}}\rangle$ are non-zero. Recall the characteristic features of each component: $\langle J_i^{\mathrm{B}}\rangle = J^{\mathrm{B}}$ is homogeneous through the chain, it has the same properties as the spin current and is proportional to the magnetic field, while $\langle J_i^{\mathrm{XXZ}}\rangle$ is spatially dependent due to dephasing, and is field-independent. In figure 8.13(b) we show the profile of the total heat current $\langle J_i^{\mathrm{H}}\rangle = J^{\mathrm{B}} + \langle J_i^{\mathrm{XXZ}}\rangle$ for a particular set of system parameters. The profile is anti-symmetrically centered around J^{B}, and acquires its space dependence from $\langle J_i^{\mathrm{XXZ}}\rangle$. Near the boundaries, the dephasing processes give energy to the system due to the interplay with the driving, so $\langle J_i^{\mathrm{H}}\rangle < \langle J_{i+1}^{\mathrm{H}}\rangle$. Away from the boundaries, dephasing induces energy losses from the system, so $\langle J_i^{\mathrm{H}}\rangle > \langle J_{i+1}^{\mathrm{H}}\rangle$.

A fundamental point to note is that as stated in Section 8.3 and earlier studies [181, 221], dephasing induces a non-equilibrium quantum phase transition from ballistic ($\gamma = 0$) to diffusive ($\gamma > 0$) spin transport in the weakly-interacting regime. Therefore both the spin current J^{S} and the heat current J^{B} satisfy a diffusion equation for finite dephasing similar to equation (5.43), which reads

$$J^{\mathrm{B}} = BJ^{\mathrm{S}} = \kappa_{\mathrm{B}}\nabla E_i^{\mathrm{B}}, \qquad \nabla E_i^{\mathrm{B}} = \langle b_{i,i+1}\rangle - \langle b_{i-1,i}\rangle = B\nabla S, \tag{8.15}$$

with E_i^{B} denoting the local energy density associated with the magnetic field. Both J^{S} and J^{B} are determined by the magnetisation imbalance through the system, and have the same conductivity, $\kappa_{\mathrm{B}} = \kappa_{\mathrm{S}}$. As shown in figure 8.14 this agrees very well with our results.

The properties of J^{B} and $\langle J_i^{\mathrm{XXZ}}\rangle$ indicate that for finite dephasing rates and magnetic fields, the total heat current at any site i of the bulk is the sum of two diffusive contributions. Each one is determined by the gradient of a different component of the local energy density, and has a different conductivity (note the values

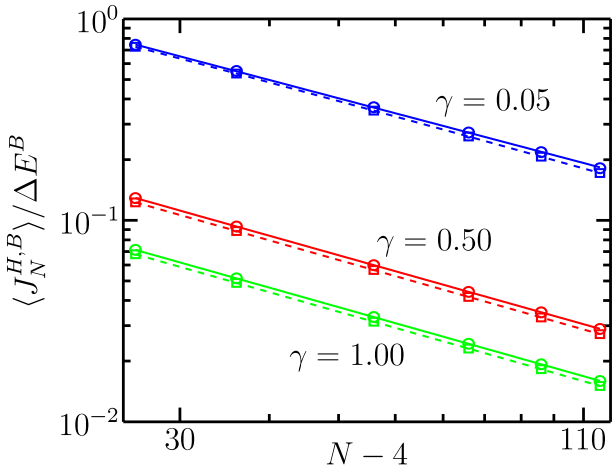

Figure 8.14. Total output heat current $\langle J_N^{\mathrm{H}}\rangle$ (□) and its contribution from the magnetic field J^{B} (○) as a function of N, for $B = 1$, $f = 0.1$, $\Gamma = 1$, $\Delta = 0.5$ and dephasing rates $\gamma = 0.05, 0.50, 1.00$. The dashed lines are guides to the eye for $\langle J_N^{\mathrm{H}}\rangle$, while the solid lines are fits of the results of J^{B} to the equation $J^{\mathrm{B}}/\Delta E^{\mathrm{B}} = \kappa_{\mathrm{B}}(N-4)^{-\alpha}$, with $\Delta E^{\mathrm{B}} = \langle b_{N-2,N-1}\rangle - \langle b_{2,3}\rangle$. For $\gamma = 0.05, 0.50, 1.00$, $\alpha = 0.94, 1.00, 1.00$ and $\kappa_{\mathrm{B}} = 15.85, 3.35, 1.86$, respectively. Note that the conductivity values differ from those of κ_{XXZ} (see figure 8.13).

of κ_{B} and κ_{XXZ} of figures 8.13 and 8.14). So we can write

$$\langle J_i^{\mathrm{H}}\rangle = J^{\mathrm{B}} + \langle J_i^{\mathrm{XXZ}}\rangle = \kappa_{\mathrm{B}}\nabla E_i^{\mathrm{B}} + \kappa_{\mathrm{XXZ}}\nabla E_i^{\mathrm{XXZ}}. \tag{8.16}$$

Our results indicate that the total heat current does not fulfill a diffusion equation, i.e., that an expression such as $\langle J_i^{\mathrm{H}}\rangle = \kappa_{\mathrm{H}}\nabla(E_i^{\mathrm{B}} + E_i^{\mathrm{XXZ}}) = \kappa_{\mathrm{H}}\nabla E_i^{\mathrm{H}}$, with E_i^{H} representing the total local energy density, is not valid[2]. Nevertheless, since it consists of the addition of two diffusive components, it is clear that the existence of dephasing processes changes the nature of the heat transport through the system for $\Delta < 1$. Therefore, similarly to spin transport, heat transport shows a dephasing-induced non-equilibrium phase transition between ballistic and diffusive behaviours in the weakly-interacting regime. Similar results has been reported recently in the

[2]This is seen by noting that the ratio $\langle J_i^{\mathrm{H}}\rangle/\nabla E_i^{\mathrm{H}}$ is not homogeneous through the bulk of the system, which results from having $\kappa_{\mathrm{B}} \neq \kappa_{\mathrm{XXZ}}$.

non-interacting case $\Delta = 0$, for a different driving scheme and smaller systems [137] and for an ion-trap quantum simulator [222].

Importantly, observe that for any combination of incoherent processes, interaction strength and system size, we can always find a magnetic field weak enough to cause $|\langle J_N^{\mathrm{XXZ}}\rangle| > J^{\mathrm{B}}$, and thus that $\langle J_N^{\mathrm{H}}\rangle < 0$. Since $\langle J_1^{\mathrm{H}}\rangle$ is always positive (both $J^{\mathrm{B}} > 0$ and $\langle J_1^{\mathrm{XXZ}}\rangle > 0$), this corresponds to a configuration in which the chain absorbs energy at both boundaries and dissipates it by dephasing processes. However, in the present work we mostly focus on cases where $\langle J_N^{\mathrm{H}}\rangle > 0$, in which the system delivers some energy to the right reservoir absorbed from the left reservoir. For such cases we observe the behaviour of the total output current $\langle J_N^{\mathrm{H}}\rangle$; this is shown in figure 8.14 as a function of the size of the system for different dephasing rates. Since J^{B} is largely dominant over $\langle J_N^{\mathrm{XXZ}}\rangle$ for the parameters of figure 8.14, the corresponding output heat current $\langle J_N^{\mathrm{H}}\rangle$ scales with N in a form very similar to J^{B}.

Finally, it has been observed that for $\Delta < 1$ the spin current decreases monotonically with the dephasing rate (see Refs. [181, 221] and Section 8.3). The same thus happens for J^{B}, as seen in figure 8.14. Since this is also the case for $\langle J_i^{\mathrm{XXZ}}\rangle$ (see figure 8.13), the total heat current $\langle J_i^{\mathrm{H}}\rangle$ decreases monotonically with γ at any site i of the chain. This shows that dephasing only degrades heat transport in the weakly-interacting regime.

8.6.2 Dephasing-enhanced heat transport

As described in Section 8.3, the spin current can be significantly enhanced by dephasing in the strongly-interacting regime. This result thus also applies to the field-dependent heat current component J^{B}. Now we consider whether a similar effect of environment assistance exists for the total heat current in the conventional

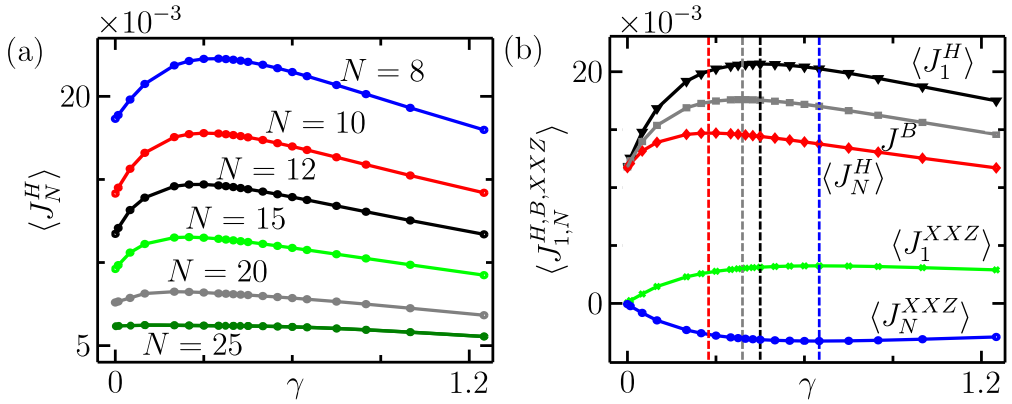

Figure 8.15. Dephasing-enhanced heat transport at weak driving, with $f = 0.1$, $\Gamma = 1$, $B = 1$ and $\Delta = 2.0$. (a). Heat current at site N as a function of γ, for several system sizes $N \leq 25$. (b). Heat currents at the boundaries and their field-dependent and independent contributions as a function of γ, for $N = 12$. Each vertical dashed line indicates the optimal dephasing rate $\gamma_{\rm opt}$ of the current plotted in the same color; $\gamma_{\rm opt} \approx 0.28, 0.39, 0.45, 0.65$ for $\langle J_N^{\rm H}\rangle, J^{\rm B}, \langle J_1^{\rm H}\rangle, \langle J_{1,N}^{\rm XXZ}\rangle$, respectively.

scenario of unidirectional transport (i.e. when there is a net energy flow from the left to the right boundary). For different values of N, the total output heat current $\langle J_N^{\rm H}\rangle$ is shown as a function of γ in figure 8.15(a). We find that for chains of small size and moderate dephasing rates, the output current can be considerably larger than that of the case $\gamma = 0$ (for example, when $N = 8$ the enhancement of the current is $\approx 19\%$), indicating environment-assisted total heat transport. For large dephasing rates, the effect is no longer visible due to the degradation of coherent dynamics by the frequent perturbation of the environment (Zeno effect) and the bulk energy dissipation.

The components of the heat current at both boundaries for $N = 12$ are shown in figure 8.15(b). We see that in contrast to the weakly-interacting regime (see figure 8.13(a)), the boundary currents $\langle J_{1,N}^{\rm XXZ}\rangle$ (and in general the currents $\langle J_i^{\rm XXZ}\rangle$ for all i) feature initial increase and subsequent decay with γ for strong interactions. So the two components of the total heat current show enhancement for moderate

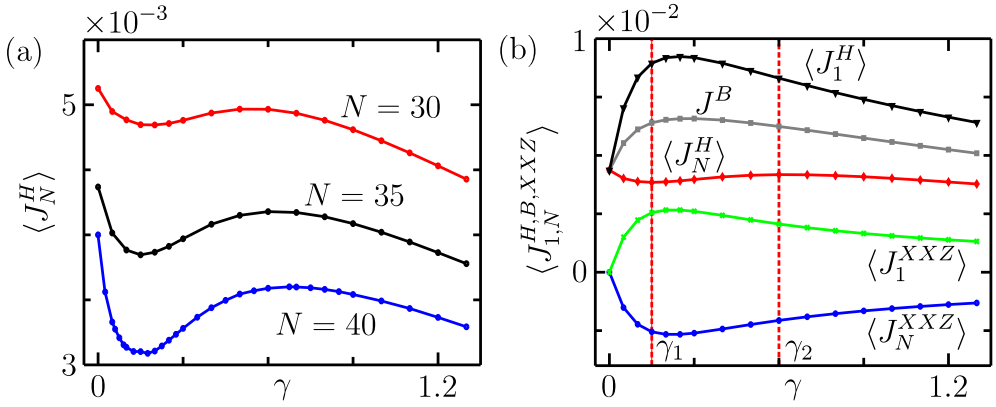

Figure 8.16. Multiple change of monotonicity of the heat transport as a function of the dephasing rate γ, with $f = 0.1$, $\Gamma = 1$, $B = 1$ and $\Delta = 2.0$. (a). Heat current at site N as a function of γ, for different system sizes $N \geq 30$. (b). Heat currents at the boundaries and their field-dependent and independent contributions as a function of γ, for $N = 35$. The vertical dashed lines correspond to the dephasing rates $\gamma_1 \approx 0.15$ and $\gamma_2 \approx 0.6$, which indicate the changes on monotonicity of $\langle J_N^{\mathrm{H}} \rangle$ for $N = 35$.

dephasing rates. Since both flow in opposite directions in the output, they compete with each other to determine the total energy delivered to the right reservoir. The corresponding optimal dephasing γ_{opt} and the rates of increase and degradation with γ are different for both; this leads to an intricate interplay between J^{B} and $\langle J_N^{\mathrm{XXZ}} \rangle$ to determine the total output heat current. As clearly seen in figure 8.15(b), dephasing-assisted heat transport compared to the dephasing-free case exists as long as J^{B} is the dominant contribution to the total current over $\langle J_N^{\mathrm{XXZ}} \rangle$, and as J^{B} features environment assistance itself.

Finally, note that in contrast to spin transport, where dephasing assistance compared to the case $\gamma = 0$ occurs for any system size, the heat transport only displays such an enhancement for small chains. For example, for the parameters used in figure 8.15, a chain with $N = 25$ already experiences enough energy dissipation in the bulk to induce a barely significant current enhancement (1.3%). Nevertheless, a different assistance effect emerges for larger systems, as shown in figure 8.16(a). For

small dephasing rates, the output heat current $\langle J_N^{\mathrm{H}} \rangle$ is initially degraded compared to the dephasing-free case. But from a rate γ_1, increasing γ leads to a significant current enhancement, until degradation is induced again after a rate γ_2 due to the Zeno effect. From figure 8.16(b) we can see why this multiple change of monotonicity, absent in the input current $\langle J_1^{\mathrm{H}} \rangle$, occurs on large chains. At small dephasing rates $\langle J_N^{\mathrm{XXZ}} \rangle$ is enhanced (negatively) faster than J^{B}, so the total current is initially degraded. At γ_1 the situation is inverted, leading to an increase of $\langle J_N^{\mathrm{H}} \rangle$ with γ. This tendency continues for moderate dephasing rates up to γ_2, even when both J^{B} and $\langle J_N^{\mathrm{XXZ}} \rangle$ are degraded by γ, since the latter decreases faster than the former. This shows that a beneficial role of dephasing for heat transport is also present in large systems.

8.7 Generality and possible realisations of dephasing assisted transport

The most important observation of the present Chapter is the increase of the conduction of spin and energy by dephasing in a very specific model, namely in a boundary-driven one-dimensional chain modeled by the spin-1/2 XXZ Hamiltonian. Nevertheless, only a few requirements are needed for the effect to arise. (i) Interactions strong enough to induce bound states of particles or excitations, so a gapped eigen-structure with bands of different widths is created. (ii) A mechanism to populate the slowest bands. (iii) A dissipative mechanism that induces transitions from slow to conducting bands. Given the basic nature of these requirements, we expect that the effect of transport enhancement is general enough to emerge in many other systems and configurations.

To begin with, in Section 8.5.3 we have observed that the dephasing enhancement

effect is not limited to integrable models. Additionally, it should not be restricted to magnetic systems, as expected from the equivalence of the one-dimensional XXZ Hamiltonian to an interacting model of spinless fermions (see Section 2.2) or of hard-core bosons (see Appendix A.1). We thus expect the effect to emerge in cases such as the Fermi-Hubbard or Bose-Hubbard model, whose experimental implementation is very well known in systems of cold atoms in optical lattices [34]. These systems also constitute ideal settings for the observation of particle bound states [36, 223]. Given the recent advances in developing driven configurations of cold-atom systems similar to that considered in our work [37–39, 143], they constitute the most prominent candidate for the experimental observation of the environment-enhanced transport we have described. We also note that realisations of dissipative spin chains with cold bosons in optical lattices have been recently proposed [224].

Furthermore, the effect should also be observed in alternative transport schemes, such as the expansion of a magnetisation wave packet through a spin chain [9, 10, 97] or of an initially-trapped cloud of cold atoms through an optical lattice. In the latter setup, standard in experiments with cold-atom systems [125, 156], an initially-prepared Mott insulator (of particle density $n \geq 2$) would expand very slowly through the lattice due to the repulsively bound pairs resulting from strong on-site interactions [223]. Such an expansion could be enhanced by breaking these bound states by the noise resulting from an underlying modulated lattice, as a recent numerical simulation suggests [157]. Other noise mechanisms such as heating, whose operational form is the same to that of the dephasing processes considered here [204], could induce the same effect.

Finally, the enhancement mechanism could also survive in the presence of weak static disorder [157]. The interplay between interactions, disorder and noise would, however, be quite intricate, since many competing effects (the environment-assisted transport described here, delocalisation [225] and subdiffusion [157] due to interac-

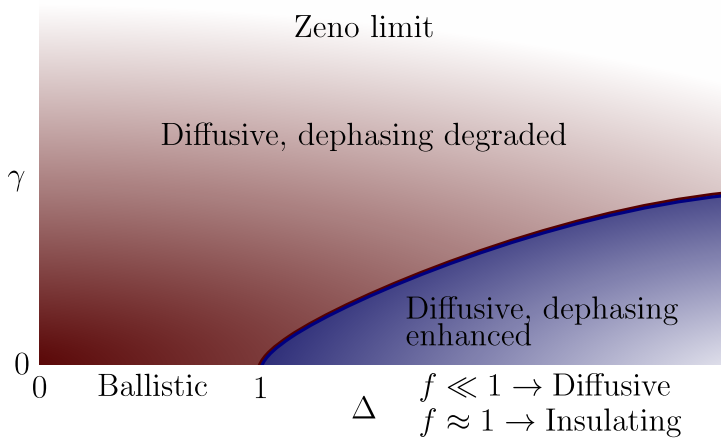

Figure 8.17. Schematic diagram of the spin and heat transport regimes in a magnetically-driven system; higher color intensities correspond to larger currents. In the absence of dephasing ($\gamma = 0$), the transport is ballistic for the weakly-interacting regime $\Delta < 1$, diffusive for the strongly-interacting regime $\Delta > 1$ and weak driving, and insulating for $\Delta > 1$ and strong driving. When dephasing is considered ($\gamma > 0$), the transport for weak interactions becomes diffusive, with the output currents decaying monotonically with γ; this corresponds to dephasing degraded transport. In contrast, for strong interactions, the transport is enhanced by moderate dephasing rates, up to an optimal rate which increases with Δ. This optimal rate establishes the boundary between enhancement and degradation (see figure 8.8(a)). Further increase of γ leads to current degradation, until reaching the Zeno limit, in which the z degrees of freedom are frozen and the dynamics of the system is weakly dependent on Δ.

tions, and breaking of localisation by noise [221, 226]) would act at the same time. Developing a comprehensive picture of such an interplay would correspond to an exciting area of future research.

8.8 Summary

In the present Chapter, we have studied the impact of dephasing processes on the spin and heat transport through a nonequilibrium one-dimensional quantum system described by the spin-1/2 XXZ Hamiltonian. Using the TEBD method to simulate the dynamics of the system established by its Lindblad master equation, we obtained

the NESS in the long-time limit and calculated spin and heat currents, magnetisation and energy profiles, and different measures of correlation.

Our main conclusions are displayed in the diagram 8.17 for both spin and heat transport. In the weakly-interacting regime $\Delta < 1$, dephasing induces a transition from ballistic ($\gamma = 0$) to diffusive ($\gamma > 0$) transport. Also, the currents are monotonically degraded by dephasing. On the other hand, in the strongly-interacting regime $\Delta > 1$, both spin and heat transport can be significantly enhanced by dephasing. For spin transport, this is most evident at maximal driving, where dephasing induces a transition from an insulating state with ferromagnetic domains to a diffusive state with linear magnetisation profile. But surprisingly, even at very weak driving dephasing can strongly enhance the spin transport for chains of any finite size. The mechanism responsible for this effect is the energy dissipation due to dephasing processes, which breaks bound states of spin excitations and induces transitions from flattened to wide bands of the eigen-structure of the system. Interestingly, in spite of such a dissipation, the transport of energy through the system can also be enhanced by dephasing, when the J^{B} component of the heat current dominates over the J^{XXZ} component.

For moderate dephasing rates, the different nature of the NESS at weak and strong interactions is revealed by the emergence of large correlations, and reflects an underlying non-equilibrium phase transition in the system. As such, dephasing enhancement is shown to be a true many-body phenomenon. Since the transport enhancement effect is also unrelated to integrability, and the conditions for its emergence are not limited to a specific model or transport scheme, we expect that our findings will also apply to many strongly correlated systems in addition to XXZ spin chains. Furthermore, given the recent advances in the study of particle and heat transport properties of ultracold atomic systems, the prospects of verifying experimentally the transport enhancement effect are promising [37–39].

Chapter 9

Transport enhancement from incoherent coupling between one-dimensional quantum conductors

In previous Chapters we have discussed how the interplay between coherent and incoherent processes leads to a rich variety of phenomena, for both single- and many-particle systems. Specifically, we have focused our attention on local dephasing and its impact on the transport properties of spin systems. In this scenario we have observed dephasing enhanced transport, arising due to a delicate balance between coherent and incoherent mechanisms. In real systems, however, other types of incoherent process take place, such as particle dissipation and noise due to correlated environments. In particular, as described in Section 7.2, several condensed matter systems such as cuprates [210–212] and some organic conductors [198, 206, 213–215] feature an interesting interplay between different transport mechanism along different directions. Namely, due to their asymmetric structure, they posses coherent particle transport along directions in which lattice sites have strong coupling, and incoherent hopping along directions of weakly-coupled sites. This is schematised in figure 7.4 for conjugated polymers and organic salts.

Motivated by the existence of this type of coherence-decoherence competition in real systems, we propose a concrete minimal model that features such a a competition, and study its transport properties in a form similar to that of previous Chapters. Specifically, we consider excitation transport through arrays of incoherently coupled one-dimensional quantum spin chains, including the possibility of strong interactions between excitations on the same chain. Using the TEBD method, we analyse the NESS that results when imposing a net spin current by means of a magnetisation imbalance across each lattice, generated by Markovian reservoirs. We find that the effective environment furnished by nearby chains significantly enhances intrachain transport for sufficiently strong interactions between excitations. In addition, such a transport enhancement increases with the size of the chains, indicating the relevance of the mechanism for bulk materials. We relate this phenomenon to the existence of superdiffusive spin transport. Importantly, the incoherent hopping of spin excitations between chains results in a much more pronounced effect than that produced by pure dephasing.

We emphasise that the simple model we consider does not account for several effects, e.g. dissipation and disorder, expected to be relevant for real systems such as organic conductors and cuprates. Nevertheless the results we present in this work are general and do not depend on the particular form of the interaction. Therefore we believe that they constitute a meaningful contribution towards the understanding of the rich phenomenology arising from the interplay between coherent and incoherent effects. The results of this Chapter have been published in reference [180].

9.1 Model of incoherently coupled spin chains

We start our study by considering a $N \times \Lambda$ rectangular two-dimensional (2D) lattice, consisting of Λ chains with N sites each (see figure 9.1). The model for coherent intrachain transport should describe conserved excitations that can hop between

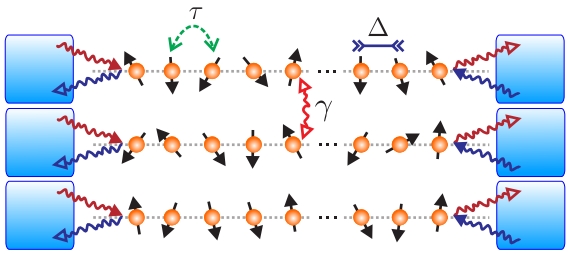

Figure 9.1. Scheme of a system of three incoherently coupled spin chains, with intrachain hopping τ, interaction strength Δ and interchain coupling γ. The blue arrows represent the right-to-left driving of the system, while the red arrows correspond to the left-to-right driving.

lattice sites and interact with each other. We therefore choose the simple spin-$\frac{1}{2}$ XXZ Hamiltonian to govern the dynamics of each chain

$$H^{(\lambda)} = \sum_{i=1}^{N-1} \tau(\sigma_i^{x(\lambda)}\sigma_{i+1}^{x(\lambda)} + \sigma_i^{y(\lambda)}\sigma_{i+1}^{y(\lambda)} + \Delta\sigma_i^{z(\lambda)}\sigma_{i+1}^{z(\lambda)}), \tag{9.1}$$

where the super-index (λ) refers to any operator of chain λ, $\sigma_i^{k(\lambda)}$ $(k = x, y, z)$ are Pauli matrices at lattice site i of chain λ, τ is the exchange coupling between nearest neighbours (in the following we take units of energy and time such that $\tau = 1$ and $\hbar = 1$), and Δ is the anisotropy, where both parameters are assumed to be the same for every chain. The total Hamiltonian of the system is then $H = \sum_{\lambda=1}^{\Lambda} H^{(\lambda)}$.

We assume that hopping also occurs between nearest-neighbour sites of neighbouring chains, with a hopping rate η. In addition, we suppose that the interchain coupling is much weaker than the coupling between sites on the same chain, so that $\eta \ll \tau$. Let t_ϕ denote the time taken for a spin excitation to lose its phase coherence, either from collisions with other spin excitations on the same chain or due to dephasing induced by an external bath, e.g. phonons. If $\eta \ll t_\phi^{-1}$, it is reasonable to neglect quantum correlations between sites of neighbouring chains, and treat the interchain coupling as a purely incoherent hopping process [206]. This is expected to be a good approximation for temperatures intermediate between the two hopping

energy scales, i.e. $\eta \ll k_B T \ll \tau$. This is easily satisfied in several systems. For example, $\eta \sim 100$K and $\tau \sim 1000$K for typical Bechgaard salts [227]. In general, this separation of energy scales can occur for a number of reasons. For example, the interchain distance may be much larger than the separation between sites on the same chain. Alternatively, the hopping in the interchain direction might be mediated by a scaffolding of different molecules in between [214], as in figure 7.4(b).

We describe the combination of coherent and incoherent dynamics by a quantum master equation of Lindblad form. The incoherent coupling between two spin chains is modeled by the jump operators

$$L_i^{(\lambda,\mu)} = \sqrt{\gamma}\sigma_i^{+(\mu)}\sigma_i^{-(\lambda)}\delta_{\lambda,\mu\pm1}, \tag{9.2}$$

representing the transfer of a spin excitation from site i of chain λ to site i of chain $\mu = \lambda \pm 1$, with rate γ. It has been previously argued [206, 228] that the incoherent hopping rate is of order $\gamma \sim \eta^2 t_\phi$. However, due to the large number of factors that can contribute to this hopping rate (e.g. temperature, collision rate, interchain distance etc.), the actual relation between η and γ is complicated [228]. We thus treat γ as a free parameter that can be varied independently.

To analyse the transport properties of this system, we drive it into a non-equilibrium configuration by coupling its boundaries to unequal reservoirs, as depicted in figure 9.1. We assume that the points of contact between the bath and any pair of neighbouring chains far apart from each other, leading to independent driving reservoirs for each chain. This driving scheme is thus similar to that used in Sections 5 and 8 for a single chain. The action of the reservoirs driving the system out of equilibrium is therefore represented by the following Lindblad operators

$$L_{\mathrm{L,R}}^{+(\lambda)} = \sqrt{\Gamma(1 \pm f)/2}\sigma_{1,N}^{+(\lambda)} \qquad L_{\mathrm{L,R}}^{-(\lambda)} = \sqrt{\Gamma(1 \mp f)/2}\sigma_{1,N}^{-(\lambda)}. \tag{9.3}$$

Here, Γ is the strength of the coupling to the reservoirs (we choose $\Gamma = 1$ in all our numerical calculations), and f is the driving parameter. Our simulations are performed with the weak driving $f = 0.1$, thus staying in the linear response regime.

Due to the finite temperature, we would also expect pure local dephasing processes to exist. However, in order to simplify the analysis, we will assume that apart from driving, the only effect of the environment is to generate incoherent hopping between chains. Importantly, we show in Section 9.3.2 that the large current enhancement induced by incoherent coupling cannot result solely from dephasing.

9.1.1 Mean-field approximation

Just like in previous Chapters, we are interested in analysing the transport properties of the system in the NESS. Nevertheless, computing the NESS for a strongly correlated two-dimensional system represents a formidable challenge, therefore an approximation scheme is necessary. In Appendix D we present an exact solution for two incoherently coupled chains in the non-interacting limit $\Delta = 0$, demonstrating that the NESS factorises as $\rho = \rho_1 \otimes \rho_2 + O(f^2)$. Since magnetisation and current expectation values are of order $O(f)$, the lowest order contribution to the NESS is sufficient to compute transport observables accurately. This observation motivates the following mean-field approximation (MFA), according to which the state of the entire system is a direct product of the states of each spin chain

$$\rho = \rho_1 \otimes \rho_2 \otimes \cdots \otimes \rho_\Lambda, \tag{9.4}$$

thus discarding the correlations between different chains. Using this mean-field ansatz, we can obtain the master equation for each chain separately after tracing out the state of the other chains.

The resulting MFA master equation for chain λ is

$$\frac{d\rho_\lambda}{dt} = -i[H^{(\lambda)}, \rho_\lambda] + \sum_{m=1}^{N} \tilde{\gamma}_m^{+(\lambda)} \left[\sigma_m^{+(\lambda)} \rho_\lambda \sigma_m^{-(\lambda)} - \frac{1}{2}\{\rho_\lambda, \sigma_m^{-(\lambda)}\sigma_m^{+(\lambda)}\} \right]$$

$$+ \tilde{\gamma}_m^{-(\lambda)} \left[\sigma_m^{-(\lambda)} \rho_s \sigma_m^{+(\lambda)} - \frac{1}{2}\{\rho_\lambda, \sigma_m^{+(\lambda)}\sigma_m^{-(\lambda)}\} \right]$$

$$\tilde{\gamma}_m^{+(\lambda)} = \frac{1}{2}\Gamma\Big[(1+f)\delta_{i,1} + (1-f)\delta_{i,N}\Big] + \frac{1}{2}\gamma[2 + \langle\sigma_m^{z(\lambda+1)}\rangle + \langle\sigma_m^{z(\lambda-1)}\rangle] := \tilde{\gamma}_m^{+\mathrm{d}(\lambda)} + \tilde{\gamma}_m^{+\mathrm{i}(\lambda)}$$

$$\tilde{\gamma}_m^{-(\lambda)} = \frac{1}{2}\Gamma\Big[(1-f)\delta_{i,1} + (1+f)\delta_{i,N}\Big] + \frac{1}{2}\gamma[2 - \langle\sigma_m^{z(\lambda+1)}\rangle - \langle\sigma_m^{z(\lambda-1)}\rangle] := \tilde{\gamma}_m^{-\mathrm{d}(\lambda)} + \tilde{\gamma}_m^{-\mathrm{i}(\lambda)},$$

where the superscripts d and i refer to driving and incoherent coupling terms, respectively. Within the MFA, the incoherent interchain coupling turns into local gain and loss processes at each chain, with rates depending on the magnetisation of the neighbouring chains. In this form, the density matrix of each chain can be evolved separately from the others by the simulation of its own master equation, with the coupling to neighbouring chains being effectively described by expectation values of local operators. This type of evolution can be performed efficiently by means of a parallel implementation [229] of the mixed-state Time Evolving Block Decimation (TEBD) algorithm. This implementation simply consists of running Λ simultaneous processes, each one for the simulation of the master equation of a single chain. At every time step, the magnetisation of each chain is calculated. Then it is communicated to the processes in which the simulations for neighbouring chains are running. With this information, the local gain and decay rates of each chain are then calculated, and the time step is performed. This process continues until the NESS is obtained.

In order to verify that the MFA gives reasonable results, we have also performed TEBD simulations of two coupled chains without the MFA for comparison. In figure 9.2 we plot the steady-state currents (defined in Section 9.1.3) obtained within each

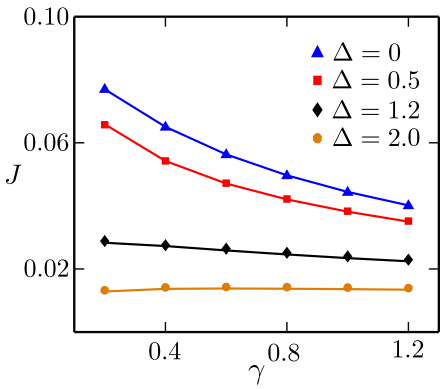

Figure 9.2. Comparison between currents for two chains obtained with and without the MFA. Mean-field current expectation values are shown as symbols, and expectation values obtained without the MFA are shown as lines.

approach for a pair of incoherently coupled chains of length $N = 20$. The two sets of results are clearly in close agreement, however the accuracy of MFA calculations is higher for smaller values of γ and Δ. The maximum error is 3.8%, when $\Delta = 2$ and $\gamma = 1.2$. We are therefore confident that the MFA gives accurate results for greater numbers of coupled chains, when quasi-exact TEBD simulations are not feasible.

9.1.2 Approximation for an infinite number of coupled chains

In the case of an infinite number of chains, the reduced density operators of all the chains are exactly the same at any time. So the problem of simulating the evolution of the entire system is reduced to that of performing the calculation for a single chain coupled twice with itself. The resulting Lindblad master equation of each chain, describing an effective non-linear self-consistent time evolution, is

$$\frac{d\rho}{dt} = -i[H,\rho] + \sum_{m=1}^{N}\left[\tilde{\gamma}_m^+\left(\sigma_m^+\rho\sigma_m^- - \frac{1}{2}\{\rho,\sigma_m^-\sigma_m^+\}\right) + \tilde{\gamma}_m^-\left(\sigma_m^-\rho\sigma_m^+ - \frac{1}{2}\{\rho,\sigma_m^+\sigma_m^-\}\right)\right], \tag{9.5}$$

where the index (λ) has been dropped for simplicity, and

$$\tilde{\gamma}_m^+ = \tilde{\gamma}_m^{+\mathrm{d}} + \gamma(1 + \langle\sigma_m^z\rangle) \qquad \tilde{\gamma}_m^- = \tilde{\gamma}_m^{-\mathrm{d}} + \gamma(1 - \langle\sigma_m^z\rangle) \tag{9.6}$$

are the effective gain and decay rates at site m.

9.1.3 Spin current

We now derive the expression for the spin current through the system. It is obtained from the local magnetisation rate of change, calculated from the master equation directly. For site i of chain λ, we have in the NESS

$$\left\langle \frac{d\sigma_i^{z(\lambda)}}{dt} \right\rangle = \mathrm{Tr}\left(\sigma_i^{z(\lambda)} \frac{d\rho_\lambda}{dt}\right) = \langle j_{i-1}^{(\lambda)}\rangle - \langle j_i^{(\lambda)}\rangle + \tilde{\gamma}_i^{+(\lambda)}(1 - \langle\sigma_i^{z(\lambda)}\rangle) - \tilde{\gamma}_i^{-(\lambda)}(1 + \langle\sigma_i^{z(\lambda)}\rangle) = 0, \tag{9.7}$$

where $j_i^{(\lambda)}$ is the longitudinal spin current through site i of chain λ,

$$j_i^{(\lambda)} = 2(\sigma_i^{x(\lambda)}\sigma_{i+1}^{y(\lambda)} - \sigma_i^{y(\lambda)}\sigma_{i+1}^{x(\lambda)}). \tag{9.8}$$

This expression is equivalent to that of the spin current through a 1D spin chain. Here, in contrast to that case, the longitudinal spin current is site-dependent in the NESS. For example, in the bulk of the system, $1 < i < N$, the difference of spin currents through nearest neighbours is

$$\langle j_i^{(\lambda)}\rangle - \langle j_{i-1}^{(\lambda)}\rangle = \gamma\big(\langle\sigma_i^{z(\lambda+1)}\rangle + \langle\sigma_i^{z(\lambda-1)}\rangle - 2\langle\sigma_i^{z(\lambda)}\rangle\big). \tag{9.9}$$

Now consider, for example, the left boundary $i = 1$. Since equation (9.8) is not defined for $i = 0$, in the NESS equation (9.7) gives

$$\langle j_1^{(\lambda)}\rangle = \gamma\big(\langle\sigma_1^{z(\lambda+1)}\rangle + \langle\sigma_1^{z(\lambda-1)}\rangle - 2\langle\sigma_1^{z(\lambda)}\rangle\big) + \Gamma f - \Gamma\langle\sigma_1^{z(\lambda)}\rangle. \tag{9.10}$$

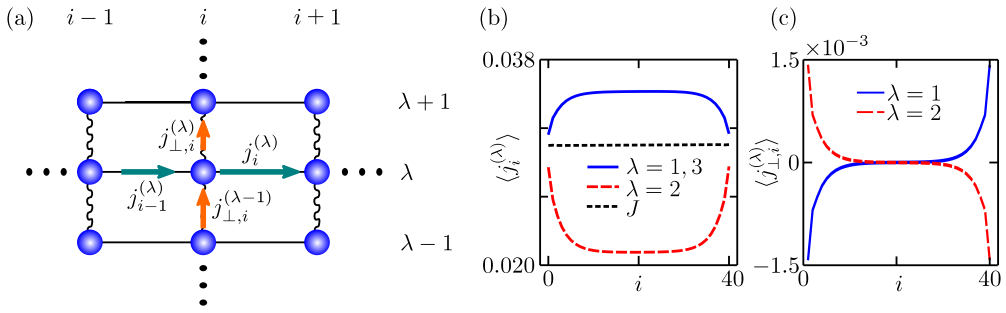

Figure 9.3. (a) Diagram of three incoherently coupled spin chains, showing the different currents flowing through site i of chain λ. The straight lines correspond to coherent coupling, while the wavy lines represent incoherent coupling. (b). Longitudinal spin current for each chain of the system, and spin current per chain $J = \langle J_i \rangle / \Lambda$, with $\Lambda = 3$, $N = 40$, $\Delta = 0.5$ and $\gamma = 0.5$. (c). Transversal spin currents for the same parameters.

A similar equation holds for the right boundary $i = N$. This leads to a natural definition of boundary currents $\langle j_0^{(\lambda)} \rangle$ and $\langle j_N^{(\lambda)} \rangle$, which allow equation (9.9) to be valid along the entire chain. These currents, which indicate the direct injection and ejection of spin excitations on the chain by the boundary reservoirs, are given by

$$\langle j_0^{(\lambda)} \rangle = \Gamma f - \Gamma \langle \sigma_1^{z(\lambda)} \rangle \qquad \langle j_N^{(\lambda)} \rangle = \Gamma f + \Gamma \langle \sigma_N^{z(\lambda)} \rangle. \tag{9.11}$$

We can associate the right hand side of equation (9.9) to the difference of spin flows between chain λ and its neighbouring chains, by defining a transversal spin current

$$\langle j_{\perp,i}^{(\lambda)} \rangle = -\gamma \big(\langle \sigma_i^{z(\lambda+1)} \rangle - \langle \sigma_i^{z(\lambda)} \rangle \big). \tag{9.12}$$

In this form, equation (9.9) can be rewritten as

$$\langle j_{i-1}^{(\lambda)} \rangle + \langle j_{\perp,i}^{(\lambda-1)} \rangle = \langle j_i^{(\lambda)} \rangle + \langle j_{\perp,i}^{(\lambda)} \rangle. \tag{9.13}$$

This balance between longitudinal and transversal spin currents is schematised in figure 9.3(a).

From equation (9.9) it follows that in the absence of incoherent coupling, the current through each chain is homogeneous in the NESS, $\langle j_i^{(\lambda)} \rangle = \text{const}$, $i = 0, \ldots, N$. In addition, from straightforward calculation, it is easily shown that in the presence of incoherent coupling, the total current per site $\langle J_i \rangle = \sum_{\lambda=1}^{\Lambda} \langle j_i^{(\lambda)} \rangle$ is homogeneous, i.e. that $\langle J_i \rangle - \langle J_{i-1} \rangle = 0$. Also note that due to the symmetry of the system considered, $\sum_{\lambda=1}^{\Lambda-1} \langle j_{\perp,i}^{(\lambda)} \rangle = 0$ for all sites i.

A concrete example of the longitudinal spin current profiles (equation (9.8)) for three chains is shown in figure 9.3(b), including the boundary currents defined in equation (9.11). Due to the symmetry of the incoherent coupling, the state and thus the currents of chains $\lambda = 1, 3$ are equal. The corresponding transversal spin currents, defined in equation (9.12), are shown in figure 9.3(c). When moving from the boundary sites $i = 1, N$ towards the centre of the system, the currents through chains $\lambda = 1, 3$ significantly increase at the expense of the current in the middle chain. This strong site dependence is reflected in large transversal currents, flowing in opposite directions. In the central sites of the system, the transversal currents are very small since the local magnetisations of neighbouring chains are very similar (see equation (9.12)). This is expected since the magnetisation of each chain must pass through zero at the same position in the centre due to the symmetric driving.

The NESS spin currents through the system, together with the magnetisation profile, determine the nature of the transport. If it is diffusive, the currents satisfy a diffusion equation:

$$\langle j_i^{(\lambda)} \rangle = -\kappa^{(\lambda)} \nabla \sigma_i^{z(\lambda)}, \tag{9.14}$$

where $\kappa^{(\lambda)}$ is the (N-independent) spin conductivity of chain λ and

$$\nabla \sigma_i^{z(\lambda)} = \langle \sigma_{i+1}^{z(\lambda)} \rangle - \langle \sigma_i^{z(\lambda)} \rangle \tag{9.15}$$

is the magnetisation difference between neighbouring spins of chain λ. On the other

hand, if the transport is ballistic $\kappa^{(\lambda)}$ diverges, resulting in a size-independent spin current. Note that since the transversal current of equation (9.12) is proportional to the local magnetisation difference along the transversal direction, it is diffusive by construction.

We now discuss the spin transport properties of the system in both the weakly ($\Delta < 1$) and strongly ($\Delta > 1$) interacting regimes, which show a completely different behaviour in the presence of incoherent interchain coupling. For this, instead of observing the spin current through each chain, we consider the total spin current *per chain*, noted by J, i.e., $J = \langle J_i \rangle / \Lambda$. Thus $J\Lambda$ is the total spin current per site in the NESS. We refer to J in the rest of the Chapter simply as the spin current; it is shown in figure 9.3(b) for a particular example. Its homogeneity along the system indicates that the NESS has been reached.

9.2 Transport in weakly interacting incoherently coupled spin chains

We initially consider the non-interacting case $\Delta = 0$. In Appendix D we obtain analytically the exact current and magnetisation expectation values. The former is given by

$$J = \frac{4f}{(\Gamma/4) + (4/\Gamma) + (N-1)\gamma/4}, \tag{9.16}$$

while the magnetisation profile is linear in the bulk, see equation (D.6). These results agree with TEBD simulations, as indicated in figure 9.4. If $\gamma = 0$, the current is independent of the size of the spin chains, indicating ballistic transport. On the other hand, a finite incoherent coupling induces a decay of the current with the length of the system $\propto N^{-1}$, typical of a diffusive conductor. In fact the bulk conductivities are easily shown to be $\kappa^{(1,2)} = 8/\gamma$. So, similarly to dephasing processes on a

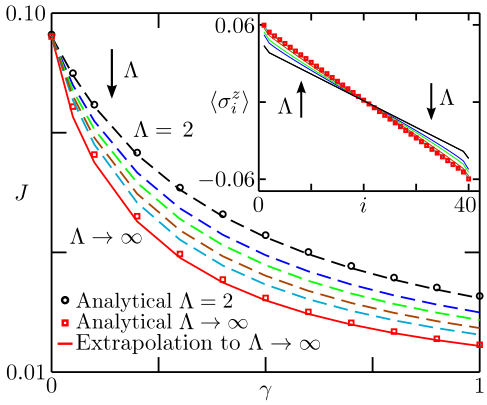

Figure 9.4. Spin current as a function of incoherent coupling γ for several numbers of non-interacting ($\Delta = 0$) chains of $N = 40$. The arrow indicates the decreasing tendency of the current as Λ increases. The dashed lines correspond to results of TEBD simulations ($\Lambda = 2, 3, 4, 6, 10$). The red solid line indicates an extrapolation of results of a finite number of chains (up to $\Lambda = 10$) to $\Lambda \to \infty$, using the simple rational function $J = (p_1\Lambda + p_2)/(\Lambda + p_3)$. The symbols indicate the analytical calculation for $\Lambda = 2$ ($\circ$) and $\Lambda \to \infty$ ($\square$). Inset: Magnetisation profile of a chain in the centre of the system ($\Lambda/2$ for Λ even, $(\Lambda + 1)/2$ for Λ odd) for $\gamma = 0.3$ and the same number of chains shown in the main panel. The solid lines correspond to the magnetisations obtained from TEBD results, and the symbols ($\square$) to the analytical approach for the self-coupled chain.

single non-interacting chain (see Section 8.2, equation (8.6)), incoherent interchain couplings induce a non-equilibrium phase transition between ballistic and diffusive regimes, with a spin current monotonically degraded by the interchain hopping.

In the limit of an infinite number of chains, described by the self-coupled chain (see Section 9.1.2), the analytical method used for two chains can also be applied (see Appendix D). We thus obtain exact expressions for the current and magnetisation, given by equations (9.16) and (D.6) respectively, with $\gamma/2$ instead of $\gamma/4$. The conductivity is thus $\kappa = 4/\gamma$, reduced compared to the case of $\Lambda = 2$. This is because each chain has two nearest neighbours rather than one, leading to a stronger degrading effect of the incoherent hopping.

In the intermediate case, i.e. for a finite number of chains $\Lambda > 2$, we use the TEBD method to obtain the NESS of the system. Characteristic results for the

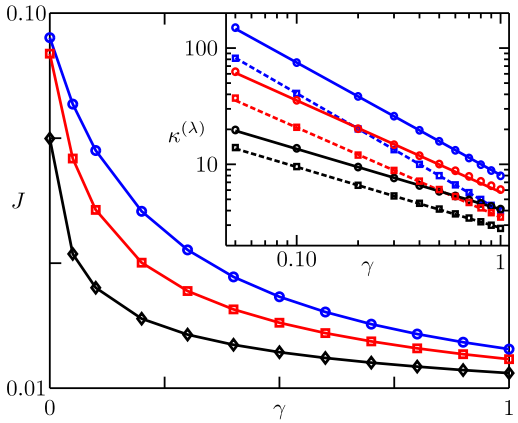

Figure 9.5. Spin current as a function of γ for $\Lambda = 10$, $N = 40$ and different interaction strengths $\Delta < 1$. The symbols correspond to TEBD results: blue ($\circ$) to $\Delta = 0$, red ($\square$) to $\Delta = 0.5$ and black ($\diamond$) to $\Delta = 0.9$; the solid lines are guides to the eye. The qualitative behaviour of the current, i.e. its monotonic decay with γ, is observed for any other value of Λ. Inset: Conductivities for $\lambda = 1$ ($\circ$, solid lines), indicating the behaviour at the boundary chains of the system, and of $\lambda = 2$ ($\square$, dashed lines), corresponding to the bulk. The symbols are TEBD results, and the lines are fits to the power law $\kappa^{(\lambda)} = \alpha_\lambda \gamma^{-\beta_\lambda}$. For $\Delta = 0$, $\beta_1 = 0.968(4)$ and $\beta_2 = 1.013(2)$. For $\Delta = 0.5$, $\beta_1 = 0.79(2)$ and $\beta_2 = 0.77(2)$. For $\Delta = 0.9$, $\beta_{1,2} = 0.52(1)$. The colors correspond to the same interaction strengths Δ of the main panel.

current and for the magnetisation profiles are shown in figure 9.4. The same qualitative features of the cases $\Lambda = 2$ and $\Lambda \to \infty$ are found, namely the spin current monotonically decreases with γ and the magnetisation profile is almost linear in the bulk. In addition, for a fixed incoherent coupling, the current decreases with the number of chains, rapidly for small values of Λ and very slowly for large values. An extrapolation of these results to the limit $\Lambda \to \infty$ agrees with the analytical approach for the self-coupled chain, as shown in figure 9.4.

Similarly to the cases of two and an infinite number of chains, the transport response induced by incoherent coupling on a system of several chains is characteristic of diffusive conductors. To see this explicitly, we observe that each chain satisfies the local diffusion equation (9.14). Since the spin current through each chain is site-dependent, we have verified that the ratio $\langle j_i^{(\lambda)} \rangle / \nabla \sigma_i^{z(\lambda)}$ (i.e. the conductivity) is

homogeneous for each λ, so the diffusion equation (9.14) holds. In addition, similarly to the analytically-solvable cases, the conductivity of each chain decays monotonically with the incoherent coupling rate, with a behaviour very well described by a decay $\kappa^{(\lambda)} \propto 1/\gamma$, as shown in figure 9.5. We also note that for $2 < \lambda < \Lambda - 1$ the conductivity is almost indistinguishable from that of $\lambda = 2, \Lambda - 1$, due to the weak effect of the boundary chains.

Now we consider weak interactions $0 < \Delta < 1$. We find that the effect of incoherent interchain coupling on the system is very similar to that on non-interacting chains. Namely a finite incoherent coupling induces a transition from ballistic ($\gamma = 0$) to diffusive ($\gamma > 0$) behaviour. The magnetisation profiles become linear, and the spin current and the conductivities of each chain decrease monotonically with γ, the latter following a power law as shown in figure 9.5. The current also decreases with Λ, approaching a limiting value when $\Lambda \to \infty$. In figure 9.5 it is also seen that for fixed values of Λ and γ, the spin transport diminishes as Δ increases, a known result for single chains in the gapless regime [9, 221].

9.3 Transport enhancement for strong intrachain coupling

We now consider the effect of incoherent interchain coupling on the transport properties of strongly interacting spin chains ($\Delta > 1$).

9.3.1 Environment assisted transport

Due to the strong correlations between spin excitations, the regime $\Delta > 1$ presents a completely different response to environmental effects to the case of weak interactions $\Delta < 1$. As described in Chapter 8 for single 1D chains, dephasing processes

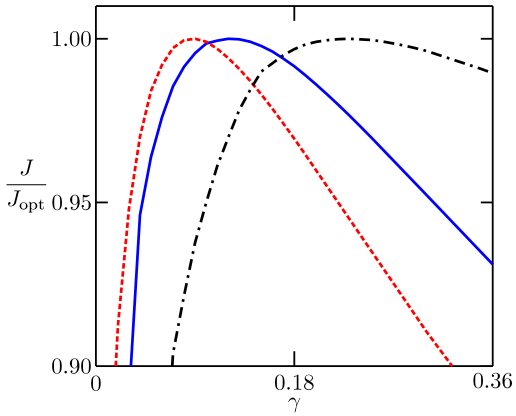

Figure 9.6. Spin transport enhancement in the strongly interacting regime due to incoherent interchain hopping. For clarity we plot the rescaled spin current J/J_{opt} as a function of γ. The solid blue line corresponds to $\Delta = 1.2$, $\Lambda = 3$ and $N = 40$. The other lines indicate the effect on the spin current when some parameters of the system are modified, i.e. when the number of chains increases (dashed red line, $\Delta = 1.2$ and $\Lambda = 10$), and when the interaction is stronger (dot-dashed black line, $\Delta = 2$ and $\Lambda = 3$). When $\gamma = 0$, $J = 4.25 \times 10^{-3}$ for $\Delta = 2$, and $J = 1.19 \times 10^{-2}$ for $\Delta = 1.2$. The corresponding optimal currents are $J_{\text{opt}} = 8.0 \times 10^{-3}$ and $J_{\text{opt}} = 1.65 \times 10^{-2}$ respectively.

can lead to a surprisingly large enhancement of the current even at weak driving. Now we show that the ability of excitations to jump incoherently across different chains leads to an even larger transport enhancement, which constitutes the main result of the present Chapter.

As shown in figure 9.6, the presence of incoherent interchain coupling increases the spin current through the system, compared to that of $\gamma = 0$, for a wide range of rates γ. The optimal coupling maximising the current γ_{opt}, which is obtained by fitting the peak to a polynomial function, strongly depends on the interaction strength, increasing with Δ. Similarly, the current enhancement grows with Δ. For example, the current increases by up to 39% for $\Delta = 1.2$ and up to 91% for $\Delta = 2$.

We now consider the effect of the system size on the transport enhancement. The optimal current J_{opt} remains almost constant for all values of Λ considered. In ad-

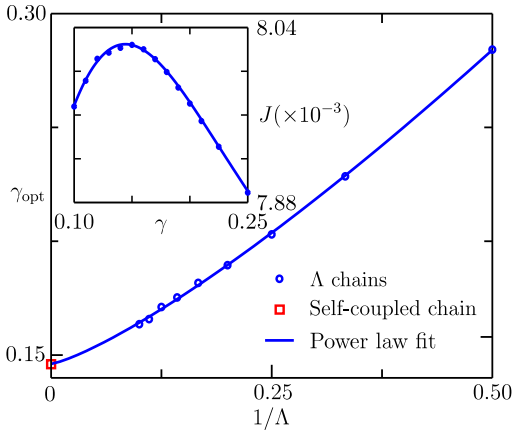

Figure 9.7. Optimal incoherent coupling as a function of the number of coupled chains Λ, for $N = 40$ and $\Delta = 2$ ($\circ$), and the optimal coupling for a self-coupled chain ($\square$). The power law fit $\gamma_{\rm opt} = a\Lambda^{-b} + \gamma_{\rm opt}^{\infty}$ is shown (solid line), which results in an optimal coupling at $\Lambda \to \infty$ of $\gamma_{\rm opt}^{\infty} = 0.146(5)$; $a = 0.33(1)$, $b = 1.3(1)$. Inset: simulations of the self-coupled chain provide an alternative method for finding the optimal coupling in the limit $\Lambda \to \infty$. Fitting the results of the simulations around the peak ($\circ$) to a polynomial function (solid line), we find the maximum current at $\gamma_{\rm opt}^{\infty} = 0.144$, consistent with the scaling analysis.

dition, the optimal coupling monotonically decreases with Λ as shown in figure 9.7, and the range of beneficial couplings narrows. Importantly, a power-law extrapolation to $\Lambda \to \infty$ strongly suggest the existence of a finite optimal incoherent coupling $\gamma_{\rm opt}^{\infty}$ in this limit. We have confirmed this result from simulations of a self-coupled chain with $\Delta = 2$, as shown in the inset of figure 9.7. The results of both approaches agree very well, giving optimal couplings of $\gamma_{\rm opt}^{\infty} = 0.146$ for the extrapolation and $\gamma_{\rm opt} = 0.144$ for the self-coupled chain. Because of this agreement, we henceforth denote by $\gamma_{\rm opt}^{\infty}$ the optimal coupling for the self-coupled chain.

Note that a simple argument qualitatively explains the decay of $\gamma_{\rm opt}$ with Λ. Consider first the case $\Lambda = 2$. Since each chain is only affected by just a single neighbouring chain, it is expected that $\gamma_{\rm opt}(\Lambda = 2) \sim 2\gamma_{\rm opt}^{\infty}$, as seen in figure 9.7. For $\Lambda = 3$, the boundary chains are coupled to a single neighbour, so their transport is optimised by $\gamma \sim 2\gamma_{\rm opt}^{\infty}$. The central chain, being coupled to two neighbours, is

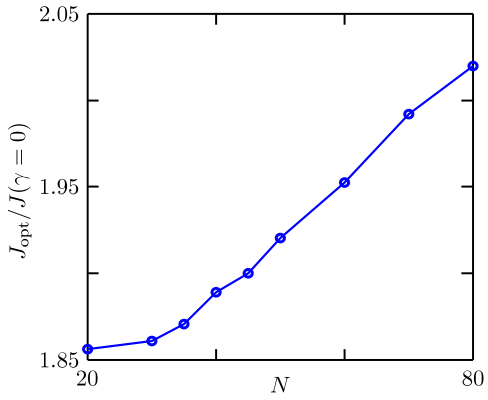

Figure 9.8. Spin current enhancement factor $J_{\rm opt}/J(\gamma=0)$ as a function of the length of the system for a self-coupled chain with $\Delta=2$ ($\circ$). The solid line is a guide to the eye.

optimised by $\gamma\sim\gamma_{\rm opt}^{\infty}$. Assuming that an average incoherent coupling optimises the transport of the entire system, we get $\gamma_{\rm opt}(\Lambda=3)\sim 5\gamma_{\rm opt}^{\infty}/3$. In general, for Λ chains, we expect

$$\gamma_{\rm opt}(\Lambda)\sim\frac{(\Lambda-2)\gamma_{\rm opt}^{\infty}+4\gamma_{\rm opt}^{\infty}}{\Lambda}=\frac{2\gamma_{\rm opt}^{\infty}}{\Lambda}+\gamma_{\rm opt}^{\infty}. \tag{9.17}$$

This simple scaling provides a good approximation to that found from the power law fit of the results of a finite number of chains, as indicated in figure 9.7.

Importantly, we observe that the enhancement effect becomes stronger as the size of the system increases. This is shown in figure 9.8 for a self-coupled chain, where the enhancement factor $J_{\rm opt}/J(\gamma=0)$ is seen to increase with N. We therefore expect that spin transport can be significantly enhanced by environmental processes even in macroscopic (anisotropic) two-dimensional systems, and thus can be observed experimentally in bulk materials.

Note that the tendency of $J_{\rm opt}/J(\gamma=0)$ with N here is entirely different to that of transport enhancement by dephasing, shown in figure 8.6(b), where the enhancement factor slowly decays and saturates with the system size. This already suggests that the transport enhancement mechanism by incoherent interchain coupling is a

much stronger effect than that of dephasing.

To understand the origin of the increase of the enhancement ratio with N, it is important to study the nature of the spin transport in the enhancement regime. To address this point we analyse the scaling with N of the spin current through a strongly interacting self-coupled chain. The results are shown in figure 9.9. In the presence of diffusive spin transport, the magnetisation profile of the chain is linear in the bulk. The local magnetisation difference is thus homogeneous, and defined as

$$\nabla\sigma_i^z = \frac{\Delta\sigma^z}{N-5} \quad \text{with} \quad \Delta\sigma^z = \langle\sigma_{N-2}^z\rangle - \langle\sigma_3^z\rangle, \tag{9.18}$$

where $N-5$ corresponds to removing two sites from either end to diminish boundary effects. Diffusive spin transport is evidenced if the system satisfies the diffusion equation

$$\frac{J}{\Delta\sigma^z} = -\frac{\kappa}{(N-5)^\alpha}, \tag{9.19}$$

with κ the spin conductivity and $\alpha = 1$. As shown in figure 9.9 for weak incoherent coupling, the results of our TEBD simulations are well described by this equation, but with $\alpha < 1$. This means that in the regime of transport enhancement, the system presents a spin current which decreases with N slower than normal diffusion, i.e. it shows superdiffusive behaviour. Thus the optimal current also shows a slower decrease than that of a diffusive conductor. Since for the diffusive regime $J(\gamma = 0) \propto N^{-1}$, a divergence of the enhancement ratio with N is found.

Finally, as shown in the upper inset of figure 9.9, the exponent α gets closer to 1 when increasing γ, the transport thus tending towards being described by normal diffusion when the incoherent effects become stronger. When γ is too large the enhancement effect disappears, since the system is perturbed so frequently that it is prevented from evolving, i.e. the Zeno effect emerges.

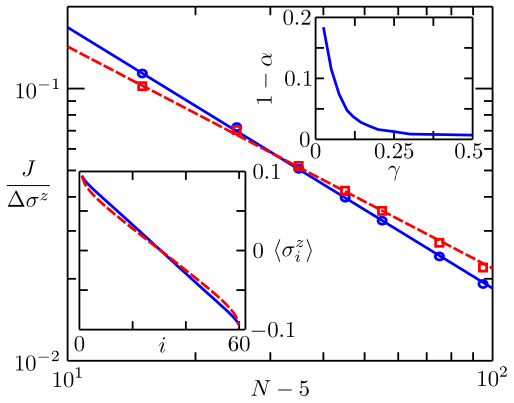

Figure 9.9. Scaling of $J/\Delta\sigma^z$ of the self-coupled chain, for $\Delta = 2$, $\gamma = 0.05$ (□) and $\gamma = 0.20$ (○). The results of the simulations fit very well to equation (9.19), giving $\kappa = 0.93(6)$ and $\alpha = 0.81(2)$ for $\gamma = 0.05$ (dashed red line), and $\kappa = 1.53(3)$ and $\alpha = 0.959(6)$ for $\gamma = 0.20$ (solid blue line). Lower inset: Corresponding magnetisation profiles of $N = 60$. Upper inset: $1 - \alpha$ as a function of γ.

9.3.2 Enhancement mechanism

We now discuss the origin of the transport enhancement in the strongly interacting regime, which is similar to that found in single chains due to dephasing processes (see Chapter 8). Recall that as explained in Section 2.5 and Appendix A, for interaction strengths $\Delta > 1$ the spectrum of the XXZ Hamiltonian (9.1) consists of several bands whose energetic separation is proportional to Δ. The highest bands are almost flat, possessing very low conductivity. These bands correspond to bound states of spin excitations, where several spins are clumped together, thus having large potential energy. When the system is driven out of equilibrium, population is transferred to bands of both high and low energy, even in the weak-driving regime as considered here. If energy-dissipating processes take place in the system, spin bound states of highly energetic bands break into states of lower potential (and total) energy, but of much higher kinetic energy, thus increasing the conductivity.

The enhancement described in our work emerges from the energy dissipation induced by the incoherent interchain coupling. To clarify this point, consider for sim-

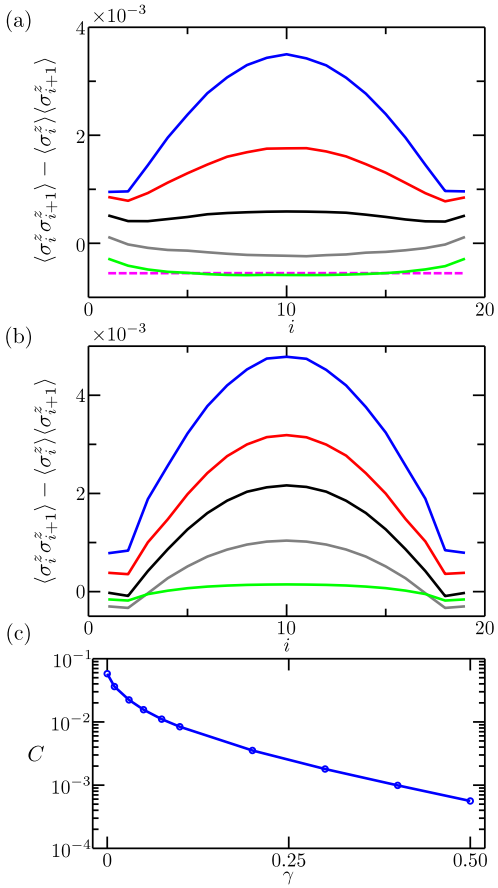

Figure 9.10. Nearest-neighbour connected correlation function for different parameters of the self-coupled chain of $N = 20$. (a) For $\gamma = 0$ and several interaction strengths Δ. From bottom to top, the solid lines correspond to $\Delta = 0.8, 1.0, 1.05, 1.1, 1.2$. The dashed line refers to $\Delta = 0$. (b) For $\Delta = 1.4$ and several incoherent coupling rates γ. From top to bottom, the lines correspond to $\gamma = 0, 0.01, 0.03, 0.1, 0.5$. (c) Sum of the nearest-neighbour correlation functions C as a function of γ for $\Delta = 1.4$.

plicity the self-coupled chain configuration described by equation (9.5)[1]. A straightforward calculation of the energy dissipation rate corresponding to the incoherent

[1]The calculation of the rate of energy dissipation is also easily performed for a finite number of chains. In this case, we obtain a sum over λ of terms like those of equation (9.20), but instead of the magnetisation at site $i + 1$ of each chain, the magnetisations of the neighbouring chains at site $i + 1$ appear. Nevertheless, since the magnetisations of all chains are similar, equation (9.20) corresponds to a good approximation.

coupling gives

$$\mathrm{Tr}(H\mathcal{L}_{\mathrm{inc}}(\rho)) = -2\gamma \sum_{j=1}^{N-1} \langle \sigma_i^x \sigma_{i+1}^x + \sigma_i^y \sigma_{i+1}^y \rangle - 4\gamma\Delta \sum_{j=1}^{N-1} (\langle \sigma_i^z \sigma_{i+1}^z \rangle - \langle \sigma_i^z \rangle \langle \sigma_{i+1}^z \rangle), \quad (9.20)$$

where $\mathcal{L}_{\mathrm{inc}}(\rho)$ is the dissipator describing the incoherent coupling. The first term in the energy dissipation rate appears due to the loss of phase coherence between neighbouring sites (see equation (8.8)), and is proportional to the hopping energy

$$K = \sum_{i=1}^{N-1} \langle \sigma_i^x \sigma_{i+1}^x + \sigma_i^y \sigma_{i+1}^y \rangle.$$

The second term is proportional to the sum of nearest-neighbour connected spin-spin correlations

$$C = \sum_{i=1}^{N-1} (\langle \sigma_i^z \sigma_{i+1}^z \rangle - \langle \sigma_i^z \rangle \langle \sigma_{i+1}^z \rangle),$$

and corresponds to a direct dissipation of the interaction energy due to the incoherent hopping, which rips spin excitations away from their nearest neighbours[2].

Intuitively, if C is positive, the spin excitations of the system are bunched together on average, while if $C < 0$ the excitations are spread out. Therefore, the sign of C gives a simple indication of how population is distributed between the bound states (bunched) and mobile states (spread out). In the absence of incoherent coupling, we have found that C undergoes a marked transition from taking negative to positive values as the interaction strength crosses the critical point $\Delta = 1$ (see figure 9.10(a)). This behaviour is a manifestation of the well known non-equilibrium phase transition from ballistic to diffusive conduction at $\Delta = 1$, and demonstrates a tendency of the spin excitations to clump together in the strongly interacting regime

[2]As observed during the derivation of equation (9.20), the terms $\langle \sigma_i^z \sigma_{i+1}^z \rangle$ are a direct consequence of the non-conserving nature of the jump operators (i.e. they result from any incoherent process described by jump operators σ^+ or σ^-). In addition, the terms $\langle \sigma_i^z \rangle \langle \sigma_{i+1}^z \rangle$ appear because the effective rates $\tilde{\gamma}_m^+$ and $\tilde{\gamma}_m^-$ are different (see equation (9.6)).

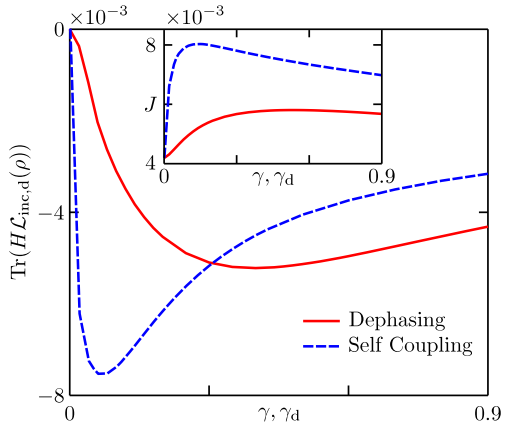

Figure 9.11. Comparison of the rate of energy dissipation due to bulk dephasing processes (equation (9.21)), and incoherent self coupling (equation (9.20)). Both cases correspond to $\Delta = 2$ and $N = 40$. For these parameters, the current for a single isolated chain is $J \approx 4.2 \times 10^{-3}$. Inset: Corresponding spin currents.

of the driven system. Importantly, even when the incoherent coupling is incorporated, our simulations always show that $C > 0$ when $\Delta > 1$ (see figures 9.10(b),(c)). More precisely, C diminishes with γ, indicating the decrease of population in bound (correlated) states with incoherent processes, but remains positive. Similarly, we always found that $K > 0$ in the strongly interacting regime. This indicates that energy is being dissipated from the system due to the incoherent interchain hopping (see equation (9.20)), transferring population from bound to mobile states and thus leading to transport enhancement.

It is important to note that the transport enhancement induced by incoherent interchain coupling is much larger than that of pure dephasing processes described by equation (8.4), with dephasing rate $2\gamma_d$. For example, as shown in figure 9.11 for $\Delta = 2$, the spin current is increased up to 37% by dephasing[3], and up to 91% by incoherent coupling. This difference can be explained by looking at the energy

[3]Note that here γ_d is defined to be twice that of Chapter 8, so the energy dissipation due to the phase-breaking effect of incoherent coupling of equation (9.20) has exactly the same form as that of dephasing, in equation (9.21).

dissipation rate due to dephasing,

$$\mathrm{Tr}(H\mathcal{L}_{\mathrm{d}}(\rho)) = -2\gamma_{\mathrm{d}} \sum_{j=1}^{N-1} \langle \sigma_i^x \sigma_{i+1}^x + \sigma_i^y \sigma_{i+1}^y \rangle, \tag{9.21}$$

with $\mathcal{L}_{\mathrm{d}}(\rho)$ the dephasing dissipator. This rate is compared to the dissipation rate from incoherent coupling in figure 9.11. Since its maximal magnitude is significantly smaller than that of incoherent coupling, more energy is dissipated by the latter, resulting in more population transfer from flat to mobile energy bands and thus to a larger current. This also shows that for $\Delta \neq 0$, the effects of incoherent coupling cannot be reproduced just by dephasing processes.

9.4 Summary

We have studied the spin transport in an anisotropic 2D spin$-\frac{1}{2}$ lattice driven out of equilibrium by Markovian boundary reservoirs. The assumption of highly anisotropic coupling allowed us to consider the system as an array of incoherently coupled chains. Each chain is described by an XXZ Hamiltonian, which contains the basic elements that constitute many-body lattice systems, namely particle hopping and interactions. Employing a mean-field approximation, we calculated the spin current and magnetisation of the NESS of the system for several parameters. This approximation, found to reproduce the transport properties of two coupled chains, facilitates an accurate and efficient dynamical simulation of the system using a parallel implementation of the TEBD algorithm [174].

We found that in the presence of weak intrachain interactions, the incoherent coupling monotonically degrades the spin conductivity of the chains. However, in the strongly interacting regime we found a significant transport enhancement due to the incoherent coupling. This enhancement can be understood as the result of incoherent

transitions from bound states to mobile bands of energy eigenstates, similar to the effect of dephasing on spin and energy transport in 1D systems. However, the direct breakdown of bound states by the incoherent hopping between neighbouring chains, which opens more paths for spin excitations to flow, provides a greater improvement than dephasing effects alone.

A self-consistent extension of the mean-field approximation enabled us to perform simulations directly in the limit of an infinite number of chains. In this configuration, we found that the enhancement of the spin current increases with the size of the system, which reveals the importance that the enhancement effect can have in bulk materials. The origin of this scaling was related to the existence of superdiffusive transport in the regime of current enhancement, becoming closer to normal diffusion as the incoherent coupling increases.

Finally, we note that the effects described in our work have so far not been found experimentally. Real materials such as organic conductors and cuprates involve more complicated effects than those considered here, which may obstruct a direct observation of the enhancement and degradation mechanisms we have described. In particular, in the absence of interactions, we expect that incoherent interchain hopping destroys disorder-induced localisation. However, when interactions are added to the picture, it is not clear how the two transport enhancement effects would combine. A model incorporating disordered site energies alongside interactions and incoherent hopping would be amenable to a numerical study using the methods described in this work. This constitutes an interesting topic for future research. Alternatively, quantum simulators such as ultracold atom systems are intrinsically free of disorder. Moreover, several experimental [37, 38, 143] and theoretical [222] advances aimed at simulating quantum transport in such systems have recently been made. This offers the prospect of observing the effects described in this work and studying them in the laboratory using current or near-future technology.

Chapter 10

Conclusions and future prospects

10.1 Summary of results

In the present thesis we have studied the non-equilibrium properties of the one-dimensional spin-1/2 XXZ Hamiltonian, driven by unequal boundary reservoirs. The steady-state response of the system to this transport scheme, described by a Lindblad master equation, has been efficiently obtained using time evolving block decimation. Our research has allowed us to identify novel phenomena regarding the conduction of magnetisation and energy, and to unravel a new mechanism of environment-enhanced transport in the strongly-interacting regime of the model.

Specifically, we have started by studying the spin transport of chains driven by a magnetic imbalance between the boundaries. We reproduced the transport regimes observed in previous research, namely ballistic transport for weak interactions, diffusive transport for strong interactions and weak driving, negative differential conductivity for larger driving and an insulating state for maximal driving. We have provided an argument to explain the origin of the insulating state, which relies on the existence of a dark state of ferromagnetic domains which is preferentially populated by the driving. This effect is shown to be a true many-body phenomenon. Then we observed that energy transport can be induced with the same driving scheme

in the presence of a homogeneous magnetic field, thus corresponding to a Peltier effect. Due to the symmetries of the driving, the energy current is proportional to the spin current. Although this result contrasts with the expected picture of ballistic energy transport for any interaction strength, we emphasise that it emerges from the particular form in which the energy current is induced.

Subsequently we have discussed the response of the system to thermal driving, inducing a different type of energy transport. In agreement to previous research, we have observed ballistic energy conduction for both weak and strong interactions if the Hamiltonian is integrable. On the other hand, the transport becomes diffusive when the integrability of the system is broken (by a staggered magnetic field). Interestingly, we have found that in the latter case the reduced density operators of two neighbouring spins are well approximated by local thermal states, plus corrections to account for the energy current across the system. In contrast, local temperatures cannot be associated to the integrable case. This corresponds to a first extension of the correspondence between absence of integrability and thermalisation to a non-equilibrium configuration.

Then we have analysed the impact of environmental coupling on the transport properties of the XXZ spin chain, motivated by recent findings of quantum effects assisted by incoherent processes. A key difference to previous studies is that we consider a linear, ordered many-body configuration. First we observe the impact of pure dephasing processes on the spin transport properties of the chain driven by a magnetic imbalance. In the weakly-interacting regime, spin transport is degraded by dephasing. On the other hand, a significant transport enhancement occurs for strong interactions at moderate dephasing rates. This effect does not seem surprising at large driving, where dephasing breaks the ferromagnetic domains that made the system an insulator. In contrast, the enhancement effect at weak driving is unexpected, given that in such a regime the system is already a diffusive conductor.

The phenomenon is seen to emerge due to energy dissipation processes which break slow bound states of spin excitations into scattering states of larger mobility. It is also seen to exist for very large systems, and to be a true many-body phenomenon. The isotropic point of the model is found to separate the degraded and enhanced transport responses, also being the point of maximal correlations even for weak dephasing. We also observed that energy transport can be enhanced by dephasing, in spite of the energy dissipation which makes it non-homogeneous across the chain.

Finally we have studied the effect of a different type of incoherent coupling. Motivated by the structure of several condensed matter systems, we have considered a configuration consisting of various one-dimensional XXZ spin chains, incoherently coupled with each other. The simulations have been performed by a mean-field approximation, which for two chains was observed to reproduce the transport properties correctly. Similarly to dephasing, the incoherent interchain coupling induces a spin transport enhancement in the strongly-interacting regime. This enhancement effect, however, is significantly larger than that of dephasing, owing to the extra energy dissipation arising from explicitly separating neighbouring spin excitations. The effect is seen to persist as the number of chains increases, tending to a limit well described by a self-coupled chain. In addition, in contrast to dephasing, incoherent interchain coupling induces an assisted-transport effect that increases with the size of the system, which relates to spin superdiffusive conduction.

Throughout the thesis we have argued that the described phenomena are general. Since the XXZ Hamiltonian contains the simplest competition between hopping and particle interactions, various of the effects we have discussed should be present in more complicated and realistic models. Also, since the XXZ Hamiltonian can be mapped to fermionic and bosonic models, the effects are not restricted to magnetic systems. In fact, systems of cold atoms in optical lattices constitute ideal scenarios to observe experimentally the physics described in the thesis, given their controllability,

single-site resolution, and the recent implementation of boundary-driven transport schemes.

10.2 Future prospects

We finalise by describing some interesting possibilities of future research.

10.2.1 Interplay of decoherence, interactions and disorder

Most of the research discussed in previous chapters was focused on the impact of the competition between interactions and decoherence on the transport properties of quantum systems. This picture is still quite idealised due to the absence of disorder, which is a very important component of several condensed-matter systems. It has been well established that in non-interacting systems, any amount of on-site disorder leads to an insulating state, a phenomenon known as Anderson localisation [230]. It is also well known that dephasing effects break Anderson localisation, and thus enhance transport [42,221,226]. In contrast, the interplay between disorder and interactions is not completely understood. While it is generally accepted that localisation is broken by weak interactions [225], which induce a delocalised state with subdifussive transport [157], the competition between strong interactions and disorder still needs to be studied. An interesting question to study is whether in the presence of self-trapping effects due to strong interactions, weak disorder can actually lead to a transport enhancement effect.

Our study has provided insight on the interplay between interactions and decoherence effects. A more complete picture should also include disorder. In fact, very few studies including interactions, decoherence and disorder have been performed so far. One of the most complete is that of reference [157], briefly described in Chapters 7 and 8. In this study, a cooperation between weak interactions and noise

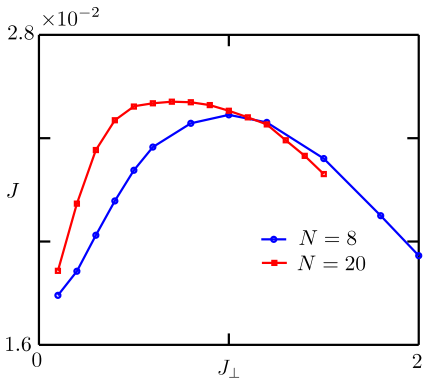

Figure 10.1. Spin transport enhancement in two coherently-coupled spin chains. For clarity, the data of $N = 20$ has been scaled by the factor 2.2. The parameters of the simulations are $\Delta = 2$, $\Delta_\perp = 0$ and $f = 0.1$.

is seen to break Anderson localisation, leading to subdiffusive transport. This study also hinted at the existence of noise-assisted transport with strong interactions in the presence of disorder. We believe that the mechanism explained in Chapter 8 partially accounts for this observation.

Some questions on the total interplay between the three effects remain open. For example, the generality of the cooperation between weak interactions and noise can be inspected with different driving schemes and types of particles. It would also be interesting to understand the interplay between the two noise-assisted transport effects, namely the breaking of Anderson localisation and of bound states at strong interactions. The solution to these problems is demanding, but feasible due to the high efficiency of tensor network algorithms. Alternatively, the direct simulation in systems of ultracold atoms could be performed with the transport scheme of references [37, 38], which has been used to study disordered systems [143].

10.2.2 Enhanced transport by coherent interchain coupling

As mentioned in Section 2.7, several materials are well described by a ladder structure, i.e. they correspond to coherently-coupled spin chains. The starting point to

study several of these materials is a system of Λ XXZ spin chains, with interchain coupling described by the Hamiltonian

$$H_{\perp} = \sum_{i=1}^{N} J_{\perp}(\sigma_i^{x(1)}\sigma_{i+1}^{x(2)} + \sigma_i^{y(1)}\sigma_{i+1}^{y(2)} + \Delta_{\perp}\sigma_{i+1}^{z(1)}\sigma_i^{z(2)}), \tag{10.1}$$

where $J_{\perp}$ and $\Delta_{\perp}$ are the hopping and spin interaction strength, respectively. There are important open questions regarding the physics of this model, so it constitutes a vast area of intense research (see reviews in [231, 232]).

A major difficulty to analyse these systems is that the local dimension of each effective site grows as 2^{Λ}, so numerical simulations of their transport properties without mean-field approximations become very demanding. Recent studies, however, have used the same driving scheme of Chapter 9 to study the spin conduction of $\Lambda = 2$ chains in the non-interacting regime $\Delta = 0$. A first expected result corresponds to the emergence of diffusive transport due to the coherent interchain coupling, given that it breaks the integrability of the model [134,135]. A more interesting result shows that even in the absence of integrability, some subspaces support ballistic transport [134]. Nevertheless, a study of the impact of coherent interchain coupling as a function of the interaction strength Δ is yet to be performed.

Some preliminary results for this case are shown in figure 10.1. Interestingly, a significant transport enhancement compared to the single-chain case is found, similarly to the case of incoherent coupling. To the best of our knowledge, the possibility of increasing the conduction of an ordered quantum system by coherently extending its dimensionality has not been reported before. Thus we believe that such an effect definitely deserves a deep analysis. Ultracold atoms in optical lattices again constitute an ideal setting to test the generality of this effect [125, 126].

Appendix A

Eigenstructure of the XXZ model for very strong interactions

In the present Appendix we analyse perturbatively the energy bands of the integrable XXZ model, in the limit of very strong interactions. Very similar results have been published in an independent recent research [233]. The Hamiltonian is

$$H = \sum_{j=1}^{N-1} \tau(\sigma_j^x \sigma_{j+1}^x + \sigma_j^y \sigma_{j+1}^y + \Delta \sigma_j^z \sigma_{j+1}^z). \tag{A.1}$$

In the following, we consider $\Delta \gg 1$. To perform the calculation in a clear form, we transform the Hamiltonian to its equivalent version for hard-core bosons.

A.1 Mapping to hard-core bosons

To go to the hard-core bosons representation, we perform the transformation

$$a_j = \sigma_j^-, \qquad a_j^\dagger = \sigma_j^+, \qquad n_j = a_j^\dagger a_j = \frac{1}{2}(1 + \sigma_j^z). \tag{A.2}$$

Here, a_j ($a_j^\dagger$) annihilates (creates) a hard-core boson at site j, and n_j is the corresponding number operator. These operators satisfy $[a_j, a_k^\dagger] = (1 - 2n_j)\delta_{jk}$ and

$\{a_j, a_j^\dagger\} = I_j$, with I_j the identity operator at site j. So in general, these operators do not satisfy usual commutation relations. Instead they commute at different sites of the chain, and anticommute at the same site. It is clear from the definition that $0 \leq \langle n_j \rangle \leq 1$, so at most one boson can occupy each site (thus the name "hard-core"). We represent a hard-core boson at site j by $|1\rangle_j$, while the empty site corresponds to $|0\rangle_j$. Introducing the new operators into the Hamiltonian (A.1), and defining $t = -2\tau$ and $V = 4\tau\Delta$, we get

$$H = \frac{V}{4}(N-1) - t\sum_{j=1}^{N-1}(a_j^\dagger a_{j+1} + a_{j+1}^\dagger a_j) + V\sum_{j=1}^{N-1} n_j n_{j+1} - \frac{V}{2}\sum_{j=1}^{N-1}(n_i + n_{i+1}). \quad \text{(A.3)}$$

This Hamiltonian consists of several terms. The first term is the energy of the system for zero or N excitations. The second term accounts for the nearest-neighbour hopping of bosons. The third stands for a nearest-neighbour density-density interaction. The final term corresponds to on-site energies, which are different for the boundary sites and the rest:

$$\frac{V}{2}\sum_{j=1}^{N-1}(n_i + n_{i+1}) = \frac{V}{2}n_1 + V\sum_{j=2}^{N-1} n_j + \frac{V}{2}n_N. \quad \text{(A.4)}$$

As seen in the following Sections, this difference of on-site energies is very important to account for some of the details of the eigenspectrum of the model.

A.2 Energies of the XXZ model

Now we examine the eigenstates and corresponding bands of the Hamiltonian (A.3) for a small number of bosons $N_{\mathrm{T}} = \sum_{j=1}^{N}\langle n_j \rangle$ in the lattice. Due to the particle-hole symmetry of the model, states of a few number of holes in a filled lattice have the same energy. Nevertheless we focus on describing the former states.

A.2.1 Highest lying state

The simplest state to consider is that of the $N_{\mathrm{T}} = 0$ sector, namely $|00\cdots0\rangle$. As shown in figure A.1, this is the highest lying state, with energy $E^{(0)} = \frac{V}{4}(N-1)$. Due to the particle-hole symmetry, the state of N excitations $|11\cdots1\rangle$ also has energy $E^{(0)}$. This is clearly seen since both the density-density interaction and the on-site terms give energies of magnitude $V(N-1)$, which cancel with each other. These states are referred to as type (a), as shown in figure A.1(a).

A.2.2 Energies for one excitation

Consider initially the case $N_{\mathrm{T}} = 1$ and $t = 0$. Then, from a direct inspection of the Hamiltonian (A.3), and using that all the density-density interaction terms vanish, it is seen that two totally degenerated (thus non-conducting) single-particle bands appear, as shown in figure A.1(a). These correspond to the following types of states.

(b) Two states of energy $E = E^{(0)} - V/2$, for the excitation being localised at one of the edges of the chain, i.e. $|00\cdots01\rangle$ and $|10\cdots00\rangle$.

(c) $N-2$ states of energy $E = E^{(0)} - V$, for the excitation localised somewhere else in the chain, i.e. of the form $|0\cdots010\cdots0\rangle$.

Turning weak hopping processes on shifts the energy of the first band and breaks the degeneracy of the second, as shown in the right panel of figure A.1. We can calculate these corrections using degenerate perturbation theory. To proceed, we note by $H^{(j)}_{B_j}$ the correction Hamiltonian of band B_j of $N_{\mathrm{T}} = j$ particles. If states $|p\rangle$ and $|q\rangle$ belong to band B_j of j particles, the first-order correction Hamiltonian element is $\langle p|H^{(j)}_{B_j}|q\rangle = \langle p|H_t|q\rangle$, with $H_t = -t\sum_{j=1}^{N-1}(b_j^\dagger b_{j+1} + b_{j+1}^\dagger b_j)$ the hopping Hamiltonian. The second-order correction Hamiltonian element is

$$\langle p|H^{(j)}_{B_j}|q\rangle = \sum_{m\in B_j'} \frac{\langle p|H_t|m\rangle\langle m|H_t|q\rangle}{E_p - E_m}, \tag{A.5}$$

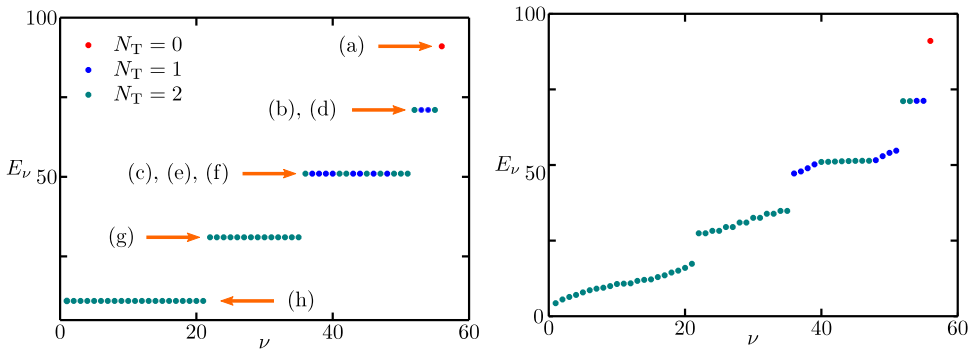

Figure A.1. Energies for zero, one and two excitations in the strongly-interacting regime, for $N = 10$, $V = 40$, $t = 0$ (left) and $t = -2$ (right). Here, and in the following figures, ν corresponds to the index of the eigenvalues of all the sectors considered. Note that in the main text, we denote the eigenvalue index of each separated band as k.

where B'_j refers to the bands of particle sector N_T different to B_j, and $|m\rangle$ to their states that connect $|p\rangle$ and $|q\rangle$ by two subsequent applications of H_t.

Consider first the band (b). Since the only two states of this band are far away from each other, and H_t does not lead a state to itself, there are no first-order corrections. For the second-order corrections, only the diagonal cases $|p\rangle = |q\rangle$ contribute. For $|p\rangle = |10\cdots00\rangle$, the single state $|m\rangle$ is $|m\rangle = |010\cdots0\rangle$, so $E_p - E_m = V/2$; similarly for $|p\rangle = |00\cdots01\rangle$. So the second-order correction Hamiltonian for the first band of $N_T = 1$ is

$$H^{(1)}_{(b)} = \frac{2t^2}{V}\begin{pmatrix} 1 & 0 \\ 0 & 1 \end{pmatrix}. \tag{A.6}$$

The corrected energies of band (b) are thus

$$E_{(b)} = E^{(0)} - \frac{V}{2} + \frac{2t^2}{V}. \tag{A.7}$$

For band (c), the dominant corrections are of first order, since states of this band are connected by a single application of H_t. The first-order correction Hamiltonian

is simply given by the tridiagonal $(N-2)\times(N-2)$ matrix

$$H^{(1)}_{(c)} = -t\begin{pmatrix} 0 & 1 & 0 & \cdots & 0 & 0 \\ 1 & 0 & 1 & \cdots & 0 & 0 \\ 0 & 1 & 0 & \cdots & 0 & 0 \\ \vdots & \vdots & \vdots & \ddots & \vdots & \vdots \\ 0 & 0 & 0 & \cdots & 0 & 1 \\ 0 & 0 & 0 & \cdots & 1 & 0 \end{pmatrix}. \tag{A.8}$$

The eigenvalues of this matrix are known [234], and lead to the following corrections:

$$E_{(c)}(k) = E^{(0)} - V - 2t\cos\left(\frac{k\pi}{N-1}\right), \quad k = 1,\ldots,N-2. \tag{A.9}$$

The band thus gets a cosine form of width $2t$, as a function of the quasi-momentum $k\pi/(N-1)$, appreciated in the right panel of figure A.1. Second-order corrections can also be calculated, but we will only show the leading correction order.

A.2.3 Energies for two excitations

First we identify the states of the $N_{\mathrm{T}} = 2$ sector when $t = 0$. The degenerated bands are shown in the left panel of figure A.1, and correspond to

(d) Two states of energy $E = E^{(0)} - V/2$, corresponding to the excitations being localised at one of the edges of the chain, i.e. $|00\cdots011\rangle$ and $|110\cdots00\rangle$.

(e) $N-3$ states of energy $E = E^{(0)} - V$, corresponding to the excitations next to each other, but none of them at the edges, i.e. of the form $|0\cdots0110\cdots0\rangle$.

(f) One state of energy $E = E^{(0)} - V$, with each excitation at a different edge, i.e. $|10\cdots01\rangle$.

(g) $2(N-3)$ states of energy $E = E^{(0)} - 3V/2$, corresponding to separated excitations, and only one of them at one edge of the chain, such as $|10\cdots010\cdots0\rangle$.

(h) $(N-3)(N-4)/2$ states of energy $E = E^{(0)} - 2V$, for separated excitations,

with none of them at the edges, i.e. of the form $|0\cdots1\cdots1\cdots0\rangle$.

We then turn the hopping on, and proceed as before; the resulting bands are shown in the right panel of figure A.1. For band (d), take $|p\rangle = |q\rangle = |110\cdots00\rangle$ as an example. Second-order corrections are needed, for which $|m\rangle = |1010\cdots00\rangle$ is the only intermediate state possible. So we get that $E_p - E_m = V$; similarly for $|p\rangle = |q\rangle = |00\cdots011\rangle$. The second-order correction Hamiltonian $H^{(2)}_{(d)}$ has two diagonal elements t^2/V, so the corrected energies for both states are

$$E_{(d)} = E^{(0)} - \frac{V}{2} + \frac{t^2}{V}. \tag{A.10}$$

For band (e), second-order corrections are also needed. The correction Hamiltonian is given by the $(N-3)\times(N-3)$ tridiagonal matrix

$$H^{(2)}_{(e)} = \frac{t^2}{V}\begin{pmatrix} 3 & 1 & 0 & \cdots & 0 & 0 \\ 1 & 2 & 1 & \cdots & 0 & 0 \\ 0 & 1 & 2 & \cdots & 0 & 0 \\ \vdots & \vdots & \vdots & \ddots & \vdots & \vdots \\ 0 & 0 & 0 & \cdots & 2 & 1 \\ 0 & 0 & 0 & \cdots & 1 & 3 \end{pmatrix}. \tag{A.11}$$

Here, the off-diagonal elements refer to hops of the two spin excitations, i.e. to transitions such as $|01100\cdots0\rangle \to |00110\cdots0\rangle$. The diagonal elements correspond to processes in which one of the excitations hops to a neighbouring site and then comes back. The eigenvalues of this matrix are known [234], giving the corrections

$$E_{(e)}(k) = E^{(0)} - V + \frac{2t^2}{V}\left(1 + \cos\left(\frac{(k-1)\pi}{N-3}\right)\right), \quad k = 1, \ldots, N-3. \tag{A.12}$$

For the state (f), the intermediate states are $|m\rangle = |010\cdots01\rangle$ and $|m\rangle = |10\cdots010\rangle$, giving a corrected energy

$$E_{(f)} = E^{(0)} - V + \frac{4t^2}{V}. \tag{A.13}$$

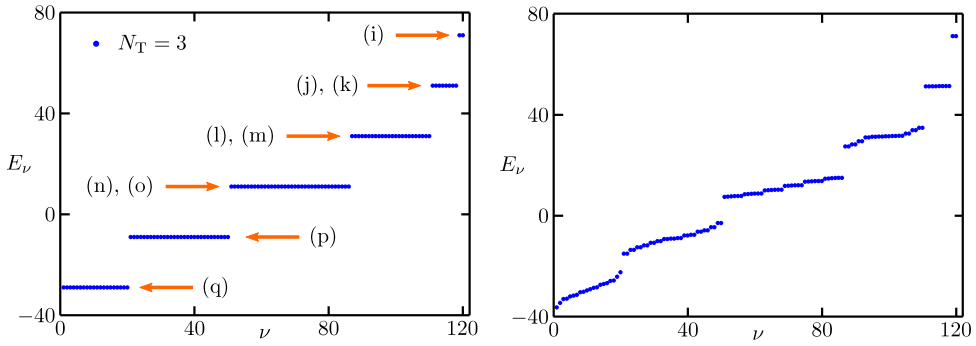

Figure A.2. Energies for three excitations, for $N = 10$, $V = 40$, $t = 0$ (left) and $t = -2$ (right). Here ν corresponds to the eigenvalue index.

For band (g), we just calculate first order corrections, since states within this band are connected by a single hopping process (for example, $|10100\cdots0\rangle$ and $|10010\cdots0\rangle$). The degeneracy is not totally lifted, since the localised spin can be at the left or the right edge; each energy level thus consists of two states, as shown in the right panel of figure A.1. The effective Hamiltonian $H^{(2)}_{(g)}$ to determine the energetic corrections is then a tridiagonal $(N-3)\times(N-3)$ matrix of the form of equation (A.8), and leads to

$$E_{(g)}(k) = E^{(0)} - \frac{3V}{2} - 2t\cos\left(\frac{k\pi}{N-2}\right), \quad k = 1,\ldots,N-3. \tag{A.14}$$

A.2.4 Energies for three excitations

As before, we first identify the degenerated bands of the case $t = 0$, which are shown in the left panel of figure A.2. These correspond to

(i) Two states of energy $E = E^{(0)} - V/2$, corresponding to the excitations being localised at one of the edges of the chain, i.e. $|00\cdots0111\rangle$ and $|1110\cdots00\rangle$.

(j) $N-4$ states of energy $E = E^{(0)} - V$, corresponding to the excitations next to each other, but none of them at the edges, such as $|0\cdots01110\cdots0\rangle$.

(k) Two states of energy $E = E^{(0)} - V$, with two excitations at one edge and the

remaining excitation at the other edge, namely $|110\cdots01\rangle$ and $|10\cdots011\rangle$.

(l) $2(N-4)$ states of energy $E = E^{(0)} - 3V/2$, for one excitation at one edge, and the other excitations next to each other but separated from the first one, at any position on the chain except at the other edge, e.g. $|100\cdots11\cdots0\rangle$.

(m) $2(N-4)$ states of energy $E = E^{(0)} - 3V/2$, corresponding to two excitations next to each other at one edge, and the remaining excitation separated at any location except the other edge. An example of this type is $|110\cdots1\cdots0\rangle$.

(n) $(N-4)(N-5)$ states of energy $E = E^{(0)} - 2V$. None of the excitations is at any boundary, and just two of them are next to each other. One example is the state $|011\cdots1\cdots0\rangle$.

(o) $(N-4)$ states of energy $E = E^{(0)} - 2V$, where the three excitations are separated from each other, and two of them are located at different edges. An example of this type of states is $|10\cdots1\cdots01\rangle$.

(p) $(N-4)(N-5)/2$ states of energy $E = E^{(0)} - 5V/2$, where the excitations are separated from each other and just one is located at one edge, such as $|01\cdots1\cdots01\rangle$.

(q) States of energy $E = E^{(0)} - 3V$, where the three excitations are separated from each other and none of them is located at any edge, such as $|0\cdots1\cdots1\cdots1\cdots0\rangle$.

Again, turning the hopping on lifts the degeneracy of the bands, as shown in the right panel of figure A.2. The perturbative calculation of the energies can be performed in a similar form to that of the previous Sections.

A.3 Perturbative correction to dark configurations

We now describe within the perturbative approach how the dark configurations

$$|\, B_n\rangle = |\, \overbrace{111\cdots111}^{n}\underbrace{000\cdots000}_{N-n}\rangle, \tag{A.15}$$

equivalent to the states of equation (5.14) in the spin language, are affected by a single particle or hole breaking away from the domain boundary. We start by defining the notation to follow. Let $|\psi_i\rangle_{\rm p}$ denote the state in which the outermost particle of the domain has hopped i sites within the empty region, so it is at site $n+i$. Also, let $|\psi_j\rangle_{\rm h}$ be the state in which the first hole has hopped j sites within the occupied domain, so it is at site $n-j+1$. So we have, for example

$$\begin{aligned}
&|\psi_1\rangle_{\rm p} = |\psi_j\rangle_{\rm h} = |\,\overbrace{11\cdots11}^{n-1}01\underbrace{00\cdots000}_{N-n-1}\rangle,\\
&|\psi_{N-n}\rangle_{\rm p} = |\,\overbrace{11\cdots11}^{n-1}\underbrace{00\cdots000}_{N-n}1\rangle \qquad |\psi_n\rangle_{\rm h} = |\,0\overbrace{11\cdots111}^{n}\underbrace{00\cdots000}_{N-n-1}\rangle.
\end{aligned} \tag{A.16}$$

The state $|\Psi_D(n)\rangle$ described in Section 5.5.1 is the perturbative correction to $|\,B_n\rangle$ due to the break-away configurations $|\psi_i\rangle_{\rm p,h}$. This correction is calculated by standard perturbation theory. The $q^{\rm th}$ order correction to this state, corresponding to the outermost particle or hole having hopped q times, is

$$|\Psi_D(n)\rangle^{(q)} = \left(\frac{-t}{V}\right)^q [(1+\delta_{q,N-n})|\psi_q\rangle_{\rm p} + (1+\delta_{q,n})|\psi_q\rangle_{\rm h}]. \tag{A.17}$$

The δ functions represent the energy shift of the states where the particle or the hole is at the right or left boundary, respectively. The corrected state is thus

$$|\Psi_D(n)\rangle \sim |B_n\rangle + \sum_{j=1}^{n-1}\left(\frac{-t}{V}\right)^{n-j+1}(1+\delta_{j,1})|\psi_{n-j+1}\rangle_{\rm h} + \sum_{j=n+1}^{N}\left(\frac{-t}{V}\right)^{j-n}(1+\delta_{j,N})|\psi_{j-n}\rangle_{\rm p}. \tag{A.18}$$

The deviation of its population from that of $|B_n\rangle$, shown in figure 5.9, is

$$\delta_n^{\rm ph}(j) = |\langle\Psi_D(n)|n_j|\Psi_D(n)\rangle - \langle B_n|n_j|B_n\rangle| = \begin{cases} 4\left(\frac{-t}{V}\right)^{2n}, & j=1\\ \left(\frac{-t}{V}\right)^{2(n-j+1)}, & 1<j\le n\\ \left(\frac{-t}{V}\right)^{2(j-n)}, & n<j<N\\ 4\left(\frac{-t}{V}\right)^{2(N-n)}, & j=N \end{cases}. \tag{A.19}$$

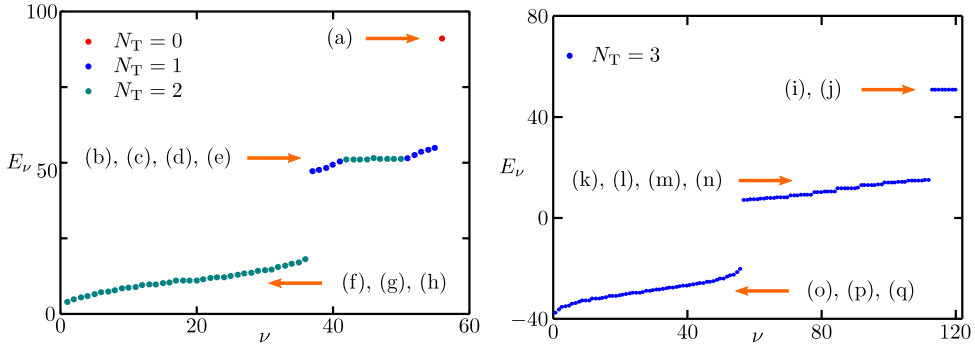

Figure A.3. Energies of Hamiltonian (A.21) for one, two excitations (left), and three excitations (right), for $N = 10$, $t = -2$ and $V = 40$.

A.4 Model with homogeneous on-site potential

Finally we examine the eigenspectrum of the hard-core boson Hamiltonian

$$H = \frac{V}{4}(N-1) - t\sum_{j=1}^{N-1}(a_j^\dagger a_{j+1} + a_{j+1}^\dagger a_j) + V\sum_{j=1}^{N-1} n_j n_{j+1} - V\sum_{j=1}^{N} n_j, \qquad \text{(A.20)}$$

which in contrast to equation (A.4), has the same on-site potential at every site. If we transform back to a spin model, we obtain

$$H = \sum_{j=1}^{N-1} \tau(\sigma_j^x\sigma_{j+1}^x + \sigma_j^y\sigma_{j+1}^y + \Delta\sigma_j^z\sigma_{j+1}^z) - \tau\Delta\sigma_1^z - \tau\Delta\sigma_N^z - 2\tau\Delta \qquad \text{(A.21)}$$

We show the corresponding bands with finite hopping for $N_T = 0, 1, 2, 3$ in figure A.3. Since now the particles at the boundaries have the same energy than particles in the bulk, several bands merge. For example, in the $t = 0$ case, states $|1100\cdots0\rangle$ and $|0110\cdots0\rangle$ are now degenerate, and there is no distinction between bands (d) and (e). Features of the original XXZ model are thus maintained, such as the existence of flat and conducting bands, separated by gaps of $O(V)$.

Appendix B

Matrix representations of operators

In the present Appendix we provide basic details of the numerical implementation of Hamiltonian and Liouvillian operators, for exact diagonalisation.

B.1 Hamiltonian

The simplest form to define the Hamiltonian of a lattice system numerically consists of performing a series of direct products between local basis operators. In particular, consider the local basis of states

$$|\uparrow\rangle = \begin{pmatrix} 1 \\ 0 \end{pmatrix} \qquad |\downarrow\rangle = \begin{pmatrix} 0 \\ 1 \end{pmatrix} \tag{B.1}$$

and the corresponding Pauli basis,

$$\sigma_i^x = \begin{pmatrix} 0 & 1 \\ 1 & 0 \end{pmatrix} \begin{matrix} \uparrow \\ \downarrow \end{matrix} \qquad \sigma_i^y = \begin{pmatrix} 0 & -i \\ i & 0 \end{pmatrix} \begin{matrix} \uparrow \\ \downarrow \end{matrix} \qquad \sigma_i^z = \begin{pmatrix} 1 & 0 \\ 0 & -1 \end{pmatrix} \begin{matrix} \uparrow \\ \downarrow \end{matrix} \tag{B.2}$$

Here we have explicitly indicated, to the right of each matrix, the correspondence between the rows of the matrices and the elements of the local basis. The same ordering applying from left to right, so for example, $(\sigma_i^y)_{\uparrow\downarrow} = -i$ and $(\sigma_i^z)_{\uparrow\uparrow} = 1$.

The two-site Hamiltonian for the XXZ model with zero magnetic field and open boundary conditions is

$$H_{12} = \tau(\sigma_1^x \otimes \sigma_2^x + \sigma_1^y \otimes \sigma_2^y + \Delta\sigma_1^z \otimes \sigma_2^z) = \tau \begin{pmatrix} \Delta & & & & \uparrow\uparrow \\ & -\Delta & 2 & & \uparrow\downarrow \\ & 2 & -\Delta & & \downarrow\uparrow \\ & & & \Delta & \downarrow\downarrow \end{pmatrix} \tag{B.3}$$

where the empty entries are zeros, and we have indicated to the right of the matrix the ordering of the local basis. Then we define the three-site Hamiltonian, taking advantage of the symmetries of the model. In this form it can be organised in diagonal blocks, each one corresponding to particular quantum numbers. In the particular case of the XXZ model, we use the conservation of total magnetisation in z direction, $S^z = \frac{1}{2}\sum_{j=1}^{N} \sigma_j^z$. First note that the Hamiltonian of two sites,

$$H_{12} = \begin{pmatrix} \mathcal{H}_{12}(1) & & \\ & \mathcal{H}_{12}(0) & \\ & & \mathcal{H}_{12}(-1) \end{pmatrix}, \tag{B.4}$$

can be considered as consisting of three sectors. The first corresponds to the sector of total magnetisation $\langle S^z \rangle = 1$ (both spins up), with Hamiltonian $\mathcal{H}_{12}(1) = \tau\Delta$, i.e. just a scalar. The second corresponds to total magnetisation $\langle S^z \rangle = 0$ (one spin up only), with 2×2 Hamiltonian

$$\mathcal{H}_{12}(0) = \tau \begin{pmatrix} -\Delta & 2 \\ 2 & -\Delta \end{pmatrix}. \tag{B.5}$$

The third sector has magnetisation $\langle S^z \rangle = -1$ (both spins down), with Hamiltonian $\mathcal{H}_{12}(-1) = \tau\Delta$. For the Hamiltonian of three sites, we have

$$H_{123} = \begin{pmatrix} \mathcal{H}_{123}(3/2) & & & \\ & \mathcal{H}_{123}(1/2) & & \\ & & \mathcal{H}_{123}(-1/2) & \\ & & & \mathcal{H}_{123}(-3/2) \end{pmatrix}. \tag{B.6}$$

Here $\mathcal{H}_{123}(3/2) = \mathcal{H}_{123}(-3/2) = 2\tau\Delta$ are the Hamiltonians of the sectors of total magnetisation $\langle S^z \rangle = \frac{3}{2}$ (three spins up) and $\langle S^z \rangle = -\frac{3}{2}$ (three spins down), respectively, and the 3×3 Hamiltonians

$$H_{123}(1/2) = H_{123}(-1/2) = 2\tau \begin{pmatrix} 0 & 1 & 0 \\ 1 & -\Delta & 1 \\ 0 & 1 & 0 \end{pmatrix} \tag{B.7}$$

correspond to the sectors of total magnetisation $\langle S^z \rangle = \frac{1}{2}$ (two spins up, one spin down) and $\langle S^z \rangle = -\frac{1}{2}$ (two spins down, one spin up). The process of adding sites continues until reaching the desired size N, keeping the correct order of the elements of the local basis so diagonal blocks of specified quantum numbers can be defined. The Hamiltonian of each block can be then diagonalised exactly with standard numerical routines, leading to a significant speedup of the calculations compared to a diagonalisation without symmetries.

B.2 Liouvillian

We can find the NESS of a Lindblad master equation from exact diagonalisation if a small number of sites is considered, since the size of the Liouvillian superoperator grows as 4^N. Calculations with this type of algorithm were only shown explicitly in figure 5.10 of Section 5.5. Nevertheless they proved to be useful to check the results of our TEBD algorithms. Obtaining the NESS ρ of the Lindblad master equation $\mathcal{L}(\rho) = 0$ is just equivalent to finding the zero-eigenvalue vector $\tilde{\rho}$ of the matrix representation of the Lindblad superoperator $\tilde{\mathcal{L}}$, since $\tilde{\mathcal{L}}\tilde{\rho} = 0$. The problem is basically reduced to defining this matrix representation.

Let Ω_n, $n = 1, \ldots, 4^N$ be the orthonormal basis elements of the operator space of N sites. In this basis, the density operator is $\rho = \sum_{n=1}^{4^N} c_n \Omega_n$. The n^{th} component of the vector representation $\tilde{\rho}$ of the state ρ is thus $\tilde{\rho}_n = c_n$. Inserting each basis

element into the master equation, we get

$$\mathcal{L}(\Omega_n) = \sum_{m=1}^{4^N} \tilde{\mathcal{L}}_{mn}\Omega_m, \tag{B.8}$$

where $\tilde{\mathcal{L}}_{mn}$ are the matrix elements of $\tilde{\mathcal{L}}$. Now we see explicitly two examples of superoperators of incoherent processes acting on a single site [178]. First, for the dephasing jump operator $L^{\mathrm{d}} = \sqrt{\gamma}\sigma^z$, the matrix representation of the corresponding Liouville superoperator is

$$\tilde{\mathcal{L}}^{\mathrm{d}} = \begin{pmatrix} 0 & 0 & 0 & 0 \\ 0 & 0 & 0 & 0 \\ 0 & 0 & -2\gamma & 0 \\ 0 & 0 & 0 & -2\gamma \end{pmatrix}. \tag{B.9}$$

A second example corresponds to a driving term with imbalance f. For the jump operators $L^+ = \sqrt{\Gamma(1+f)/2}\sigma^+$ and $L^- = \sqrt{\Gamma(1-f)/2}\sigma^-$, the matrix representations of the respective Liouville superoperators are

$$\tilde{\mathcal{L}}^+ = \Gamma\left(\frac{1+f}{2}\right)\begin{pmatrix} 0 & 0 & 0 & 0 \\ 1 & -1 & 0 & 0 \\ 0 & 0 & \frac{1}{2} & 0 \\ 0 & 0 & 0 & \frac{1}{2} \end{pmatrix}, \quad \tilde{\mathcal{L}}^- = \Gamma\left(\frac{1-f}{2}\right)\begin{pmatrix} 0 & 0 & 0 & 0 \\ -1 & -1 & 0 & 0 \\ 0 & 0 & \frac{1}{2} & 0 \\ 0 & 0 & 0 & \frac{1}{2} \end{pmatrix}. \tag{B.10}$$

The matrix representation of the total driving superoperator is

$$\tilde{\mathcal{L}}_{\mathrm{driv}} = \tilde{\mathcal{L}}^+ + \tilde{\mathcal{L}}^- = \Gamma\begin{pmatrix} 0 & 0 & 0 & 0 \\ f & -1 & 0 & 0 \\ 0 & 0 & -\frac{1}{2} & 0 \\ 0 & 0 & 0 & -\frac{1}{2} \end{pmatrix}. \tag{B.11}$$

The other superoperators are obtained in a similar form. After $\tilde{\mathcal{L}}$ is obtained by adding all the terms contributing to the master equation, its zero-eigenvalue vector $\tilde{\rho}$ is obtained from standard numerical diagonalisation routines.

Appendix C

Derivation of the Lindblad equation

In this Appendix we derive the Lindblad master equation (5.2) for the nonequilibrium systems studied in the present thesis. First we explain the general process to obtain the Lindblad master equation of an open system coupled to an environment, from the microscopic equations of motion. Then we apply the result to the particular case of an XXZ chain driven by magnetic reservoirs at the boundaries and subject to bulk dephasing (one-site jump operators). Finally we describe how to obtain the two-site reservoirs for thermal driving, not from the equations of motion but from imposing that they induce local thermal states at the boundaries.

C.1 General derivation of a master equation

We initially consider a system of interest with Hamiltonian $H_{\rm S}$, surrounded by an environment with Hamiltonian $H_{\rm B}$. Both are coupled by an interaction Hamiltonian $H_{\rm I}$, with coupling strength α. So the total Hamiltonian in the Schrödinger picture is $H = H_{\rm S} + H_{\rm B} + \alpha H_{\rm I}$. The interaction Hamiltonian can be written in the form

$$H_{\rm I} = \sum_k A_k \otimes B_k = \sum_k A_k^\dagger \otimes B_k^\dagger, \tag{C.1}$$

where A_k and B_k are system and environment operators, respectively. The dynamics of the universe (system + environment) is given by the Liouville-von Neumann equation of its density operator

$$\frac{d\rho(t)}{dt} = -i[H, \rho(t)]. \tag{C.2}$$

To perform the calculation, we move to the interaction picture, where we denote the operators by the $\sim$ symbol. The relationship between an operator $O(t)$ in the Schrödinger picture and the corresponding $\tilde{O}(t)$ in the interaction picture is

$$\tilde{O}(t) = e^{i(H_\mathrm{S}+H_\mathrm{B})t} O(t) e^{-i(H_\mathrm{S}+H_\mathrm{B})t}. \tag{C.3}$$

In this case, the equation of motion of the universe density operator reads

$$\frac{d}{dt}\tilde{\rho}(t) = -i\alpha[\tilde{H}_\mathrm{I}, \tilde{\rho}(t)] \equiv \alpha \mathcal{V}(t)\tilde{\rho}(t), \tag{C.4}$$

where $\mathcal{V}(t)$ is a superoperator acting on $\tilde{\rho}(t)$. We wish to obtain a master equation for the reduced density operator of the system $\tilde{\rho}_\mathrm{S}(t)$. To do so, we follow the Nakajima-Zwanzig projection operator technique [130, 177]. The basis of the method is to determine the equation of motion of the projection of the state of the universe onto the system. We define the projection superoperators $\mathcal{P}$ and $\mathcal{Q}$ according to

$$\mathcal{P}\tilde{\rho} = \mathrm{Tr}_\mathrm{B}(\tilde{\rho}) \otimes \tilde{\rho}_\mathrm{B} \equiv \tilde{\rho_\mathrm{S}} \otimes \tilde{\rho}_\mathrm{B}, \qquad \mathcal{Q} = I - \mathcal{P}, \tag{C.5}$$

with I the identity operator and $\tilde{\rho}_\mathrm{B}$ some fixed state of the environment, which can be chosen to be, for example, a thermal state at temperature T

$$\tilde{\rho}_\mathrm{B} = \rho_\mathrm{B} = \frac{e^{-H_\mathrm{B}/T}}{\mathrm{Tr}\left(e^{-H_\mathrm{B}/T}\right)}, \tag{C.6}$$

equal in both the Schrödinger and interaction pictures. From the definition it is seen that $\mathcal{P}\tilde{\rho}$ projects the state of the universe onto the system degrees of freedom, and thus gives the complete information of $\tilde{\rho}_{\mathrm{S}}$. On the other hand, $\mathcal{Q}$ projects onto the environmental degrees of freedom. It is easily proven that the defined superoperators satisfy the conditions $\mathcal{P}^2 = \mathcal{P}$, $\mathcal{Q}^2 = \mathcal{Q}$ and $\mathcal{P}\mathcal{Q} = \mathcal{Q}\mathcal{P} = 0$, the first two indicating that they are truly projection operators. Another important property to be used later is that for the states and interactions in which we are interested, $\mathcal{P}\mathcal{V}(t)\mathcal{P} = 0$. This result can be proved by calculating $\mathcal{P}\mathcal{V}(t)\mathcal{P}\tilde{\rho} \propto \mathrm{Tr}_{\mathrm{B}}(B_k\rho_{\mathrm{B}}) = 0$, where we assume that the expectation values of the environment operators vanish in the fixed environmental state ρ_{B}. This is actually what happens in the cases studied in the present thesis, where ρ_{B} is a thermal or grand-canonical state and B_k are excitation creation or annihilation operators (see Section C.2).

After introducing the projection superoperators and their basic properties, we can proceed with the derivation of the Lindblad equation. The idea of the Nakajima-Zwanzig technique is to obtain an evolution equation for $\mathcal{P}\tilde{\rho}$. For this, we apply $\mathcal{P}$ and $\mathcal{Q}$ to (C.4). Then, inserting $I = \mathcal{P} + \mathcal{Q}$ between $\mathcal{V}(t)$ and $\tilde{\rho}(t)$ we find

$$\frac{d}{dt}\mathcal{P}\tilde{\rho}(t) = \alpha\mathcal{P}\mathcal{V}(t)\mathcal{P}\tilde{\rho}(t) + \alpha\mathcal{P}\mathcal{V}(t)\mathcal{Q}\tilde{\rho}(t) \tag{C.7a}$$

$$\frac{d}{dt}\mathcal{Q}\tilde{\rho}(t) = \alpha\mathcal{Q}\mathcal{V}(t)\mathcal{P}\tilde{\rho}(t) + \alpha\mathcal{Q}\mathcal{V}(t)\mathcal{Q}\tilde{\rho}(t). \tag{C.7b}$$

It is readily observed that the solution of (C.7b) is

$$\mathcal{Q}\tilde{\rho}(t) = G(t,t_0)\mathcal{Q}\tilde{\rho}(t_0) + \alpha\int_{t_0}^{t} dsG(t,s)\mathcal{Q}\mathcal{V}(s)\mathcal{P}\tilde{\rho}(s). \tag{C.8}$$

where $\tilde{\rho}(t_0)$ is the state at an initial time t_0, and

$$G(t,t') = \mathcal{T}e^{\alpha\int_{t'}^{t}\mathcal{Q}\mathcal{V}(s)ds}. \tag{C.9}$$

Inserting this result in (C.7a), we get

$$\begin{aligned}\frac{d}{dt}\mathcal{P}\tilde{\rho}(t) = \alpha\mathcal{P}\mathcal{V}(t)\mathcal{P}\tilde{\rho}(t) + \alpha\mathcal{P}\mathcal{V}(t)G(t,t_0)\mathcal{Q}\tilde{\rho}(t_0) \\ + \alpha^2\int_{t_0}^{t} ds\mathcal{P}\mathcal{V}(t)G(t,s)\mathcal{Q}\mathcal{V}(s)\mathcal{P}\tilde{\rho}(s),\end{aligned} \tag{C.10}$$

which is known as the Nakajima-Zwanzig equation [130]. It is simplified by assuming that the initial state of the universe is the product $\tilde{\rho}(t_0) = \tilde{\rho}_{\mathrm{S}}(t_0) \otimes \rho_{\mathrm{B}}$, so

$$\mathcal{P}\tilde{\rho}(t_0) = \tilde{\rho}(t_0) \quad \Rightarrow \quad \mathcal{Q}\tilde{\rho}(t_0) = \tilde{\rho}(t_0) - \mathcal{P}\tilde{\rho}(t_0) = 0. \tag{C.11}$$

Because of this result, the second term of equation (C.10) vanishes. In addition, using that $\mathcal{P}\mathcal{V}(t)\mathcal{P} = 0$, equation (C.10) reduces to

$$\frac{d}{dt}\mathcal{P}\tilde{\rho}(t) = \alpha^2\int_{t_0}^{t} ds\mathcal{P}\mathcal{V}(t)G(t,s)\mathcal{Q}\mathcal{V}(s)\mathcal{P}\tilde{\rho}(s) \equiv \int_{t_0}^{t} ds\mathcal{K}(t,s)\mathcal{P}\tilde{\rho}(s), \tag{C.12}$$

which defines the memory kernel $\mathcal{K}(t,s)$. Note that this integro-differential equation is still exact, and takes into account the memory effects of the dynamics. Since it is very difficult to find its solution, a perturbative approach is required to make it tractable with analytical or numerical methods [130]. The approximation to be considered is that of weak coupling α between system and environment, which is usually referred to as the Born approximation. To include it in the derivation, the kernel is expanded up to lowest order in α, so we get

$$\mathcal{K}(t,s) = \alpha^2\mathcal{P}\mathcal{V}(t)\mathcal{Q}\mathcal{V}(s)\mathcal{P} + O(\alpha^3). \tag{C.13}$$

Using the definition of $\mathcal{Q}$ and that $\mathcal{P}\mathcal{V}(t)\mathcal{P} = 0$, we obtain

$$\frac{d}{dt}\mathcal{P}\tilde{\rho}(t) = \alpha^2\int_{t_0}^{t} ds\mathcal{P}\mathcal{V}(t)\mathcal{V}(s)\mathcal{P}(\tilde{\rho})(s). \tag{C.14}$$

Now we use the explicit definition of the projectors and of $\mathcal{V}(t)$, as given by equation (C.4). We also take $t_0 = 0$, and do the change of variable $s \to t - s$, to get the equation of motion for the reduced density operator of the system [177]

$$\frac{d}{dt}\tilde{\rho}_{\mathrm{S}} = -\alpha^2 \int_0^t ds \mathrm{Tr}_{\mathrm{B}} \left[\tilde{H}_{\mathrm{I}}(t), \left[\tilde{H}_{\mathrm{I}}(t-s), \tilde{\rho}_{\mathrm{S}}(t-s) \otimes \rho_{\mathrm{B}}\right]\right]. \tag{C.15}$$

Note that the previous equation can be obtained by different forms. For example, it can be derived by iterating the Liouville-von Neumann equation twice, and by assuming that during the entire evolution, the state of the universe is the product $\tilde{\rho}(t) = \tilde{\rho}_{\mathrm{S}}(t) \otimes \rho_{\mathrm{B}}$ [130]. The latter condition is assumed to be valid due to the weak coupling approximation; nevertheless its validity is degraded with time, as observed from a direct numerical comparison between $\tilde{\rho}(t)$ and $\tilde{\rho}_{\mathrm{S}}(t) \otimes \rho_{\mathrm{B}}$ [177]. In the derivation presented here, such an approximation was not required. It was not assumed that the state was a product at all time (just at the initial time), but the appearance of $\tilde{\rho}_{\mathrm{S}}(t-s) \otimes \rho_{\mathrm{B}}$ results from using the projection operators.

To proceed, we need to write explicitly the interaction Hamiltonian in the interaction picture $\tilde{H}_{\mathrm{I}}$ in a simple form. To do so, we first consider the A_k operators of equation (C.1) in the Schrödinger picture. Assuming that the Hamiltonian of the system H_{S} has a discrete eigenspectrum, with eigenvalues ε, we define the operators

$$A_k(\nu) = \sum_{\varepsilon' - \varepsilon = \nu} \Pi(\varepsilon) A_k \Pi(\varepsilon'), \tag{C.16}$$

where $\Pi(\varepsilon)$ is the projection operator onto the space of the eigenvalue ε, and the sum is over all eigenenergies ε and ε' that have a fixed difference ν. Since $H_{\mathrm{S}} = \sum_\varepsilon \varepsilon \Pi(\varepsilon)$, it is straightforward to check that

$$[H_{\mathrm{S}}, A_k(\nu)] = -\nu A_k(\nu), \qquad [H_{\mathrm{S}}, A_k^\dagger(\nu)] = \nu A_k^\dagger(\nu); \tag{C.17}$$

It also follows directly from definition (C.16) that

$$A_k = \sum_\nu A_k(\nu), \qquad A_k^\dagger = \sum_\nu A_k^\dagger(\nu). \tag{C.18}$$

In the interaction picture, operator $A_k(\nu)$ is written as

$$\tilde{A}_k(\nu) = e^{iH_{\rm S}t} A_k(\nu) e^{-iH_{\rm S}t} = e^{it\sum_\varepsilon \varepsilon\Pi(\varepsilon)} \left(\sum_{\varepsilon''-\varepsilon'=\nu} \Pi(\varepsilon') A_k \Pi(\varepsilon'') \right) e^{-it\sum_\varepsilon \varepsilon\Pi(\varepsilon)}. \tag{C.19}$$

A similar calculation is performed for $A_k^\dagger(\nu)$, to show that

$$\tilde{A}_k(\nu) = e^{-i\nu t} A_k(\nu), \qquad \tilde{A}_k^\dagger(\nu) = e^{i\nu t} A_k^\dagger(\nu). \tag{C.20}$$

So using equations (C.1), (C.18) and (C.20) the interaction picture interaction Hamiltonian is shown to be

$$\begin{aligned} \tilde{H}_{\rm I} &= e^{i(H_{\rm S}+H_{\rm B})t} H_{\rm I} e^{-i(H_{\rm S}+H_{\rm B})t} = \sum_\nu \sum_k \tilde{A}_k(\nu) \otimes \tilde{B}_k(t) \\ &= \sum_\nu \sum_k e^{-i\nu t} A_k(\nu) \otimes \tilde{B}_k(t) = \sum_\nu \sum_k e^{i\nu t} A_k^\dagger(\nu) \otimes \tilde{B}_k^\dagger(t), \end{aligned} \tag{C.21}$$

where in the last equality we have used that $\tilde{H}_{\rm I}$ is self-adjoint, and

$$\tilde{B}_k(t) = e^{iH_{\rm B}t} B_k e^{-iH_{\rm B}t}, \qquad \tilde{B}_k^\dagger(t) = e^{iH_{\rm B}t} B_k^\dagger e^{-iH_{\rm B}t} \tag{C.22}$$

are the environment operators in the interaction picture. Now that we have written $\tilde{H}_{\rm I}$ in the simple form of equation (C.21), we insert it in the master equation (C.15). Developing the commutators, we obtain

$$\begin{aligned} \frac{d}{dt}\tilde{\rho}_{\rm S}(t) = \alpha^2 \sum_{k,l} \sum_{\nu,\nu'} \int_0^t ds \Big(& \langle \tilde{B}_l(t) \tilde{B}_k^\dagger(t-s) \rangle e^{-i\nu t} A_l(\nu) \tilde{\rho}_{\rm S}(t-s) A_k^\dagger(\nu') e^{i\nu'(t-s)} \\ & - \langle \tilde{B}_l^\dagger(t) \tilde{B}_k(t-s) \rangle e^{i\nu t} A_l^\dagger(\nu) A_k(\nu') e^{-i\nu'(t-s)} \tilde{\rho}_{\rm S}(t-s) \Big) + \text{h. c.} \end{aligned}$$

At this point, another approximation is required to make the equation local in time. Namely, we assume that the reservoir correlation functions $\langle \tilde{B}_l(t)\tilde{B}_k^\dagger(t-s)\rangle$ and $\langle \tilde{B}_l^\dagger(t)\tilde{B}_k(t-s)\rangle$ decay very fast in time. This is, if τ_{C} is the characteristic time over which the system changes appreciably and τ_{B} is the decay time of the correlation functions, we suppose that $\tau_{\mathrm{B}} \ll \tau_{\mathrm{C}}$. This assumption is called the Markov approximation, and indicates that the time over which the environment retains memory of its dynamics is very small. Since during the correlation time τ_{B} the state of the system varies very slowly, we can approximate it by the expansion

$$\tilde{\rho}_{\mathrm{S}}(t-s) \approx \tilde{\rho}_{\mathrm{S}}(t) - s\frac{d}{dt}\tilde{\rho}_{\mathrm{S}}(s=0) + \cdots = \tilde{\rho}_{\mathrm{S}}(t) + O(\alpha^2). \tag{C.23}$$

This is, during the correlation time τ_{B}, the system is in a constant state. Also, due to the fast decay of the correlation functions, we can let the upper limit of the integral to be infinite. In addition, the reservoir correlations are homogeneous in time since, for example

$$\begin{aligned}\langle \tilde{B}_l(t)\tilde{B}_k^\dagger(t-s)\rangle &= \mathrm{Tr}_{\mathrm{B}}\left(\rho_{\mathrm{B}} e^{iH_{\mathrm{B}}t}B_l e^{-iH_{\mathrm{B}}t}e^{iH_{\mathrm{B}}(t-s)}B_k^\dagger e^{-iH_{\mathrm{B}}(t-s)}\right)\\ &= \mathrm{Tr}_{\mathrm{B}}\left(\rho_{\mathrm{B}} e^{iH_{\mathrm{B}}s}B_l e^{-iH_{\mathrm{B}}s}B_k^\dagger\right) = \langle \tilde{B}_l(s)\tilde{B}_k^\dagger(0)\rangle.\end{aligned} \tag{C.24}$$

If we define the Fourier transforms of the environment correlation functions

$$\Gamma_{k,l}(\nu) = \alpha^2 \int_0^\infty ds \langle \tilde{B}_k^\dagger(s)\tilde{B}_l(0)\rangle e^{i\nu s}, \tag{C.25}$$

we obtain the master equation

$$\begin{aligned}\frac{d}{dt}\tilde{\rho}_{\mathrm{S}}(t) = \sum_{k,l}\sum_{\nu,\nu'}\Bigg(&\Gamma_{k,l}(\nu)e^{i(\nu'-\nu)t}\left[A_l(\nu)\tilde{\rho}_{\mathrm{S}}(t), A_k^\dagger(\nu')\right]\\ &+ \Gamma_{l,k}^*(\nu)e^{i(\nu-\nu')t}\left[A_l(\nu'), \tilde{\rho}_{\mathrm{S}}(t)A_k^\dagger(\nu)\right]\Bigg).\end{aligned} \tag{C.26}$$

This equation is still not in a Lindblad form, so it might not define a completely

positive map. A new approximation is thus required to eliminate the time exponentials and to leave the equation in the desired form. The usual form to proceed consists of performing the rotating-wave approximation [130, 177]. The idea of this approach is to assume that the energy differences $|\nu - \nu'|$ are much larger than the rate at which the state of the system changes, i.e. that $|\nu - \nu'| \gg \alpha^2$. This means that the time exponentials in equation (C.26) with $\nu \neq \nu'$ correspond to terms that oscillate very rapidly around zero, and in average can be neglected. The only terms that survive are those of $\nu = \nu'$. Making this approximation, and going back to the Schrödinger picture, leads to a Lindblad master equation.

In the type of system considered in the present thesis, however, this approximation has problems. First, the relation $|\nu - \nu'| \gg \alpha^2$ is not necessarily valid for an XXZ Hamiltonian, which for $\Delta > 1$ has a degenerate spectrum and very narrow bands if the hopping τ is weak, as discussed in Appendix A. Even for the case $\Delta = 0$, which has an eigenspectrum of the form shown in equation (C.35) (see Section C.2), the difference between the first neighbouring eigenvalues of large systems scales as

$$\omega_2 - \omega_1 \propto \cos\left(\frac{2\pi}{N-1}\right) - \cos\left(\frac{\pi}{N-1}\right) \approx \frac{3\pi^2}{(N+1)^2} \sim N^{-2}. \tag{C.27}$$

Thus for very large systems, it is clear that the condition for the rotating-wave approximation will not be fulfilled. A second complication is that the operators $A_k(\nu)$ defined in equation (C.16) appear in the resulting Lindblad equation, acting on the state $\rho_{\mathrm{S}}(t)$. These operators are very hard to build, since they require the knowledge of all the eigenvalues and eigenstates of H_{S}, something which for correlated systems of several sites is not possible to obtain (see Appendix B). Besides, even if these eigenstates are known, the operators $A_k(\nu)$ are highly non-local, and thus hard to handle. A third problem is that it has been observed that the rotating-wave approximation can lead to unphysical results for spin chains thermally driven out of

equilibrium [139].

An alternative approximation that leads to the desired Lindblad form of the master equation is the so-called wide-band limit [235]. This consists of assuming that the bandwidths of the reservoirs, proportional to their hopping rates (τ_{L} and τ_{R}), are much larger than the bandwidth of the system, which is $\propto \tau$. This is, in the wide-band limit we suppose that $\tau \ll \tau_{\mathrm{L,R}}$. Thus the energy dependence of the rates $\Gamma_{k,l}(\nu)$ defined in equation (C.25) can be neglected, so $\Gamma_{k,l}(\nu) = \Gamma_{k,l}$. We can decompose these rates as

$$\Gamma_{k,l} = \frac{1}{2}\gamma_{k,l} + iS_{k,l}, \tag{C.28}$$

where the components are

$$\begin{aligned} \gamma_{k,l} &= \Gamma_{k,l} + \Gamma^*_{l,k} = \alpha^2 \int_{-\infty}^{\infty} ds \langle \tilde{B}^\dagger_k(s) B_l(0) \rangle, \\ S_{k,l} &= \frac{1}{2i}(\Gamma_{k,l} - \Gamma^*_{l,k}). \end{aligned} \tag{C.29}$$

Now we take equation (C.26) back to the Schrödinger picture, to get the master equation for $\rho_{\mathrm{S}}(t)$. We then obtain

$$\frac{d}{dt}\rho_{\mathrm{S}}(t) = -i[H_{\mathrm{S}}, \rho_{\mathrm{S}}(t)] + \sum_{k,l}\left(\Gamma_{k,l}\left[A_l \rho_{\mathrm{S}}(t), A^\dagger_k\right] + \Gamma^*_{l,k}\left[A_l, \rho_{\mathrm{S}}(t) A^\dagger_k\right]\right). \tag{C.30}$$

Note that the oscillating terms of (C.26) have been removed just by going back to the Schrödinger picture, in contrast to the case of the rotating wave approximation, where they were assumed to be $\delta_{\nu,\nu'}$. We now use the decomposition (C.28), and consider that $\gamma^*_{l,k} = \gamma_{k,l}$ and $S^*_{l,k} = S_{k,l}$. Then we finally get the master equation for the reduced density operator of the system in Lindblad form

$$\frac{d}{dt}\rho_{\mathrm{S}}(t) = -i[H_{\mathrm{S}} + H_{\mathrm{Shift}}, \rho_{\mathrm{S}}(t)] + \sum_{k,l}\gamma_{k,l}\left(A_l \rho_{\mathrm{S}}(t) A^\dagger_k - \frac{1}{2}\{A^\dagger_k A_l, \rho_{\mathrm{S}}(t)\}\right), \tag{C.31}$$

where the shift Hamiltonian is defined by

$$H_{\text{Shift}} = \sum_{k,l} S_{k,l} A_k^\dagger A_l. \tag{C.32}$$

Recall that the "jump operators" of equation (C.31), namely A_k and $A_k^\dagger$, act locally, making it tractable from numerical methods such as the Time Evolving Block Decimation (see Chapter 4).

C.2 Application to magnetically-driven spin chains

Now we need to specify the particular system to be considered, to calculate the rates $\gamma_{k,l}$ and to identify the jump operators that appear in the master equation (C.31). First, recall that the system Hamiltonian studied in the present thesis is the XXZ model with magnetic field,

$$H_{\text{S}} = \sum_{j=1}^{N-1} \tau(\sigma_j^x \sigma_{j+1}^x + \sigma_j^y \sigma_{j+1}^y + \Delta \sigma_j^z \sigma_{j+1}^z) + \sum_{j=1}^{N} B_j \sigma_j^z. \tag{C.33}$$

We assume that at both the left (L) and the right (R) boundaries of the spin chain there are magnetic leads, which take it to a non-equilibrium configuration. The simplest model for these leads corresponds to non-interacting XX spin chains with open boundary conditions, with Hamiltonian

$$H_{\text{B}} = \sum_{S=\text{L,R}} \sum_{k_S=1}^{N_S} \tau_S \left(\sigma_{k_S}^x \sigma_{k_S+1}^x + \sigma_{k_S}^y \sigma_{k_S+1}^y \right). \tag{C.34}$$

It is more convenient to consider the diagonalised version of the XX Hamiltonian, which from the equivalent spinless fermion model described in Section 2.2 is easily

found to be (see, for example, Chapter 3 of Ref. [236])

$$H_{\mathrm{B}} = \sum_{S=\mathrm{L,R}} \sum_{q_S} \omega_{q_S}^S c_{q_S}^\dagger c_{q_S}, \qquad \omega_{q_S}^S = 2\tau_S \cos\left(\frac{q_S \pi}{N_S + 1}\right), \tag{C.35}$$

with $q_S = 1, \ldots, N$. The $c^\dagger$ and c operators create and annihilate spinless fermions, respectively, so $\{c_{q_S}^\dagger, c_{q'_S}\} = \delta_{q_S, q'_S}$. When applied to the vacuum $|0\rangle$, $c^\dagger$ creates a delocalised fermion:

$$c_{q_S}^\dagger |0\rangle = \sqrt{\frac{2}{N_S + 1}} \sum_{k_S=1}^{N} \sin\left(\frac{q_S \pi k_S}{N_S + 1}\right) |k_S\rangle, \tag{C.36}$$

where $|k_S\rangle$ denotes an excitation at site k_S of chain S. The interaction Hamiltonian between system and environment is taken to be

$$\alpha H_I = \sum_{q_{\mathrm{L}}} T_{\mathrm{L}} \left(c_{q_{\mathrm{L}}}^\dagger \sigma_1^- + c_{q_{\mathrm{L}}} \sigma_1^+\right) + \sum_{q_{\mathrm{R}}} T_{\mathrm{R}} \left(c_{q_{\mathrm{R}}}^\dagger \sigma_N^- + c_{q_{\mathrm{R}}} \sigma_N^+\right), \tag{C.37}$$

where T_{L} and T_{R} are the hopping rates between the system and the left and right reservoirs, respectively. We thus assume that the delocalised excitations annihilated at the reservoirs are created at the boundary sites of the chain. Given this interaction, we identify the A_k and B_k operators of equation (C.1) as

$$\begin{gathered} A_1 = \sigma_1^-, \quad A_2 = \sigma_1^+, \quad A_3 = \sigma_N^-, \quad A_4 = \sigma_N^+ \\ B_1 = \sum_{q_{\mathrm{L}}} c_{q_{\mathrm{L}}}^\dagger, \quad B_2 = \sum_{q_{\mathrm{L}}} c_{q_{\mathrm{L}}}, \quad B_3 = \sum_{q_{\mathrm{R}}} c_{q_{\mathrm{R}}}^\dagger, \quad B_4 = \sum_{q_{\mathrm{R}}} c_{q_{\mathrm{R}}}, \end{gathered} \tag{C.38}$$

and assign $\alpha_{\mathrm{L}} = T_{\mathrm{L}}$ and $\alpha_{\mathrm{R}} = T_{\mathrm{R}}$ as coupling strengths to the left and right reservoirs, respectively.

To obtain the Lindblad master equation that results when the degrees of freedom of the reservoirs are discarded, we need to calculate the rates $\gamma_{k,l}$ defined in (C.29),

which result when integrating the reservoir correlation functions. For this, the interaction picture operators $\tilde{B}_k(t)$ at time $t = s$ are required. These are obtained by solving the interaction picture motion equation

$$\frac{d}{dt}\tilde{B}_k(t) = i[H_{\rm B}, \tilde{B}_k(t)], \tag{C.39}$$

which simply results from taking the time derivative of (C.3). We illustrate the calculation for $\gamma_{1,1}$; the other diagonal rates $\gamma_{k,k}$ are obtained in the same form. From the process, it will be clear that the off-diagonal rates $\gamma_{k,l}$ $(k \neq l)$ are zero.

Using the environment Hamiltonian (C.35), it follows after a few steps that the equation of motion for $\tilde{c}_{q_{\rm L}}$ becomes

$$\frac{d}{dt}\tilde{c}_{q_{\rm L}}(t) = -i\omega^{\rm L}_{q_{\rm L}}\tilde{c}_{q_{\rm L}}(t) \quad \Rightarrow \quad \tilde{c}_{q_{\rm L}}(t) = c_{q_{\rm L}}e^{-it\omega^{\rm L}_{q_{\rm L}}}. \tag{C.40}$$

So the rate $\gamma_{1,1}$ is

$$\gamma_{1,1} = |T_{\rm L}|^2 \sum_{q_{\rm L},q'_{\rm L}} \int_{-\infty}^{\infty} ds \langle \tilde{c}_{q_{\rm L}}(s) c^\dagger_{q'_{\rm L}} \rangle = |T_{\rm L}|^2 \sum_{q_{\rm L}} \left(1 - \langle c^\dagger_{q_{\rm L}} c_{q_{\rm L}} \rangle\right) \left(\int_{-\infty}^{\infty} ds e^{-is\omega^{\rm L}_{q_{\rm L}}} \right), \tag{C.41}$$

where we have used the anti-commutation property of the c operators. Considering that the reservoirs are infinitely large, their eigen-spectrum is continuous, so the sums can be replaced by integrals over q. Then we change to an integral over energy, which is killed by the $\delta(\omega^{\rm L}_q)$ function that results from the integral over s. So we obtain that

$$\gamma_{1,1} = \Gamma_{\rm L}(1 - f_{\rm L}) \quad \text{with} \quad \Gamma_{\rm L} = 2\pi |T_{\rm L}|^2 g_{\rm L}(0). \tag{C.42}$$

Here, $g_{\rm L}(0)$ is the energy density of states of the left reservoir evaluated at zero frequency, and $f_{\rm L} = \langle c^\dagger_{N/2} c_{N/2} \rangle$ is the population of the zero frequency state. Similarly,

the other diagonal rates are given by

$$\gamma_{2,2} = \Gamma_{\mathrm{L}} f_{\mathrm{L}}, \quad \gamma_{3,3} = \Gamma_{\mathrm{R}}(1 - f_{\mathrm{R}}), \quad \gamma_{4,4} = \Gamma_{\mathrm{R}} f_{\mathrm{R}}. \tag{C.43}$$

As noted from equation (C.41), when calculating off-diagonal rates $\gamma_{k,l}$, expectation values such as $\langle c^{\dagger}_{q_{\mathrm{L}}} c_{q_{\mathrm{R}}} \rangle$ or $\langle c_{q_{\mathrm{L}}} c_{q_{\mathrm{L}}} \rangle$ appear. These values are zero, given the environment states we are assuming. Thus only the diagonal terms survive. To control the non-equilibrium forcing with a single parameter, we consider a symmetric driving with $\Gamma_{\mathrm{L}} = \Gamma_{\mathrm{R}} = \Gamma$, and define $f_{\mathrm{L,R}} = 1/2(1 \pm f)$. If the shift Hamiltonian H_{Shift} is neglected, as is usually the case [21], we finally get the Lindblad master equation (5.2)

$$\frac{d}{dt}\rho_{\mathrm{S}}(t) = -i[H_{\mathrm{S}}, \rho_{\mathrm{S}}(t)] + \sum_k \left(L_k \rho_{\mathrm{S}}(t) L_k^{\dagger} - \frac{1}{2}\{L_k^{\dagger} L_k, \rho_{\mathrm{S}}(t)\} \right), \tag{C.44}$$

with the jump operators (5.4)

$$L^{+}_{\mathrm{L,R}} = \sqrt{\Gamma(1 \pm f)/2}\, \sigma^{+}_{1,N} \quad L^{-}_{\mathrm{L,R}} = \sqrt{\Gamma(1 \mp f)/2}\, \sigma^{-}_{1,N} \tag{C.45}$$

accounting for the driving process.

C.3 Lindblad term for dephasing in spin chains

We follow a very similar process to obtain the Lindblad jump operators corresponding to dephasing. For this, again consider a spin chain with the Hamiltonian (C.33). This time, assume that each site j is coupled to a local bosonic reservoir, described by the Hamiltonian

$$H_{\mathrm{B}} = \sum_{j=1}^{N} \sum_k \omega_k b^{\dagger}_{j,k} b_{j,k}. \tag{C.46}$$

Here, $b^\dagger_{j,k}$ and $b_{j,k}$ create and annihilate phonons at mode k of the reservoir of site j, with corresponding site-independent frequency ω_k. The coupling between the spin chain and the environment is given by

$$H_{\rm I} = \sum_{j=1}^{N} \sum_{k} g_k \sigma_j^z \left(b^\dagger_{j,k} + b_{j,k} \right), \tag{C.47}$$

where we also considered site-independent coupling strength g_k between mode k and the spins at each site. Assuming the wide-band limit for the environment, a Lindblad master equation (C.31) is obtained. We identify the operators

$$A_j = \sigma_j^z, \quad \alpha B_i = \sum_k g_k \left(b^\dagger_{j,k} + b_{j,k} \right). \tag{C.48}$$

As in Section C.2, it is clear that the off-diagonal rates $\gamma_{i,i'}$ are zero, and only the diagonal (site-independent) rates $\gamma_{i,i} \equiv \gamma$ survive. These are given by

$$\gamma = \sum_{k,k'} \int_{-\infty}^{\infty} ds g^*_k g_{k'} \left(\langle \tilde{b}^\dagger_{j,k}(s) b_{j,k'} \rangle + \langle \tilde{b}_{j,k}(s) b^\dagger_{j,k'} \rangle \right). \tag{C.49}$$

To obtain the interaction-picture operators at time s, we solve equation (C.39) for both. It is easily obtained that

$$\tilde{b}^\dagger_{j,k}(t) = b^\dagger_{j,k} e^{i\omega_k t}, \quad \tilde{b}_{j,k}(t) = b_{j,k} e^{-i\omega_k t}. \tag{C.50}$$

Replacing these equations into (C.49), taking the continuum limit for the momentum variable, and changing to an integral over energy, we finally obtain $\gamma = 2\pi G(0)|g|^2(1+2p)$, where $G(E)$ is the energy density of states of the environment at energy E, g is the coupling between the spins and the bosonic mode of zero frequency, and p is the population of the state of zero frequency in the thermal state $\rho_{\rm B}$ assumed for the environment. The dephasing jump operator at site j thus

corresponds to $L_j^{\mathrm{d}} = \sqrt{\gamma}\sigma_j^z$, whose effects in the dynamics of the XXZ model were discussed in Chapter 8.

C.4 Two-site thermal driving

To drive the system out of equilibrium by a temperature imbalance, we use the so-called two-site bath operators [11, 22, 63]. These operators are designed to induce a Gibbs state of a given (target) temperature and chemical potential on a pair of isolated spins with Hamiltonian $h = h_{1,2}$ and total magnetisation operator $M = \sigma_1^z + \sigma_2^z$. Here we present a brief review of how to define them. The idea is to find a superoperator $\mathcal{L}_{\mathrm{B}}(\rho)$ which satisfies the equation $\mathcal{L}_{\mathrm{B}}(\rho_{\mathrm{B}}) = 0$, with a Gibbs state at temperature T and chemical potential μ

$$\rho_{\mathrm{B}} = Z^{-1}\exp\left(-h/T + \mu M\right), \quad Z = \mathrm{Tr}(\exp\left(-h/T + \mu M\right)) \tag{C.51}$$

being the only eigenvector of $\mathcal{L}_{\mathrm{B}}$ with zero eigenvalue, all the other eigenvalues being -1. This particular choice of the driving leads to the fastest convergence to ρ_{B} [11]. To build the superoperator $\mathcal{L}_{\mathrm{B}}$, we start by diagonalising the thermal state of the target temperature, $\rho_{\mathrm{B}} = V^\dagger d V$, with $d = \mathrm{diag}(d_0, d_1, d_2, d_3)$ a diagonal matrix. Now we build the "diagonal" superoperator $\mathcal{L}_{\mathrm{B}}^{\mathrm{diag}}$, whose only zero-eigenvalue eigenstate is d, i.e. $\mathcal{L}_{\mathrm{B}}^{\mathrm{diag}}(d) = 0$. If we express the matrix d in the form

$$d = \frac{1}{4}\sum_{n_1,n_2=0}^{3} c_{n_1,n_2}\sigma_1^{n_1}\otimes\sigma_2^{n_2} \equiv \sum_{n=0}^{15} C_n\Omega^n, \tag{C.52}$$

with $\sigma^0 = \mathcal{I}$ (single-site identity), $\sigma^1 = \sigma^z$, $\sigma^2 = \sigma^x$ and $\sigma^3 = \sigma^y$, and with $\Omega^n = 1/4(\sigma_1^{n_1}\otimes\sigma_2^{n_2})$ the basis elements for two sites satisfying $4\mathrm{tr}(\Omega^{n\dagger}\Omega^m) = \delta_{nm}$,

it is easily shown that $d = C_0\Omega^0 + C_1\Omega^1 + C_4\Omega^4 + C_5\Omega^5$, with coefficients

$$\begin{aligned} C_0 &= d_0 + d_1 + d_2 + d_3, \qquad & C_1 &= d_0 - d_1 + d_2 - d_3, \\ C_4 &= d_0 + d_1 - d_2 - d_3, \qquad & C_5 &= d_0 - d_1 - d_2 + d_3. \end{aligned} \tag{C.53}$$

Then it is easily shown that the conditions specified above are satisfied if the non-zero elements of the matrix representation of the "diagonal" superoperator are

$$(\mathcal{L}_{\mathrm{B}}^{\mathrm{diag}})_{m,m} = -1, \quad m = 1, \ldots, 15 \qquad (\mathcal{L}_{\mathrm{B}}^{\mathrm{diag}})_{j,0} = C_j/C_0, \quad j = 1, 4, 5. \tag{C.54}$$

We now use the "diagonal" superoperator to define the matrix form of the superoperator $\mathcal{L}_{\mathrm{B}}$ inducing the thermal state ρ_{B}. First we express ρ_{B} in the Ω^n basis, $\rho_{\mathrm{B}} = \sum_{n=0}^{15} \rho_n \Omega^n$. So the matrix representations of the superoperators satisfy

$$\sum_{m,n} C_m (\mathcal{L}_{\mathrm{B}}^{\mathrm{diag}})_{m,n} C_n = 0, \quad \sum_{m,n} \rho_m (\mathcal{L}_{\mathrm{B}})_{m,n} \rho_n = 0, \tag{C.55}$$

for $m, n = 0, \ldots, 15$. Combining the previous results it is shown that

$$C_m = 4 \sum_n \rho_n \mathrm{tr}(V \Omega^n V^\dagger \Omega^m). \tag{C.56}$$

Replacing this result in the left equality of Eq. (C.55), it is obtained that

$$\sum_{i,j} \rho_i \left(\sum_{m,n} \left(R^\dagger\right)_{im} \left(\mathcal{L}_{\mathrm{B}}^{\mathrm{diag}}\right)_{m,n} R_{n,j} \right) \rho_j = 0, \tag{C.57}$$

where we have defined the matrix elements $R_{i,j} = 1/4\mathrm{tr}\left(V^\dagger \Omega^i V \Omega^j\right)$. Comparing the second equality of Eq. (C.55) and Eq. (C.57), we finally obtain $\mathcal{L}_{\mathrm{B}} = R^\dagger \mathcal{L}_{\mathrm{B}}^{\mathrm{diag}} R$, which relates the matrix forms of the "diagonal" and complete superoperators.

Appendix D

Analytic approach to nonequilibrium noninteracting spin chains

Following the method proposed by Žnidarič [178, 181], we derive in the present Appendix an analytic approximation for the NESS of two limit cases of the system of non-interacting ($\Delta = 0$) incoherently coupled spin chains, namely for $\Lambda = 2$ and $\Lambda \to \infty$. We consider first the case of two chains, and propose the following ansatz for the total NESS:

$$\rho = \frac{1}{2^{2N}} \left(I + \sum_{\lambda=1}^{2} \sum_{j=1}^{N} a_j^{(\lambda)} \sigma_j^{z(\lambda)} + \frac{b}{8} \sum_{\lambda=1}^{2} \sum_{k=1}^{N-1} j_k^{(\lambda)} + \cdots \right) \equiv \frac{1}{2^{2N}} \left(I + A + B + \cdots \right). \quad \text{(D.1)}$$

Here I is the identity operator of the entire system, and A and B are functions of spin operators in z direction and spin currents, respectively. As seen below, A and B scale with f, so the approximation only gives the NESS up to first order in the driving strength. Nevertheless, this is enough to obtain exact results of the current and magnetisation of the chains for all values of f, since to obtain r-point correlation functions, an expansion up to order r is needed [181]. It is easily shown that the local magnetisation and the spin current are given by $\langle \sigma_j^{z(\lambda)} \rangle = \mathrm{Tr}(\rho \sigma_j^{z(\lambda)}) = a_j^{(\lambda)}$ and $\langle j_k^{(\lambda)} \rangle = \mathrm{Tr}(\rho j_k^{(\lambda)}) = b$. The master equation for the NESS reads

$$d\rho/dt = \mathcal{L}_{\mathrm{H}}(\rho) + \mathcal{L}_{\mathrm{driv}}(\rho) + \mathcal{L}_{\mathrm{d}}(\rho) + \mathcal{L}_{\mathrm{inc}}(\rho) = 0, \quad \text{(D.2)}$$

where $\mathcal{L}_{\rm H}(\rho) = -i[H,\rho]$, and $\mathcal{L}_{\rm driv}(\rho)$, $\mathcal{L}_{\rm d}(\rho)$ and $\mathcal{L}_{\rm inc}(\rho)$ are the Lindblad terms corresponding to driving at the boundaries, dephasing and interchain coupling, respectively. Since both chains are equal, they have the same dynamics and steady state, so we set $a_j^{(\lambda)} = a_j$. Using the ansatz we obtain, up to order f

$$\mathcal{L}_{\rm H}(\rho) = \frac{1}{2^{2N}} \sum_{\lambda=1}^{2} \Big(b(\sigma_N^{z(\lambda)} - \sigma_1^{z(\lambda)}) + \sum_{i=1}^{N-1} (a_i - a_{i+1}) j_i^{(\lambda)} \Big) \tag{D.3}$$

$$\mathcal{L}_{\rm d}(\rho) = -\frac{\gamma_{\rm d}}{2^{2N}} \frac{b}{2} \sum_{\lambda=1}^{2} \sum_{k=1}^{N-1} j_k^{(\lambda)}, \qquad \mathcal{L}_{\rm inc}(\rho) = -\frac{\gamma}{2^{2N}} \frac{b}{8} \sum_{\lambda=1}^{2} \sum_{k=1}^{N-1} j_k^{(\lambda)}, \tag{D.4}$$

$$\mathcal{L}_{\rm driv}(\rho) = \frac{1}{2^{2N}} \sum_{\lambda=1}^{2} \Gamma \Big(f\sigma_1^{z(\lambda)} - a_1 \sigma_1^{z(\lambda)} - \frac{b}{16} j_1^{(\lambda)} - f\sigma_N^{z(\lambda)} - a_N \sigma_N^{z(\lambda)} - \frac{b}{16} j_{N-1}^{(\lambda)} \Big). \tag{D.5}$$

To obtain the $N+1$ coefficients b and a_i we need $N+1$ different equations, which result from equating to zero the coefficients in front of each operator. From the equations in front of $\sigma_1^{z(\lambda)}$ and $\sigma_N^{z(\lambda)}$ we obtain $a_1 = f - b/\Gamma$ and $a_N = -a_1$. From the equations of the coefficients in front of $j_i^{(\lambda)}$ we find (with $1 < i < N$)

$$a_i = f - b\Big(\frac{\Gamma}{16} + \frac{1}{\Gamma} + (i-1)\frac{\gamma}{8} + (i-1)\frac{\gamma_{\rm d}}{2} \Big), \quad b = \frac{4f}{\frac{\Gamma}{4} + \frac{4}{\Gamma} + (N-1)\frac{\gamma}{4} + (N-1)\gamma_{\rm d}}. \tag{D.6}$$

Note that up to $O(f)$, the total state of the system ρ is a product of the states of each chain ρ_1 and ρ_2 ($\rho = \rho_1 \otimes \rho_2$, mean-field approximation), given by

$$\rho_\lambda = \frac{1}{2^N} \Big(I + \sum_{j=1}^{N} a_j \sigma_j^{(\lambda)z} + \frac{b}{8} \sum_{k=1}^{N-1} j_k^{(\lambda)} \Big), \tag{D.7}$$

For the case $\Lambda \to \infty$ with homogeneous incoherent coupling γ, described in Section 9.1.2 (self-coupled chain), we assume an ansatz of the form (D.7), and obtain

$$\mathcal{L}_{\rm inc}(\rho) = -\frac{\gamma}{2^N} \frac{b}{4} \sum_{k=1}^{N-1} j_k. \tag{D.8}$$

The NESS is then equivalent to that of of two chains, with $\gamma/2$ instead of $\gamma/4$.

Bibliography

[1] P. A. Lee, N. Nagaosa, and X.-G. Wen. Doping a Mott insulator: Physics of high-temperature superconductivity. *Rev. Mod. Phys.*, 78:17–85, 2006.

[2] M. Z. Hasan and C. L. Kane. *Colloquium*: Topological insulators. *Rev. Mod. Phys.*, 82:3045–3067, Nov 2010.

[3] N. W. Ashcroft and N. D. Mermin. *Solid State Physics*. Thomson Learning, United States, 1976.

[4] S. Blundell. *Magnetism in Condensed Matter*. Oxford University Press, Oxford, 2009.

[5] H. Bethe. Zur Theorie der Metalle. Eigenwerte un Eigenfunktionen der linearen Atomkette. *Z. Phys.*, 71:205, 1931.

[6] B. Sutherland. *Beautiful Models. 70 Years of Exactly Solved Quantum Many-Body Problems*. World Scientific, Singapore, 2007.

[7] M. Takahashi. *Thermodynamics of One-Dimensional Solvable Models*. Cambridge University Press, 1999.

[8] F. Heidrich-Meisner, A. Honecker, D. C. Cabra, and W. Brenig. Zero-frequency transport properties of one-dimensional spin-$\frac{1}{2}$ systems. *Phys. Rev. B*, 68:134436, 2003.

[9] D. Gobert, C. Kollath, U. Schollwöck, and G. Schütz. Real-time dynamics in spin-1/2 chains with adaptive time-dependent density matrix renormalization group. *Phys. Rev. E*, 71:036102, 2005.

[10] S. Langer, F. Heidrich-Meisner, J. Gemmer, I. P. McCulloch, and U. Schollwöck. Real-time study of diffusive and ballistic transport in spin-1/2 chains using the adaptive time-dependent density matrix renormalization group method. *Phys. Rev. B*, 79(21):214409, 2009.

[11] T. Prosen and M. Žnidarič. Matrix product simulations of non-equilibrium steady states of quantum spin chains. *J. Stat. Mech.*, page P02035, 2009.

[12] M. Žnidarič. Spin transport in a one-dimensional anisotropic heisenberg model. *Phys. Rev. Lett.*, 106:220601, 2011.

[13] C. Karrasch, J. E. Moore, and F. Heidrich-Meisner. Real-time and real-space spin and energy dynamics in one-dimensional spin-$\frac{1}{2}$ systems induced by local quantum quenches at finite temperatures. *Phys. Rev. B*, 89:075139, 2014.

[14] X. Zotos, F. Naef, and P. Prelovšek. Transport and conservation laws. *Phys. Rev. B*, 55:11029, 1997.

[15] A. Klümper and K. Sakai. The thermal conductivity of the spin-$\frac{1}{2}$ XXZ chain at arbitrary temperature. *J. Phys. A: Math. Gen.*, 35:2173, 2002.

[16] K. Sakai and A. Klümper. Non-dissipative thermal transport in the massive regimes of the XXZ chain. *J. Phys. A: Math. Gen.*, 36:11617, 2003.

[17] K. Louis and C. Gros. Diverging magnetothermal response in the one-dimensional Heisenberg chain. *Phys. Rev. B*, 67:224410, 2003.

[18] F. Heidrich-Meisner, A. Honecker, and W. Brenig. Transport in quasi one-dimensional spin-1/2 systems. *Eur. Phys. J. Special Topics*, 151:135, 2007.

[19] S. Langer, M. Heyl, I. P. McCulloch, and F. Heidrich-Meisner. Real-time energy dynamics in spin-1/2 Heisenberg chains. *Phys. Rev. B*, 84:205115, 2011.

[20] G. Benenti, G. Casati, T. Prosen, and D. Rossini. Negative differential conductivity in far-from-equilibrium quantum spin chains. *Europhys. Lett.*, 85:37001, 2009.

[21] G. Benenti, G. Casati, T. Prosen, D. Rossini, and M. Žnidarič. Charge and spin transport in strongly correlated one-dimensional quantum systems driven far from equilibrium. *Phys. Rev. B*, 80:35110, 2009.

[22] M. Žnidarič. Transport in a one-dimensional isotropic Heisenberg model at high temperature. *J. Stat. Mech.*, 2011:P12008, 2011.

[23] V. Popkov. Alternation of sign of magnetization current in driven XXZ chains with twisted XY boundary gradients. *J. Stat. Mech.*, 2012:P12015, 2012.

[24] V. Popkov and M. Salerno. Anomalous currents in a driven XXZ chain with boundary twisting at weak coupling or weak driving. *J. Stat. Mech.*, 2013:P02040, 2013.

[25] V. Popkov, Mario Salerno, and G. M. Schütz. Behavior of magnetic currents in anisotropic Heisenberg spin chains out of equilibrium. *Phys. Rev. E*, 85:031137, 2012.

[26] U. Schollwöck. The density-matrix renormalization group. *Rev. Mod. Phys.*, 77:259–315, 2005.

[27] F. Verstraete, V. Murg, and J. I. Cirac. Matrix product states, projected entangled pair states, and variational renormalization group methods for quantum spin chains. *Adv. Phys.*, 57:143, 2008.

[28] J. I. Cirac and F. Verstraete. Renormalization and tensor product states in spin chains and lattices. *J. Phys. A: Math. Theor.*, 42:504004, 2009.

[29] U. Schollwöck. The density-matrix renormalization group in the age of matrix product states. *Ann. Phys.*, 326:96, 2011.

[30] G. Vidal. Efficient simulation of one-dimensional quantum many-body systems. *Phys. Rev. Lett.*, 93:040502, 2004.

[31] M. Zwolak and G. Vidal. Mixed-state dynamics in one-dimensional quantum lattice systems: A time-dependent superoperator renormalization algorithm. *Phys. Rev. Lett.*, 93:207205, 2004.

[32] F. Verstraete, J. J. Garcia-Ripoll, and J. I. Cirac. Matrix product density operators: simulation of finite-temperature and dissipative systems. *Phys. Rev. Lett.*, 93:207204, 2004.

[33] M. Georgescu, I. S. Ashhab, and Franco Nori. Quantum simulation. *Rev. Mod. Phys.*, 86:153–185, 2014.

[34] I. Bloch, J. Dalibard, and W. Zwerger. Many-body physics with ultracold gases. *Rev. Mod. Phys.*, 80:885–964, 2008.

[35] J. Simon, W. S. Bakr, R. Ma, M. E. Tai, P. M. Preiss, and M. Greiner. Quantum simulation of antiferromagnetic spin chains in an optical lattice. *Nature*, 472:307, 2011.

[36] T. Fukuhara, P. Schauß, M. Endres, S. Hild, M. Cheneau, I. Bloch, and C. Gross. Microscopic observation of magnon bound states and their dynamics. *Nature*, 502:76, 2013.

[37] J. P. Brantut, J. Meineke, D. Stadler, S. Krinner, and T. Esslinger. Conduction of ultracold fermions through a mesoscopic channel. *Science*, 337:1069, 2012.

[38] D. Stadler, S. Krinner, J. Meineke, J. P. Brantut, and T. Esslinger. Observing the drop of resistance in the flow of a superfluid Fermi gas. *Nature*, 491:736, 2012.

[39] J. P. Brantut, C. Grenier, J. Meineke, D. Stadler, S. Krinner, C. Kollath, T. Esslinger, and A. Georges. A thermoelectric heat engine with ultracold atoms. *Science*, 342:713, 2013.

[40] G. S. Engel, T. R. Calhoun, E. L. Read, T. K. Ahn, T. Mancal, Y. C. Cheng, R. E. Blankenship, and G. R. Fleming. Evidence for wavelike energy transfer through quantum coherence in photosynthetic systems. *Nature*, 446:782, 2007.

[41] G. S. Schlau-Cohen, A. Ishizaki, T. R. Calhoun, N. S. Ginsberg, M. Ballottari, R. Bassi, and G. R. Fleming. Elucidation of the timescales and origins of quantum electronic coherence in LHCII. *Nature Chem.*, 4:389, 2012.

[42] M. B. Plenio and S. F. Huelga. Dephasing-assisted transport: quantum networks and biomolecules. *New J. Phys.*, 10:113019, 2008.

[43] M. Mohseni, P. Rebentrost, S. Lloyd, and A. Aspuru-Guzik. Environment-assisted quantum walks in photosynthetic energy transfer. *J. Chem. Phys.*, 129:174106, 2008.

[44] I. Kassal and A. Aspuru-Guzik. Environment-assisted quantum transport in ordered systems. *New J. Phys.*, 14:053041, 2012.

[45] S. F. Huelga and M. B. Plenio. Vibrations, quanta and biology. *Contemp. Phys.*, 54:181, 2013.

[46] F. Verstraete, M. M. Wolf, and J. I. Cirac. Quantum computation and quantum-state engineering driven by dissipation. *Nat. Phys.*, 5:633, 2009.

[47] S. Diehl, A. Micheli, A. Kantian, B. Kraus, H. P. Büchler, and P. Zoller. Quantum states and phases in driven open quantum systems with cold atoms. *Nat. Phys.*, 4:878, 2008.

[48] Z. Cai and T. Barthel. Algebraic versus exponential decoherence in dissipative many-particle systems. *Phys. Rev. Lett.*, 111:150403, 2013.

[49] E. Lieb, T. Schultz, and D. Mattis. Two soluble models of an antiferromagnetic chain. *Ann. Phys. (N.Y.)*, 16:407, 1961.

[50] G. D. Mahan. *Many-Particle Physics. Third Edition.* Kluwer Academic/-Plenum Publishers, New York, 2000.

[51] C. D. Batista and G. Ortiz. Algebraic approach to interacting quantum systems. *Adv. Phys.*, 53:1, 2004.

[52] M. Karbach and G. Müller. Introduction to the Bethe Ansatz I. *Comput. Phys.*, 11:36, 1997.

[53] T. Giamarchi. *Quantum Physics in One Dimension.* Oxford University Press, Oxford, 2004.

[54] M. Karbach, K. Hu, and G. Müller. Introduction to the Bethe Ansatz II—. *arXiv:cond-mat/0008018*, 2000.

[55] Yichen Huang, C. Karrasch, and J. E. Moore. Scaling of electrical and thermal conductivities in an almost integrable chain. *Phys. Rev. B*, 88:115126, 2013.

[56] E. Orignac, R. Chitra, and R. Citro. Thermal transport in one-dimensional spin gap systems. *Phys. Rev. B*, 67:134426, 2003.

[57] J. Sirker, R. G. Pereira, and I. Affleck. Diffusion and ballistic transport in one-dimensional quantum systems. *Phys. Rev. Lett.*, 103:216602, 2009.

[58] J. Sirker, R. G. Pereira, and I. Affleck. Conservation laws, integrability, and transport in one-dimensional quantum systems. *Phys. Rev. B*, 83(3):035115, 2011.

[59] Caux. J.-S. and J. Mossel. Remarks on the notion of quantum integrability. *J. Stat. Mech.*, 2011:P02023, 2011.

[60] T. Prosen and M. Žnidarič. Eigenvalue Statistics as an Indicator of Integrability of Nonequilibrium Density Operators. *Phys. Rev. Lett.*, 111:124101, 2013.

[61] D. A. Rabson, B. N. Narozhny, and A. J. Millis. Crossover from Poisson to Wigner-Dyson level statistics in spin chains with integrability breaking. *Phys. Rev. B*, 69:054403, 2004.

[62] C. Mejía-Monasterio, T. Prosen, and M. Casati. Fourier's law in a quantum spin chain and the onset of quantum chaos. *Europhys. Lett.*, 72:520, 2005.

[63] M. Žnidarič, T. Prosen, G. Benenti, G. Casati, and D. Rossini. Thermalization and ergodicity in one-dimensional many-body open quantum systems. *Phys. Rev. E*, 81:051135, 2010.

[64] E. Canovi, D. Rossini, R. Fazio, G. E. Santoro, and A. Silva. Quantum quenches, thermalization, and many-body localization. *Phys. Rev. B*, 83:094431, 2011.

[65] M. V. Berry and M. Tabor. Level clustering in the regular spectrum. *Proc. R. Soc. Lond. A*, 356:375, 1977.

[66] F. Haake. *Quantum signatures of chaos.* Springer, Berlin, 2001.

[67] A. A. Tsirlin, A. Maisuradze, J. Sichelschmidt, W. Schnelle, P. Höhn, R. Zinke, J. Richter, and H. Rosner. Hidden magnetic order in CuNCN. *Phys. Rev. B*, 85:224431, 2012.

[68] T. Ami, M. K. Crawford, R. L. Harlow, Z. R. Wang, D. C. Johnston, Q. Huang, and R. W. Erwin. Magnetic susceptibility and low-temperature structure of the linear chain cuprate Sr_2CuO_3. *Phys. Rev. B*, 51:5994–6001, 1995.

[69] A. V. Sologubenko, K. Giannò, H. R. Ott, A. Vietkine, and A. Revcolevschi. Heat transport by lattice and spin excitations in the spin-chain compounds $SrCuO_2$ and Sr_2CuO_3. *Phys. Rev. B*, 64:054412, 2001.

[70] A. V. Rozhkov and A. L. Chernyshev. Thermal conductivity of quasi-one-dimensional antiferromagnetic spin-chain materials. *Phys. Rev. Lett.*, 94:087201, 2005.

[71] N. Hlubek, X. Zotos, S. Singh, R. Saint-Martin, A. Revcolevschi, B. Büchner, and C. Hess. Spinon heat transport and spin-phonon interaction in the spin-1/2 Heisenberg chain cuprates Sr_2CuO_3 and $SrCuO_2$. *J. Stat. Mech.*, 2012:P03006, 2012.

[72] N. Hlubek. *Magnetic heat transport in one-dimensional quantum antiferromagnets*. PhD thesis, Technische Universität Dresden, 2010.

[73] A. A. Tsirlin and H. Rosner. Uniform spin-chain physics arising from NCN bridges in CuNCN, the nitride analog of the copper oxides. *Phys. Rev. B*, 81:024424, 2010.

[74] A. V. Sologubenko, H. R. Ott, G. Dhalenne, and A. Revcolevschi. Universal behavior of spin-mediated energy transport in $S = 1/2$ chain cuprates: $BaCu_2Si_2O_7$ as an example. *Europhys. Lett.*, 62:540, 2003.

[75] S. Lebernegg, A. A. Tsirlin, O. Janson, R. Nath, J. Sichelschmidt, Yu. Skourski, G. Amthauer, and H. Rosner. Magnetic model for $A_2CuP_2O_7$ (A =Na, Li): One-dimensional versus two-dimensional behavior. *Phys. Rev. B*, 84:174436, 2011.

[76] M. B. Stone, D. H. Reich, C. Broholm, K. Lefmann, C. Rischel, C. P. Landee, and M. M. Turnbull. Extended Quantum Critical Phase in a Magnetized Spin-1/2 Antiferromagnetic Chain. *Phys. Rev. Lett.*, 91:037205, 2003.

[77] A. V. Sologubenko, K. Berggold, T. Lorenz, A. Rosch, E. Shimshoni, M. D. Phillips, and M. M. Turnbull. Magnetothermal Transport in the Spin-$\frac{1}{2}$ Chains of Copper Pyrazine Dinitrate. *Phys. Rev. Lett.*, 98:107201, 2007.

[78] E. Shimshoni, D. Rasch, P. Jung, A. V. Sologubenko, and A. Rosch. Large thermomagnetic effects in weakly disordered Heisenberg chains. *Phys. Rev. B*, 79:064406, 2009.

[79] J. B. Torrance and M. Tinkham. Excitation of Multiple-Magnon Bound States in $CoCl_2 \cdot 2H_2O$. *Phys. Rev.*, 187:595–606, 1969.

[80] S. K. Niesen, G. Kolland, M. Seher, O. Breunig, M. Valldor, M. Braden, B. Grenier, and T. Lorenz. Magnetic phase diagrams, domain switching, and quantum phase transition of the quasi-one-dimensional Ising-like antiferromagnet $BaCo_2V_2O_8$. *Phys. Rev. B*, 87:224413, 2013.

[81] R. Coldea, D. A. Tennant, E. M. Wheeler, E. Wawrzynska, D. Prabhakaran, M. Telling, K. Habicht, P. Smeibidl, and K. Kiefer. Quantum Criticality in an Ising Chain: Experimental Evidence for Emergent E8 Symmetry. *Science*, 327:177, 2010.

[82] O. Janson, A. A. Tsirlin, and H. Rosner. Antiferromagnetic spin-1/2 chains in $(NO)Cu(NO_3)_3$: A microscopic study. *Phys. Rev. B*, 82:184410, 2010.

[83] H.-A. Krug von Nidda, L. E. Svistov, M. V. Eremin, R. M. Eremina, A. Loidl, V. Kataev, A. Validov, A. Prokofiev, and W. Aßmus. Anisotropic exchange in $LiCuVO_4$ probed by ESR. *Phys. Rev. B*, 65:134445, 2002.

[84] D. V. Zakharov, J. Deisenhofer, H.-A. Krug von Nidda, P. Lunkenheimer, J. Hemberger, M. Hoinkis, M. Klemm, M. Sing, R. Claessen, M. V. Eremin, S. Horn, and A. Loidl. Spin dynamics in the low-dimensional magnet TiOCl. *Phys. Rev. B*, 73:094452, 2006.

[85] R. M. Eremina, M. V. Eremin, V. N. Glazkov, H.-A. Krug von Nidda, and A. Loidl. Anisotropic exchange interactions in $CuGeO_3$ probed by electron spin resonance spectroscopy. *Phys. Rev. B*, 68:014417, 2003.

[86] D. Schmidiger, S. Mühlbauer, A. Zheludev, P. Bouillot, T. Giamarchi, C. Kollath, G. Ehlers, and A. M. Tsvelik. Symmetric and asymmetric excitations of a strong-leg quantum spin ladder. *Phys. Rev. B*, 88:094411, 2013.

[87] A. A. Tsirlin, I. Rousochatzakis, D. Kasinathan, O. Janson, R. Nath, F. Weickert, C. Geibel, A. M. Läuchli, and H. Rosner. Bridging frustrated-spin-chain and spin-ladder physics: Quasi-one-dimensional magnetism of $BiCu_2PO_6$. *Phys. Rev. B*, 82:144426, 2010.

[88] C. Hess, H. ElHaes, A. Waske, B. Büchner, C. Sekar, G. Krabbes, F. Heidrich-Meisner, and W. Brenig. Linear Temperature Dependence of the Magnetic Heat Conductivity in $CaCu_2O_3$. *Phys. Rev. Lett.*, 98:027201, 2007.

[89] A. V. Sologubenko, K. Giannó, H. R. Ott, U. Ammerahl, and A. Revcolevschi. Thermal Conductivity of the Hole-Doped Spin Ladder System $Sr_{14-x}Ca_xCu_{24}O_{41}$. *Phys. Rev. Lett.*, 84:2714, 2000.

[90] C. Hess, H. ElHaes, B. Büchner, U. Ammerahl, M. Hücker, and A. Revcolevschi. Magnon-Hole Scattering and Charge Order in $Sr_{14-x}Ca_xCu_{24}O_{41}$. *Phys. Rev. Lett.*, 93:027005, 2004.

[91] H. Yamaguchi, K. Iwase, T. Ono, T. Shimokawa, H. Nakano, Y. Shimura, N. Kase, S. Kittaka, T. Sakakibara, T. Kawakami, and Y. Hosokoshi. Unconventional Magnetic and Thermodynamic Properties of $S = 1/2$ Spin Ladder with Ferromagnetic Legs. *Phys. Rev. Lett.*, 110:157205, 2013.

[92] A. W. Garrett, S. E. Nagler, D. A. Tennant, B. C. Sales, and T. Barnes. Magnetic Excitations in the $(VO)_2P_2O_7$. *Phys. Rev. Lett.*, 79:745–748, 1997.

[93] D. N. Haines and J. E. Drumheller. Bound-magnon dominance of the magnetic susceptibility of the one-dimensional Heisenberg $S = 1/2$ ferromagnet cyclohexylammonium trichlorocuprate (II). *Phys. Rev. Lett.*, 58:2702–2705, 1987.

[94] W. S. Bakr, A. Peng, M. E. Tai, R. Ma, J. Simon, J. I. Gillen, S. Fölling, L. Pollet, and M. Greiner. Probing the Superfluid - to - Mott Insulator Transition at the Single-Atom Level. *Science*, 329:547, 2010.

[95] J. F. Sherson, C. Weitenberg, M. Endres, M. Cheneau, I. Bloch, and S. Kuhr. Single-atom-resolved fluorescence imaging of an atomic Mott insulator. *Nature*, 467:68, 2010.

[96] L.-M. Duan, E. Demler, and M. D. Lukin. Controlling spin exchange interactions of ultracold atoms in optical lattices. *Phys. Rev. Lett.*, 91:090402, 2003.

[97] S. Jesenko and M. Žnidarič. Finite-temperature magnetization transport of the one-dimensional anisotropic Heisenberg model. *Phys. Rev. B*, 84:174438, 2011.

[98] C. Karrasch, J. H. Bardarson, and J. E. Moore. Finite-Temperature Dynamical Density Matrix Renormalization Group and the Drude Weight of Spin-1/2 Chains. *Phys. Rev. Lett.*, 108:227206, 2012.

[99] C. Karrasch, J. Hauschild, S. Langer, and F. Heidrich-Meisner. Drude weight of the spin-$\frac{1}{2}$ XXZ chain: Density matrix renormalization group versus exact diagonalization. *Phys. Rev. B*, 87:245128, 2013.

[100] S. J. Blundell and K. M. Blundell. *Concepts in Thermal Physics. Second Edition.* Oxford University Press, Oxford, 2010.

[101] F. Heidrich-Meisner. *Transport Properties Of Low-Dimensional Quantum Spin Systems.* PhD thesis, Technischen Universität Carolo-Wilhelmina zu Braunschweig, 2005.

[102] S. Furukawa, D. Ikeda, and K. Sakai. Thermomagnetic power and figure of merit for spin-1/2 Heisenberg chain. *J. Phys. Soc. Jpn.*, 74:3241, 2005.

[103] P. Prelovšek, S. El Shawish, X. Zotos, and M. Long. Anomalous scaling of conductivity in integrable fermion systems. *Phys. Rev. B*, 70:205129, 2004.

[104] S. Grossjohann and W. Brenig. Hydrodynamic limit for the spin dynamics of the Heisenberg chain from quantum Monte Carlo calculations. *Phys. Rev. B*, 81:012404, 2010.

[105] J. Herbrych, P. Prelovšek, and X. Zotos. Finite-temperature Drude weight within the anisotropic Heisenberg chain. *Phys. Rev. B*, 84:155125, 2011.

[106] R. Steinigeweg and J. Gemmer. Density dynamics in translationally invariant spin-$\frac{1}{2}$ chains at high temperatures: A current-autocorrelation approach to finite time and length scales. *Phys. Rev. B*, page 184402, 2009.

[107] N. Bloembergen. On the interaction of nuclear spins in a crystalline lattice. *Physica (Amsterdam)*, 15:386, 1949.

[108] P. G. de Gennes. Inelastic magnetic scattering of neutrons at high temperatures. *J. Phys. Chem. Solids*, 4:223, 1958.

[109] M. Steiner, J. Villain, and C. G. Windsor. Theoretical and experimental studies on one-dimensional magnetic systems. *Adv. Phys.*, 25:87, 1976.

[110] K. Fabricius and B. M. McCoy. Spin diffusion and the spin-1/2 XXZ chain at $T = \infty$ from exact diagonalization. *Phys. Rev. B*, 57:8340, 1998.

[111] K. Sakai and A. Klümper. Non-dissipative Thermal Transport and Magnetothermal Effect for the Spin-1/2 Heisenberg Chain. *J. Phys. Soc. Jpn.*, 74:196, 2005.

[112] M. Suzuki. Ergodicity, constants of motion, and bounds for susceptibilities. *Physica (Amsterdam)*, 51:277, 1971.

[113] P. Mazur. Non-ergodicity of phase functions in certain systems. *Physica (Amsterdam)*, 43:533, 1969.

[114] T. Prosen. Open XXZ Spin Chain: Nonequilibrium Steady State and a Strict Bound on Ballistic Transport. *Phys. Rev. Lett.*, 106:217206, 2011.

[115] T. Prosen. Families of Quasilocal Conservation Laws and Quantum Spin Transport. *Phys. Rev. Lett.*, 111:057203, 2013.

[116] B. S. Shastry and B. Sutherland. Twisted boundary conditions and effective mass in Heisenberg-Ising and Hubbard rings. *Phys. Rev. Lett.*, 65:243–246, 1990.

[117] J. Benz, T. Fukui, A. Klümper, and C. Scheeren. On the Finite Temperature Drude Weight of the Anisotropic Heisenberg Model. *J. Phys. Soc. Jpn. Suppl.*, 74:181, 2005.

[118] X. Zotos. Finite Temperature Drude Weight of the One-Dimensional Spin-1/2 Heisenberg Model. *Phys. Rev. Lett.*, 82:1764–1767, 1999.

[119] R. Steinigeweg and W. Brenig. Spin Transport in the XXZ Chain at Finite Temperature and Momentum. *Phys. Rev. Lett.*, 107:250602, 2011.

[120] R. Steinigeweg, J. Gemmer, and W. Brenig. Spin-current autocorrelations from single pure-state propagation. *Phys. Rev. Lett.*, 112:120601, 2014.

[121] J. V. Alvarez and C. Gros. Conductivity of quantum spin chains: A quantum Monte Carlo approach. *Phys. Rev. B*, 66:094403, 2002.

[122] C. Karrasch, R. Ilan, and J. E. Moore. Nonequilibrium thermal transport and its relation to linear response. *Phys. Rev. B*, 88:195129, 2013.

[123] F. Heidrich-Meisner, A. Honecker, and W. Brenig. Thermal transport of the XXZ chain in a magnetic field. *Phys. Rev. B*, 71:184415, 2005.

[124] A. Läuchli and C. Kollath. Spreading of correlations and entanglement after a quench in the one-dimensional BoseHubbard model. *J. Stat. Mech.*, 2008:P05018, 2008.

[125] J. P. Ronzheimer, M. Schreiber, S. Braun, S. S. Hodgman, S. Langer, I. P. McCulloch, F. Heidrich-Meisner, I. Bloch, and U. Schneider. Expansion dynamics of interacting bosons in homogeneous lattices in one and two dimensions. *Phys. Rev. Lett.*, 110:205301, 2013.

[126] L. Vidmar, S. Langer, I. P. McCulloch, U. Schneider, U. Schollwöck, and F. Heidrich-Meisner. Sudden expansion of Mott insulators in one dimension. *Phys. Rev. B*, 88:235117, 2013.

[127] M. Rigol, V. Dunjko, and M. Olshanii. Thermalization and its mechanism for generic isolated quantum systems. *Nature*, 452:854, 2008.

[128] Marcos Rigol. Breakdown of thermalization in finite one-dimensional systems. *Phys. Rev. Lett.*, 103:100403, 2009.

[129] S. Datta. *Quantum Transport: Atom to Transistor*. Cambridge University Press, 2005.

[130] H.-P. Breuer and F. Petruccione. *The theory of open quantum systems*. Oxford University Press, Oxford, 2002.

[131] T. Prosen and M. Žnidarič. Diffusive high-temperature transport in the one-dimensional Hubbard model. *Phys. Rev. B*, 86:125118, 2012.

[132] T. Prosen. Exact Nonequilibrium Steady State of an Open Hubbard Chain. *Phys. Rev. Lett.*, 112:030603, 2014.

[133] I. Pižorn. One-dimensional Bose-Hubbard model far from equilibrium. *Phys. Rev. A*, 88:043635, 2013.

[134] M. Žnidarič. Coexistence of diffusive and ballistic transport in a simple spin ladder. *Phys. Rev. Lett.*, 110:070602, 2013.

[135] M. Žnidarič. Magnetization transport in spin ladders and next-nearest-neighbor chains. *Phys. Rev. B*, 88:205135, 2013.

[136] C. Mejía-Monasterio and Wichterich. Heat transport in quantum spin chains. Stochastic baths vs quantum trajectories. *Eur. Phys. J. Special Topics*, 151:113, 2007.

[137] D. Manzano, M. Tiersch, A. Asadian, and H. J. Briegel. Quantum transport efficiencies and Fourier's law. *Phys. Rev. E*, 86:061118, 2012.

[138] J. Wu and M. Berciu. Heat transport in quantum spin chains: the relevance of integrability. *Phys. Rev. B*, 83:214416, 2011.

[139] H. Wichterich, M. J. Henrich, H.-P. Breuer, J. Gemmer, and M. Michel. Modeling heat transport through completely positive maps. *Phys. Rev. E*, 76:031115, 2007.

[140] M. Michel, O. Hess, H. Wichterich, and J. Gemmer. Transport in open spin chains: A Monte Carlo wave-function approach. *Phys. Rev. B*, 77:104303, 2008.

[141] L. Zhang, J.-S. Wang, and B. Li. Ballistic magnetothermal transport in a Heisenberg spin chain at low temperatures. *Phys. Rev. B*, 78:144416, 2008.

[142] S. Ajisaka, F. Barra, C. Mejí-Monasterio, and T. Prosen. Nonequlibrium particle and energy currents in quantum chains connected to mesoscopic Fermi reservoirs. *Phys. Rev. B*, 86:125111, 2012.

[143] S. Krinner, D. Stadler, J. Meineke, J.-P. Brantut, and T. Esslinger. Superfluidity with disorder in a thin film of quantum gas. *Phys. Rev. Lett.*, 110:100601, 2013.

[144] C. Hess, C. Baumann, U. Ammerahl, B. Büchner, F. Heidrich-Meisner, W. Brenig, and A. Revcolevschi. Magnon heat transport in $(\mathrm{Sr}, \mathrm{Ca}, \mathrm{La})_{14}\mathrm{Cu}_{24}\mathrm{O}_{41}$. *Phys. Rev. B*, 64:184305, 2001.

[145] M. Montagnese, M. Otter, X. Zotos, D. A. Fishman, N. Hlubek, O. Mityashkin, C. Hess, R. Saint-Martin, S. Singh, A. Revcolevschi, and P. H. M. van Loosdrecht. Phonon-magnon interaction in low dimensional quantum magnets observed by dynamic heat transport measurements. *Phys. Rev. Lett.*, 110:147206, 2013.

[146] N. Hlubek, P. Ribeiro, R. Saint-Martin, A. Revcolevschi, G. Roth, G. Behr, B. Büchner, and C. Hess. Ballistic heat transport of quantum spin excitations as seen in $SrCuO_2$. *Phys. Rev. B*, 81:020405, 2010.

[147] N. Hlubek, P. Ribeiro, R. Saint-Martin, S. Nishimoto, A. Revcolevschi, S.-L. Drechsler, G. Behr, J. Trinckauf, J. E. Hamann-Borrero, J. Geck, B. Büchner, and C. Hess. Bond disorder and breakdown of ballistic heat transport in the spin-$\frac{1}{2}$ antiferromagnetic Heisenberg chain as seen in Ca-doped $SrCuO_2$. *Phys. Rev. B*, 84:214419, 2011.

[148] A. Mohan, N. Sekhar Beesetty, N. Hlubek, R. Saint-Martin, A. Revcolevschi, B. Büchner, and C. Hess. Bond disorder and spinon heat transport in the $S = \frac{1}{2}$ Heisenberg spin chain compound Sr_2CuO_3: From clean to dirty limits. *Phys. Rev. B*, 89:104302, 2014.

[149] E. Shimshoni, N. Andrei, and A. Rosch. Thermal conductivity of spin-$\frac{1}{2}$ chains. *Phys. Rev. B*, 68:104401, 2003.

[150] A. L. Chernyshev and A. V. Rozhkov. Thermal transport in antiferromagnetic spin-chain materials. *Phys. Rev. B*, 72:104423, 2005.

[151] T. Kawamata, N. Kaneko, M. Uesaka, M. Sato, and Y. Koike. Enhancement of Thermal Conductivity due to Spinons in the One-Dimensional Spin System $SrCuO_2$. *J. Phys.: Conf. Ser.*, 200:022023, 2010.

[152] C. Hess, B. Büchner, U. Ammerahl, L. Colonescu, F. Heidrich-Meisner, W. Brenig, and A. Revcolevschi. Magnon Heat Transport in Doped La_2CuO_4. *Phys. Rev. Lett.*, 90:197002, 2003.

[153] K. R. Thurber, A. W. Hunt, T. Imai, and F. C. Chou. ^{17}O NMR study of $q = 0$ spin excitations in a nearly ideal $S = 1/2$ 1D Heisenberg antiferromagnet, Sr_2CuO_3, up to 800 K. *Phys. Rev. Lett.*, 87:247202, 2001.

[154] F. L. Pratt, S. J. Blundell, T. Lancaster, C. Baines, and S. Takagi. Low-Temperature Spin Diffusion in a Highly Ideal $S = \frac{1}{2}$ Heisenberg Antiferromagnetic Chain Studied by Muon Spin Relaxation. *Phys. Rev. Lett.*, 96:247203, 2006.

[155] H. Maeter, A. A. Zvyagin, H. Luetkens, G. Pascua, Z. Shermadini, R. Saint-Martin, A. Revcolevschi, C. Hess, B Büchner, and H.-H. Klauss. Low temperature ballistic spin transport in the $S = 1/2$ antiferromagnetic Heisenberg chain compound $SrCuO_2$. *J. Phys.: Condens. Matter*, 25:365601, 2013.

[156] U. Schneider, L. Hackermüller, J. P. Ronzheimer, S. Will, S. Braun, T. Best, I. Bloch, E. Demler, S. Mandt, D. Rasch, and A. Rosch. Fermionic transport and out-of-equilibrium dynamics in a homogeneous Hubbard model with ultracold atoms. *Nature Phys.*, 8:213, 2012.

[157] C. D'Errico, M. Moratti, E. Lucioni, L. Tanzi, B. Deissler, M. Inguscio, G. Modugno, M. B. Plenio, and F. Caruso. Quantum diffusion with disorder, noise and interaction. *New J. Phys.*, 15(4):045007, 2013.

[158] S. Krinner, D. Stadler, D. Husmann, J.-P. Brantut, and T. Esslinger. Observation of quantized conductance in neutral matter. *arXiv:1404.6400*, page 1, 2014.

[159] C. Grenier, C. Kollath, and A. Georges. Probing thermoelectric transport with cold atoms. *arXiv:1209.3942v4*, 2012.

[160] S. R. White and A. E. Feiguin. Real-time evolution using the density matrix renormalization group. *Phys. Rev. Lett.*, 93:076401, 2004.

[161] A. J. Daley, C. Kollath, U. Schollwöck, and G. Vidal. Time-dependent density-matrix renormalization-group using adaptive effective Hilbert spaces. *J. Stat. Mech.*, 2004:P04005, 2004.

[162] G. Vidal. Efficient classical simulation of slightly entangled quantum computations. *Phys. Rev. Lett.*, 91:147902, 2003.

[163] M. A. Nielsen and I. L. Chuang. *Quantum Computation and Quantum Information*. Cambridge University Press, Cambridge, 2000.

[164] M. Žnidarič, T. Prosen, and I. Pižorn. Complexity of thermal states in quantum spin chains. *Phys. Rev. A*, 78:022103, 2008.

[165] K. Modi, A. Brodutch, H. Cable, T. Paterek, and V. Vedral. The classical-quantum boundary for correlations: Discord and related measures. *Rev. Mod. Phys.*, 84:1655–1707, 2012.

[166] G. Vidal, J. I. Latorre, E. Rico, and A. Kitaev. Entanglement in Quantum Critical Phenomena. *Phys. Rev. Lett.*, 90:227902, 2003.

[167] Luigi Amico, Rosario Fazio, Andreas Osterloh, and Vlatko Vedral. Entanglement in many-body systems. *Rev. Mod. Phys.*, 80:517–576, 2008.

[168] Mark Srednicki. Entropy and area. *Phys. Rev. Lett.*, 71:666–669, 1993.

[169] P. Calabrese and J. Cardy. Entanglement entropy and quantum field theory. *J. Stat. Mech.*, 2004:P06002, 2004.

[170] T. Grujic, S. R. Clark, S. Felicetti, G. Romero, E. Solano, D. G. Angelakis, and D. Jaksch. Long-range correlations break mean-field bistabilities in a driven-dissipative XY-model. *To be submitted to Phys. Rev. Lett.*, 2014, 2014.

[171] S. R. White. Density matrix formulation for quantum renormalization groups. *Phys. Rev. Lett.*, 69:2863, 1992.

[172] S. R. White. Density-matrix algorithms for quantum renormalization groups. *Phys. Rev. B*, 48:10345, 1993.

[173] M. Suzuki. General theory of fractal path integrals with applications to many-body theories and statistical physics. *J. Math. Phys.*, 32:400, 1991.

[174] S. Al-Assam, S. R. Clark, D. Jaksch, and TNT Development Team. TNT Library Alpha Version, http://www.tensornetworktheory.org, 2012.

[175] J. J. Mendoza-Arenas, T. Grujic, D. Jaksch, and S. R. Clark. Dephasing enhanced transport in nonequilibrium strongly correlated quantum systems. *Phys. Rev. B*, 87:235130, 2013.

[176] J. J. Mendoza-Arenas, S. Al-Assam, S. R. Clark, and D. Jaksch. Heat transport in an XXZ spin chain: from ballistic to diffusive regimes and dephasing enhancement. *J. Stat. Mech.*, 2013:P07007, 2013.

[177] A. Rivas, A. D. K. Plato, S. F. Huelga, and M. B. Plenio. Markovian master equations: a critical study. *New J. Phys.*, 12:113032, 2010.

[178] M. Žnidarič. Solvable quantum nonequilibrium model exhibiting a phase transition and a matrix product representation. *Phys. Rev. E*, 83(1):011108, 2011.

[179] D. Burgarth and V. Giovannetti. Full Control by Locally Induced Relaxation. *Phys. Rev. Lett.*, 99:100501, 2007.

[180] J. J. Mendoza-Arenas, M. T. Mitchison, S. R. Clark, J. Prior, D. Jaksch, and M. B. Plenio. Transport enhancement from incoherent coupling between one-dimensional quantum conductors. *New J. Phys.*, 16:053016, 2014.

[181] M. Žnidarič. Exact solution for a diffusive nonequilibrium steady state of an open quantum chain. *J. Stat. Mech.*, 2010:L05002, 2010.

[182] T. Prosen. Exact Nonequilibrium Steady State of a Strongly Driven Open XXZ Chain. *Phys. Rev. Lett.*, 107:137201, 2011.

[183] V. Popkov and R. Livi. Manipulating energy and spin currents in nonequilibrium systems of interacting qubits. *New J. Phys.*, 15:023030, 2013.

[184] M. Hartmann, G. Mahler, and O. Hess. Existence of Temperature on the Nanoscale. *Phys. Rev. Lett.*, 93:080402, 2004.

[185] M. Hartmann. Minimal length scales for the existence on local temperature. *Contemp. Phys.*, 47:89, 2006.

[186] Artur García-Saez, Alessandro Ferraro, and Antonio Acín. Local temperature in quantum thermal states. *Phys. Rev. A*, 79:052340, 2009.

[187] T. Kinoshita, T. Wenger, and D. S. Weiss. A quantum Newton's cradle. *Nature*, 440:900, 2006.

[188] M. Rigol, V. Dunjko, V. Yurovsky, and M. Olshanii. Relaxation in a completely integrable many-body quantum system: An *AbInitio* study of the dynamics of the highly excited states of 1d lattice hard-core bosons. *Phys. Rev. Lett.*, 98:050405, 2007.

[189] A. Polkovnikov, K. Sengupta, A. Silva, and M. Vengalattore. Colloquium: Nonequilibrium dynamics of closed interacting quantum systems. *Rev. Mod. Phys.*, 83:863–883, 2011.

[190] M. Rigol and M. Srednicki. Alternatives to eigenstate thermalization. *Phys. Rev. Lett.*, 108:110601, 2012.

[191] P. Jung, R. W. Helmes, and A. Rosch. Transport in Almost Integrable Models: Perturbed Heisenberg Chains. *Phys. Rev. Lett.*, 96:067202, 2006.

[192] T. Prosen and M. Žnidarič. Long-Range Order in Nonequilibrium Interacting Quantum Spin Chains. *Phys. Rev. Lett.*, 105:060603, 2010.

[193] G. Benenti, G. Casati, T. Prosen, and K. Saito. Colloquium: Fundamental aspects of steady state heat to work conversion. *arXiv:1311.4430*, 1:1, 2013.

[194] S. R. White. Minimally Entangled Typical Quantum States at Finite Temperature. *Phys. Rev. Lett.*, 102:190601, 2009.

[195] T. Barthel. Precise evaluation of thermal response functions by optimized density matrix renormalization group schemes. *New J. Phys.*, 15:073010, 2013.

[196] C. Karrasch, J. H. Bardarson, and J. E. Moore. Reducing the numerical effort of finite-temperature density matrix renormalization group calculations. *New J. Phys.*, 15:083031, 2013.

[197] P. Ball. The dawn of quantum biology. *Nature*, 474:272, 2011.

[198] E. Collini and G. D. Scholes. Coherent intrachain energy migration in a conjugated polymer at room temperature. *Science*, 323:369, 2009.

[199] A. W. Chin, J Prior, R. Rosenbach, F. Caycedo-Soler, S. F Huelga, and M. B. Plenio. The role of non-equilibrium vibrational structures in electronic coherence and recoherence in pigmentprotein complexes. *Nat. Phys.*, 9:113, 2013.

[200] H. Lee, Y. C. Cheng, and G. R. Fleming. Coherence dynamics in photosynthesis: protein protection of excitonic coherence. *Science*, 316:1462, 2007.

[201] A. W. Chin, A. Datta, F. Caruso, S. F. Huelga, and M. B. Plenio. Noise-assisted energy transfer in quantum networks and light-harvesting complexes. *New. J. Phys.*, 12:065002, 2010.

[202] F. Caruso, A. W. Chin, A. Datta, S. F. Huelga, and M. B. Plenio. Highly efficient energy excitation transfer in light-harvesting complexes: The fundamental role of noise-assisted transport. *J. Chem. Phys.*, 131:105106, 2009.

[203] G. D. Scholes, G. R. Fleming, A. Olaya-Castro, and R. van Grondelle. Lessons from nature about light harvesting. *Nature Chem.*, 3:763, 2011.

[204] D. Poletti, J.-S. Bernier, A. Georges, and C. Kollath. Interaction-Induced Impeding of Decoherence and Anomalous Diffusion. *Phys. Rev. Lett.*, 109:045302, 2012.

[205] I. Carusotto and C. Ciuti. Quantum fluids of light. *Rev. Mod. Phys.*, 85:299–366, 2013.

[206] D. Jérome and H.J. Schulz. Organic conductors and superconductors. *Advances in Physics*, 31:299–490, 1982.

[207] A. J. Leggett, S. Chakravarty, A. T. Dorsey, Matthew P. A. Fisher, Anupam Garg, and W. Zwerger. Dynamics of the dissipative two-state system. *Rev. Mod. Phys.*, 59:1–85, 1987.

[208] J. L. Bredas, J. E. Norton, J. Cornil, and V. Coropceanu. Molecular understanding of organic solar cells: the challenges. *Acc. Chem. Res.*, 42:1691, 2009.

[209] J. Vogelsang, T. Adachi, J. Brazard, D. A. Vanden-Bout, and P. F. Barbara. Self-assembly of highly ordered conjugated polymer aggregates with long-range energy transfer. *Nature Mater.*, 10:942, 2011.

[210] M. Turlakov and A. J. Leggett. Interlayer c-axis transport in the normal state of cuprates. *Phys. Rev. B*, 63:064518, 2001.

[211] George A. Levin. Phenomenology of conduction in incoherent layered crystals. *Phys. Rev. B*, 70:064515, 2004.

[212] B. Vignolle, B. J. Ramshaw, James Day, David LeBoeuf, Stéphane Lepault, Ruixing Liang, W. N. Hardy, D. A. Bonn, Louis Taillefer, and Cyril Proust. Coherent c-axis transport in the underdoped cuprate superconductor $YBa_2Cu_3O_y$. *Phys. Rev. B*, 85:224524, 2012.

[213] M. V. Kartsovnik, P. D. Grigoriev, W. Biberacher, and N. D. Kushch. Magnetic field induced coherence-incoherence crossover in the interlayer conductivity of a layered organic metal. *Phys. Rev. B*, 79:165120, 2009.

[214] M. Dressel, K. Petukhov, B. Salameh, P. Zornoza, and T. Giamarchi. Scaling behavior of the longitudinal and transverse transport in quasi-one-dimensional organic conductors. *Phys. Rev. B*, 71:075104, 2005.

[215] B. Köhler, E. Rose, M. Dumm, G. Untereiner, and M. Dressel. Comprehensive transport study of anisotropy and ordering phenomena in quasi-one-dimensional $(TMTTF)_2X$ salts ($X = PF_6, AsF_6, SbF_6, BF_4, ClO_4, ReO_4$). *Phys. Rev. B*, 84:035124, 2011.

[216] M. Dressel. Quantum criticality in organic conductors? Fermi liquid versus non-Fermi-liquid behaviour. *J. Phys.: Condens. Matter*, 23:293201, 2011.

[217] V. Kendon and B. Tregenna. Decoherence can be useful in quantum walks. *Phys. Rev. A*, 67:042315, 2003.

[218] D. Manzano. Quantum transport in networks and photosynthetic complexes at the steady state. *PLoS ONE*, 8(2):e57041, 2013.

[219] M. B. Plenio and S. F. Huelga. Entangled light from white noise. *Phys. Rev. Lett.*, 88:197901, 2002.

[220] H. Krauter, C. A. Muschik, K. Jensen, W. Wasilewski, J. M. Petersen, J. I. Cirac, and E. S. Polzik. Entanglement generated by dissipation and steady state entanglement of two macroscopic objects. *Phys. Rev. Lett.*, 107:080503, 2011.

[221] M. Žnidarič. Dephasing-induced diffusive transport in the anisotropic Heisenberg model. *New J. Phys.*, 12:043001, 2010.

[222] A. Bermudez, M. Bruderer, and M. B. Plenio. Controlling and measuring quantum transport of heat in trapped-ion crystals. *Phys. Rev. Lett.*, 111:040601, 2013.

[223] K. Winkler, G. Thalhammer, F. Lang, R. Grimm, J. H. Denschlang, A. J. Daley, A. Kantian, H. P. Büchler, and P. Zoller. Repulsively bound atom pairs in an optical lattice. *Nature*, 441:853, 2006.

[224] H. Schwager, J. I. Cirac, and G. Giedke. Dissipative spin chains: Implementation with cold atoms and steady-state properties. *Phys. Rev. A*, 87:022110, 2013.

[225] D. M. Basko, I. L. Aleiner, and B. L. Altshuler. Metal-insulator transition in a weakly-interacting many-electron system with localized single-particle states. *Ann. Phys. (N. Y.)*, 321:1126, 2006.

[226] M. Žnidarič and M. Horvat. Transport in a disordered tight-binding chain with dephasing. *Eur. Phys. J. B.*, 86:1, 2013.

[227] E. Arrigoni. Crossover to Fermi-liquid behavior for weakly coupled Luttinger liquids in the anisotropic large-dimension limit. *Phys. Rev. B*, 61:7909–7929, Mar 2000.

[228] G. Soda, D. Jérome, M. Weger, J. Alizon, J. Gallice, H. Robert, J. M. Fabre, and L. Giral. Electronic properties of TTF-TCNQ: an NMR approach. *J. Phys. France*, 38:931, 1977.

[229] P. Pacheco. *An Introduction to Parallel Programming*. Morgan Kaufmann, United States, 2011.

[230] P. W. Anderson. Absence of Diffusion in Certain Random Lattices. *Phys. Rev.*, 109:1492, 1958.

[231] C. Hess. Heat conduction in low-dimensional quantum magnets. *Eur. Phys. J. Special Topics*, 151:73, 2007.

[232] M.T. Batchelor, X.W. Guan, N. Oelkers, and Z. Tsuboi. Integrable models and quantum spin ladders: comparison between theory and experiment for the strong coupling ladder compounds. *Adv. Phys.*, 56:465, 2007.

[233] A. Sharma and M. Haque. Fine structures in the spectrum of the open-boundary Heisenberg chain at large anisotropies. *Phys. Rev. A*, 89:043608, 2014.

[234] R. T. Gregory and D. L. Karney. *A Collection of Matrices for Testing Computational Algorithms*. Robert E. Krieger Publishing Co., New York, 1978.

[235] N. S. Wingreen, K. W. Jacobsen, and J. W. Wilkins. Inelastic scattering in resonant tunneling. *Phys. Rev. B*, 40:11834–11850, 1989.

[236] W. Barford. *Electronic and Optical Properties of Conjugated Polymers*. Oxford University Press, Oxford, 2005.